UNIVERSITY OF SOUTHAMPTON

FACULTY OF ENGINEERING, SCIENCE & MATHEMATICS

School of Ocean and Earth Science

Three–dimensional traveltime tomography of Ascension Island and the Mendocino Triple Juction area

by

Christos P. Evangelidis

This dissertation is submitted for the degree of Doctor of Philosophy

August 2004

UNIVERSITY OF SOUTHAMPTON

ABSTRACT

FACULTY OF ENGINEERING, SCIENCE & MATHEMATICS

SCHOOL OF OCEAN AND EARTH SCIENCES

Doctor of Philosophy

THREE–DIMENSIONAL TRAVELTIME TOMOGRAPHY OF ASCENSION ISLAND AND THE MENDOCINO TRIPLE JUNCTION AREA

by Christos P. Evangelidis

Seismic traveltime tomography was performed on two wide-angle three-dimensional datasets in the regions around Ascension Island and the Mendocino Triple Junction.

Ascension Island forms the summit of a large volcanic edifice in the equatorial Atlantic. The experiment covers an area roughly 80 km $\times$ 70 km and consists of offshore shots received on land and at sea. The shallow extrusive part of the Ascension edifice reveals two main high velocity regions coinciding with the highest topography on land and a gravity maximum off the west coast of the island, respectively. These features are connected to a high velocity intrusive core that is created either within or on the top of oceanic Layer 3 and is interpreted as a possible relic magma chamber. The thickness of the surface low velocity region is similar to that observed at Hawaii, Jasper Seamount and Great Meteor Seamount, suggesting a similar process of edifice construction. There is no evidence for magmatic underplating beneath Ascension Island. There is no simple flexural model that explains the shape of the Moho beneath the island, perhaps because of the long lived volcanism and the proximity of the island to the Mid-Atlantic Ridge and the Ascension Fracture Zone. The second experiment collected wide-angle seismic data around the Mendocino Triple Junction in and offshore northern California, and covered an area roughly 280 km $\times$ 270 km. The results of a first arrival tomographic model are complemented by the results of a model based on P_g arrivals. In addition to the seismic tomography model, the hypocentre of earthquakes that occurred within the study area between 1977 and 2002 are relatively relocated using source-specific station terms and waveform cross correlation techniques. A unifying 3D picture of the Mendocino triple junction velocity structure is in agreement with most previously published 2D seismic studies. Apart from extending the major velocity features in three-dimensions, this study also reveals significant offline features that were not imaged before. High velocity bodies within the North America crust are possibly related to outliers of the Coastal Range ophiolites. The San Andreas fault cuts through the crust, separating the Pacific plate from North America. It passes onshore north of Point Delgada, with the King Range terrane being a part of the Pacific plate or a sliver in the boundary zone. Offshore, within the Vizcaino block, an oceanic high velocity body is observed within the upper crust, independent from the underlying lower crust. North of the Mendocino fault the subducting Gorda slab appears to be internally deformed as it approaches the triple junction in a series of dipping vertical velocity offsets, from northwest to southeast, and intra-slab seismicity in NE–SW lineations. The relocated Petrolia earthquake, in April 1992, is a Cascadia thrust event that triggers shallower events up-dip the thrust and within the North America accreted terranes, as well as events deep into the subducting slab and the subducting Moho.

Finally, some limitations of the forward and inverse methods used in active source tomography have been also explored.

Graduate School of the Southampton Oceanography Centre

This PhD dissertation by

Christos P. Evangelidis

has been produced under the supervision of the following persons

Supervisors

Dr. Timothy Henstock

Dr. Timothy Minshull

Prof. Bob Whitmarsh

Chair of Advisory Panel

Prof. Harry Bryden

DECLARATION OF AUTHORSHIP

I, **Christos P. Evangelidis**, declare that the thesis entitled

Three–dimensional traveltime tomography of Ascension Island and the Mendocino Triple Juction area

and the work presented in it are my own. I confirm that:

- this work was done wholly or mainly while in candidature for a research degree at this University;
- where any part of this thesis has previously been submitted for a degree of any other qualification at this University or any other institution, this has been clearly stated;
- where I have consulted the published work of others, this is always clearly attributed;
- where I have quoted from the work of others, the source is always given. With the exception of such quotations, this thesis is entirely my own work;
- I have acknowledged all main sources of help;
- where the thesis is based on work done by myself jointly with others, I have made clear exactly what was done by others and what I have contributed myself;
- parts of this work have been publiced as: Evangelidis, C.P., Minshull, T.A. and Henstock, T.J. Three-dimensional crustal structure of Ascension Island from active source seismic tomography, 2004, *Geophysical Journal International*, **159**, 311–325.

Signed:

Date:

To my parents

Chapter 1

Introduction

Seismology, a branch of the various geophysical applications, studies elastic waves transmitted through the Earth to deduce its internal structure and the physics of earthquakes. The energy of large magnitude earthquakes transmitted from their source to conveniently located stations enabled seismologists to discover large-scale structural divisions within the earth, such as the Moho velocity discontinuity which separates the crust from the mantle (Mohorovicic, 1910).

Passive seismic studies rely on a station network that is deployed in the area of interest to record local, regional, and teleseismic earthquakes, in terms of distance between the earthquake hypocentre and the station, over a relatively long period of time (months or years). Despite providing a relatively cheap source for seismic experiments, earthquakes' unpredictable occurrence, their relative hypocentral uncertainty and the fact that they occur mostly at plate boundaries limits considerably the resolution that these sources provide in most areas.

Although, exploration seismology uses controlled man-made sources (active sources), it basically follows the same approach used in passive experiments with the deployed station network remaining in place for short periods (days).

1.1 Seismic tomography

In seismic tomography, cross-sectional images of the Earth's internal structure are reconstructed from observations and recordings of differences in the passage of seismic waves through the Earth. These waves can be assessed either using full waveforms (waveform tomography) or just arrivals of a particular seismic phase. In the latter case, the primary technique measures the time required for natural or man-made elastic waves to travel from their source to receivers deployed on land or at sea. These arrival times and their differences contain information on

the seismic velocities of the medium they travelled through. Thus, in so-called seismic traveltime tomography, the traveltimes are the observable data and the velocity structure of the Earth interior are the model parameters that should relate mathematically to the data. Evaluation of the model parameters requires the application of inverse theory as well as forward modelling. In a forward problem with known model parameters we can predict some measurements/data for particular conditions. In the inverse problem the reverse procedure is applied, where we estimate model parameters from observations/data.

As a simple example, consider a homogeneous Earth where an earthquake wave travels from its hypocentre, with velocity c, to the surface. The recorded time T of the wave arrival at different seismographs to the surface is related to the distance x from the hypocentre by equation $T(x) = \frac{1}{c}x + t_o$, where t_o is the time the event occurred at its origin. In this case, the forward theory can be applied by knowing the velocity c and the origin time t_o and by solving the formula for any desired distance, to predict the time the wave arrives at each station. For the simplest inverse problem some recorded times T_i are known for a set of distances x_i in various stations and we wish to determine the model parameters c and t_o. This is a simple problem of fitting a straight line to the data, even though it is much harder than the forward evaluation of a formula. The problem becomes more complicated if the hypocentral location parameters are unknown and consequently the assumed distances x_i. In this case, which represents the traditional earthquake location problem, an average velocity distribution c has to be assumed in order to estimate the hypocentral parameters from observed traveltimes.

In wide-angle seismic experiments a station network deployed either on land and/or at sea records seismic waves, usually from active sources, at long offsets. Traveltimes of wide-angle refractions and reflections allow the construction of 2D or 3D velocity models. Although 2D datasets are acquired more cheaply and modelled faster, the 3D exploration of structures is becoming more desirable, as it produces a more complete picture of the structure of an area. Usually, the traveltime arrival data in wide-angle tomography experiments either originate as waves reflected at velocity discontinuities, like the P_mP or S_mS reflections at the Moho boundary, or, more often, from waves refracted through the crust, P_g, S_g, and the upper mantle, P_n, S_n. A review of the forward and inverse theory in traveltime tomography and their applications to the algorithms used in this thesis are described in Chapter 2.

1.2 Aims, objectives and structure of this study

The main aim of this study is to obtain two three-dimensional velocity models by applying seismic tomography methods in two wide-angle experiments in geologically contrasting regions.

The first wide-angle dataset is from the area of Ascension Island, which forms the summit of a large volcanic edifice in the equatorial Atlantic. The experiment covers an area of roughly 80 km $\times$ 70 km and consists of offshore shots received at ocean bottom hydrophones and sonobuoys offshore, and land stations on the island. Controlled source seismic studies of oceanic volcanic islands can give useful information on the rheology of the underlying lithosphere and the magmatic processes that create such volcanic edifices. For example, seismic models provide useful constraints on the volume and shape of volcanic edifices, allowing conclusions to be drawn on magma generation rates (e.g., Watts et al., 1997). Moreover, lithospheric flexure, related to the duration of the edifice loading and the resulting dynamic effects in the underlying mantle, can be measured by mapping the Moho and the top of the oceanic crust. A detailed description of the aims and objectives, analysis and inversion approach, and the results of the wide angle seismic experiment acquired on and around Ascension Island is given in Chapter 3.

The second experiment collected wide-angle seismic data around the Mendocino triple junction, on and offshore northern California. The experiment spans a change in tectonics from the southern end of the Cascadia subduction zone into the northernmost part of the San Andreas strike slip fault system. The area covered is roughly 280 km $\times$ 270 km and consists of offshore and onshore shots received at OBH/S offshore, and land stations. A three-dimensional velocity model of the triple junction area is useful to understand the geological evolution of the Californian margin and to assess potential earthquake hazards for this very active area. A detailed description of the aims and objectives, analysis and inversion approach, and the results of the wide angle seismic experiment acquired around Mendocino triple junction is given in Chapter 4. In addition to the seismic tomography model, the hypocentres of earthquakes that occurred within the study area, between 1977 and 2002, are relatively relocated using source-specific station terms and waveform cross correlation techniques to better comprehend the tectonic evolution of the area. The earthquake relocation modelling and results, together with a discussion integrating the tomography and earthquake relocation results are given in Chapter 5.

The modelling of these two active source wide-angle experiments is performed

using two different tomographic algorithms; Jive3D by Hobro et al. (2003) for the Ascension Island and FAST by Zelt & Barton (1998) for the Mendocino region. Using these two algorithms, that differ in the forward, inverse and parameterisation approach, it is possible to explore some limitations of the active source tomography methods. For the forward step, where synthetic traveltimes are calculated through an assumed velocity model, the differences between a raytracing perturbation method (e.g. Virieux & Farra, 1991) and a finite difference eikonal solver (e.g. Vidale, 1990) can be addressed in terms of precision, the ability to obtain traveltimes for all observed arrivals and, finally, through computing requirements. The inversion approach for the two experiments will differ as both depend on the forward method and the parametrisation of the model. Despite these differences, the main objective is to develop three-dimensional velocity models that are as much independent as possible from the initial ones. Finally, the way resolution is estimated in a 3D tomographic model is also sought. In this study a 3D checkerboard test is applied to the final models, obtaining the most linear resolution results and imaging the resolved velocity anomalies in all dimensions. Chapter 6 summarises the tomography limitations were met through modelling these two datasets, followed by conclusions on the results of both experiments. This study is completed with some thoughts on additional future work.

Chapter 2

Traveltime Tomography

2.1 Forward problem

2.1.1 Introduction

The first step towards the solution of the inverse problem in traveltime tomography is an efficient method for the calculation of traveltimes in a three-dimensional structure. Forward calculation through an initial guessed model will produce a vector of synthetic traveltimes $\mathbf{t_{calc}}$. The travel time residual vector $\mathbf{r}$ describes the difference between the observed traveltimes $\mathbf{t}_{obs}$ and the calculated synthetic traveltimes $\mathbf{t_{calc}}$ as:

$$\mathbf{r} = \mathbf{t_{obs}} - \mathbf{t_{calc}}. \tag{2.1}$$

The travel time residual vector $\mathbf{r}$ is the subject of optimisation in the inversion step.

A brief summary of the derivation of the wave and the ray equations is given in the following section. For more detailed descriptions and derivations, refer to textbooks such as Shearer (1999), Lay & Wallace (1995) and Officer (1974). A description of the basic methods in traveltime calculations follows, with emphasis on the methods used in this project.

2.1.2 Derivation of the wave, eikonal, and ray equations

The equation of motion for a homogeneous continuum with absence of body forces (e.g. gravity) is

$$\rho \frac{\partial^2 u_i}{\partial t^2} = \frac{\partial \sigma_{ij}}{\partial x_j}, \tag{2.2}$$

where ρ is the density, $\mathbf{u}$ the displacement, σ_{ij} the stress tensor for an arbitrary element in the continuum and i, j, k the three-dimensions indexes. Stress and strain are linked in an isotropic elastic solid by *Hooke's Law*

$$\sigma_{ij} = \lambda\epsilon_{kk}\delta_{ij} + 2\mu\epsilon_{ij}, \tag{2.3}$$

where ϵ_{kk} is the change in volume per unit volume (dilatation), ϵ_{ij} the components of the strain tensor for this arbitrary element, λ and μ the two parameters of the elastic modulus (Lame parameters) and δ_{ij} is the *Kronecker delta* function ($\delta_{ij} =$ 1 for i = j, $\delta_{ij} = 0$ for i $\neq$ j). The strain-displacement relationship is

$$\epsilon_{ij} = \frac{1}{2}\left(\frac{\partial u_i}{\partial x_j} + \frac{\partial u_j}{\partial x_i}\right). \tag{2.4}$$

We combine the homogeneous equation of motion (2.2), Hooke's Law (2.3) and strain-displacement relationship (2.4) to derive an *equation of motion* for an isotropic linear elastic medium with no body forces:

$$\rho\frac{\partial^2\mathbf{u}}{\partial t^2} = (\lambda + 2\mu)\nabla(\nabla\cdot\mathbf{u}) - \mu\nabla\times\nabla\times\mathbf{u}. \tag{2.5}$$

This is a standard form of the seismic wave equation in homogeneous media and is only an approximate expression, which has neglected the gravity and velocity gradient terms, and has assumed a linear elastic, isotropic Earth model. Equation (2.5) represents a complicated, three-dimensional, partial differential equation for displacements in a continuum, which are initiated by a unspecified source. *Helmholtz's* decomposition theorem represents the displacement field $\mathbf{u}$ as

$$\mathbf{u} = \nabla\phi + \nabla\times\mathbf{\Psi}, \qquad \nabla\cdot\mathbf{\Psi} = 0 \tag{2.6}$$

where ϕ is a curl-free scalar potential field and $\mathbf{\Psi}$ is a divergence-free vector potential field. Physically, this means that a curl-free field involves no shear motion and a divergence-free field involves motion with no change in volume. Using the vector identity

$$\nabla\times\nabla\times\mathbf{\Psi} = -\nabla^2\mathbf{\Psi} \qquad \text{for} \qquad \nabla\cdot\mathbf{\Psi} = 0, \tag{2.7}$$

we may rewrite equation (2.5) as

$$\nabla\left[(\lambda + 2\mu)\nabla^2\phi - \rho\ddot{\phi}\right] + \nabla\times\left[\mu\nabla^2\mathbf{\Psi} - \rho\ddot{\mathbf{\Psi}}\right] = 0. \tag{2.8}$$

This equation is satisfied if

$$\nabla^2\phi - \frac{1}{\alpha^2}\frac{\partial^2\phi}{\partial t^2} = 0 \qquad \text{and} \qquad \nabla^2\boldsymbol{\Psi} - \frac{1}{\beta^2}\frac{\partial^2\boldsymbol{\Psi}}{\partial t^2} = 0 \tag{2.9}$$

where

$$\alpha = \sqrt{\frac{\lambda + 2\mu}{\rho}} \qquad \text{and} \qquad \beta = \sqrt{\frac{\mu}{\rho}}. \tag{2.10}$$

Solving the equation of motion (2.5) involves solving wave equations like (2.9) where the displacement field comprises two different wave types: compressional waves travelling at P–wave velocity α and shear waves travelling at S–wave velocity β, with both distinct velocities determined by the material properties of the medium. Although the wave equations have been derived under the homogeneous media assumption, they are a good approximation for heterogeneous media, if the elastic properties of the medium do not change significantly over a single wavelength. Solutions of (2.9) are of the form (for P-waves)

$$\phi = A(\mathbf{x})e^{-i\omega T(\mathbf{x})} \tag{2.11}$$

where $T(\mathbf{x})$ is a phase factor and A is the local amplitude. Substituting (2.11) to (2.9) we obtain

$$\nabla^2 A - \omega^2 A|\nabla T|^2 - i[2\omega\nabla A \cdot \nabla T + \omega A\nabla^2 T] = -\frac{A\omega^2}{\alpha^2}. \tag{2.12}$$

The real part of this equation gives

$$\nabla^2 A - \omega^2 A|\nabla T|^2 = -\frac{A\omega^2}{\alpha^2}, \tag{2.13}$$

and dividing this equation by $A\omega^2$ and rearranging, we have

$$|\nabla T|^2 - \frac{1}{\alpha^2} = \frac{\nabla^2 A}{A\omega^2}. \tag{2.14}$$

Using the high frequency approximation where ω is sufficiently large the term in $1/\omega^2$ can be ignored and equation (2.14) becomes

$$|\nabla T|^2 = \frac{1}{\alpha^2}. \tag{2.15}$$

A similar equation can be derived for S–waves. Therefore, a general form of the previous equation is

$$|\nabla T|^2 = \frac{1}{c^2} \tag{2.16}$$

where c is the local P–wave velocity α or S–wave velocity β. This is the standard form of the *eikonal equation*. We can also write the previous equation in the expanded form

$$|\nabla T|^2 = \frac{\partial^2 T}{\partial x_i^2} + \frac{\partial^2 T}{\partial x_j^2} + \frac{\partial^2 T}{\partial x_k^2} = u^2 \tag{2.17}$$

where $u = 1/c$ is the slowness and the phase vector $T(\mathbf{x})$ is called also the travel time function.

Equation (2.17) is of fundamental importance because it leads directly to the concept of rays, which is useful when the slowness u is not constant but a function of space coordinates, $u(\mathbf{x})$. The eikonal equation is an approximate solution valid only if velocity and amplitude gradients in the medium are small over one seismic wavelength. It forms the basis for ray theoretical approaches to model seismic wave propagation and calculate traveltimes within a medium. The solution of the eikonal equation, $T(\mathbf{x}) = constant$, represents surfaces in three-dimensional space where points on them undergo the same motion at a given instant of time and they called *wavefronts*. Local normals to these surfaces are called *rays* and define the direction of the energy propagation. Therefore, the function $T(\mathbf{x})$ represents the time required for a wavefront to reach $\mathbf{x}$ as it propagates with local slowness in a direction parallel to the rays.

Consider a three-dimensional wave surface $T(\mathbf{x})$ and a ray which is normal to the wavefront, characterised by travelling arc length s in time t. The direction cosines dx_i/ds, dx_j/ds, dx_k/ds associated with the ray must satisfy:

$$\left(\frac{dx_i}{ds}\right)^2 + \left(\frac{dx_j}{ds}\right)^2 + \left(\frac{dx_k}{ds}\right)^2 = 1 \tag{2.18}$$

The gradient of a function (surface) is oriented normal to that function and therefore $\nabla T(\mathbf{x}) \propto s$. We can then see that $\partial T(\mathbf{x})/\partial x_i$ is proportional to dx_i/ds for the i dimension in space and therefore

$$\frac{dx_i}{ds} = n\frac{\partial T}{\partial x_i} \tag{2.19}$$

where n is a constant. Substituting (2.19) for all spatial coordinates to (2.18) and comparing with (2.17) indicates that (2.18) is the eikonal equation if $n = c = 1/u$

so that:

$$\frac{1}{c}\frac{d\mathbf{x}}{ds} = \nabla T. \tag{2.20}$$

Differentiating (2.20) along the raypath s we obtain the *raypath equation*:

$$\frac{d}{ds}\left(\frac{1}{c(\mathbf{x})}\frac{d\mathbf{x})}{ds}\right) = \nabla\left(\frac{1}{c(\mathbf{x})}\right) \tag{2.21}$$

where s is the path length parameter, $c(\mathbf{x})$ the 3D velocity field and $\mathbf{x}$ the position vector along the ray. Equation (2.21) can also be written as a set of 6 coupled first-order equations (Thurber & Kissling, 2000):

$$\frac{d\mathbf{x}}{ds} = c(\mathbf{x})\mathbf{p} \qquad \text{and} \qquad \frac{d\mathbf{p}}{ds} = \nabla\left(\frac{1}{c}\right) \tag{2.22}$$

where $\mathbf{p} = \nabla T$ is the slowness vector. Equation (2.21) and (2.22) determine the rays in terms of the velocity field. When the ray trajectory has been obtained, travel times can be calculated with integration of the *eikonal* along the raypath:

$$T = \int_{path} |\nabla T| ds = \int_{path} \left(\frac{1}{c(\mathbf{x}(s))}\right) ds. \tag{2.23}$$

The integration of this scalar quantity will not depend on the direction of integration, resulting the principle of *reciprocity*, where traveltime from A to B is equal to traveltime from B to A.

2.1.3 Raytracing methods

The number of methods and techniques of calculating traveltimes and determining raypaths is too large to be presented in detail here. Thurber & Kissling (2000) give a brief but concise description of the methods to date. This methods could be exact or approximate and fall into four different computational style categories: shooting, bending, perturbation and grid-based techniques.

The shooting and bending methods are termed as the standard methods using differential equations (2.21) and (2.22). The bending method assumes an initial path estimate fixed at both end-points and perturbs the path until it will satisfy the ray equations. The shooting method with a specified propagation direction and starting point adjusts iteratively the propagation direction until it reaches the target point. Both methods suffer from high computational cost, possible convergence to a local minimum and instability due to their non-linear nature. Julian & Gubbins (1977) present a complete overview of these techniques.

Perturbation methods start with a path that is close to the desired raypath and calculate perturbations to this path in order to bring it closer to the true raypath. Starting paths can be either real raypaths estimated with a shooting method with an end-point not so far from the desired one, or paths that are not true raypaths but that connect the real end points. Based on the ray equations two perturbation methods types have been developed using the *Lagrangian Formulation* and the *Hamiltonian Formulation* of the ray equations.

The Lagrangian Formulation uses Equation (2.21) and is described in full by Snieder & Sambridge (1992). Points in the original and perturbed paths can be related either by being positioned at equivalent fractional distances of the total arc length or being displaced in a normal direction to the reference curve (Thurber & Kissling, 2000). The Paraxial approach based on the Hamiltonian Formulation of the ray equation is described in the next section. Additionally to the previous two perturbation methods the Integral Method which involves double integration of equation (2.21) was proposed by Sun (1993). An alternative of the previous methods which does not require solving of the differential equation (2.21) and (2.22) is the Fermat's Principle Approach which tries to minimise directly the travel time integral from the source to receiver, by estimating perturbations to the path (Thurber & Kissling, 2000).

Alternatively, the calculation of the traveltime field from a source to all other points of a grid using *finite differences* or *graph theory* is a very popular and fast approach for the calculation of traveltimes and the estimation of raypaths and are termed as *Grid-Based Methods*. For the graph methods a set of nodes is connected with all possible paths. The length of the path segments are the corresponding traveltimes and the shortest path is identified via sorting routines (e.g. Moser, 1991). The requirement for a large number of nodes in order to obtain computational accuracy is the greatest disadvantage of this method.

In the next two sections we describe the two different forward methods incorporated in the tomographic algorithms that were used in this project: the ray perturbation method using the Hamiltonian Formulation approach described by Virieux & Farra (1991) and used in Jive3D (Hobro et al., 2003), and the finite difference technique described by Vidale (1990), with modifications by Hole & Zelt (1995), used in FAST (Zelt & Barton, 1998).

2.1.4 Ray-perturbation – Paraxial approximation

The perturbation method which follows the Hamiltonian Formulation of the ray equation is described in detail by Virieux et al. (1988), Farra (1990), Virieux & Farra (1991), and Hobro (1999), and is used in the forward step of the Jive3D tomography algorithm (Hobro et al., 2003). Although analytical computation of raypaths is not possible for complex but smoothly varying velocity media this ray perturbation method allows a semi-analytical solution to be obtained by ray-tracing within a medium with constant gradient of the slowness squared $u^2(\mathbf{x})$, which makes analytical solutions both for raytracing and application of the ray perturbation method simpler (Farra, 1990).

The Hamiltonian for isotropic media proposed by Burridge (1976) is

$$H(\mathbf{x},\mathbf{p};\tau) = \frac{1}{2}[\mathbf{p}^2 - u^2(\mathbf{x})] \tag{2.24}$$

where $\mathbf{x}$, $\mathbf{p}$ the position and slowness vectors, $u(\mathbf{x})$ the slowness function and τ the ray parameter defined by $u\delta\tau = \delta s$ and consequently is related to traveltime T with:

$$dT = u^2(\mathbf{x})d\tau. \tag{2.25}$$

The Hamiltonian formulation for ray equations (with respect to τ) can be derived:

$$\frac{d\mathbf{x}}{d\tau} = \nabla_p H = \mathbf{p} \qquad \text{and} \qquad \frac{d\mathbf{p}}{d\tau} = -\nabla_x H = \frac{1}{2}\nabla_x u^2 = u\nabla_x u \tag{2.26}$$

where ∇_x and ∇_p denote gradients with respect to the vectors $\mathbf{x}$ and $\mathbf{p}$ respectively. Note that τ does not have any particular physical meaning, but increases along the raypath. It is just mathematically convenient to describe the velocity structure in terms of the slowness squared function $u^2(\mathbf{x})$.

The squared slowness within an element of the medium where the gradient $\mathbf{\Gamma}$ of the squared slowness is constant is:

$$u^2(\mathbf{x}) = u_0^2 + \mathbf{\Gamma}\cdot\mathbf{x}. \tag{2.27}$$

Putting (2.24) and (2.27) into (2.26) and solving the ray tracing equations gives

$$\mathbf{p}(\tau) = \frac{1}{2}\mathbf{\Gamma}(\tau - \tau_0) + \mathbf{p}(\tau_0) \tag{2.28}$$

$$\mathbf{x}(\tau) = \frac{1}{4}\mathbf{\Gamma}(\tau - \tau_0)^2 + (\tau - \tau_0)\mathbf{p}(\tau_0) + \mathbf{x}(\tau_0) \tag{2.29}$$

where $\mathbf{x}(\tau_0)$ and $\mathbf{p}(\tau_0)$ are the initial position and slowness of the ray in this element. We can calculate traveltime by direct integration of the relation (2.25) using equation (2.26):

$$T(\tau) = \int_{\tau_0}^{\tau} u^2(\mathbf{x}) d\tau \tag{2.30}$$

and, finally, using equations (2.28) and (2.29) the total traveltime is obtained

$$\begin{aligned} T(\tau) = T(\tau_0) + [u_0^2 + \mathbf{\Gamma} \cdot \mathbf{x}(\tau_0)](\tau - \tau_0) \\ + \frac{1}{2}\mathbf{\Gamma} \cdot \mathbf{p}(\tau_0)(\tau - \tau_0)^2 + \frac{1}{12}\mathbf{\Gamma}^2(\tau - \tau_0)^3. \end{aligned} \tag{2.31}$$

Assuming that a ray has been traced in the reference medium with slowness distribution $u_0(\mathbf{x})$, a smooth perturbation of the squared slowness of the model

$$\mathbf{u^2} = \mathbf{u_0^2} + \Delta\mathbf{u^2}, \tag{2.32}$$

will produce a corresponding perturbation in the Hamiltonian $H = H_0 + \Delta H$ where H_0 is the Hamiltonian for the reference medium and $\Delta H = -\frac{1}{2}\Delta u^2$. From Farra (1990) the perturbation to the position and slowness is

$$\begin{aligned} \Delta\mathbf{x}(\tau) = \Delta\mathbf{x}(\tau_0) + (\tau - \tau_0)\Delta\mathbf{p}(\tau_0) \\ + \frac{1}{2}\int_{\tau_0}^{\tau} (\tau - \tau')\nabla(\Delta u^2(\mathbf{x}))d\tau' \end{aligned} \tag{2.33}$$

$$\Delta\mathbf{p}(\tau) = \Delta\mathbf{p}(\tau_0) + \frac{1}{2}\int_{\tau_0}^{\tau} \nabla(\Delta u^2(\mathbf{x}))d\tau', \tag{2.34}$$

where $\Delta\mathbf{x}(\tau_0)$ and $\Delta\mathbf{p}(\tau_0)$ is the previous perturbation, which will be equal to zero if it is the first perturbation applied to the reference ray. The perturbation of the traveltime along the perturbed ray is

$$\Delta T(\tau) = \int_{\tau_0}^{\tau} \mathbf{\Gamma} \cdot \Delta\mathbf{x} d\tau' + \int_{\tau_0}^{\tau} \Delta u^2[\mathbf{x_0}(\tau')]d\tau'. \tag{2.35}$$

Equations (2.33), (2.34) and (2.35) are expressed in terms of the parameter τ, the known initial values of $\mathbf{x}$ and $\mathbf{p}$ and the slowness squared function. Taylor's expansion of all the integral terms reveals polynomial expressions which can be solved analytically. This first order linear technique of perturbing rays is termed as the paraxial approximation (Virieux & Farra, 1991).

Virieux & Farra (1991) proposed a finite element method in which the medium is discretized into cells with quadratic B-spline interpolation of the square of the

slowness between them in order to avoid problems with second-order discontinuities at the edges of cells. All rays are traced through the medium in a cell-by-cell basis, where ray and paraxial ray tracing is performed analytically within each cell. Raytracing reduces to connecting the solutions between cells. Hobro (1999) developed a binary search algorithm to determine the values of τ at which intersections occur between rays and surfaces of the model.

When the final position, final slowness and traveltime have been determined for a ray segment within each cell in the grid, the *Frèchet* derivatives, that relate the model parameters (velocity and interface) within this cell with the traveltimes, are obtained. Small perturbations of the raypath within the cell produce very small changes in the traveltime. Changes in slowness along the raypath are related to changes in traveltimes by

$$\Delta T \approx \int_{\mathbf{x_0}(s)} \Delta u(\mathbf{x}) ds, \tag{2.36}$$

which is the change of slowness integrated along the original raypath (Hobro, 1999). Therefore, the Frechet derivative of traveltime with respect to jth model parameter is

$$\frac{\partial T}{\partial m_j} = \frac{\partial}{\partial m_j} \int_{\mathbf{x_0}(s)} u(\mathbf{x}) ds = \int_{s_1}^{s_2} \frac{\partial [u(\mathbf{x})]}{\partial m_j} ds = \int_{s_1}^{s_2} \frac{\partial [u^2(\mathbf{x})]}{\partial m_j} d\tau. \tag{2.37}$$

Expanding (2.37) we get expressions of derivatives that relate characteristics of the medium such as $u^2(\mathbf{x_0})$, $\mathbf{\Gamma_0}$ and $\Delta u^2(\mathbf{x})$ to model parameters. Such derivatives can be evaluated considering that the slowness squared field within each cell is described by

$$u^2(\mathbf{x}) = \sum_{j=1}^{27} B_2^{3D}(\mathbf{x}, \mathbf{x_j}) m_j, \tag{2.38}$$

where $B_2^{3D}(\mathbf{x}, \mathbf{x_j})$ is the quadratic B-spline in three dimensions, $m_1, \cdots, m_{27}$ are the slowness squared B-spline coefficients and $\mathbf{x}_1, \cdots, \mathbf{x}_{27}$ the corresponding node positions of 27 model parameters that influence the slowness squared function within the cell (Hobro, 1999). To solve for the inverse problem the model parameters have to be converted back to units of velocity by the relation ($m_c = 1/\sqrt{m_u^2}$) and the Frechet derivatives by the relation

$$\frac{\partial T}{\partial m_c} = -\frac{2}{(m_u)^2} \frac{\partial T}{\partial m_u^2}. \tag{2.39}$$

Changes in traveltimes due to perturbation of interface depth are related, using

Snell's Law (Hobro, 1999), by

$$\Delta T = \delta p_3 \delta z \tag{2.40}$$

where δp_3 is the change in the vertical component of the slowness vector and δz the change in interface depth. Interfaces are defined using the cubic B-spline function

$$z(\mathbf{x}) = \sum_{j=1}^{16} B_3^{2D}(\mathbf{x}, \mathbf{x_j}) m_j, \tag{2.41}$$

where $B_3^{2D}(\mathbf{x}, \mathbf{x_j})$ is the cubic B-spline in two dimensions, $m_1, \cdots, m_{16}$ are the depth B-spline coefficients and $\mathbf{x}_1, \cdots, \mathbf{x}_{16}$ the corresponding node positions of 16 depth parameters that influence the depth function within the cell (Hobro, 1999). Therefore Frechet derivatives for interface depth parameters can be evaluated from

$$\frac{\partial T}{\partial m_j} = \delta p_3 \frac{\partial z}{\partial m_j} = \delta p_3 B_3^{2D}(\mathbf{x}, \mathbf{x_j}). \tag{2.42}$$

Rays are traced from a small number of sources to a large number of targets. For marine experiments, using the principle of reciprocity (see section 2.1.2), sources represent receivers and targets shots. Phases represent traveltime arrivals having passed through different sequence of layers or interfaces. At first a 3D ray-fan, for each phase, is propagated through the model from each source to the target surface. Each ray is defined by its coordinates x,y at the point of arrival on the target surface and the angles θ, ϕ defining the direction of heading as the ray is leaving the source. The following function describes each ray for each phase:

$$\mathbf{x} = \mathbf{f}(\Theta) \tag{2.43}$$

where $\mathbf{x} = (x, y)$ and $\Theta = (\theta, \phi)$. Dividing the previous two-dimensional function into segments where the function is monotonic, the maximum and minimum values of x, y are recorded. As a next stage, the target coordinates x_{tar}, y_{tar} are compared with the maximum and minimum values of each segment in order to identify in which segment these coordinates belong to, giving an initial estimate of Θ values to hit the target. These values are used to shoot a ray through the model towards the target, calculating the Frechet derivatives and the traveltimes. The coordinates of the arrival point are refined by successive linear interpolation of previously-traced rays within a specified tolerance (Hobro et al., 2003).

2.1.5 Finite–difference approach

The seismic traveltimes through a 3D gridded velocity model can be alternatively calculated using a finite difference approximation to the eikonal equation. Finite-difference operators are equivalent to the plane-wave approximation at the grid-cell level (Hole & Zelt, 1995). The grid based method was developed by Vidale (1988) for 2D velocity models, and Vidale (1990) for 3D velocity models, and modified by Hole & Zelt (1995) to handle large, sharp velocity contrasts. This method is described here and is used in the forward step of the FAST tomography algorithm (Zelt & Barton, 1998). As we already have shown, the eikonal equation

$$|\nabla t|^2 = \frac{\partial^2 t}{\partial x^2} + \frac{\partial^2 t}{\partial y^2} + \frac{\partial^2 t}{\partial z^2} = u^2 \tag{2.44}$$

where t the is the traveltime, x, y, z the Cartesian coordinate axes and u the slowness, relates the gradient of traveltime to slowness structure. Approximating the differential terms with finite differences, Vidale (1988, 1990) and Hole & Zelt (1995) give 1D, 2D and 3D operators as illustrated in Fig (2.1). For the 1D case the operator is

$$t_0 = t_1 + hu \tag{2.45}$$

where t_n the traveltime at the nth node, h the grid spacing and u the slowness between the nodes (Fig 2.1 a). For the 2D case the traveltime at the corner of the operator (Fig 2.1 b) is related to the known times at the other three corners by

$$t_0 = t_3 + \sqrt{2h^2u^2 - (t_2 - t_1)^2}. \tag{2.46}$$

For the 3D case, depending on the situation, three different schemes are used,

$$t_0 = t_7 + \frac{1}{\sqrt{2}}\Bigg(6h^2u^2 - (t_3 - t_2)^2 - (t_2 - t_1)^2 - \\ - (t_1 - t_3)^2 - (t_6 - t_5)^2 - (t_5 - t_4)^2 - (t_4 - t_6)^2\Bigg)^{1/2}, \tag{2.47}$$

$$t_0 = t_2 + \sqrt{2h^2u^2 - 0.5(t_4 - t_5)^2 - (t_1 - t_3)^2}, \tag{2.48}$$

$$t_0 = t_2 + \sqrt{2h^2u^2 - 0.25\Big[(t_1 - t_3)^2 + (t_5 - t_4)^2\Big]}, \tag{2.49}$$

where the operators are shown schematically in Fig 2.1 c d e respectively. The slowness u in equation 2.48 is the average slowness of the two cubes shown in Fig.

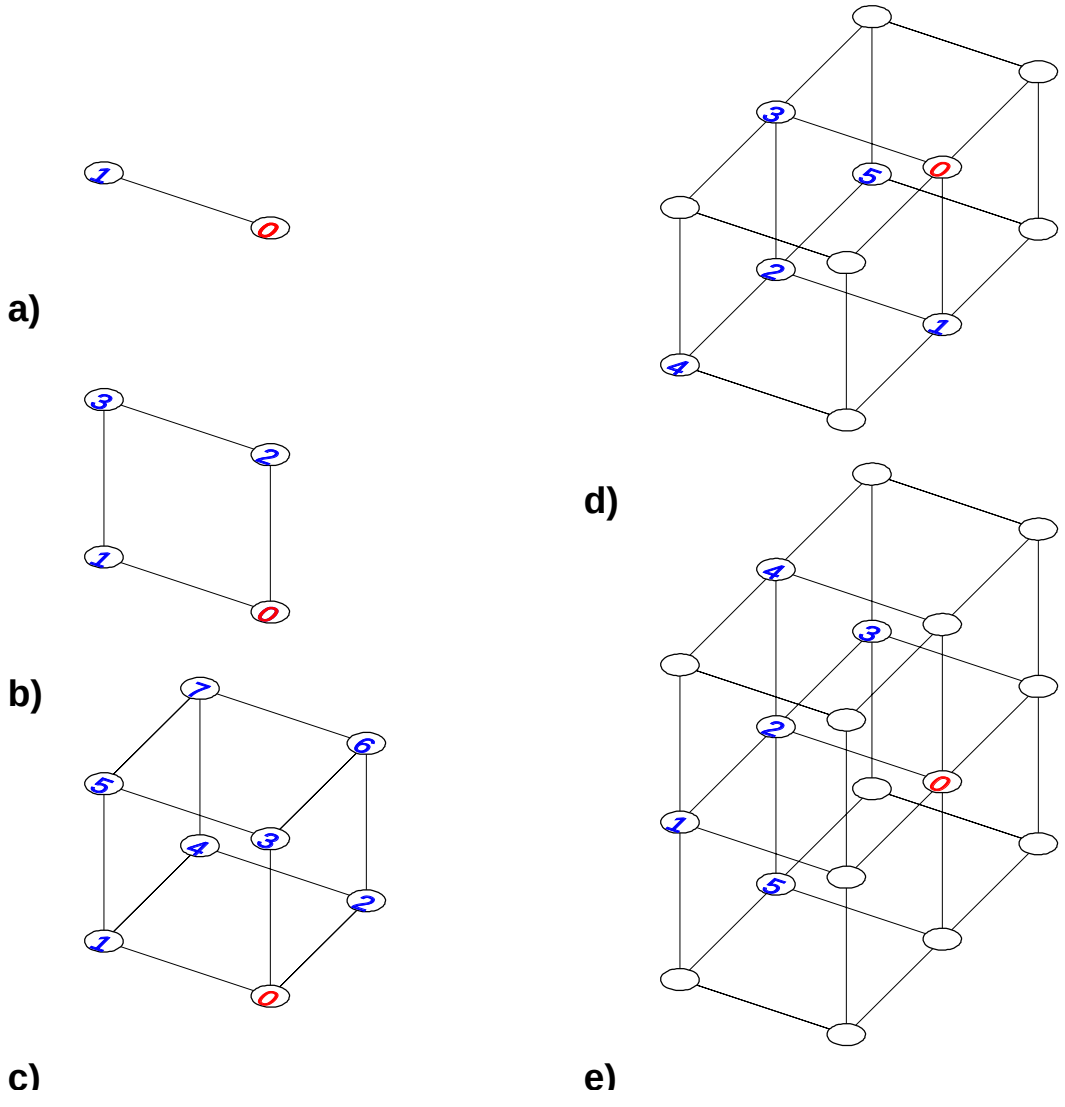

Figure 2.1: The geometry of the five finite difference operators used for computing traveltimes at node 0 on a uniform spaced grid. For each operator traveltime at node 0 is calculated knowing the traveltime at the other numbered grid points (marked in blue) and the grid spacing.

(2.1 d). For equation 2.49 the slowness u is the average slowness of the four cubes shown in Fig. (2.1 e).

Using a 3D velocity model that is sampled in discrete points with equal horizontal and vertical spacing an array of the same dimension as the velocity structure is created to record the traveltimes. First the grid point nearest to the source location is identified and the traveltimes to the four adjacent nodes are calculated with the 1D operator of equation 2.45 (Fig. 2.2, blue circles). The next four nodes will be timed using the 2D operator in equation 2.46 (Fig. 2.2, green squares) (Vidale, 1988). Expanding in the third dimension the traveltimes to each grid point of a 5x5x5 point volume surrounding the nearest grid point is calculated. Each side of

this box consists of nodes that are sorted in order of increasing traveltime from the node just behind them in the previous box. The minimum traveltime node will not have any known neighbours in this particular side so equation 2.49 is used to extrapolate values from the five nodes lying on the side behind this one (Fig. 2.1 e). When one node on this side has been timed the next one will be timed from equation 2.48 (Fig. 2.1 d). Having two timed nodes in this side the traveltime to the next node will be calculated with the most accurate equation 2.47 (Fig. 2.1 d) which is used for timing the majority of the nodes. The calculation continues iteratively for a 7x7x7 box that surrounds the previous volume and so on, in an 'expanding' cube, until traveltimes for all the grid points have been calculated. The calculation of traveltimes in grid volumes that differ from the previous ones by 2 grid points ensures that errors from the curvature of the wavefront are less than the errors introduced by an assumption of straight raypaths (Vidale, 1990).

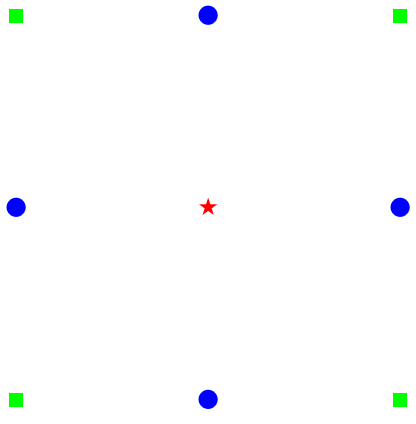

Figure 2.2: The source grid point marked as red star and the first eight points that surround the initial point. Traveltimes to blue circles calculated with 1D operators and green squares with 1D or 2D operators.

A modification was added to the method by Hole & Zelt (1995) to account for large velocity contrasts that could make diffracted or head waves travel along the edges or the sides of the expanding cubes. For example, at the grid node 0 in Fig (2.1 c) possible arrivals include: body waves that travel through the grid with times calculated using the operator in Eq. 2.47; diffracted or head waves that travel across one of the faces of the grid cell with times calculated using the 2D operator in Eq. 2.46 for all the faces that surround the grid node 0; and finally, diffracted or head waves that travel across one of the edges of the cell with times calculated using the 1D operator in Eq. 2.45 for all the edges that surround the grid node 0 (Hole & Zelt, 1995). Therefore a total of eight 3D operators, twelve 2D operators and six 1D operators can be applied to calculate the traveltime at

any grid node and based on the Fermat's principle the arrival with the shortest time is the correct one.

Following Vidale's (1990) method we can calculate traveltimes on a face of a volume from only points within the volume. It is, however, possible to have a first arrival from critically refracted waves travelling backwards. To account for this possibility Hole & Zelt (1995) proposed that during the calculation of traveltimes at nodes of an expanding volume, a flag could be raised whenever traveltimes predicted from waves travel along edges or faces. When the traveltimes have been calculated for the entire model the propagation will reverse using a wall (usually the bottom side) as a starting point. The new traveltimes will replace the forward predicted ones only if they are shorter, based on Fermat's principle of the shortest time path. Reverse propagation may be repeated multiple times in complex models.

Povdin & Lecomte (1991) solved the problem of large velocity contrasts, through the use of a parallel processing scheme, proposing a similar method which uses three separate operators in the the case of Fig (2.1 b) and sixteen operators in the the case of Fig (2.1 c) and performing a reverse propagation every time a head wave has been observed to travel along edges or faces and not at the end when the entire model had been calculated.

2.1.6 Comparison of forward methods

Raytracing of traveltime arrivals within heterogeneous media is difficult for three major reasons. First, any two points of interest might be connected by many paths in the model and therefore it is easy to miss the one with the minimum traveltime. Second, rays traced from a source cannot reach shadow zones within the model since the recorded signal is a diffracted arrival due to a secondary source. Shooting methods (e.g. Virieux & Farra, 1991) have trouble finding the correct raypath in the presence of a shadow zone; Small changes in the take-off angle results in a large change in the raypath with no ray turning within a low velocity zone. Using this method the hit rate, which represents the ratio between traced rays and observed traveltime arrivals, is typically found to be between 80% and 90% for various 2D and 3D models (e.g. Tong et al., 2003), although we obtained 95% in the Ascension study (see Chapter 3). Bending methods of raytracing (e.g. Julian & Gubbins, 1977) give a solution to this problem without however ensuring that this is not a local minimum. Third, as the acquisition of 3D datasets becomes easier and cheaper, the forward methods need to calculate many travel

	Raytracing	Finite Difference eikonal solvers
Multiple arrivals	yes	Only First and PmP
Computational Time	Long	Short
Required Memory	Regular	Increases with grid spacing
Hit Rate	less than 100%	100% of geometrical rays
Accuracy	Best	depends on grid size

Table 2.1: Major characteristics compared between forward methods

paths to a large number of sources, making the raytracing methods impractical as computer requirements for memory and execution time become unreasonable. The use of finite difference eikonal solvers on the other hand guarantees a global minimum geometrical first arrival for a shot-receiver pair, in shorter computing times. Whether this arrival is refracted, direct or diffracted will be however unknown. On the other hand raytracing methods are able to trace multiple rays to a point allowing tomography modelling using multiple picked traveltime phases (e.g. P_g, P_mP, P_n).

Accuracy is one of the challenges of each forward method. Although most methods require fine sampling of the velocity grid, raytracing methods tend to be more accurate than finite differences eikonal solvers, mainly because of the velocity model parameterisation. Raytracing equations can be derived for velocity parameterisations that allow lateral and vertical velocity gradients between the grid nodes, like the quadratic B-splines in Hobro et al. (2003), whereas the finite differences eikonal solvers require constant velocities between nodes. The accuracy of the latter depends more strongly on the grid size (Husen & Kissling, 2001). Despite calculation of traveltimes being much faster than ray perturbation calculations, the need for a very dense 3D grid to obtain accurate traveltimes increases the requirements for computer memory. Moreover, the finite difference method used by Zelt & Barton (1998) requires the same grid spacing for the bathymetry/topography interface, forcing the creation of very dense 3D velocity grids in order to avoid introduced traveltime errors due to great velocity differences across an interface. A comparison between calculated traveltimes with Virieux & Farra (1991) and Zelt & Barton (1998) methods will be attempted in Chapter 3. The accuracy of finite difference traveltimes through different grid sizes will approached in Chapter 4. Table 2.1 summarises the major characteristics of raytracing and finite difference codes.

2.2 Inverse problem

2.2.1 Introduction

The starting point in the analysis of the inverse problem in seismic tomography is the description of the data and the model. Forward calculation through an initial guessed model will produce the travel time residual vector $\mathbf{r}$ (see equation 2.1). Small perturbations $\delta\mathbf{m}$ from a model $\mathbf{m}$ will relate linearly to the traveltime misfit $\mathbf{r}$ as:

$$\mathbf{r} = \mathbf{G}\delta\mathbf{m}, \tag{2.50}$$

where $\mathbf{G}$ is a matrix that contains the partial derivatives of traveltimes with respect to the model parameters (Frechet derivatives), estimated in the forward step. Equation (2.50) is simply the Taylor expansion for the current model $\mathbf{m} + \delta\mathbf{m}$ where the higher order terms are ignored. Minimising the misfit $\mathbf{r}$ will eventually reveal the model perturbations according to the equation:

$$\delta\mathbf{t} = \mathbf{r} - \mathbf{G}\delta\mathbf{m} \approx 0. \tag{2.51}$$

However, if the model perturbation is significant, the path the energy follows (raypath) might change. Therefore, the above linear approximation is only valid for small changes in model parameters. Subsequently, if this linear problem was well constrained $\mathbf{G}$ could easily be inverted to obtain $\delta\mathbf{m}$:

$$\delta\mathbf{m} = \mathbf{G}^{-1}\mathbf{r}. \tag{2.52}$$

In reality, in seismic tomography there are model parameters that are not constrained by any data (underdetermined parts) and parameters that are constrained by multiple data (overdetermined parts). In other words, there are parts with fewer equations than unknowns and parts with more equations than unknowns. Under these circumstances the matrix $\mathbf{G}$ will be ill-conditioned and cannot be directly inverted. Methods to overcome this problem by introducing priori information or smoothing constraints will be discussed in the following section.

2.2.2 Misfit length and minimisation approach

Because of the ill-conditioning, it is unlikely that all elements of $\delta\mathbf{t}$ will be reduced to zero. Hence we wish to minimise $\delta\mathbf{t}$ and require a method of measurement of the traveltime misfit to a given model. Length methods estimate the solution of

an inverse problem by finding the model parameters that minimise a particular measure of length of the estimated misfit. The most commonly used measures of length are termed norms and are the sum of the elements of a vector raised in a power n:

$$L_1 \quad \text{norm:} \quad ||\mathbf{x}||_1 = \left[\sum_i |x_i|^1 \right] \tag{2.53}$$

$$L_2 \quad \text{norm:} \quad ||\mathbf{x}||_2 = \left[\sum_i |x_i|^2 \right]^{1/2} \tag{2.54}$$

$$L_n \quad \text{norm:} \quad ||\mathbf{x}||_n = \left[\sum_i |x_i|^n \right]^{1/n}. \tag{2.55}$$

Higher norms apply more weighting to the largest elements of $\mathbf{x}$. When, for example, $n \to \infty$ the norm gives nonzero weight only to the largest element

$$L_\infty \quad \text{norm:} \quad ||\mathbf{x}||_\infty = \max_i |x_i|. \tag{2.56}$$

The choice of norms depends on the quality of the data. If the data are sufficiently accurate and the outliers are important values then a higher order norm is chosen. When the data are noisy a lower order norm is used to avoid weighting considerably noise into the misfit. The common choice of the L_2 norm implies that the data errors follow a Gaussian distribution (Menke, 1989).

The least squares method which uses the L_2 norm can be extended to a linear inverse problem in a straightforward manner. The best-fit model perturbations δm_i will be those that lead to the smallest overall error e

$$e = \sum_i (r_i - G_i \delta m_i)^2 \tag{2.57}$$

for i model parameters. The problem then requires finding the minimum of $e(\delta\mathbf{m})$ by setting the derivatives of e with respect to the model parameters to zero and solving the resulting equations (Menke, 1989). In a matrix notation (2.57) is expressed as:

$$e = \delta\mathbf{t}^T \delta\mathbf{t} = (\mathbf{r} - \mathbf{G}\delta\mathbf{m})^T (\mathbf{r} - \mathbf{G}\delta\mathbf{m}), \tag{2.58}$$

with a solution

$$\delta\mathbf{m} = [\mathbf{G^T G}]^{-1} \mathbf{G^T} \delta\mathbf{t} \tag{2.59}$$

if $[\mathbf{G^T G}]^{-1}$ exists.

Finally, a better way to assess the quality of the fit of the produced model to

the observed picks is the χ^2 estimator

$$\chi^2 = \frac{1}{n}\sum_{i=1}^{n}\left(\frac{r_i}{\sigma_i}\right)^2, \tag{2.60}$$

where n the total number of modelled traveltime residuals r_i and σ_i the corresponding uncertainty. Provided that the uncertainties are reliable measurements of the standard deviation of the picks, then the fit of the model matches on average the assigned uncertainties and $\chi^2 = 1$.

2.2.3 Damped and smoothed least squares

Seismic tomography models consist, as stated before, of underdetermined parameters that are not sampled by any rays and overdetermined parts that are sampled by many rays. In the case that rays are crossing neighbouring parts of the model for equal distances then these parts cannot be resolved individually and are also termed underdetermined. For the underdetermined parts of the model there will be an infinite number of solutions δm for which the prediction error e will be minimised. To choose one appropriate solution requires adding to the problem some information not described by the equation $\mathbf{r} = \mathbf{G}\delta\mathbf{m}$. This information, called *a priori* information, can take many forms, and consists of assumptions that are not constrained by the real data (Menke, 1989). An a priori assumption could be that the solution is "simple", where the simplicity is just a measure of the length of the solution under the L_2 norm ($L = \delta\mathbf{m}^\mathbf{T}\delta\mathbf{m} = \sum(\delta m_i)^2$). We determine a solution that minimises a combination Ψ of the prediction error e and the solution length of the model parameters:

$$\Psi(\delta\mathbf{m}) = e + \lambda L = \delta\mathbf{t}^\mathbf{T}\delta\mathbf{t} + \lambda\delta\mathbf{m}^\mathbf{T}\delta\mathbf{m} \tag{2.61}$$

where λ is a weighting factor. If λ is large enough then both the underdetermined and overdetermined parts of the solution will be minimised without minimising the prediction error e and, therefore, not giving a true solution determined from the data. If, on the other hand, λ is set to zero then the prediction error will be minimised without taking into consideration the prior information second term that will minimise the length of the underdetermined part of the solution. The solution to the inverse problem (2.61) becomes:

$$\delta\mathbf{m} = [\mathbf{G}^\mathbf{T}\mathbf{G} + \lambda\mathbf{I}]^{-1}\mathbf{G}^\mathbf{T}\delta\mathbf{t} \tag{2.62}$$

and is called the damped least squares solution since the underdeterminacy of the inverse problem is said to have been damped (Menke, 1989). Therefore in a damped least squares approach only parts of the model that are sampled by rays will be changed in order to fit the data, whereas all other parts will remain unchanged.

Additional information can be incorporated in to the least squares minimisation by weighting the individual parameters of the data $\delta\mathbf{t}$ or model $\delta\mathbf{m}$ vectors. For example, the prediction error e_i of the observed traveltime picks with the smallest uncertainties could have greater weighting in the calculation of the overall error e such that:

$$e = \delta\mathbf{t}^T {\mathbf{C_d}}^{-1} \delta\mathbf{t} \tag{2.63}$$

where $\mathbf{C_d}$ is the data covariance matrix describing the prior uncertainty in the picks. Assuming that the picks are independent, $\mathbf{C_d}$ and its inverse will be diagonal, with nonzero elements the squared uncertainty of each traveltime pick. Weighting can also be applied in the solution length term of equation (2.61) and usually represents a measure of smoothness in the model. Smoothness in a continuous function can easily be quantified as a norm of its first derivative in the case of flatness or second derivative in the case of roughness (Menke, 1989). (see also section 2.3.1). The first derivative in discrete models is defined as the difference between two neighbouring parameters $(m_1 - m_2)$ whereas the second derivative is the difference between three neighbouring parameters $(m_1 - 2m_2 + m_3)$. The roughness of the vector $\delta\mathbf{m}$ will be $\mathbf{s} = \mathbf{S}\delta\mathbf{m}$ where $\mathbf{S}$ have rows containing [$\cdots$1 -2 1$\cdots$]. The smoothing part of the solution in the least squares sense will then take the form:

$$L = \mathbf{s}^T\mathbf{s} = [\mathbf{S}\delta\mathbf{m}]^T[\mathbf{S}\delta\mathbf{m}] = \delta\mathbf{m}^T\mathbf{S}^T\mathbf{S}\delta\mathbf{m} = \delta\mathbf{m}^T {\mathbf{C_m}}^{-1} \delta\mathbf{m} \tag{2.64}$$

where ${\mathbf{C_m}}^{-1}$ is a model weighting matrix. Minimising a combination of weighted prediction error (2.63) and weighted solution error (2.64) gives

$$\Psi(\delta\mathbf{m}) = \delta\mathbf{t}^T {\mathbf{C_d}}^{-1} \delta\mathbf{t} + \lambda\delta\mathbf{m}^T {\mathbf{C_m}}^{-1} \delta\mathbf{m} \tag{2.65}$$

called the weighted damped least squares formulation with a solution

$$\delta\mathbf{m} = [\mathbf{G}^T {\mathbf{C_d}}^{-1} \mathbf{G} + \lambda {\mathbf{C_m}}^{-1}]^{-1} \mathbf{G}^T {\mathbf{C_d}}^{-1} \delta\mathbf{t}. \tag{2.66}$$

The least squares minimisation for the additional solution length in the right

hand side of equation (2.61) $\delta\mathbf{m}^T\delta\mathbf{m}$ is not always a reliable approach since, in an inverse problem, we may require the perturbations of the model parameters to be close in a value different than zero (e.g. the average value of velocity parameters). We therefore introduce the generalised term

$$L = ((\mathbf{m_o} + \delta\mathbf{m}) - \mathbf{m_a})^T((\mathbf{m_o} + \delta\mathbf{m}) - \mathbf{m_a}) \tag{2.67}$$

where $\mathbf{m_o}$ the initial model parameters, $\delta\mathbf{m}$ the model perturbation, and $\mathbf{m_a}$ the slowness values to which we want our new model to be close. The functional we seek to minimise in the least squares sense will take the general form:

$$\Psi(\delta\mathbf{m}) = \delta\mathbf{t}^T{\mathbf{C_d}}^{-1}\delta\mathbf{t} + \lambda\Big[(\mathbf{m_o} + \delta\mathbf{m}) - \mathbf{m_a}\Big]^T{\mathbf{C_m}}^{-1}\Big[(\mathbf{m_o} + \delta\mathbf{m}) - \mathbf{m_a}\Big] \tag{2.68}$$

The choice of $\mathbf{m_a}$ defines the a priori information we introduce to the model. A requirement that the new model has to be close to the old one ($\mathbf{m_a} = \mathbf{m_o}$) resembles the damped least squares approach (2.65). A smoothed least squares approach, where the new model parameters are not required to be close to any values, is defined when $\mathbf{m_a}$ is set to zero. The way to ensure that the new model is within the linear limits, and that the unconstrained and constrained parts will take values within typical boundaries, is controlled by smoothness defined in the weighting matrix ${\mathbf{C_m}}^{-1}$. The construction of the matrix ${\mathbf{C_m}}^{-1}$ will define the smoothing approach. Therefore the inversion approach is defined, complementary to the forward method followed, by the choice of $\mathbf{m_a}$ and $\mathbf{C_m}$. We may finally write the smoothed least squares objective function as:

$$\Psi(\delta\mathbf{m}) = (\mathbf{r} - \mathbf{G}\delta\mathbf{m})^T{\mathbf{C_d}}^{-1}(\mathbf{r} - \mathbf{G}\delta\mathbf{m}) + \lambda(\mathbf{m_o} + \delta\mathbf{m})^T{\mathbf{C_m}}^{-1}(\mathbf{m_o} + \delta\mathbf{m}). \tag{2.69}$$

This objective function is the subject of minimisation in the inversion algorithms used in this thesis (Hobro et al., 2003; Zelt & Barton, 1998). This smoothed least squares objective function can also be written as the regularised linear system:

$$\begin{bmatrix} {\mathbf{C_d}}^{-1/2}\mathbf{G} \\ \sqrt{\lambda}{\mathbf{C_m}}^{-1/2} \end{bmatrix}\delta\mathbf{m} = \begin{bmatrix} {\mathbf{C_d}}^{-1/2}\mathbf{r} \\ -\sqrt{\lambda}{\mathbf{C_m}}^{-1/2}\mathbf{m_o} \end{bmatrix}. \tag{2.70}$$

A combination of both the damped and smoothed squares could also be the subject of minimisation

$$\Psi(\delta\mathbf{m}) = (\mathbf{r} - \mathbf{G}\delta\mathbf{m})^T{\mathbf{C_d}}^{-1}(\mathbf{r} - \mathbf{G}\delta\mathbf{m}) \quad +$$

$$+ \quad \lambda_D(\delta\mathbf{m})^T {\mathbf{C_{m_D}}}^{-1}(\delta\mathbf{m}) + \lambda_S(\mathbf{m_o}+\delta\mathbf{m})^T {\mathbf{C_{m_S}}}^{-1}(\mathbf{m_o}+\delta\mathbf{m}), \quad (2.71)$$

where ${\mathbf{C_{m_D}}}^{-1}$, ${\mathbf{C_{m_S}}}^{-1}$ the weighting matrices for the damping and smoothing term respectively and λ_D, λ_S control the strength of the damping and smoothing constraints. This formulation is employed in other inversion codes (e.g., Toomey et al., 1994; Van Avendonk et al., 1998).

2.2.4 Solving the inverse step: Conjugate gradient method

Minimisation of the smoothed least squares objective function (2.69), as introduced in section 2.2.2, requires to find the gradient $\nabla\Psi$, set it to zero, and solve the resulting equation. The gradient of the approximate quadratic function (2.69) takes the form:

$$\nabla\Psi(\delta\mathbf{m}) = 2\Big[(\mathbf{r}-\mathbf{G}\delta\mathbf{m})^T {\mathbf{C_d}}^{-1}\mathbf{G} + \lambda(\mathbf{m_o}+\delta\mathbf{m})^T {\mathbf{C_m}}^{-1}\Big], \quad (2.72)$$

and the curvature, the *Hessian* , of function (2.69) is:

$$\nabla^2\Psi(\delta\mathbf{m}) = 2(-\mathbf{G}^T {\mathbf{C_d}}^{-1}\mathbf{G} + \lambda {\mathbf{C_m}}^{-1}). \quad (2.73)$$

Minimisation of the objective function seeks an updated model perturbation $\delta\mathbf{m}$ that improves the fit to the data and is small enough to lie within the region of linearity (see section 2.2.1). Jumping from the initial model to the minimum (Shaw & Orcutt, 1985) will not necessarily satisfy this condition. A way to overcome this problem is to introduce a damping term (see equation 2.71) that restricts the model changing too much, but this will bias the solution towards the initial model. A better approach is to minimise the objective function towards the minimum, stopping before the end of the linearity region (Hobro, 1999). In other words, the model can 'creep' to a solution when $\mathbf{m_0}$ in each iteration equals the solution of the previous iteration. In this way the regularisation does not smooth or damp a solution close to the initial model but close to the previous step solution.

One of the most efficient and fastest ways (Nolet, 1987) to step down a quadratic function is the *conjugate gradient method* described by Hestenes & Stiefel (1952). We will give only a brief description of the method and we refer the reader tp detailed overviews of the method in various texts (e.g., Press et al., 1992; Scales, 1987; Tarantola, 1987). In the simple case that the model has only two parameters then the model space will be two-dimensional. As an example consider a long narrow valley. Starting from the sides of the valley and aiming at the lowest point

in it, we could follow the direction of the steepest descent (gradient) in steps. The new gradient after the first local minimum will follow a direction perpendicular to the direction just travelled, which is not always to the direction pointing the lowest point of the valley. The so-called *steepest descent method* is a slow inefficient method which requires many steps to reach the global minimum. Therefore, we seek a way not to proceed along the direction of the new gradient but to a conjugate direction to the old gradient and all the previous ones. The conjugate gradient algorithm will minimise alternately in two steps; first across the valley to the valley floor and then along the long axis to the lowest point.

Successive minimisations of the objective function along its different dimensions in the parameter space will calculate each time the parameter value defined by this dimension. This parameter need not to be recalculated again as long as the new directions where the minimisation will be performed are conjugate to the previous ones (Press et al., 1992). Therefore, the value $\delta\mathbf{m}$ is calculated in successive iterations i by

$$\delta\mathbf{m}_i = \delta\mathbf{m}_{i-1} + \alpha_i \mathbf{h}_i \tag{2.74}$$

where α_i the step length along the vector of steepest descent and $\mathbf{h}_i$ the descent vector followed. First we choose $\delta\mathbf{m}_0 = 0$ and $\mathbf{h}_0 = \mathbf{g}_0 = \nabla\Psi(\mathbf{0})$. The vector of steepest descent in each step is

$$\mathbf{g}_i = -\nabla\Psi(\delta\mathbf{m}_{i-1}), \tag{2.75}$$

where $\mathbf{g}_0 = \mathbf{h}_0$, and the descent vector is

$$\mathbf{h}_i = \mathbf{g}_i + \beta_i \mathbf{h}_{i-1}, \tag{2.76}$$

where

$$\beta_i = \frac{(\mathbf{g}_i - \mathbf{g}_{i-1})^T \mathbf{g}_i}{\mathbf{g}_i^T \mathbf{g}_i}. \tag{2.77}$$

Finally, the step length along the vector of steepest descent is given as:

$$\alpha_i = \frac{\mathbf{g}_i^T \mathbf{h}_i}{\mathbf{h}_i^T \mathbf{H} \mathbf{h}_i}. \tag{2.78}$$

From the previous equations, α_i and $\mathbf{h}_i$ can be estimated for each step and subsequently, with equation 2.74, the update vector $\delta\mathbf{m}$ is calculated. The number of iterations could be as high as the number of the inverted model parameters. This number, therefore, controls the size of the update model vector and may be used to ensure that the model lies within the region of linearity, by performing

only few iterations towards the minimum (Hobro et al., 2003).

2.3 Three dimensional tomography algorithms

Three dimensional tomography algorithms can be classified into different groups according to the type of arrivals modelled and whether they invert for velocity parameters only, or for velocity and depth parameters. In summary, Zelt & Barton (1998), Toomey et al. (1994) and Hole (1992) invert only first arrivals for velocity parameters, Van Avendonk et al. (1998) inverts both reflected and refracted arrivals for velocity parameters and, finally, Hobro et al. (2003), Zelt et al. (1999) and in practice Rawlinson et al. (2001) invert both reflected and refracted arrivals for velocity and depth parameters. Although Zelt et al. (1996) also falls in the last group they use a layer stripping approach rather than a simultaneous inversion. Other ways to classify 3D tomography algorithms are the type of model parametrisation, the forward modelling method, the type of function which is minimised (see section 2.2.3) and the way the matrix $\mathbf{C_m}$ is constructed. In the following sections we describe the algorithms used in this thesis and give a brief description for the other methods, pointing out the independent characteristics of each code.

2.3.1 Jive3D approach

The Jive3D algorithm (Hobro et al., 2003; Hobro, 1999) is based on the 2D algorithm of McCaughey & Singh (1997). The algorithm inverts simultaneously for both velocity and depth parameters in a three-dimensional model using refracted and reflected seismic phases. The model is defined from velocity layers separated by interfaces, where layers are defined by non-uniform regular 3D grids of velocity nodes and interfaces by non-uniform regular 2D grids of depth nodes. Interfaces bound the velocity layers and define velocity discontinuities where reflected phases may produced. Velocities and depth functions are continuous and smooth, and are defined within the grids with quadratic and cubic B-splines, respectively (see section 2.1.4). Receivers can be placed everywhere within the model and sources can be placed either on top of an interface (land experiments) or at a constant depth level (marine shots).

For the forward modelling a ray perturbation method by Virieux & Farra (1991) is used, where rays are traced from a small number of sources to a large number of targets. Phases represent refracted or reflected traveltime arrivals that

pass through different sequence of layers or interfaces. During the inversion each phase minimises the misfit for one layer or interface. For a detailed description of the calculation of traveltimes with the ray perturbation method and the estimation of the Frechet derivatives see section 2.1.4.

The regularised objective function is similar to equation 2.69

$$\Psi(\delta\mathbf{m}) = (\mathbf{r} - \mathbf{G}\delta\mathbf{m})^T {\mathbf{C_d}}^{-1}(\mathbf{r} - \mathbf{G}\delta\mathbf{m}) + \lambda[\mathbf{m}^T {\mathbf{C_m}}^{-1}\mathbf{m}]. \tag{2.79}$$

Parameter λ controls the relative importance between the misfit and roughening terms. The matrix $\mathbf{C_d}$ is diagonal with non-zero elements the squared prior uncertainty (standard deviation) σ_i^2 of the ith traveltime. Elements are normalised by the reciprocal of total available picks n_{total} and not only the traced ones n_{traced}, where $n_{traced} \leq n_{total}$. The roughening matrix ${\mathbf{C_m}}^{-1}$ contains the second derivative finite difference operators for 3D and 2D, for layers and interfaces respectively. For the edges of layers and interfaces the first derivative finite difference operators are used. The matrix ${\mathbf{C_m}}^{-1}$ resembles the squared matrix $\mathbf{S}$ where

$${\mathbf{C_m}}^{-1} = \mathbf{S}^T\mathbf{S} = \sum_i^n {\mathbf{S_L}}^T\mathbf{S_L} + \sum_j^m {\mathbf{S_I}}^T\mathbf{S_I} \tag{2.80}$$

for m layers and n interfaces where $\mathbf{S_L} = \mathbf{S_{L_x}} + \mathbf{S_{L_y}} + \mathbf{S_{L_z}}$ for the ith 3D layer, and $\mathbf{S_I} = \mathbf{S_{I_x}} + \mathbf{S_{I_y}}$ for the jth 2D interface. In all the previous matrices the only three nonzero elements along each row are [1 $\cdots$ -2 $\cdots$ 1] corresponding to three adjacent cells in each dimension. Each squared product within the summation of equation (2.80) is normalised to allow variations in physical size and node density among different layers or interfaces. Additionally, weighting among smoothing constraints in different dimensions, such as lateral and vertical velocity fields, or smoothing constraints between layers and interfaces can be applied.

Since the model consists of velocity and depth parameters a normalisation is applied to avoid bias towards a particular parameter type. The normalisation factor

$$n = \sqrt{\sum_{all j,k} (a_i)_{j,k}^2} \tag{2.81}$$

is the root mean square value of all Frechet derivatives of the same parameter type. All Frechet derivatives for each parameter type are then normalised by the reciprocal of n and all model parameters multiplied by n. This normalisation preserves the product $\mathbf{G}\delta\mathbf{m}$ but balances the gradient $\nabla\Psi\delta\mathbf{m}$. Finally, following a creeping strategy (Shaw & Orcutt, 1985), equation (2.79) is minimised with the

conjugate gradient method.

2.3.2 FAST approach

One of the most widely used inversion algorithm for 3D tomographic studies was proposed by Zelt & Barton (1998). Parametrisation of the model is defined by uniform spaced grids both for the forward and the inverse step. Only one velocity grid is defined which normally resembles a crustal or lithospheric layer. The inversion grid might, however, use longer spacing than the forward one. The velocity within each cell equals the average of the velocities of the nodes at the eight corners of the cell, and consequently the partial derivative matrix $\mathbf{G}$ will have elements corresponding to the length of each ray travelled through each cell. Only one interface can be defined and is used as a boundary that separates upper parts of the model that will remain unchanged during the inversion. This interface usually resembles the bathymetry and/or topography and has similar grid spacing to the velocity layer. For a particular lateral position, the closest node to the interface takes a velocity value that equals the average of the true velocity over half the node spacing above and below the node. Receivers and sources can be placed anywhere within the model grid.

For the forward step the finite difference eikonal solver by Vidale (1990) with modifications to handle large, sharp velocity contrasts Hole & Zelt (1995) calculates, initially, traveltimes in the uniform forward grid, and subsequently rays are traced, following Fermat's principle, usually from receivers to sources. An interface that is not sampled densely enough can introduce large timing errors for nodes close to sources (OBH, land stations). In this case, we could picture a source hanging over an interface. To time the nodes around the sources, a small cube around them will have velocities different for timing nodes that are above or below the source.

The regularised inversion tries to minimise a functional similar to equation 2.69

$$\Psi(\delta\mathbf{m}) = (\mathbf{r}-\mathbf{G}\delta\mathbf{m})^T{\mathbf{C_d}}^{-1}(\mathbf{r}-\mathbf{G}\delta\mathbf{m}) + \lambda\Big[\mathbf{m}^T{\mathbf{C_{m_h}}}^{-1}\mathbf{m} + s_z\mathbf{m}^T{\mathbf{C_{m_v}}}^{-1}\mathbf{m}\Big]. \quad (2.82)$$

where ${\mathbf{C_{m_h}}}^{-1}$ and ${\mathbf{C_{m_v}}}^{-1}$ the horizontal and vertical roughening matrices, respectively. Parameters λ and s_z control the relative importance of the terms. The matrix $\mathbf{C_d}$ is diagonal with non-zero elements the squared prior uncertainty σ_i^2 of the ith traveltime. Roughening matrices ${\mathbf{C_{m_h}}}^{-1}$, ${\mathbf{C_{m_v}}}^{-1}$ contain second derivative finite difference operators for 2D and 1D respectively. The horizontal roughen-

ing matrix $\mathbf{C_{m_h}}^{-1}$ resembles the squared matrix $\mathbf{S_h}$ ($\mathbf{C_{m_h}^{-1}} = \mathbf{S_h}^T\mathbf{S_h}$). In the sparse matrix $\mathbf{S_h}$ the only five non zero elements along each row are equal to [1 $\cdots$ 1 -4 1 $\cdots$ 1] corresponding to a central cell and four adjacent cells in X, Y direction. The vertical roughening matrix $\mathbf{C_{m_v}}^{-1}$ resembles the squared matrix $\mathbf{S_v}$ ($\mathbf{C_{m_v}}^{-1} = \mathbf{S_v}^T\mathbf{S_v}$). The sparse matrix $\mathbf{S_v}$ has only three non zero elements along each row equal to [1 $\cdots$ -2 $\cdots$ 1] corresponding to a central cell and two adjacent cells in the vertical direction. The elements of both matrices are normalised by the reciprocal of slowness in the central cell to avoid greater smoothness in regions of higher slowness. Finally, minimisation of equation (2.82) is performed with the conjugate gradient method.

2.3.3 Other 3D methods

Alternative three-dimensional tomography algorithms for active source experiments have been proposed by Toomey et al. (1994), Van Avendonk et al. (1998), Hole (1992), Zelt et al. (1999), Rawlinson et al. (2001) and Bohm et al. (2000).

One of the first regularised 3D tomographic algorithms was introduced by Toomey et al. (1994). The code inverts for first arrivals in a 3D medium. Given a bathymetric relief, the seismic velocity structure is represented by a grid that is sheared vertically to follow the bathymetry. The grid spacing can be different in the three dimensions. For the forward step traveltimes are calculated following the graph method with a sorting shortest path technique by Moser (1991). For the inverse step the functional (2.71) is the subject of minimisation as a combination of both the damped and smoothed least squares formulation. Differential weighting for the importance of the penalty function, horizontal and vertical smoothing, and prior model assumptions is allowed. The penalty matrix $\mathbf{C_{m_D}}$ is a diagonal matrix which consists of the fractional uncertainties of the individual model parameters times the slowness value in the prior model. Smoothing constraints, normalised by the previous slowness model, are applied over a defined scale length with decreasing weighting with distance, in contrast with the nearest neighbour interaction applied in the codes of Hobro et al. (2003) and Zelt & Barton (1998).

Van Avendonk et al. (1998), based on Toomey et al. (1994), introduced a new code with the same parametrisation approach. To avoid overprediction of traveltimes (Van Avendonk et al., 1998), the raypaths are approximated by the graph approach of Moser (1991) and optimised by the ray-bending tool of Moser et al. (1992). A two step graph calculation will also give the raypaths and traveltimes for a reflected phase. Minimisation of a weighted combination of data misfit,

prior model assumptions, and smoothing constraints is employed (equation 2.71). The smoothing matrix $\mathbf{C_m}$ contains first derivative operators representing a flatness penalty function. Perturbations of reflector depth are not included in the linearised inversion and reflection traveltimes are used only for constraining the velocity model, assuming a reflecting interface. For both tomography approaches described above minimisation is performed employing the jumping strategy (Shaw & Orcutt, 1985) where equation (2.71) is solved with the sparse matrix solver LSQR by Paige & Saunders (1982).

Apart from the regularised tomography code (FAST), Zelt & Barton (1998) also used a 3D backprojection approach by Hole (1992) in which traveltime residuals are distributed along their raypaths independently of all other rays, using the same forward parametrisation and finite difference calculation of traveltimes as for the regularised method. The basis of this method is that no matrix is inverted, but the perturbation of slowness within each model cell is a weighted sum of the raypath-average slowness perturbation of all raypaths passing through the cell over the number of rays passing through the cell. Zelt & Barton (1998) modified the original code of Hole (1992), where within each cell, the slowness perturbation for a particular ray, is proportional to the prior slowness and weighted by the inverse of the pick uncertainty. Not all slowness cells within the model have to change, accounting for the fact that rays might pass through areas of known structure. This approach results in rapid convergence. Although the method requires minimum computational and memory resources, the results are usually very rough and smeared. A development to the backprojection code by Zelt et al. (1996) allowed inversion for both velocity and depth parameters following a layer stripping approach. The reflected traveltimes were calculated by applying twice, for each source, the finite difference algorithm of Vidale (1990) for the downgoing and upgoing reflected wave (Hole & Zelt, 1995).

Zelt et al. (1999) expanded the regularised inversion of Zelt & Barton (1998) and presented an application of an algorithm that inverts simultaneously refracted and reflected arrivals for velocity and depth parameters. Reflected traveltimes were calculated from Hole & Zelt (1995) and interface partial derivatives were calculated based on Zelt & Smith (1992). After each iteration, the updated velocity structure is linearly stretched or compressed between the updated and the initial interface position to account for the increased or decreased thickness of each layer.

Finally, irregular grid methods can provide an alternative to the regularised inversion codes that use regular grids and smoothing or damping constraints to account for cells that are not sampled by any rays. Rawlinson et al. (2001) in-

troduced a tomography method inverting for both refracted and reflected arrivals seeking a layer velocity and interface geometry. The model is composed by layers in which velocity varies with depth but not laterally. Lateral velocity variations could be represented, only, by perturbations of the depth to interfaces that separate the layers. Interfaces are described by a cubic B-spline surface and first arrival traveltimes are calculated by a shooting method where a raypath within each layer is defined as a circular arc segment (Rawlinson et al., 2001). For the inversion step the damped least squares formulation (eq. 2.65) is the subject of minimisation, solving for perturbations in velocities, velocity gradients and depths of interfaces using a subspace solution method (e.g., Williamson, 1990). The approach is similar to that of Hobro et al. (2003) with the difference that there are no lateral variations in the velocity within each layer, and the smoothing term in equation 2.69 smooths the perturbations to the model and not the model itself.

Another irregular grid method, employing a 3D adaptive tomography algorithm that uses Delaunay triangles and Voronoi polygons, was proposed by Bohm et al. (2000). Based on an initial velocity grid, rays are traced through constant velocity cells (Vesnaver, 1996). The local resolution is fitted to the available raypaths, by means of adding grid points where the null space density is low, or the local gradient is high, and removing them elsewhere. A singular value decomposition of the matrix $\mathbf{G}$ in equation 2.50 will estimate automatically the null space. For the inversion step a simple non-regularised solver is used and the computing time depends roughly linearly on the grid resolution. Raytracing will require most computing effort (Bohm et al., 2000) for this method.

Comparison of all the above algorithms would be possible with a benchmark model for both the forward and inverse step. It is however quite difficult mainly because of the different parametrisation approaches used in these codes. For regular grid methods the parametrisation followed by Toomey et al. (1994) and Van Avendonk et al. (1998) will be more precise than Zelt & Barton (1998) avoiding introduction of uncertainties due to coarsely sampled bathymetry and requiring coarser grids for the forward steps. An ideal tomography code will use this parametrisation, employ a fast finite difference forward method and apply a smoothing approach as in Hobro et al. (2003) or Zelt & Barton (1998). It is also required that ideal codes should be able to invert simultaneously both reflected and refracted phases for interfaces and velocity layers. Irregular grid methods may be the way forward since they reduce considerably the required number of inversion parameters but they have to overcome the problem of appropriate velocity parameterisation which will require irregular cells with varying velocities within them.

Finally, not all of these tomography codes are publicly available and published in detail, intended either for completely personal or institutional use (e.g. Zelt et al., 1999), or as a commercial application (e.g. Bohm et al., 2000).

Chapter 3

Ascension Island seismic experiment

3.1 Introduction

Ascension Island (7°57'S, 14°23'W) lies about 100 km west of the Mid Atlantic Ridge, between the Ascension Fracture Zone and the Bode Verde Fracture Zone (Fig 3.1). The Ascension volcanic edifice, lying on 7 Ma oceanic lithosphere, is 60 km in diameter and rises 4 km from the surrounding ocean floor. Although the island itself covers only 92 km^2, the area of the edifice is over 2000 km^2 (Brozena, 1986).

In this chapter we describe the analysis of a wide angle seismic dataset acquired on and around the island. Velocities are determined by the three-dimensional tomographic inversion of traveltime picks, and model resolution is determined using a checkerboard test. Gravity modelling supports our seismic results.

3.2 Geology–Geophysics of the Ascension region

Ascension Island is the summit of a large volcanic cone built up on the seafloor by eruption and intrusion of mafic, intermediate and silicic alkaline magmas. Although there is no historic record of volcanic activity on Ascension, some surface lava flows are only a few hundred years old (Atkins et al., 1964), suggesting that this island may have been the most volcanically active of all South Atlantic islands over the last 10^4 years (Brozena, 1986). The central and the eastern parts of the island surface are composed of trachyte and rhyolite lava flows and flow domes, pyroclastic deposits and mafic lava flows. The southern, western and northern

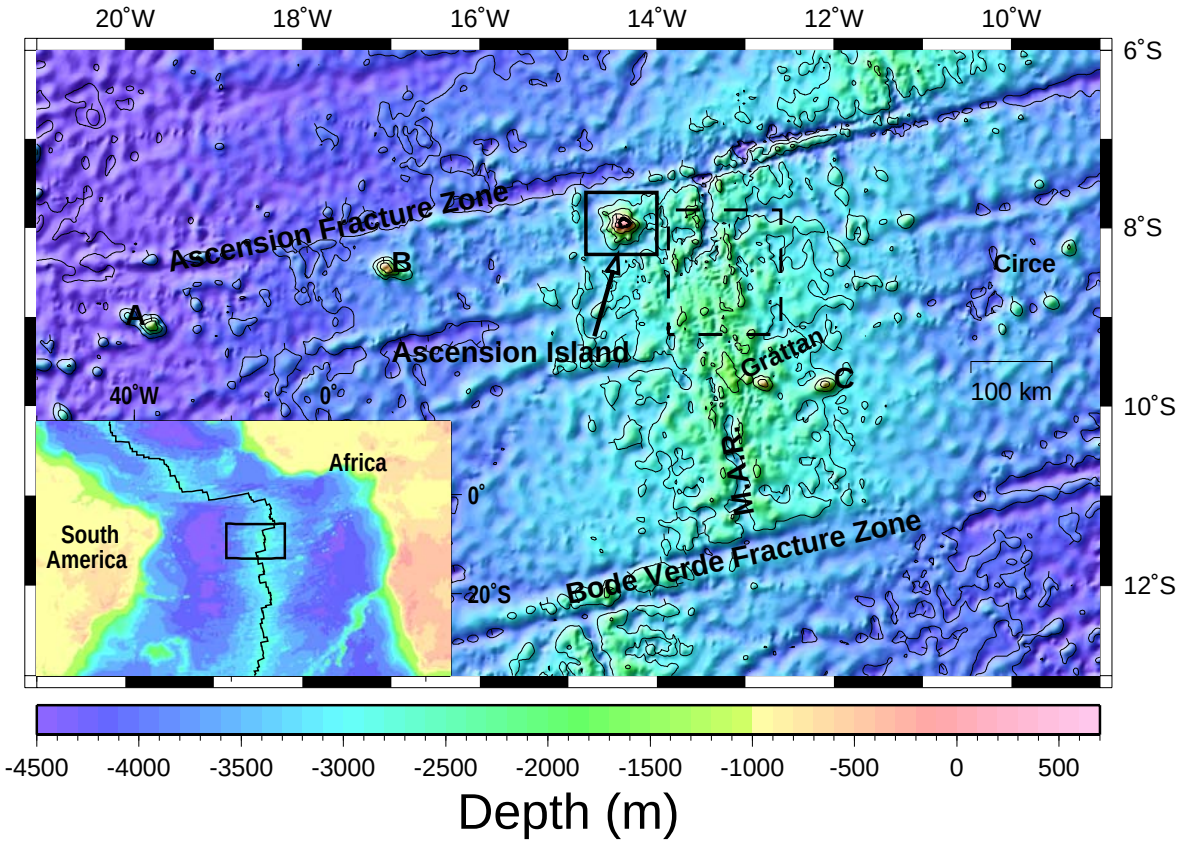

Figure 3.1: The location of Ascension island relative to Mid-Atlantic Ridge (M.A.R.), Ascension and Bode Verde Fracture Zones. The bathymetry and topography are taken from Smith & Sandwell (1997). Bold box marks our study area (Fig 3.4). Inset map shows the position of the Ascension area in the equatorial South Atlantic. Grattan Seamount, seamount A, B, C and Circe Seamount are marked. Dashed box marks the study area of Minshull et al. (2003a).

parts have less relief and comprise mafic lava flow plains and scoria cones (Weaver et al., 1996).

A geothermal exploration well, ASC1 (Nielson & Stiger, 1996), was drilled to 3126 m depth, the approximate level of the ocean floor surrounding the volcanic edifice. From the base of the hole to 1966 m depth the section is composed largely of basalt. Between 1966 and 887 m the sequence is composed mainly of hyaloclastites, capped by a 237 m thick basalt flow and finally covered by another hyaloclastite section. Above about 900 m depth the rocks are interpreted to have been formed in a subaerial environment. Most of the felsic rocks lie above this depth, increasing in volume closer to the surface, suggesting they are a recent

feature in the volcanic history of the island (Nielson & Stiger, 1996).

The equatorial South Atlantic is a region of large left-lateral Mid-Atlantic Ridge (MAR) offsets. The Ascension Fracture Zone is the northern-most significant right-lateral offset (Brozena, 1986). Ascension Island and several large seamounts (seamounts A, B, Grattan, C and Circe) lie between the Ascension Fracture Zone and Bode Verde Fracture Zone (Fig. 3.1). There is a regular spacing between Ascension Island, seamount A and seamount B. Such occurrence of discrete, nearly regularly spaced, volcanoes may be caused by the interaction of flexural stresses, imposed by the seamounts volcanic loads, with magma flow (Hieronymus & Bercovici, 2001a).

The presence of a mantle melting anomaly in the Ascension area has been suggested on the basis of bathymetric, geophysical and geochemical data. Effects of this possible hotspot on the MAR include a 500-700 m broad positive depth anomaly along the ridge crest, coinciding with a poorly defined rift valley (Fig 3.1) and the lack of seismicity between 8°30'S and 10°00'S. In this region the MAR has a morphology more typical of fast spreading ridges (Brozena, 1986; Bruguier et al., 2003). Schilling et al. (1985) suggested that the drift of the MAR axis away from an 'Ascension' plume results in asthenospheric flow towards the westward migrating ridge axis. In this model, basalts recovered from the inflated region of the ridge axis have compositions that result from mixing mid-ocean ridge and ocean island basalt sources. Pb isotope data show that the source of Ascension Island lavas could not represent the end-member required by this hypothesis, and suggest that if an off-axis plume is involved, it cannot lie beneath Ascension Island (Hanan et al., 1986). Possible alternative locations include Circe seamount (Schilling et al., 1985; Hanan et al., 1986), and Grattan seamount (Bourdon & Hemond, 2001). However, the cause of the recent magmatic activity at Ascension Island remains unclear. Brozena (1986) proposed that Ascension Island is the product of the flow of hot material from an off-axis plume to the spreading axes and then along the ridge crest to the Ascension Fracture Zone. In this model, the older and thicker lithosphere north of the fracture zone acts as a barrier that diverts this flow, resulting in the creation of seamounts far away from the plume.

An alternative model involves tapping magma from mantle heterogeneities (Sleep, 1984; Zindler et al., 1984). On the basis of gravity and wide-angle seismic data from the ridge axis close to Ascension island, Minshull et al. (1998) and Bruguier et al. (2003) suggested that any plume in the area must be weak and intermittent, or alternatively that the thickened crust was produced by melting of localised mantle heterogeneities, as in other areas of the Mid-Atlantic Ridge such

as at 33°S, 14°N and 35°N.

A flexural moat around 200 m deep can be traced all around Ascension Island except to the north, where the topography is influenced by the Ascension Fracture Zone (Minshull & Brozena, 1997). An east to west increase in gravity across the island cannot be explained by simple flexural models and was attributed to density variations within the island itself (Minshull & Brozena, 1997). These authors inferred an elastic thickness (T_e) of 3 ± 1 km with a loading duration of 1 Ma and a mean density for the volcanic edifice of 2500 kg m^{-3} . The value of T_e was, however, anomalously low compared with values of 6–13 km for slow-spreading ridge axes (e.g. Blackman & Forsyth, 1991). The low value was attributed to the combined effects of the high plate curvature beneath the island, which produces bending stresses that are limited by the yield stress envelope, and the addition of hot material to the crust, which causes thermal rejuvenation of the thin lithosphere beneath the island.

3.2.1 Aims and objectives of the 3D tomography experiment around the Ascension edifice

A three-dimensional crustal velocity model of the Ascension edifice can address questions that concern either the edifice itself and the general evolution of the equatorial South Atlantic area, or the general construction mechanism of edifice emplacement on top of pre-existing oceanic crust. The seismic model will provide useful constraints on the volume and shape of the volcanic edifice, leading to conclusions about the magma source, the volcanic history and evolution through time, and possible correlations of surface geological, topography and gravity anomaly features with deeper structures. Additionally, an active source seismic study of this oceanic volcanic island can also give useful information on the rheology of the underlying lithosphere and the magmatic processes that create such volcanic edifices. The flexure of the lithosphere, directly associated with lithosphere mechanics, can be quantified by mapping the shapes of the top of the oceanic crust and the Moho. Moreover, the structure and thickness of the extruded and intruded material can also be compared with those in other oceanic volcanic edifices to investigate similar processes in edifice construction.

3.3 Seismic experiment and data

A four day seismic experiment was conducted in May 1999 around the island of Ascension (Fig 3.4). Our wide-angle dataset consists of 3653 shots from a

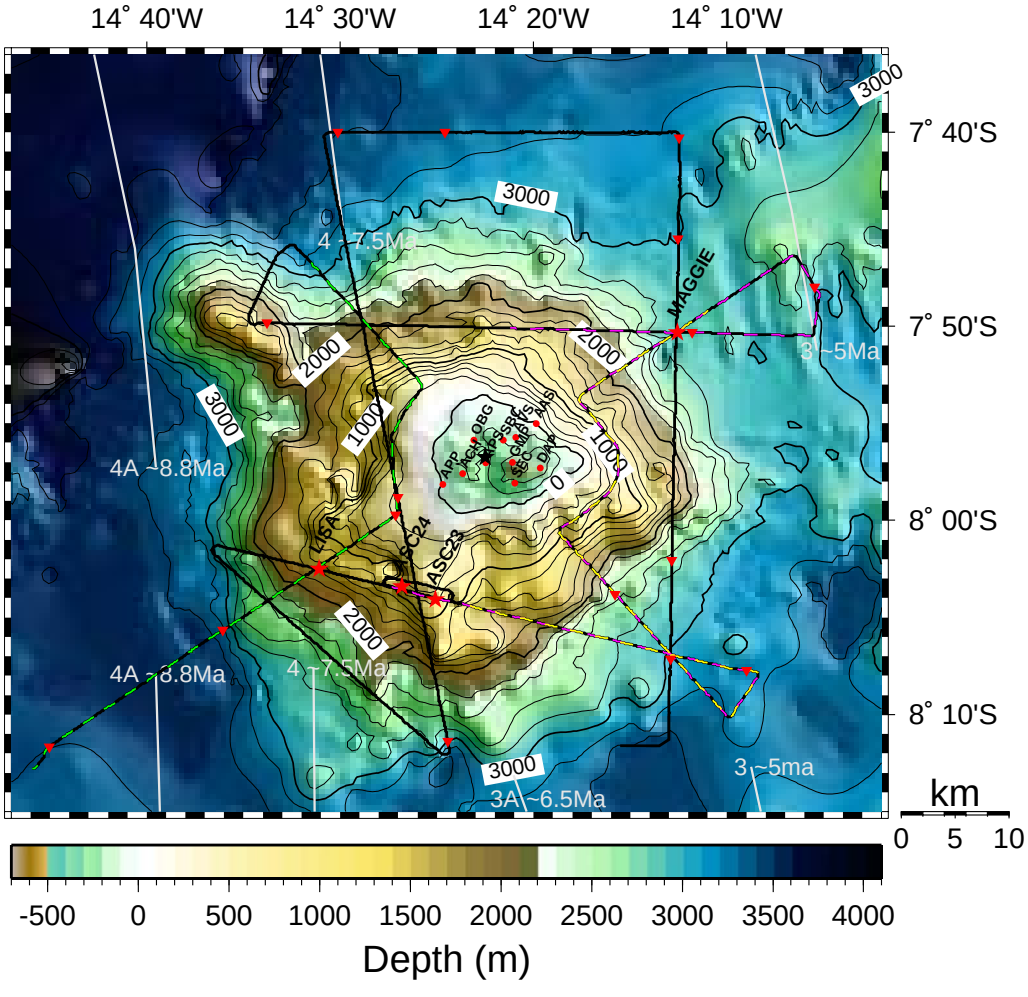

Figure 3.2: The Ascension study area with bathymetry and topography. The position of the receivers (red) and the shots around the island are shown (solid line). Landstations are marked as filled red circles, OBH as rec stars and sonobuoys as red inverted triangles. Black star on land marks the position of ASC1 borehole. Dashed coloured lines show the parts of the shooting track that contribute to the record sections of Fig. 3.4 (SBC-green, MAGGIE-yellow, ASC23-purple). Light gray lines mark magnetic isochron picks (Brozena, 1986), with isochron ages according to Cande & Kent (1995).

6186 cu.in. airgun array, fired at a one minute interval along a series of tracks around the island. The airgun array was towed at a depth of 20 m and, with an average speed of 4 knots, the mean shot spacing was 116 m. The shot locations

lie between 3 and 45 km from the coast of the island (Fig 3.4). The shots used for this study were recorded on four ocean bottom hydrophones (OBH) and ten land stations. Subsets of these shots were also recorded on 31 disposable sonobuoys, of which 14 contributed usefully to our study. Two of the OBHs (ASC23 and ASC24) are permanently installed on the seafloor for monitoring the Comprehensive Test Ban Treaty. The shots were used to relocate and calibrate these hydrophones by Harben et al. (1999). Additionally, two OBHs (Maggie and Lisa) were deployed above the seabed and within the ocean sound channel for a study of the coupling of seismic energy into the island slope. The land stations consisted of three-component seismometers with a natural frequency of 2 Hz.

The bathymetry used in this study is the combination of different datasets from shipping tracks and two swath surveys (Mitchell, 2003). The data were filtered by a L1 norm to create median positions in the parts of the study area which they are not covered by the dataset. All the (x,y,z) triples are then used as input in an adjustable tension continuous curvature surface gridding algorithm (Smith & Wessel, 1990). The data coverage of the area is fairly good, especially for a radius of around 40 km from the centre of the island (Fig.3.3).

Shot positions were determined from differential GPS and OBH locations were calculated from the direct-wave arrivals for crossing tracks. The total drift of the sonobuoys between the deployment location and the largest offset's pick location

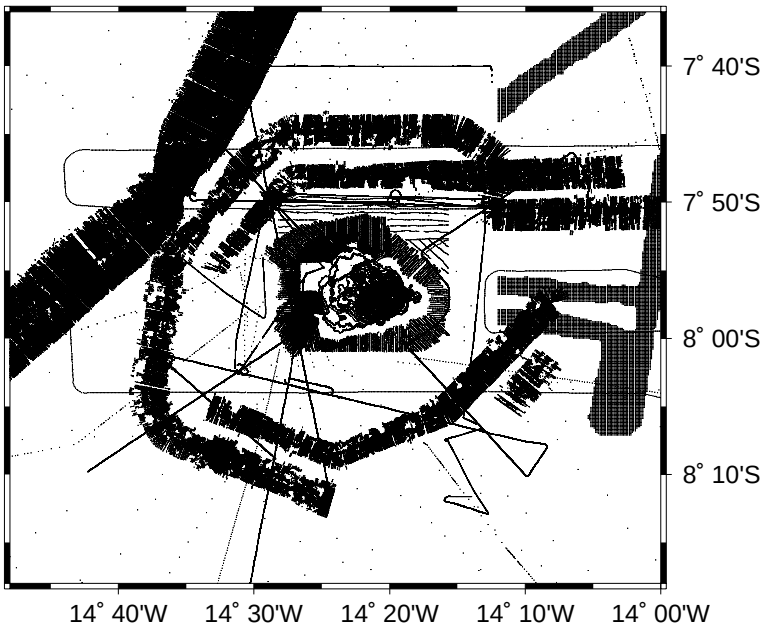

Figure 3.3: The Ascension study area showing the sampling points for the various bathymetry datasets combined by Mitchell (2003). Thick black patches mark the swath surveys.

was calculated from the water-wave arrivals, and had a mean value of ~ 0.2 km. Sonobuoy locations were assumed to be at the centre of the drift path, and the drift contributes to errors in both sonobuoy location and water depth beneath sonobuoys. For one sonobuoy that had an internal GPS receiver, the difference in water depth between the initial and final position was 71 m over a very steep slope. Assuming a constant velocity of 1.5 kms^{-1} for the water layer, a traveltime error of ~ 50 ms would result from this difference. Assigned pick uncertainties take account of such errors.

For the OBHs and the land stations two wide-angle seismic phases were picked: a refraction from the upper and lower crust (P_g), visible out to ranges of ~ 50 km, and a reflection from the crust-mantle boundary (P_mP) observed usually at offsets between 15–35 km. In addition, refractions from the upper mantle (P_n) were picked for some instruments. Three representative record sections with P_g, P_mP and P_n phases visible are shown in Figure 3.4. For the sonobuoys, only P_g was picked, since longer range phases are obscured by noise. The sampling coverage of the picks is good, especially for the crust and the Moho around and beneath Ascension Island itself. Generally, shots around the island gave P_g arrivals at all three types of receivers. P_mP arrivals were recorded for almost all the shooting tracks around the island in both land and OBH receivers. However, sampling of the Moho directly underneath the edifice was mainly from OBH and shot pairs located on opposite sides of the island. P_n picks were recorded mainly by Land-stations and some OBH receivers due to the larger maximum offsets available for these receivers. In total, 34204 P_g, 5798 P_mP and 2341 P_n traveltimes were picked manually and the picking uncertainties were estimated visually and assigned one by one. The uncertainty for crustal refractions is between 30 and 150 ms for OBH and land stations. Since the crustal arrivals in the sonobuoy data are generally noisier, the picking uncertainties are higher, between 100 and 200 ms. The mean P_g uncertainty for all picks is 64 ms. For the P_mP reflections the assigned uncertainties vary between 90 and 150 ms, with a mean value of 100 ms. Uncertainties in P_n are between 90 and 150 ms and the mean value is 96 ms.

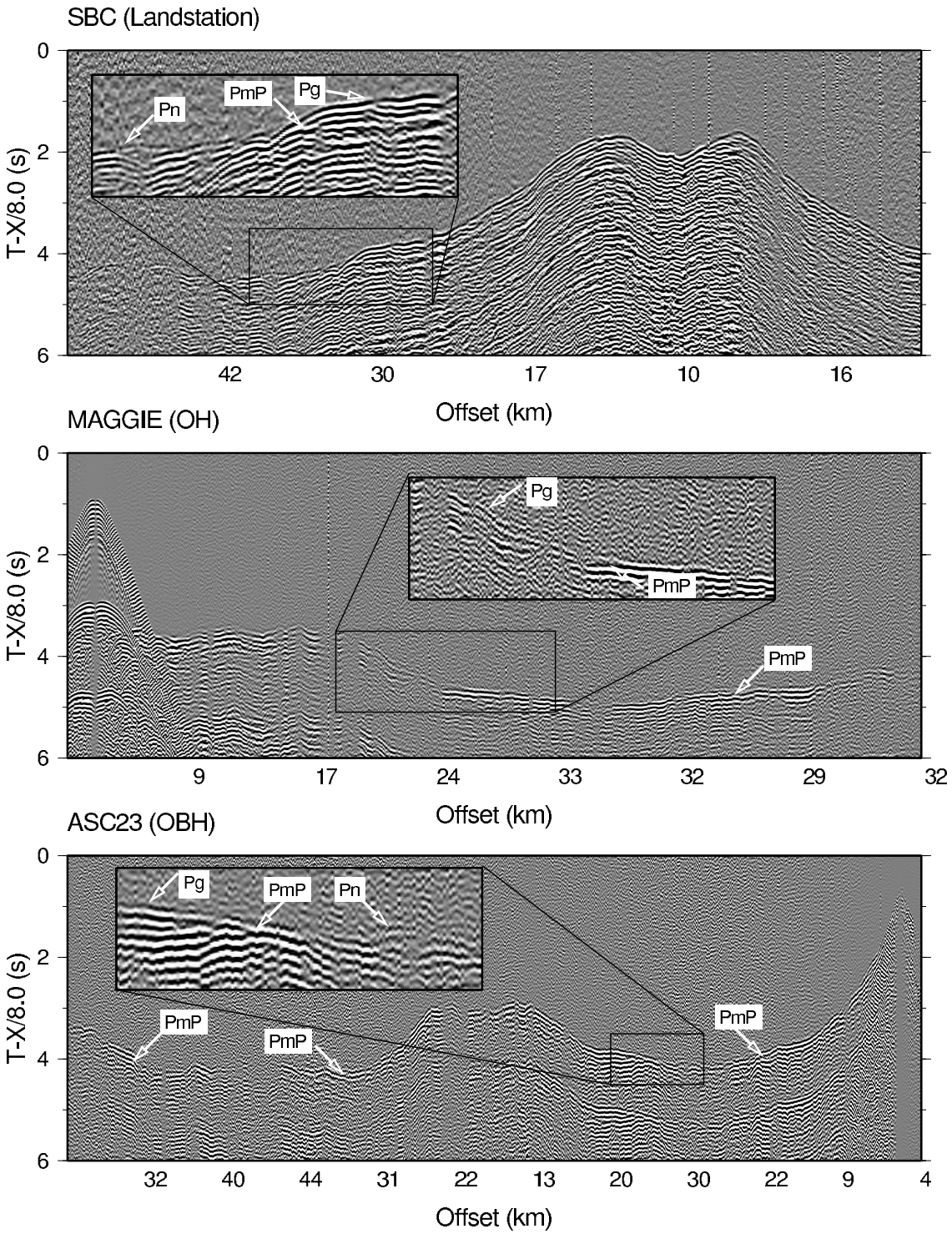

Figure 3.4: Minimum phase bandpass filtered data for landstation SBC, for ocean hydrophone Maggie, located in the middle of the water column, and for OBH ASC23. Filter corner frequencies are 5–9–15–20 Hz, 3–5–15–18 Hz and 5–9–15–20 Hz, respectively. Data are displayed with a gain proportional to source-receiver range and a linear moveout correction at 8 kms^{-1}. Refracted crustal arrivals (P_g), Moho reflections (P_mP) and upper mantle refractions (P_n) are shown. Insets show examples of phase identification. Note that shooting track includes turns and that the surface trace of each section is marked with a different colour along the shooting track in figure .

3.4 Modelling

3.4.1 Three-dimensional tomographic method

For the three–dimensional velocity modelling of the study area we used the Jive3D algorithm (Hobro et al., 2003). We choose this approach since it allows simultaneous inversion for velocity and boundary depth parameters in a three-dimensional model using both refracted and reflected seismic phases. For the forward modelling the ray perturbation method of Virieux & Farra (1991) was used. After identifying some initial estimated shooting angles, Frechet derivatives and traveltimes are computed using the ray perturbation method described in section 2.1.4.

During the first few steps of the inversion, λ values (see eq. 2.79) are kept high, in order to make a crude estimate of model velocities, and interface depths. This smooth model is likely to have good ray coverage during the next forward step. Subsequently, λ values are decreased in order to allow more structure in the model.

3.4.2 Initial Model construction and parameterisation

The starting model for the inversion consists of two layers: a water layer with a constant velocity, and a crustal layer with a smoothly varying velocity gradient. Since the inversion algorithm allows layers to have varying velocity gradients, there is no requirement to split the crustal layer into two different layers representing oceanic Layers 2 and 3. The bathymetry grid, combined with the island surface topography, is used as one of the interfaces, with a node spacing of 0.5 km. The assigned uncertainty of the traveltime picks accounts for possible depth errors within the interface cells. The use of cubic B-splines means that the depth within each cell of the interface grid is a function of the 16 neighbouring node values (Hobro, 1999). Given a minimum uncertainty of 30 ms in the dataset and velocity of 1.5 kms^{-1}, the difference between the measured depth and interpolated grid value within each cell has to be less than 45 m for depth variations to be adequately modelled by the grid. A sparse grid with node spacing of 1 km was found to satisfy this constraint. We chose to use a denser grid (0.5 km $\times$ 0.5 km), since it is the sparsest one in which the actual given depths (or heights) of the receivers are kept within 10 m of the grid values at the same coordinates. The crustal layer is defined by a three-dimensional grid with a horizontal velocity node spacing of 5 km, and a vertical node spacing of 0.5 km. The crust-mantle interface (Moho) is defined by a surface grid with 5 km spacing of depth nodes. Synthetic traveltimes

for 95% of the observed traveltimes are obtained through the initial forward step. The absence of rays between some source-receiver pairs is likely due to the lack of a geometric raypath between these pairs in the starting model.

3.4.3 Traveltime inversion and regularisation

During the inversion modelling we applied a different degrees of smoothing between horizontal and vertical velocity perturbations (λ_V), and between velocity and depth parameters (λ_I). Additionally, the degree of smoothing was different for the crustal layer (λ_{L_C}), and the upper mantle layer (λ_{L_M}) that was added in the final stages of modelling. In this way the regularisation part of the objective function consists of the horizontal velocity smoothing term multiplied by λ_L, the vertical velocity smoothing term multiplied by $\lambda_L \cdot \lambda_V$ and the interface smoothing term multiplied by λ_I.

Analysis of a two-dimensional subset of the data revealed that the survey area is likely to have different vertical and horizontal velocity gradients, as is common in the oceanic crust (Klingelhöfer et al., 2001). This means that different horizontal and vertical smoothing strengths are required. The ratio between these regularisation strengths was chosen on the basis that model perturbations should modify vertical gradients more than horizontal gradients. The behaviour of the inversion was tested by inspection of isovelocity contour plots of two-dimensional cross-sections. We started the inversion allowing 2.5 times ($\lambda_V = 0.4$) less vertical than horizontal smoothing (Table 3.1).

A layer stripping approach was followed, in which the layers and interfaces were modelled in order of increasing depth. The crustal velocity grid was modelled first using 34204 crustal refracted arrivals that constrain this layer only (P_g refractions). Starting with a high regularisation strength, 36 iterations were performed. The process was divided into six steps and in each step the regularisation strength (λ_{L_C}) was reduced by a factor of 10, allowing the model to develop gradually more structure (Table 3.1 and 3.2). Each step had 6 inversion iterations, where the first 3 iterations were performed with as many conjugate gradient iterations as the number of the model parameters (100%, see section 2.2.4). Although this procedure required long computer run times for each iteration (e.g. $\sim$12 hours on Sun Blade), it was important in order to ensure that the produced model after each iteration has minimal dependence on the previous one. For the next 3 iterations the number of the conjugate gradient iterations was 10% of the number of model parameters in order to reduce computer run time, since the major changes in

model structure were already obtained from the previous iterations.

Step	No. Phases	Grid size	P_g Layer λ_{L_C}	Vertical λ_V	Interface λ_I	P_n Layer λ_{L_M}
1	1	$5 \times 5 \times 0.5$	1	0.4		
2			10^{-1}	0.4		
3			10^{-2}	0.4		
4			10^{-4}	0.4		
5			10^{-5}	0.4		
6			10^{-6}	0.4		
7	2		10^{-6}	0.4	10^{-4}	
8			10^{-6}	0.4	10^{-5}	
9			10^{-6}	0.4	10^{-6}	
7		$2.5 \times 2.5 \times 0.5$	10^{-6}	0.2	10^{-6}	
8			10^{-7}	0.2	10^{-6}	
12	3		10^{-7}	0.5	10^{-6}	10^{-1}

Table 3.1: λ value applied in each step of the inversion. The regularisation part of the objective function consists of the horizontal velocity smoothing term multiplied by λ_L, the vertical velocity smoothing term multiplied by $\lambda_L \cdot \lambda_V$ and the interface smoothing term multiplied by λ_I.

		Pg		PmP		Pn		Total
Step	Total χ^2	Misfit (sec)	Hit Rate (%)	Misfit (sec)	H. Rate (%)	Misfit (sec)	H. Rate (%)	Misfit (sec)
1	35.06	0.334	91					0.334
2	34.99	0.328	91					0.328
3	34.87	0.328	91					0.328
4	23.48	0.262	91					0.262
5	11.12	0.208	94					0.208
6	5.52	0.155	95					0.155
7	3.46	0.119	95	0.113	89			0.118
8	3.48	0.120	93	0.110	90			0.118
9	3.49	0.119	92	0.101	84			0.116
10	3.02	0.113	93	0.101	94			0.111
11	1.69	0.087	94	0.086	94			0.087
12	1.66	0.086	94	0.082	94	0.159	52	0.089

Table 3.2: The total χ^2 and RMS misfit for each step, accompanied by the misfit for each phase independently

Once a good fit had been achieved ($\chi^2 = 5.6$), the P_mP reflections were added and three simultaneous inversion steps (18 iterations) for both the crustal layer and the Moho were performed. The λ_{L_C} was mainly kept fixed and λ_I was decreased gradually (Table 3.1). In order to allow the model to resolve more structure in

the horizontal direction and therefore decrease the traveltime misfit, we resampled the crust layer with a horizontal velocity node spacing of 2.5 km and carried out two more inversion steps of six iterations each. In each iteration, to improve computational times, We performed 10% of the possible conjugate gradient iterations since the difference between the resulting model and a model resulting from using 100% of these iterations was negligible in several trial cases. λ_{L_C} was then decreased and λ_I was held fixed since P_mP picks were already fitted with this degree of smoothing (Table 3.2). The ratio of vertical to horizontal degree of smoothing λ_V was also decreased as the grid spacing was smaller.

Finally, for the last step, the P_n refractions and an upper mantle layer were incorporated and a simultaneous inversion for all phases was performed. In this step we increased the vertical to horizontal smoothing, allowing more structure to be developed in the horizontal direction but keeping at the same time the highest hit rate for all phases. The low hit rate for P_n is due to the high smoothing factor applied within the upper mantle (Table 3.1), which prevents much modification of this layer. The small number of P_n picks and the spatially invariant smoothing parameter means that a rougher model will overfit the data in some places and consequently some picks will be lost in other places. Since the χ^2 and RMS misfit are good for both P_g and P_mP we chose to stop the inversion here. Table 3.1 summarises the applied λ for each step, layer and interface, and Table 3.2 the resulting χ^2, hit rate and the RMS misfit for each step and phase.

To check the misfit of the final crustal model for the full dataset we then calculated traveltimes for all P_g picks with the finite difference eikonal solver of Zelt & Barton (1998) (see section 2.1.5). The RMS traveltime misfit for the same 94% of picks traced with the eikonal solver and a 0.1 km grid spacing was 95ms compared to the the ray perturbation method RMS misfit of 86 ms. Additionally, the finite differences revealed that the RMS misfit for the 6% of untraced picks with the ray perturbation method is 77 ms. We therefore conclude that the additional 6% of P_g data would not contribute significant additional information to our final crustal model since they are already fitted better than the rest of the picks.

The final residuals between observed and calculated traveltimes for each receiver type and phase are shown in Fig. 3.5. For the P_g and P_mP phases the fit for OBHs and land stations is very good, with less than 100 ms misfit for the majority of the picks. The large P_g misfit for the sonobuoys may be attributed to unknown off-line components of drift over the steep seafloor topography. The fit for the P_n phase is adequate given the high smoothing factor.

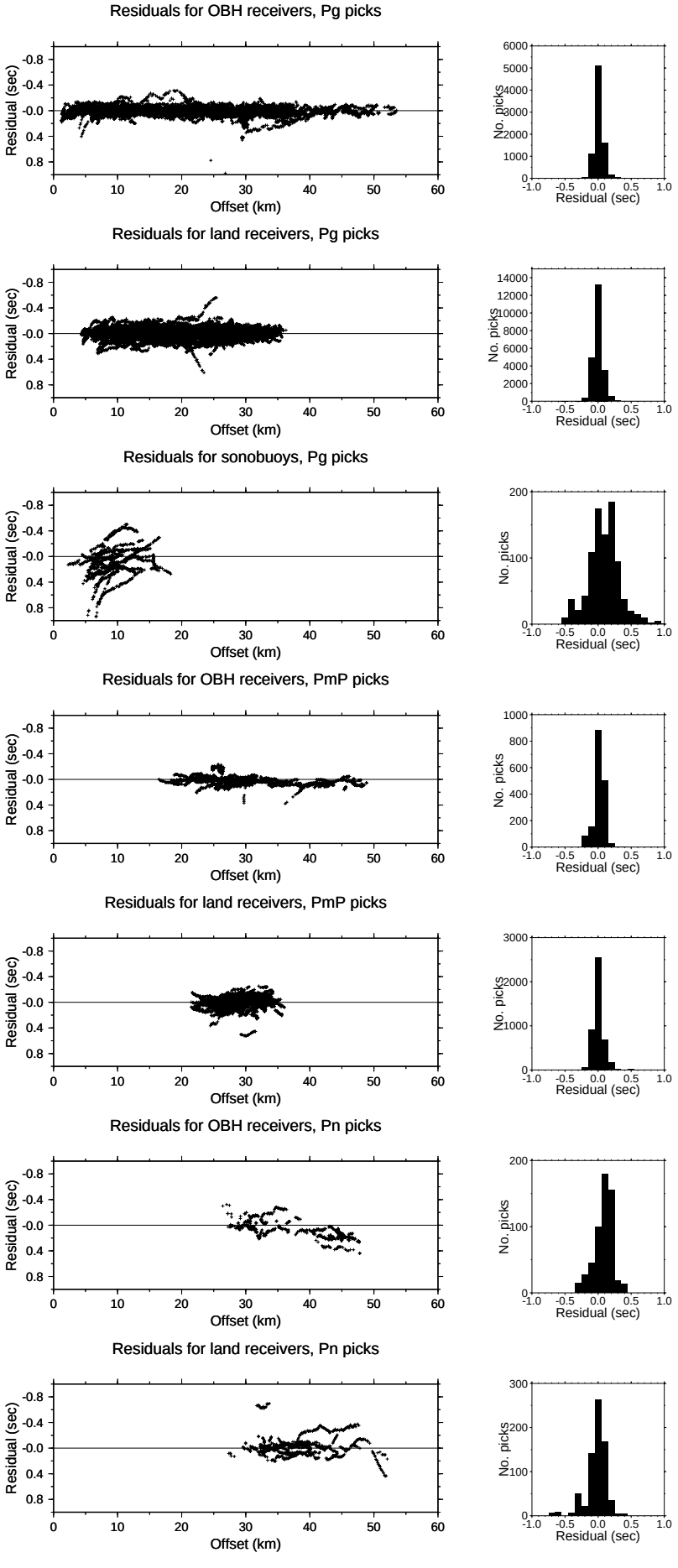

Figure 3.5: Residuals between observed and calculated traveltimes for the final model. Each receiver type and each phase are plotted separately. Histograms show the number of picks for different residual values.

3.5 Results

3.5.1 3D resolution analysis

In order to test for the resolvability of the velocity features in the crustal layer, a checkerboard resolution test (Hearn & Ni, 1994) was performed. Cuboids of ±2% velocity perturbation were added to the final velocity model and synthetic traveltimes were calculated for the same shot–receiver geometry. The quadratic B-spline velocity interpolation function defines velocity values in the transition between opposite sign cuboids. The ±2% variation from the final model is large enough to provide a traveltime perturbation greater than the noise level, without considerably changing the ray paths from those in the final model, and allowed calculation of synthetic traveltimes for more than 80% of the actual shot-receiver pairs. Two different cuboid sizes were tested: a finer grid of 5x5x1 km size and a coarser grid of 7.5x7.5x1.5 km size in X, Y and Z directions respectively. The calculated synthetic arrivals were inverted using the same approach as for the real data, starting from the original starting model. The model is well resolved in the upper 6 km for lateral features of 5 km in size (Fig. 3.6–3.7), particularly within 15–20 km of the centre of the island. For these depths the model resolves ±0.2 km s^{-1} velocity perturbations (Fig. 3.6 a–b and e–f). Between 6 and 9 km depth the model is resolved for lateral features 7.5 km in size and velocity perturbation of ±0.3 km s^{-1} (Fig. 3.6 c–d and g–h). Velocity perturbations 1 km high are well resolved in the upper 6 km of the model. For the deeper parts of the model to ∼9 km depth the vertical resolution is nearer 1.5 km (Fig. 3.7). As expected, the resolution is better closer, shallower and directly beneath the island, since the ray coverage is denser there.

The anomaly cuboids of the initial model tend to become more spherical in the final model, demonstrating that the final model is a smoothed version of the reality. Since the smoothing factor was larger in the horizontal than the vertical direction, the model resolves vertical velocity changes better than horizontal ones (Fig. 3.6 and Fig. 3.7).

3.5.2 Seismic structure

In the final model, crustal P wave velocities are higher beneath the edifice, lower on the flanks of the island, and similar to those of normal oceanic crust away from the edifice. We illustrate lateral variations in the velocity structure by displaying our final model as a perturbation from a reference model. The reference model

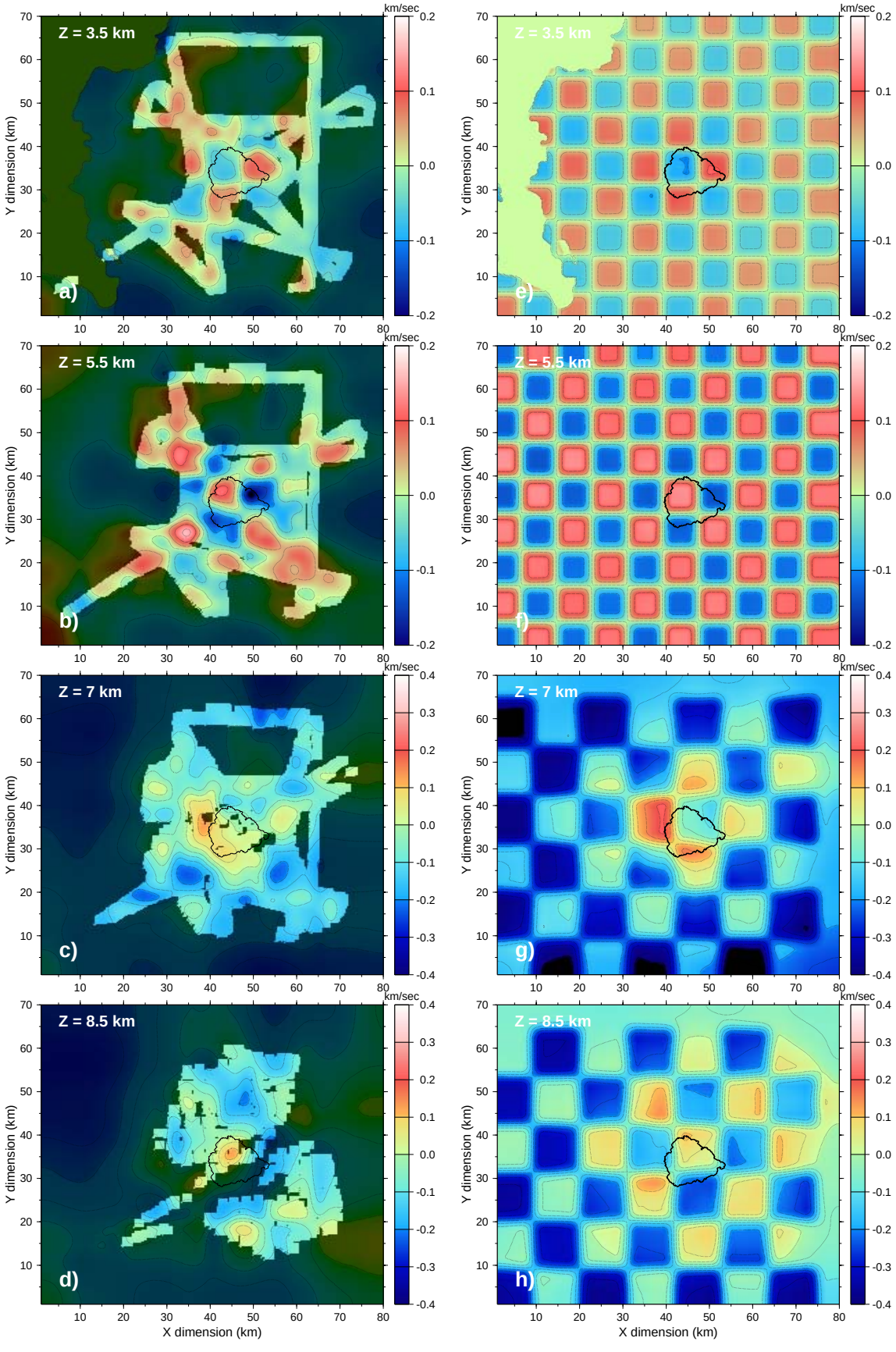

Figure 3.6: Representative horizontal slices through the results of the checkerboard resolution test. Right panels show the velocity perturbations added to the final model and left panels are the recovered velocity perturbations at the same depths. Panels a–b and e–f represent 5x5 km lateral velocity anomalies, whereas panels c–d and g–h represent 7.5x7.5 km lateral velocity anomalies. Highlighted areas in panels a–d are sampled from P_g rays. The contour interval is 0.1 kms^{-1}.

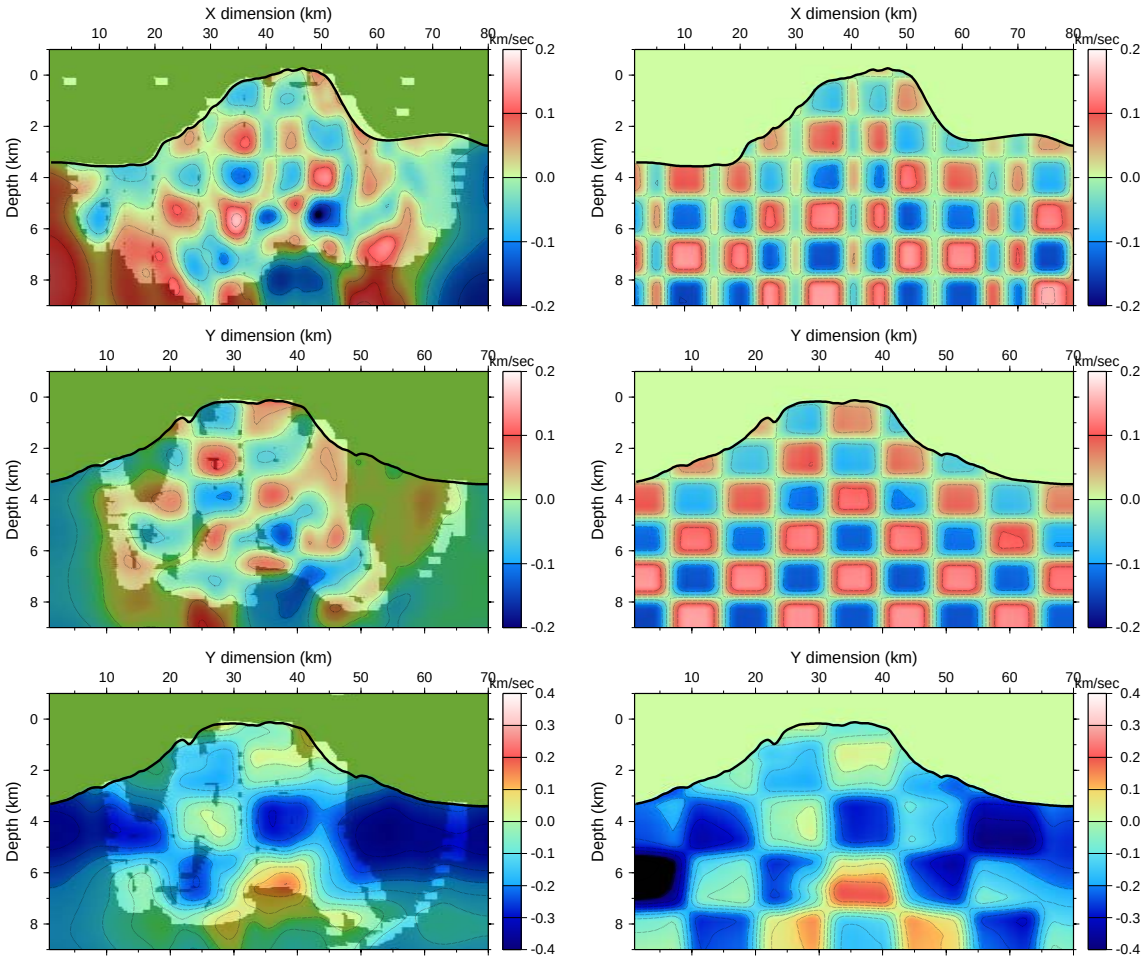

Figure 3.7: Representative vertical slices through the result of the checkerboard resolution test. Right panels show the perturbations added to the final model and left panels are the recovered perturbations. The upper and middle results use 5x5x1 km velocity discrepancies, whereas the bottom result uses 7.5x7.5x1.5 km velocity discrepancies. The first profile is profile 1 in Fig. 3.8. The lower two results are for a N-S profile at X=37 km. All three slices cross the offshore high velocity region but only the upper slice crosses the high velocity region beneath the centre of the island. Highlighted areas in the left panels are sampled by P_g rays. The contour interval is 0.1 kms^{-1}. Top slice shows irregular checkerboard shapes because it is oblique to the model axes.

was constructed by fitting trend surfaces to 2D slices through the model (Fig 3.8). As the reference model would be expected to vary laterally due to the steep bathymetry, we chose to fit quadratic rather than planar surfaces.

In the upper 7 km of the crust, the dominant feature is a higher velocity core beneath the edifice, draped by lower velocities (Fig. 3.8 and 3.9 a–e). This core covers an area of ∼20 by 20 km centred below the western part of the island, and has velocities 1–2 kms^{-1} higher than the surroundings (Fig. 3.8). Above 2.5–3.5 depth the high velocity core splits into two smaller regions with a velocities of

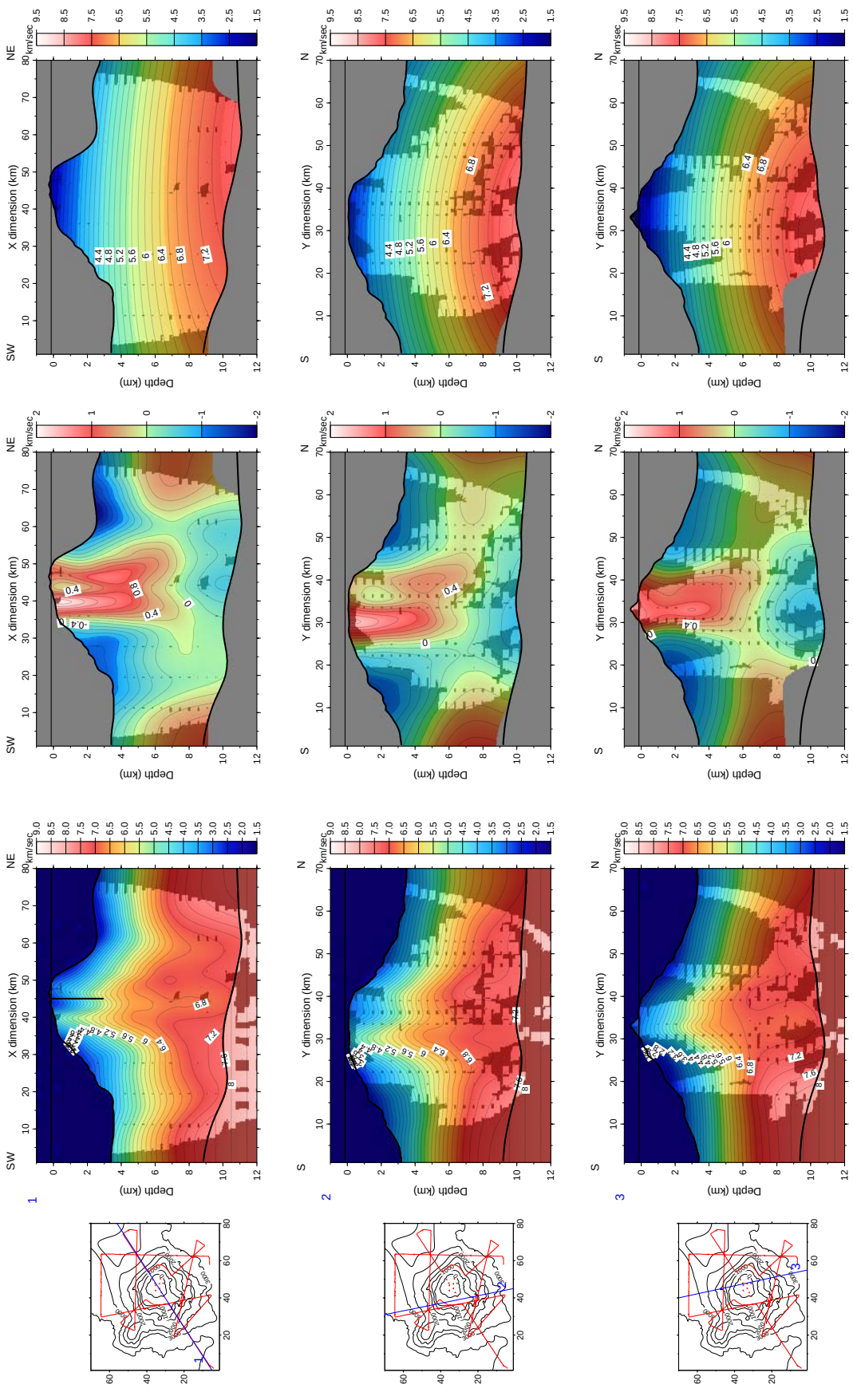

Figure 3.8: Vertical slices through the final velocity model (1–3). Shadowed areas are not sampled by P_g, P_mP or P_n rays in the forward step. Maps show the surface traces of these slices (blue lines), with the receivers and the shots. Left panels show the velocities for each profile, centre panels show perturbations from a quadratic surface fit to the same velocities and right panels show the quadratic surface. The contour interval is 0.2 kms^{-1} and black solid lines mark the surface topography and the Moho interface. Thin horizontal solid line shows the sea surface. Horizontal axes are labelled with X or Y coordinates. Thick black vertical line in left panel for profile 1 shows the position of the ASC1 borehole and the depth that it reached.

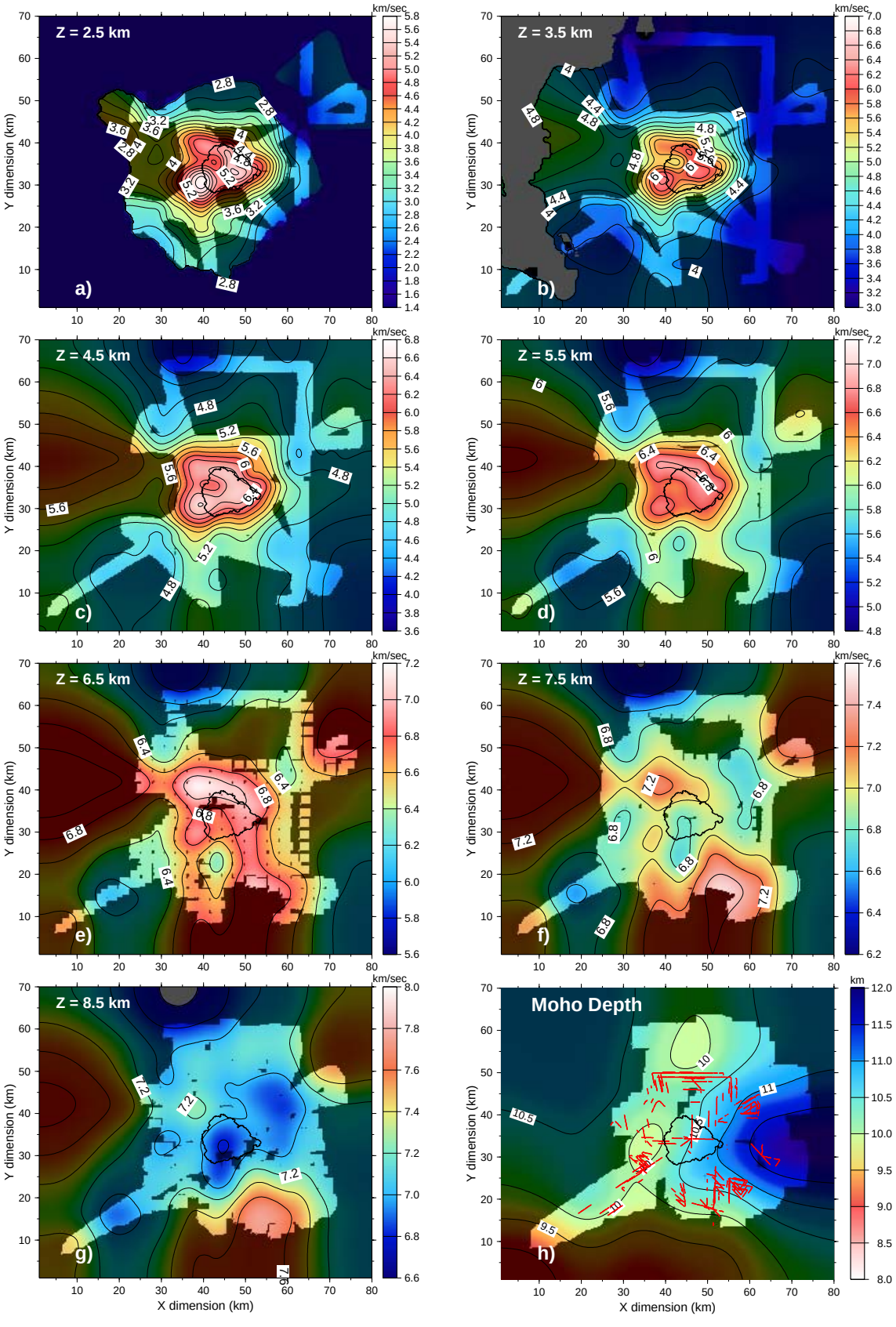

Figure 3.9: Horizontal slices through the final velocity model at 1 km depth increments (a–g). Shadowed areas are not sampled by P_g, P_mP or P_n rays in the forward step. The colour velocity scale varies between slices. Velocities are in kms^{-1}. Moho depth is shown in section h with red dots indicating the CMPs of the reflections. Shaded area is the part of this interface that is not sampled by P_mP or P_n rays. Black solid line marks the coastline of Ascension island.

5.5–6 kms^{-1}. One of these lies directly beneath the highest summit of the island (Green Mountain) and the second slightly offshore to the southwest (Fig. 3.8 and 3.9 a–b). The diameter of these features is ∼5 km. At 4.5–5.5 km depth, the high velocity core broadens (Fig. 3.9 c–d). Finally, at ∼6.5–7 km depth the positive velocity anomaly becomes indistinguishable from the background reference model (Fig. 3.8 and 3.9 e–f). This central area seems to be connected at depth with a high velocity region 10 km south of the island, which does not correlate with structures at the surface. Although the high velocity central area dies out gradually at around 6–7 km depth, this deeper anomaly reaches the deepest depths sampled by our data (Fig. 3.8 section 2 and 3.9 e–g). From 7 km to 8.5 km depth the velocities directly beneath the edifice have values between 6.8 and 7 kms^{-1} (Fig. 3.8 and 3.9 f–g).

Comparison between the two-dimensional model of Klingelhöfer et al. (2001) and a similar slice through our final model reveals that, in the region where there is in-line coverage, the RMS velocity difference is 0.75 kms^{-1} and the RMS difference in Moho depth is 1.35 km. Hence the addition of data from offline shots has added significant extra information.

3.5.3 Moho topography

In general the Moho depth increases towards the East (Figure 3.9 h). To the north, west and south of the island the average Moho depth is around 10.2 km. There are two regions where the depth is less than 10 km; the first is slightly offshore of the west coast of the island and the second around 10 km north of the island. Beneath the eastern and northeastern flank of the edifice, Moho depth contours are semicircular and depths increase from ∼10.4 to 11.8 km. This increase in depth does not form a Moho depression directly beneath the edifice as would be expected from plate flexure, but is located closer to the Mid-Atlantic Ridge axis to the east. The centre of the depression is however at the same latitude as the edifice. The southwestern part of the model shows a gradual decrease in Moho depth away from the edifice from 10 km to ∼9 km.

3.5.4 Gravity modelling

Comparison between the observed gravity anomaly and an anomaly calculated from the 3D tomographic model provides an additional constraint on the validity of the seismic model. The crustal P-wave velocities were converted into densities to generate a 3D density model. The water layer was assigned a constant density

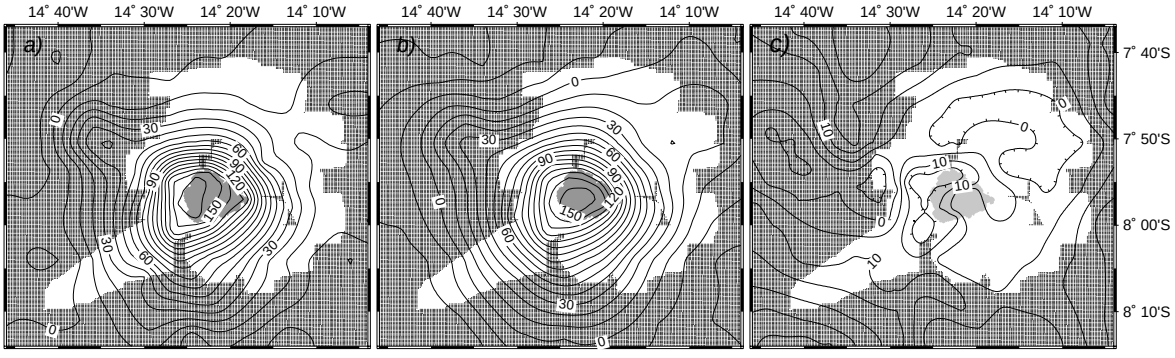

Figure 3.10: (a) Observed gravity anomaly (Minshull & Brozena, 1997). (b) Calculated anomaly for a density model derived from the 3D velocity model (see text). (c) Difference between observed and predicted gravity anomaly with an RMS difference of 9.2 mGal for the whole region and 5.7 mGal for the region where the Moho is constrained. The area where the Moho boundary is not sampled by P_mP or P_n rays is shaded. Contour interval is 10 mGal for a and b, and 5 mGal for c.

of 1.03 g cm^{-3}. Velocities between 1.5 and 4.5 kms^{-1} were converted to densities ρ using a fourth order polynomial fit (Zelt, 1989) to the dataset of Ludwig et al. (1970):

$$\rho = -0.6997 + 2.2302u - 0.598u^2 + 0.07036u^3 - 0.0028311u^4 \qquad (3.1)$$

To account for the porosity changes in layer 2 and deeper, the velocity-density relationship of Carlson & Raskin (1984) was used for velocities greater than 4.5 kms^{-1}. Upper mantle densities were set to a constant value of 3.30 g cm^{-3}.

23 isodensity surfaces were extracted from the converted 3D density model, defining the boundaries between homogeneous layers of different density. The gravity contribution of each interface was calculated using the Fourier transform formulation of Parker (1972), using the first five terms in the Taylor series expansion. The total gravity anomaly is the sum of the contributions of all the individual layer boundaries.

We used the gravity dataset compiled by Minshull & Brozena (1997) (Fig. 3.10 a), who combined shipboard gravity data, measurements on land (MacFarlane, 1968; Dash & Milsom, 1973), and satellite data (Smith & Sandwell, 1997) for all areas more than 10 km away from the ship tracks. Parker's method calculates gravity on a horizontal plane, so Bouguer anomalies on land were calculated assuming a density of 2.3 g cm^{-3} (Minshull & Brozena, 1997), and the subaerial part of the model was removed. The conversion of the velocity model into densities gives a mean subaerial density of 2.25 g cm^{-3}, confirming that the Bouguer

corrections applied are reasonable.

The grid of the anomaly due to the model (Fig. 3.10 b) was subtracted from the observed anomaly grid and the residual anomaly was sampled at the points where gravity measurements exist. After subtracting a planar trend from the sampled points, to remove effects of deep lithospheric density variations unconstrained by our seismic data, we regridded the residual anomaly (Fig. 3.10 c) and calculated a 9.2 mGal root-mean-square (RMS) misfit between observed and predicted gravity. The RMS anomaly misfit for the region of the model where the Moho is constrained is 5.7 mGal. Minshull & Brozena's (1997) RMS misfit for the same area was 13.5 mGal. This improvement in misfit gives additional confidence in the validity of our velocity model.

3.6 Discussion

The dominant features of our velocity model at shallow depths are the two high velocity cores, more than 5 km apart, with velocities at least 1 kms^{-1} higher than that of the surrounding rocks. These two features are clearly resolved: the model is very well resolved in this area (Fig. 3.7) for features of 25 km^3 in volume and velocity discrepancies of ± 0.2 kms^{-1}. One high velocity region is located directly beneath the highest peak of the volcano (at X=50,Y=35 km in Fig. 3.9). The other region has a maximum velocity anomaly of $\sim$2 kms^{-1}, is centred slightly off the west coast of the island (Fig. 3.8 and 3.9 a–d), and coincides with the residual gravity anomaly maximum observed by Minshull & Brozena (1997) (at X=40,Y=30 km). Lithologic interpretation of the ASC1 borehole (Nielson & Stiger, 1996), between these two high velocity regions (Fig. 3.8, profile 1), suggests an extrusive origin in the upper 3 km. The two regions merge at depth.

The deeper part of the high velocity region, between $\sim$3 km and $\sim$7 km depth and with velocities more than 0.4 kms^{-1} higher than the surroundings, could be interpreted as a central frozen magma chamber that acted as a source for two different volcanic fractures. Hieronymus & Bercovici (2001b) suggested that, in ocean island volcanoes, tensile flexural stresses at the base of the lithosphere cause overpressure in vertical magma-filled fractures sourced from a magma reservoir at lithostatic pressure. If supply of new magma ceases, the fracture will not close but solidify in situ; such dykes may contribute to the shallower high velocity regions. The high velocity body beneath Ascension Island extends for $\sim$40 km in north-south direction, $\sim$30 km in west-east direction and from the surface to $\sim$6.5 km depth (Fig. 3.8 and 3.11). High velocity bodies beneath volcanoes are common. Foulger & Toomey (1989) discovered a high velocity body beneath the Grensdalur volcano in Iceland, interpreting it as a solidified magma chamber or alternatively a complex of dykes and intrusive sheets that fed the volcano. High-velocity bodies beneath inferred rift zones in the Canary Islands have also been attributed to shallow-level dyke intrusion (Krastel & Schmincke, 2002). High velocities are also observed beneath the summits and rift zones of Kilauea and Mauna Loa volcanoes, interpreted as volcanic cores composed of solidified ultramafic cumulates that represent the upper crustal magma reservoirs and pathways (Okubo et al., 1997). A recent study of the MAR at 35^oN reveals a 0.5 kms^{-1} velocity anomaly beneath three seamounts at the segment centre which may correspond to a frozen magma chamber that fed the overlying volcanoes (Hosford et al., 2001).

Velocities on the island and in its submarine flanks and aprons are 2.5–3.5 kms^{-1}

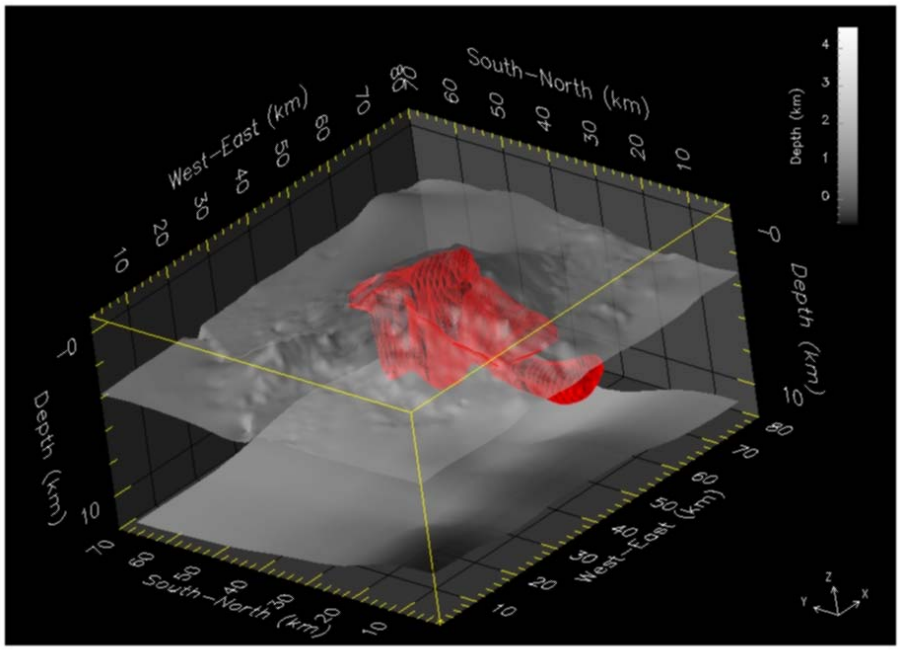

Figure 3.11: Three dimensional representation of the velocity body with at least 0.4 kms^{-1} higher velocities than the surroundings (see Fig. 3.8, right panels). The anomaly body is shown by plotting the 0.4 kms^{-1} anomaly contour that lies on slices parallel with the Y axis (red colour), with 1 km spacing. The seafloor interface is also shown.

(Fig. 3.8 and Fig. 3.9–a), significantly lower than those observed in normal oceanic crust, except at very shallow depths beneath ridge axes (Fig. 3.12). The southwest side of the edifice shows low velocities within both the submarine flanks and the aprons whereas in the northwest part the low velocity layer is thick on the apron but very thin on the submarine flank. The extent of the low velocity layer on the aprons is longer on the northeastern side of the edifice where the topographic relief of the flanks is steeper (Fig. 3.8 profile 1). Klingelhöfer et al. (2001) suggested that the older SW flank of Ascension island has been more strongly eroded and therefore produced more low velocity clastic material. Additionally, small landslides have been identified by Mitchell (2003) on the eastern steep flanks of the island. Velocities lower than those of normal oceanic crust have been identified on the submarine flanks and aprons of various seamounts and volcanic islands. Based on observations from La Palma, Staudigel & Schmincke (1984) suggested that during late stages of seamount evolution, as the seamount top approaches depths where explosive volcanism is possible, clastic processes are responsible for the formation of 70% of the material deposited. As the production of large amounts of clastic material on the volcano and its flanks continues, the material slides on the steep

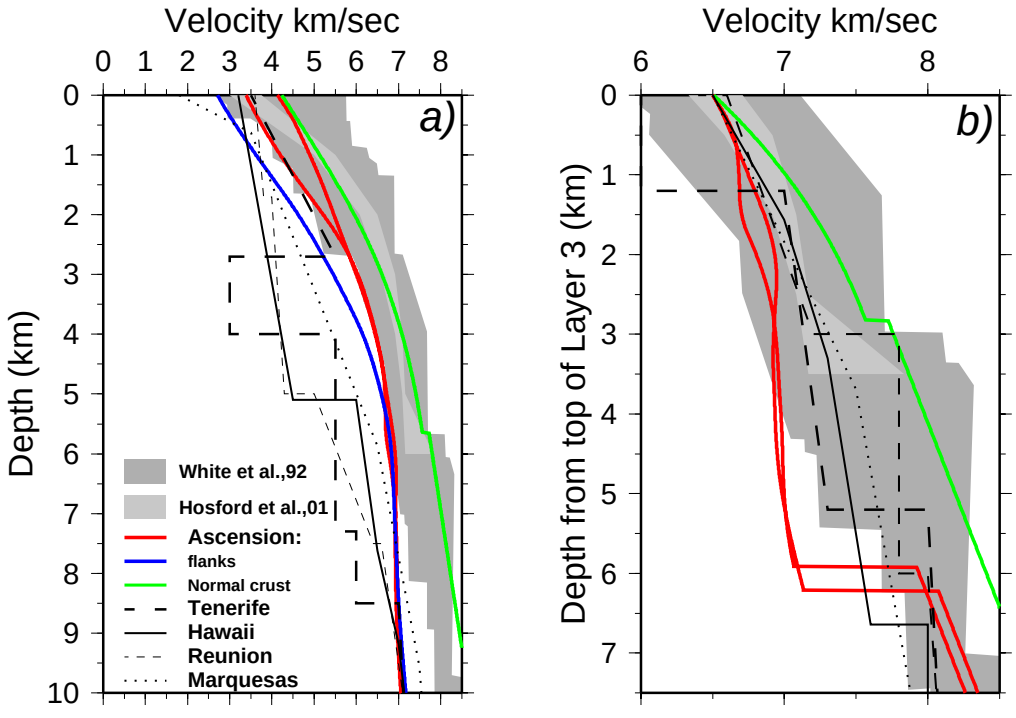

Figure 3.12: (a) Comparison of velocity-depth profiles passing through the high velocity core in the 3D final model (red thick lines) with profiles in various volcanic islands, such as Tenerife (Watts et al., 1997), the Marquesas islands (Caress et al., 1995), Hawaii (Watts et al., 1985) and Reunion (Charvis et al., 1999), and velocity ranges of normal oceanic crust, east and west of the Mid-Atlantic Ridge at 35^{o}N (Hosford et al., 2001) and for 0–127 Ma Atlantic crust (White et al., 1992). Blue thick line represents the velocity profile through the east flank of the island and the green profile is extracted from the sampled part of the southwest corner in the model. (b) Same velocity profiles hanging from the 6.5 kms^{-1} contour to allow comparison of layer 3 velocities.

flanks, creating debris flows which are deposited in the aprons of the seamount. Steep flanks prevent the deposition of material and increase the maximum transport distance of the volcaniclastics deeper to the aprons (Staudigel & Schmincke, 1984). Similarly, a low velocity layer that thins gradually away from the island of Tahiti and extends to about 220 km has been identified by Grevemeyer et al. (2001) and attributed as a product of debris flows. Low velocities on the northern flank and apron of Gran Canaria have been identified as volcaniclastic and hemipelagic sediments (Krastel & Schmincke, 2002), whereas large landslides have been suggested as an important mechanism to form low velocity complex structures on the flanks and aprons of Great Meteor seamount (Weigel & Grevemeyer, 1999). We therefore suggest that the clastic material in Ascension Island has been transported towards the aprons, especially on the NE flank which is probably too steep

to allow deposition of material. Here, the volcaniclastic material travelled longer distances from the top of the edifice. Low velocities within the summit of the edifice may be attributed to the presence of hyaloclastites, lava flows and breccias, such as those observed at the surface by Weaver et al. (1996).

Assuming that the transition between Layer 2 and 3 lies between the 6.2 and 6.6 kms^{-1} isovelocity contours in normal oceanic crust, the thickness of oceanic Layer 2 for the Ascension edifice varies between 3.5 and 6.5 km, and this layer comprises almost half of the total crustal thickness (Fig. 3.8 and 3.9 c–d). Hammer et al. (1994), comparing the relatively small Jasper seamount with the large volcanic island of Hawaii, found that these two shield volcanoes have rather different ratios between the thicknesses of these layers. Although Hawaii is much larger in volume than Jasper seamount, they both have a $\sim$4 km thick layer with velocities less than 6 kms^{-1}. A low velocity layer of similar thickness has been also found in Great Meteor Seamount (Weigel & Grevemeyer, 1999). Therefore we add support for the suggestion that small volcanic edifices appear to contain a much larger proportion of low-velocity material than their larger counterparts (Hammer et al., 1994).

The possible Layer 2/3 boundary, between the 6.2 and 6.6 kms^{-1} isocontours (Fig. 3.8), shallows beneath the centre of the edifice, so that Layer 3 appears to be unusually thick. The high velocity core is still distinguishable for at least $\sim$1.5 km below this boundary, indicating that it consists, at least partly, of intrusive rocks. A similar structure has been observed at Great Meteor Seamount (Weigel & Grevemeyer, 1999). An alternative model could involve intrusion on top of Layer 3 of material with similar velocities, masking a downward bending of Layer 2/3 boundary due to the lithospheric loading. In this case, the original Layer 2/3 boundary could be located at the bottom of the high velocity anomaly (Fig. 3.8).

The upper 4 km of layer 3, shows velocities that lie within the bounds of White et al. (1992) for 0–127 Ma Atlantic oceanic crust but are lower than those found on the ridge axis at 35^{o}N (Fig. 3.12–b). Hawaii, Tenerife and Reunion have similar velocity patterns to that of Ascension Island. The lack of crustal velocities higher than 7.4 kms^{-1} and of intracrustal wide-angle reflections suggests that any magmatic underplating beneath Ascension Island must, if present, be thin (Fig. 3.12–b and Fig. 3.8). The velocity-depth profile extracted from the southwest corner of our model falls within the velocity ranges for normal oceanic crust and has, at greater depths, higher velocities than the profiles passing through the centre of the edifice (Fig. 3.12, green profile).

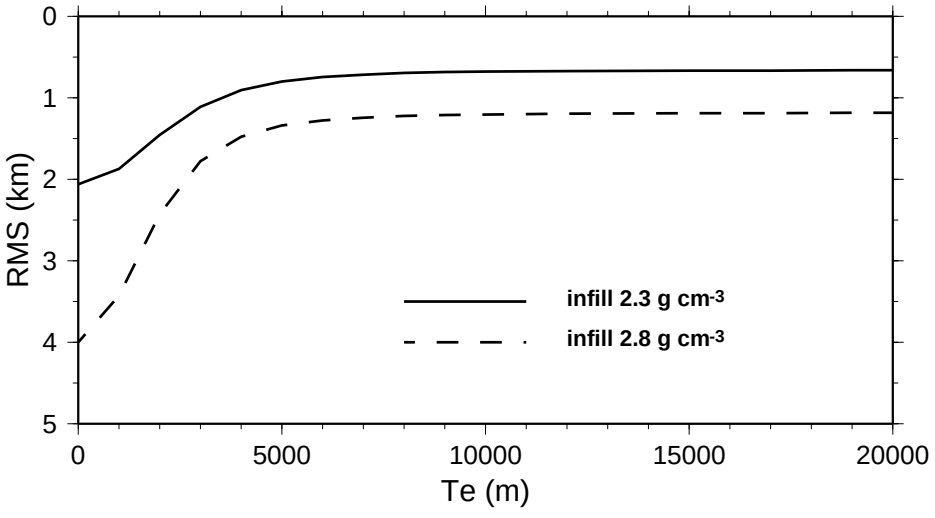

Figure 3.13: Elastic thickness (T_e) versus RMS difference between the Moho calculated from the tomographic inversion (with a planar trend removed), and a plane flexed elastically by the Ascension Island load, with a load density of 2.3 g cm^{-3} and infill densities of 2.3 g cm^{-3} (solid line) or 2.8 g cm^{-3} (dashed line).

Constraints on the effective elastic thickness of the lithosphere from the 3D Moho geometry were investigated using the approach of Watts & ten Brink (1989) and Watts (1994). Following the reasoning of Minshull & Brozena (1997) we take 3100 m as a reference basement depth prior to loading and assume that the depression created by the load is filled with material of the same density. Using the converted 3D density model we calculated a mean load density of 2.3 g cm^{-3} for depths less than 3100 m in the edifice. This value is significantly lower than the 2.8 g cm^{-3} density of normal oceanic crust (Carlson & Herrick, 1990), and provides further support for the suggestion that the densities of ocean island volcanoes are lower than those commonly assumed (Minshull & Charvis, 2001).

The response of the Moho interface to loading of the lithosphere with different elastic thicknesses (T_e), load densities derived from our 3D density model, and constant infill densities between 2.3 and 2.8 g cm^{-3}, was compared with the seismically derived Moho depth. A planar trend was removed from the seismic Moho since any such trend cannot be explained by a flexural model with uniform T_e. The RMS misfit between the original and calculated Moho interface is always more than 0.6 km, showing that there is no simple flexural model that explains the shape of the Moho beneath Ascension Island. However, independent of the infill assigned density, the RMS misfit increases steeply for T_e shallower than 6 km, suggesting that T_e values significantly less than 6 km are unlikely (Fig. 3.13).

Our T_e estimation, and that of Minshull & Brozena (1997), who inferred a lower T_e value, assume that that load emplacement occurred sufficiently far from the

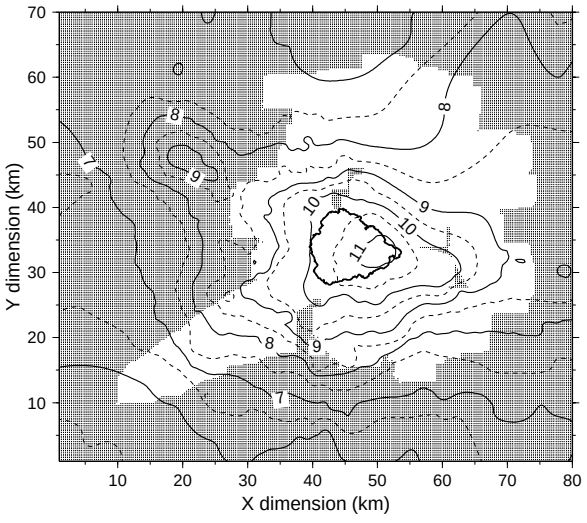

Figure 3.14: The crustal thickness in km, obtained by subtracting the bathymetry and topography from the Moho interface. Grey-shaded area is the region that is not sampled by P_mP or P_n rays. Thick black line marks the coastline of Ascension island.

ridge axis and the Ascension Fracture Zone to be unaffected by any free boundary. The difference between our model and that of Minshull & Brozena (1997), which both fit the gravity well, arises because our seismic results indicate a load density even smaller than the relatively low value of 2.5 g cm^{-3} inferred from gravity data alone. Although the published ages of surface samples from the island are all less than 1.5 Ma, recent $40_{Ar}/39_{Ar}$ dating of material from the ASC1 borehole (Fig. 3.8, profile 1) reveals ages of up to 3.6 Ma (Minshull et al., 2003b) in the upper 2 km of the edifice. These results, the shallow bathymetry between the island and the ridge axis (Minshull & Brozena, 1997; Klingelhöfer et al., 2001), and the increase of crustal thickness in the study area from ∼6 km to the SW to ∼8 km to the E–NE (Fig. 3.14), suggest long lived volcanism rather than rapid emplacement of the edifice. The Moho increases in depth towards the warmer weaker lithosphere close to the ridge axis. Much of the volcanic edifice may have been emplaced before 3.6 Ma, with its centre less than 40 km from the ridge axis, and plate bending strongly influenced by the adjacent plate boundary.

3.7 Conclusions

From our wide-angle seismic tomographic study of Ascension Island we conclude the following:

(1). The crustal structure at shallow depths is characterised by two high velocity regions. One coincides with the highest topographic peak of the volcano, and the other coincides with the gravity anomaly maximum offshore the west coast of the island. Both velocity anomalies could represent volcanic plugs.

(2). Deeper in the crust, a high velocity intrusive core reaching ~6.5 km depth is connected to the two shallower volcanic features. This feature is interpreted as a possible frozen magma chamber. This high velocity intrusive core could have been created either within or on top of oceanic Layer 3. The region of anomalously high velocities has an approximate volume of ~7000 km^3.

(3). A 3.5–6.5 km layer with oceanic Layer 2 velocities comprises almost half of the total crustal thickness, similar to structures observed at Hawaii and Jasper seamount in the Pacific and Great Meteor seamount in the Atlantic. Therefore we add support to the suggestion that the thickness of this layer is independent of the size and age of the edifice.

(4). Upper crustal velocities in Ascension Island are, in general, lower than those of normal oceanic crust at equivalent depths, due to the presence of greater thicknesses of extrusive volcanic material within the edifice and of volcaniclastics on its flanks and aprons. Away from the edifice the velocity structure becomes similar to that of normal oceanic crust. We find no seismic evidence for magmatic underplating beneath Ascension Island.

(5). No simple flexural model can explain the shape of the Moho beneath Ascension Island. If a uniform effective elastic thickness is assumed, a value of at least 6 km is inferred. However, lateral variations in lithospheric strength may have contributed significantly to the observed structure.

(6). The mean density of the volcanic load was inferred to be ~2.3 g cm^{-3}, which is significantly lower than the 2.8 g cm^{-3} density of normal oceanic crust and than load densities commonly assumed in gravity studies of flexure due to seamount loading.

Chapter 4

Mendocino Triple Junction seismic experiment

4.1 Introduction

The Mendocino Triple Junction (MTJ) is formed by the interaction of three lithospheric plates (e.g. Atwater, 1970, 1989) (Fig 4.1). Geological, seismic reflection and earthquake studies define the MTJ as a ∼25 km broad region of deformation southeast of Cape Mendocino near the town of Petrolia (Clarke, 1992; McLaughlin et al., 1997). South of the MTJ, the Pacific plate moves northwards with respect to North America plate along the complex San Andreas strike slip system. In the north the Gorda plate, a remnant of the Farallon plate, subducts along the Cascadia subduction zone (CSZ). The Mendocino transform fault (MTF) separates the two oceanic plates. The bathymetry of the area is affected by the tectonic processes, with the subduction trench and the accretionary prism being well defined northwards, whereas south of the Mendocino Transform Fault a deformed triangular block (Vizcaino block) is visible in the northeastern corner of the Pacific plate as an anomalously shallow region. The strike slip movement includes both the Maacama and Barlett Springs fault systems that run in parallel and to the east of SAF.

In this chapter, analysis of a wide angle seismic dataset acquired onshore and offshore the Mendocino triple junction area is described. An overview of the geological and geophysical background of the area is followed by the experiment description. Velocities are determined by the three-dimensional tomographic modelling of traveltime picks, and model resolution is determined using a checkerboard test.

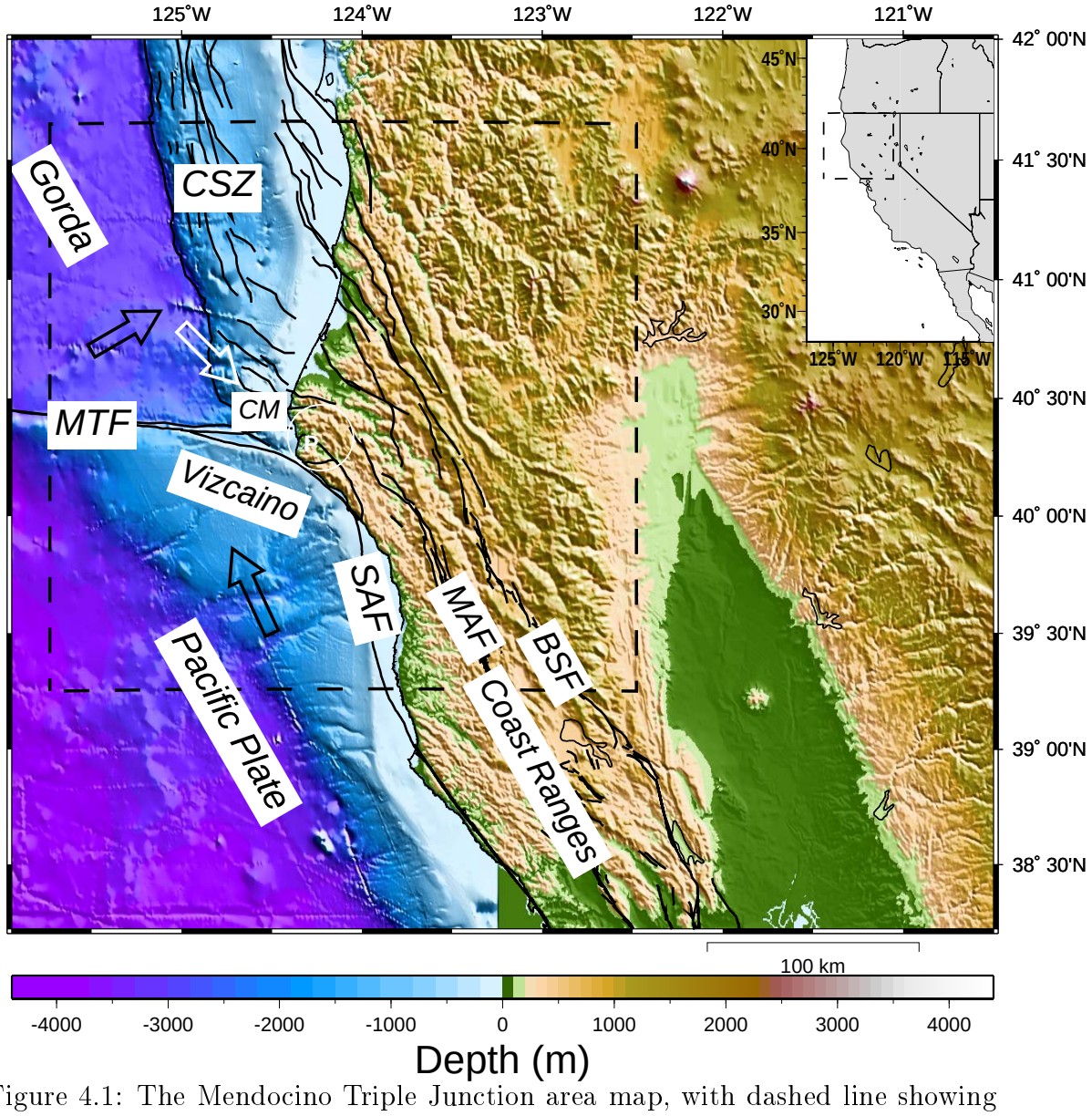

Figure 4.1: The Mendocino Triple Junction area map, with dashed line showing the experiment area used for this study. The circle shows the MTJ by Clarke (1992). Black arrows show direction of plate movement relative to a fixed North America, whereas white arrow indicates the Gorda plate motion relative to a fixed Pacific plate. Bold lines indicate mapped faults in land and the accretionary prism. Maacama and Barlett Springs fault systems are visible east of the San Andreas Fault. MTF: Mendocino transform fault, CSZ: Cascadia subduction zone, MTJ: Mendocino triple junction, SAF: San Andreas fault system, MAF: Maacama fault, BSF: Barlett Springs fault, CM: Cape Mendocino, P: Petrolia

4.2 Geology and Geophysics of the Mendocino Triple Junction region

4.2.1 Surface geology and seismicity

The surface geology of northern California around the MTJ reflects the oceanic plate subduction and accretion beneath North America which has been active since the Early Cretaceous (Fig. 4.2). The Franciscan complex, a Mesozoic-Cenozoic accretionary wedge sequence, increases in age and metamorphic grade eastwards. It is divided into the Coastal belt (a Tertiary accretionary complex), the Central belt (an Early Jurassic to ~Tertiary tectonic melange), and the Eastern belt (Jurassic to Cretaceous blueschist facies rocks) (e.g. Blake et al., 1985). North of the triple junction, near Eureka, the Franciscan complex is overlain in places by the deformed sediments of the Cenozoic Eel River forearc basin, which reach 4 km thickness in places (Clarke, 1992). Northeast of the MTJ the Franciscan complex is overlain by the Klamath terrane, which is composed of Paleozoic to Late Jurassic arc rocks (Harper, 1980). The active Mount Shasta and Lassen Peak volcanoes

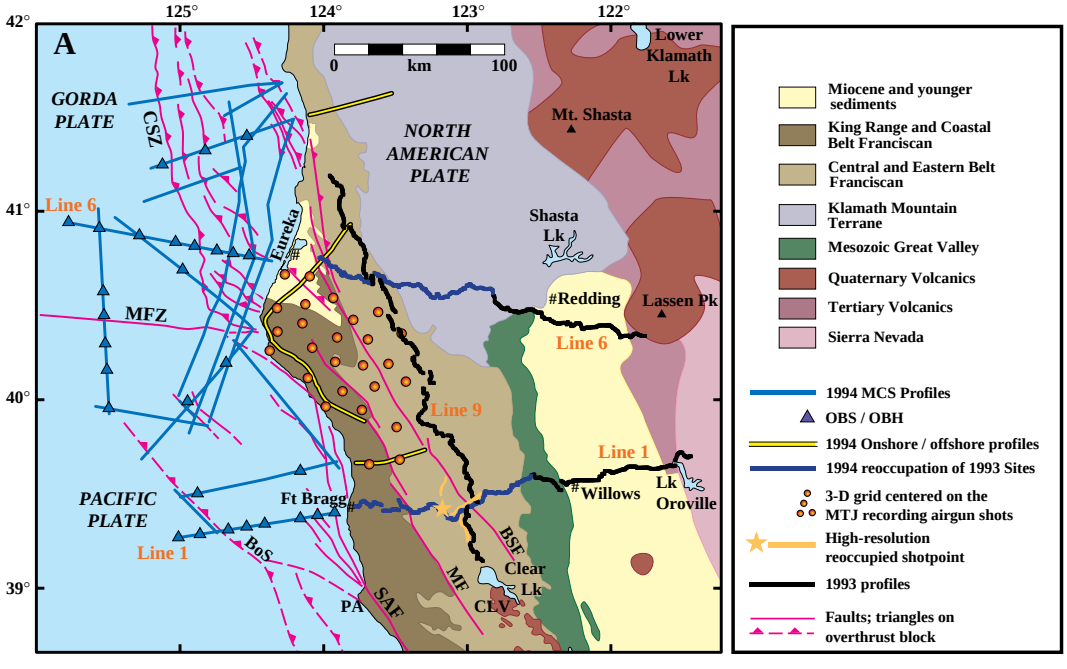

Figure 4.2: Simple geological map of the Mendocino triple junction area. The experiment geometry is also shown. The only part of this experiment not used in this study is the solid black marked extensions of land line 1 and 6. Red lines mark the USGS mapped faults. MFZ: Mendocino fracture zone, CSZ: Cascadia subduction zone, SAF: San Andreas fault system, MF: Maacama fault system, BSF: Barlett Springs fault system, PA: Point Arena, CLV: Clover Valley, BoS: Base of slope

relate to the ongoing subduction of the Gorda plate beneath North America. South of the Mendocino fault a Mesozoic–Paleogene Andean type geology is observed, with the Franciscan subduction complex, the Great Valley forearc basin, and the Sierra Nevada magmatic arc, from west to east respectively (Dickinson, 1981).

The high seismicity of Mendocino area is mainly the result of the Pacific and Gorda ongoing plate movements relative to the North America. Around Cape Mendocino, there is a large concentration of right-lateral strike-slip events, at

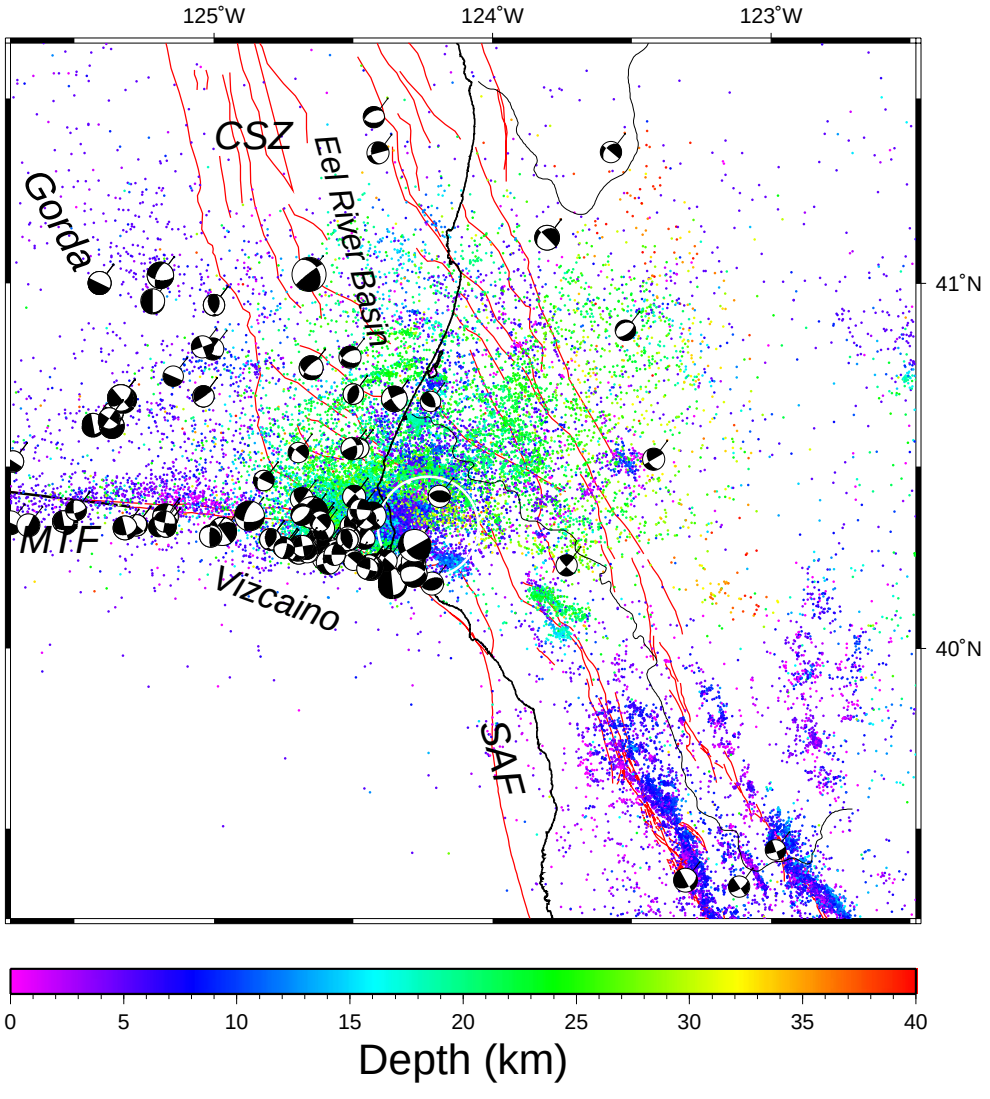

Figure 4.3: Northern California Seismic Network catalogue locations, recorded between 1977 and 2002, plotted versus depth. Focal mechanisms of events occurring between 5 and 40 km depth and with $M > 4$ are also plotted. The circle shows the MTJ broad region by Clarke (1992). Red lines mark the USGS mapped faults. MTF: Mendocino Transform fault, CSZ: Cascadia subduction zone, SAF: San Andreas fault.

depths less than 15 km, with planes striking to the southwest (Fig. 4.3), defining the uncertain position of the Mendocino fault (Oppenheimer et al., 1993). Deeper events between 20 and 40 km are concentrated roughly north of 40°00′S and west of 123°00′W and are related to the subduction zone (Fig. 4.3). The abrupt cessation of deep events to the south of an ESE extension of the Mendocino fault is associated with the southern end of the Gorda slab (e.g. Beaudoin et al., 1996b). Oppenheimer et al. (1993) have suggested that the North America–Gorda plate boundary is locked and can generate large earthquakes like the 25 April 1992 magnitude 7.1 Petrolia event.

South of Cape Mendocino the seismicity is concentrated within the North American plate along the dextral strike slip fault systems of Maacama and Barlett Springs. Both fault zones show discrete active fault strands (Castillo & Ellsworth, 1993). Focal mechanisms show a dominant right-lateral motion with northwest trending and northeast dipping planes.

4.2.2 Triple junction evolution and slab window

The northward migration of MTJ started around 27 Ma. Initially, the Farallon plate (FAR) was subducting underneath the North American plate (Fig. 4.4 a). When the Pacific-Farallon oceanic spreading system collided with the subduction zone, roughly at today's California–Mexico border, the dextral strike–slip San Andreas system (SAF) was initiated (Atwater, 1970, 1989). The strike slip system has extended progressively as parts of the oceanic plate north of the Mendocino Fracture Zone, and south of the current contact between the oceanic spreading ridge and the continental lithosphere, continued to subduct. This process created today's geometry where the MTJ in northern California and Rivera Triple Junction (RTJ), offshore Mexico, migrate in opposite directions extending the San Andreas strike slip system (Fig. 4.4 b). Subduction continues to the north of the MTJ where the Gorda and Juan de Fuca plates, remnants of the Farallon plate, subduct underneath North America.

The existence of a slab window beneath North America, first proposed by Dickinson & Snyder (1979), will be required by the geometry, after the Pacific-Farallon ridge contacted the subduction zone, assuming that the Farallon segment continued to subduct into the mantle with no new lithosphere being created back into the ridge. This window will be a growing triangular missing section in the subducting lithospheric slab beneath the continent, with its northern edge migrating northwards with MTJ (Fig. 4.4 b). This empty space at the base of

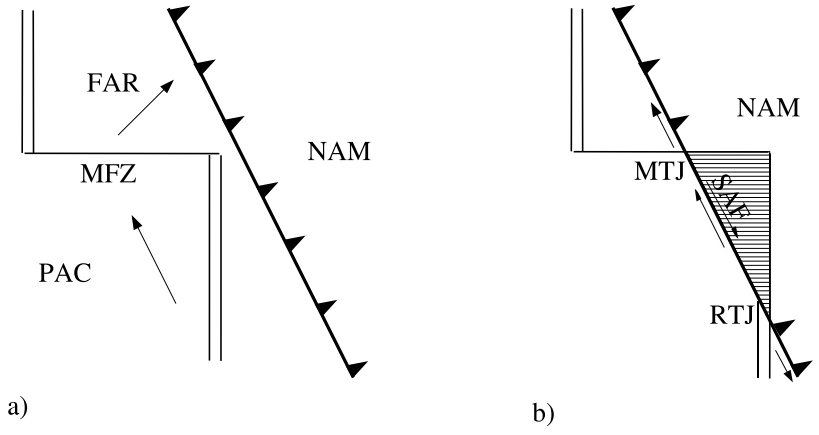

Figure 4.4: The evolution of the plate boundaries prior to 29 Ma (a), and after the collision of spreading centre with the subduction zone (b). Arrows in (a) show plate motion relative to NAM and in (b) the opposite direction migration of the triple junctions. Shadowed region in (b) marks the area of the suggested slab window. FAR: Farallon plate, PAC: Pacific plate, NAM: North America plate, MFZ: Mendocino fracture zone, MTJ: Mendocino triple junction, RTJ: Rivera Triple Junction, SAF: San Andreas fault system.

the continental crust could be filled by mafic magma created by asthenospheric upwelling (underplating) with the underlying mantle cooling to produce thicker lithosphere (Fig. 4.5 a). Supporting evidence for this hypothesis is the northward younging trend of volcanism in the Coast Ranges, that follows the passage of the triple junction (e.g. Liu & Furlong, 1992), a positive heat flow anomaly consistent with a source at ∼20 km depth (Lachenbruch & Sass, 1980), and a relative low velocity anomaly in the upper mantle of the area (e.g. Benz et al., 1992). However, for some of these observations, there are alternative scenarios that do not require asthenospheric upwelling (Hole et al., 1998). These include the existence of a gap between the northern end of the Pacific plate and the southern edge of the subducting Gorda slab as the reason for a short pulse in the northward advancing volcanism, and shear heating along the strike slip faults as a source for the shallow heat anomaly (Hole et al., 1998). Finally, the negative velocity anomaly in the upper mantle comes from a teleseismic tomography model that takes no account of crustal thickness variations through the model and assumes 30 km thick crust (Benz et al., 1992). A thicker crust beneath the Coast Ranges south of MTJ,

could also explain the observed time delays.

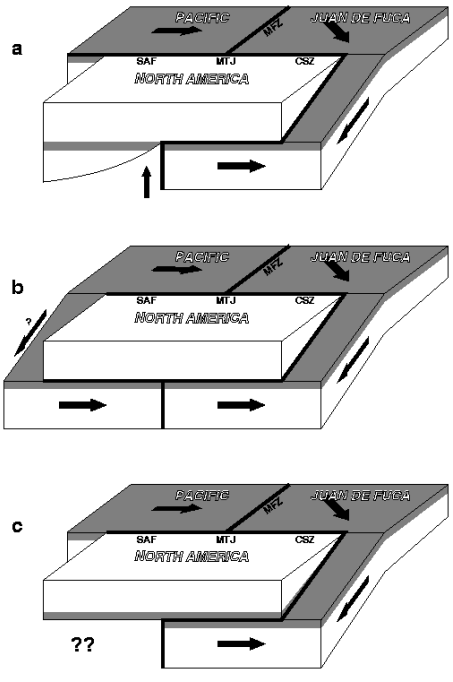

Figure 4.5: Three simplified models for the evolution of plate boundaries beneath North America (after (Hole et al., 1998)). Grey areas represent mafic rocks and arrows the relative plate motions with respect to a stable North America. Black thick lines represent active plate boundaries. a) The slab window beneath North America is filled by asthenospheric upwelling, forming thicker lithosphere. b) Oceanic crust originated from the Farallon plate, attached to the Pacific or to the overlying North America plate fills the slab window and moves northwards. Upwelling might still occur in places. c) Hypothetical model where high velocity mafic rocks existed in the bottom of the continental plate prior to the MTJ passage. This model does not explain how the slab window is filled.

Alternatively to the asthenospheric upwelling scenario, some oceanic crust at the top of the slab window beneath the Coast Ranges, could underlie North America and move northwards following MTJ migration, with some subduction still happening (Fig. 4.5 b). Bohannon & Parsons (1996), based on thermal and rheological modelling, suggested that Farallon slab fragments did not subduct, but remained in place beneath the North America margin due to friction forces caused by buoyancy, countering the slab-pull forces. In this kinematic model the slab window forms further eastwards and well beneath the lithosphere and it has little or no effect in the overlying continental lithosphere. The Farallon fragments could be attached to the Pacific plate, with the transform boundary lying on top of it and the strike–slip faults creating an eastward dipping detachment surface on top of the oceanic crust (Brocher et al., 1994). The strike slip system could also cut through the oceanic slab causing the seizure of the slab from the overlying

continental crust. In this case the slab window still exists but further downdip and north or south from the existing oceanic crust beneath the continent (Hole et al., 1998). The existence of non-subducted Farallon fragments was observed further south from the MTJ area, where a mafic layer beneath the Coast Ranges is attached to the Monterey microplate and strike slip faults cut through it (e.g. Howie et al., 1993). A third explanation for the existence of the mafic layer beneath the Coast Ranges requires that the high velocity material was there before the passage of the triple junction (e.g. ophiolites). This model does not explain however how the slab window is filled, requiring additional application of the first or the second model (Fig. 4.5 c).

4.2.3 San Andreas strike slip system and North America structure

The San Andreas fault system consists of three subparallel right-lateral strike-slip faults: the San Andreas fault to the west, the Maacama fault 45–50 km eastwards and the Barlett Springs fault 35–40 km further inland (Fig. 4.1 and 4.2). The San Andreas fault offshore is often shown as splaying into two branches with the western branch remaining offshore and the eastern one returning onshore and intersecting with the projection of the Mendocino transform fault near Petrolia. The area between these two branches of SAF is the King Range, part of the Coast Ranges. A total slip rate of the strike slip system at ∼40 mm/yr was estimated by Freymueller et al. (1999) based on GPS observations (San Andreas 17.4 mm/yr, Maacama 13.9 mm/yr, Barlett Springs 8.2 mm/yr). Since the relative plate motion between Pacific and North America is 46 mm/yr, the additional slip is probably distributed, east of the elastically deforming Sierran block, in the western Nevada shear zone and the Basin and Range.

A generally high topography is observed in the Mendocino triple junction area, complementary to uplift of the Coast Range terranes by up to ∼4 mm/yr (Merritts, 1996), and deformation and uplift of the Eel River forearc basin (Gulick & Meltzer, 2002). Moreover, based on a north–south wide angle profile which crossed the transition from the subduction to the strike-slip regime, Beaudoin et al. (1998) observed an overthickened ∼35 km North American crust along the eastward projection of the Mendocino fault. The North America crust thins to ∼25 km to the north and south. The Gorda plate beneath North America is dipping southwards, with its southern end extending beneath the onshore projection of the Mendocino fault. Local earthquake tomography in the area (Verdonck &

Zandt, 1994), reveals similar results. The higher crustal thickness observed in the transition area could be attributed to isostatic response to a slab window (Zandt & Furlong, 1982), or tectonic thickening of the Franciscan complex due to the northward convergence of the Pacific plate, associated perhaps with alteration and melting due to upwelling asthenosphere (Beaudoin et al., 1998). Furlong & Govers (1999), based on a thermal-mechanical finite element 2D model, proposed that there is an ephemeral thickening followed by thinning of the crust as a result of the triple junction migration.

4.2.4 Pacific and Gorda structure and interaction

The northeast corner of the Pacific plate is a triangular shaped, shallow region, bounded by the Mendocino transform fault to the north and the San Andreas fault to the east (Fig 4.1). The Vizcaino block is believed to have been formed initially as a Franciscan accretionary prism which later has been transferred to the Pacific plate as the plate boundary has migrated eastwards. Increased lower crustal thickness in the block was suggested by Leitner et al. (1998) and Henstock & Levander (2003), from analysis of various offshore and onshore–offshore wide angle profiles. A total of ∼30 km north-south shortening was estimated but the structure is inconsistent with any ongoing transfer of Gorda material across the Mendocino fault (Henstock & Levander, 2003). The block was possibly deformed when the Pacific crust was still young, in response of the Pacific–Juan de Fuca/Gorda plate compression. This event happened before the deposition of the 11 Ma old undeformed sediments that lie on top of the NE corner of the block (Godfrey et al., 1998). The Moho beneath the block also shows a root and was deformed possibly by the same event that thickened the lower crust (Leitner et al., 1998). The strong Pacific plate incorporates the King Range onshore (Fig. 4.2) where the same thickness lower crustal layer can be traced, with the Pacific–North America boundary suggested to run below King Range and not offshore (Henstock & Levander, 2003). The Pacific-Juan de Fuca compression has elevated the Vizcaino block up to 1.5 km above the Gorda Plate seafloor along the Mendocino transform fault. This process created the steep north facing Gorda escarpment (Fig. 4.1) and an adjacent basement ridge (Leitner et al., 1998).

The Gorda plate, which is currently taking all the deformation, can be traced flexing downwards by the strong Pacific plate, as it is approaching MTF from the north, relative to a fixed Pacific frame (Henstock & Levander, 2003). The rigid Pacific plate acts as a barrier and the north-south compression makes the

Gorda plate rotate clockwise and deform along northeast-southwest left lateral strike slip faults (Gulick et al., 2001). Seismic results show no evidence that Gorda plate underthrusts under the Pacific plate, or obducts over it (Gulick et al., 2001). The Eel River basin is deformed, shortened, and uplifted as a result of the Gorda underthrusting beneath North America and the MTJ northward migration (Gulick & Meltzer, 2002). The northeast-southwest trend of the faults within the Gorda crust is in contrast with the northwest-southeast trend of faults within the overlying Eel River forearc basin (Fig. 4.3), suggesting decoupling between the southern Gorda plate and the North American accretionary prism.

4.2.5 Strike slip–Slab window–Subduction, a unifying seismic view?

Seismic experiments around the MTJ (Beaudoin et al., 1994, 1996b; Godfrey et al., 1997; Henstock et al., 1997; Henstock & Levander, 2000a, 2003) show a high velocity mafic layer at the base of the crust which dips gently from the Pacific and Gorda plates eastwards, beneath North America. Henstock et al. (1997), based on a wide angle profile across the continental margin south of MTJ, imaged this 5-10 km thick high velocity layer at the base of the crust extending from the Pacific plate to 50 km east of SAF. This layer deepens gently towards the east but at the San Andreas and Maacama fault zones shows vertical offsets, suggesting that the two strike–slip fault systems cut through the entire crust. Similarly Hole et al. (2000), based on a 3D smooth wide angle model, interpreted steep slopes of the 6.5 km s^{-1} isovelocity contour beneath San Andreas and Mendocino faults as a smoothed image of near vertical offsets of the mafic layer, which exists in all three plates, but in different depths. The San Andreas system should then cut the entire crust from the triple junction southwards to at least the area where the fault is $\sim$2 Ma old, at $39°20'$N. All the above indicate that the high velocity layer beneath North America is not attached to the Pacific plate, ruling out tectonic models that require unsubducted Farallon fragments moving northwards attached to the Pacicic plate. Whereas north of the Mendocino fault the mafic layer represents oceanic crust, across SAF the high velocity layer is produced either from material attached to the continental crust prior to the MTJ passage or by accreted material due to asthenospheric upwelling after the passage of MTJ.

On the other hand, based on the results of the offshore-onshore profile by Henstock et al. (1997), Henstock & Levander (2000a) inferred that evidence of some weak asthenospheric upwelling in this profile since considerably lower velocities in

the upper mantle of this area have not been observed, at least for the first 5–10 km beneath the Moho. Moreover, Levander et al. (1998) and Henstock & Levander (2000b) working on seismic data from a high-density array deployed along part of the same profile, near Lake Pillsbury, observed strong short-offset reflections from the lower crust and Moho boundary. The reflections have been attributed to discrete or continuous zones of fluid 300 m and 100 m thick, respectively. The source of this fluid is within the upper mantle, representing lenses of partial melt.

The increased seismicity in the southeast corner of the Gorda plate, associated with discontinuous reflections beneath the accretionary prism (Gulick et al., 1998) suggest fragmentation of the Gorda plate. These Gorda fragments could flow past the edge of the rigid Pacific plate into the slabless window east of the San Andreas fault system (Henstock et al., 1999). The possibility that part of the Gorda plate underplates the accreted terranes would explain both the high velocities observed in the upper mantle and the limited partial melting due to asthenospheric upwelling (Henstock et al., 1999). The uplifting of the accreted Coast Range terranes is also explained in this model due to the north-south contraction of the terranes in the strike slip area south, and the subduction area north.

4.2.6 Aims and objectives of the 3D tomography experiment around the Mendocino Triple Junction

The effects of the triple junction northward migration on the crust and the upper mantle of the area can be addressed by studying the three-dimensional velocity structure of the area. Three main groups of questions need to be answered for the triple junction region, each focusing on the geometry and the structure across the three lithospheric plate boundaries of the region. The shape of the subduction boundary between the Gorda slab and the overlying North American crust and its possible association with large earthquake events, like the Petrolia 7.1 Ms event in 1992, is of major importance for the assessment of hazards in the area. Moreover, a three-dimensional velocity model can image the deformation and a possible segmentation of the Gorda slab, as a result of the convergence with the strong Pacific plate. The crustal thickness across the Mendocino transform fault and a comparison between the near surface plate boundary and the Mendocino transform boundary in the lower crust can give additional information on the interaction between the two plates. The southernmost extent of the subducting slab beneath North America will indicate or not the extension of the Gorda oceanic crust within the suggested slabless window beneath North America. A three-

dimensional model will map an upper mantle low velocity area in the region where the slabless window is expected to confirm asthenospheric upwelling. In the south of the triple junction, imaging of the vertical extent of the San Andreas fault boundary between the Pacific and North America is of fundamental importance, since it will reveal if an onshore paleotrench boundary exists and its potential large earthquake hazard. Furthermore, the position and geometry of the San Andreas fault offshore and onshore will indicate the shape and extent of the Pacific plate. Additionally, assuming the San Andreas fault as a locked strike slip zone, potential earthquake locations could be suggested. Finally, the internal structure of the northeastern corner of the Pacific plate (Vizcaino block) will reveal the evolution of this area prior or after the strike slip regime initiation.

4.3 Seismic experiment and data

The Mendocino dataset used in this study consists of a series of 2D and 3D wide angle experiments acquired in a three year period between 1992 and 1994 (Fig. 4.6). Initially, four detonated shots from the U.S. Geological Survey on September 1992

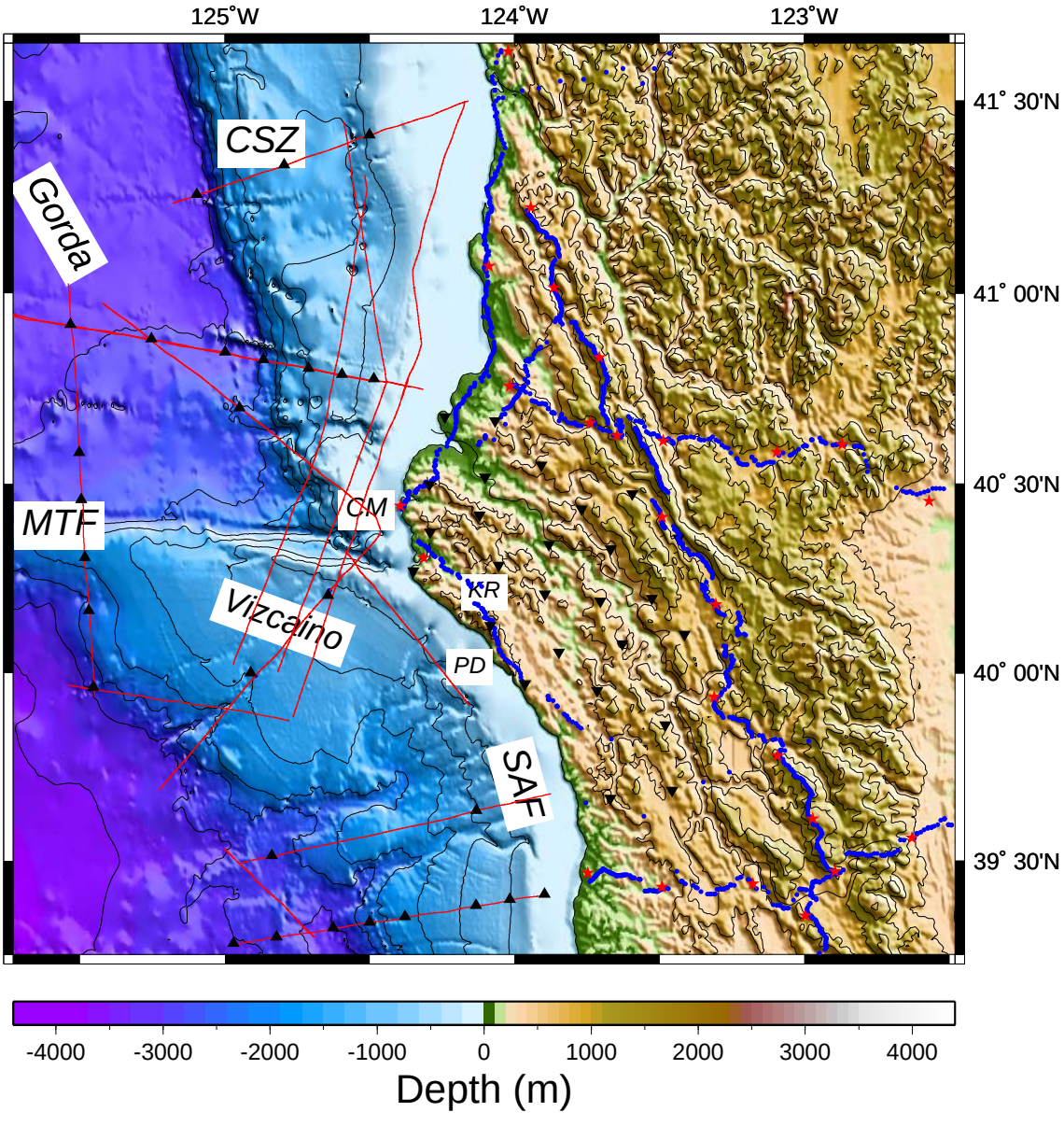

Figure 4.6: The Mendocino Triple Junction study area with topography from USGS and bathymetry from GEODAS. Offshore shot lines (red solid lines) were recorded on land into three densely sampled and two sparsely sampled profiles (blue dots). Additionally, four land profiles with explosive shots (red stars) were also recorded on inline receivers (blue dots). Receivers of the 3D land array are marked as black inverted triangles and OBH/S as black triangles. MTF: Mendocino Transform fault, CSZ: Cascadia subduction zone, SAF: San Andreas fault, CP: Cape Mendocino, KR: King Range, PD: Point Delgada.

were used for a 200 instrument *calibration* line (Klemperer & Beaudoin, 1994)

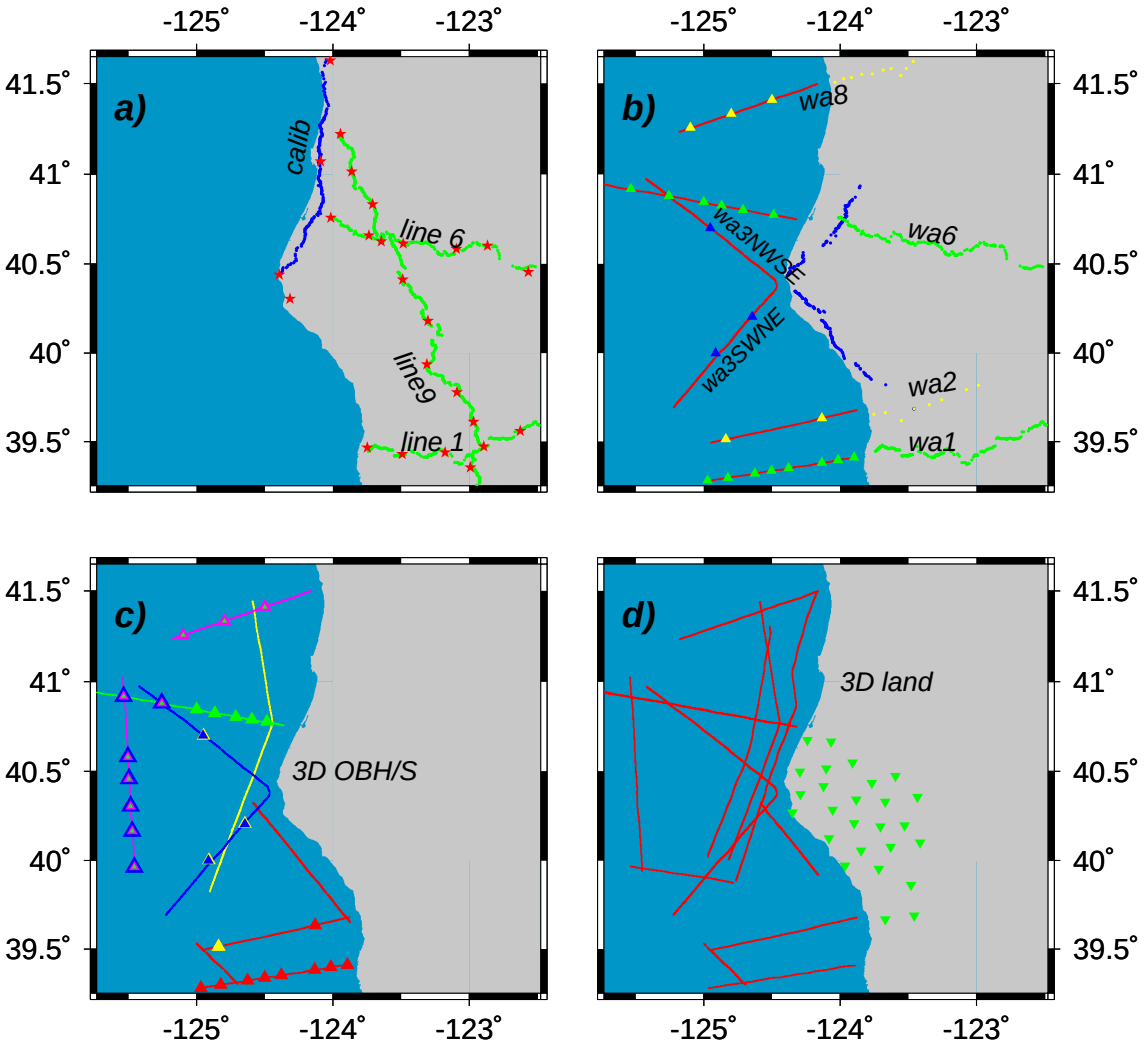

Figure 4.7: Experiment maps showing shot (red colour) and receiver positions (green or blue colour). (a) 2D land profiles representing lines 1, 6 and 9 (green colour) and the *calibration* line (blue colour). (b) Offshore–onshore 2D profiles, where receiver positions for lines *wa1* in south and *wa6* in the north are marked in green. Receivers of line *wa3* are marked in blue. Sparsely sampled profiles *wa2* in the south and *wa8* in the far north are marked in yellow. (c) 3D OBH/S array where coloured shooting tracks were recorded to similar colour receivers. Multicoloured receivers recorded more than one group of shooting tracks. (d) 3D array where shooting tracks offshore were received on a land array (green inverted triangles).

along the coast (Fig 4.7–a). On August 1993, three more onshore seismic lines (Godfrey et al., 1996) (*line1*, *line6*, and *line9*) were recorded from shots detonated in drill holes with 30 m to 60 m depth (Fig 4.7–a). Finally, on June-July 1994, shots from a 8385 in^3 tuned airgun array deployed by the *R/V Ewing* produced a series of tracks with a shot spacing of 50 m or 125 m which were recorded along onshore profiles (Henstock & Levander, 1996) (Fig 4.7–b), a 3D array of OBH/OBS offshore (Trehu & et. al., 1998) (Fig 4.7–c), and a 3D array on land

(Beaudoin et al., 1996a) (Fig 4.7–d). Multichannel data were also recorded on a 160 channel, 4 km streamer. Land stations for profiles *wa1* and *wa6* coincide with the previously shot land lines *line1* and *line6*. Profile *wa1* consists of 121 Refteks and profile *wa6* of 129 Refteks (Fig 4.7–b). Shots along line *wa3* were recorded continuously starting in the northwest and heading southeast towards Cape Mendocino and then turning southwest. The shots were recorded on a land array of 128 Refteks along onshore extensions of the offshore shots (Fig 4.7–b). On these three lines the nominal spacing between receivers is ∼1 km. Two more profiles with ∼10 km receiver spacing were also recorded: profile *wa2* in the south with 8 Refteks and profile *wa8* in the north with 10 Refteks (Fig 4.7–b). Together these profiles provide a framework of 280 by 270 km surrounding the Mendocino triple junction region. Within this framework a sparse areal array of 29 Refteks on land with 15 km spacing recorded the shooting of all the seismic lines at sea (Fig. 4.6 and Fig 4.7–c). A series of successive deployments of OBH and OBS from the *R/V Wecoma* have also produced a pseudo-array of 31 receiver positions offshore (Fig 4.7–c).

Previous geophysical work on parts of the same data includes 2D modelling of the *calibration* line by Beaudoin et al. (1994), the onshore-offshore lines *wa1* by Henstock et al. (1997) and Henstock & Levander (2000a), *wa3* by Henstock & Levander (2003), the land lines *line1*, *line3*, and *line9* by Beaudoin et al. (1996b, 1998) and Godfrey et al. (1997). Leitner et al. (1998) and Godfrey et al. (1998) imaged the Vizcaino block with offshore refraction-reflection and reflection profiles, respectively, whereas Gulick et al. (2001, 1998) and Gulick & Meltzer (2002) processed offshore reflection profiles imaging the southeastern edge of the Gorda slab and the accretionary prism north of the Mendocino fault. Finally, Hole et al. (2000) presented a 3D first arrival model from part of the data recorded in the 3D land array. The final model is very coarse and smooth with a spatial resolution of 30 km horizontally and 3 km vertically and a smoothing operator of 40 km and 4 km, respectively, as the general differences in the 3D velocity structure, rather than the absolute velocity values and smaller scale structure, were sought (Hole et al., 2000).

Wide-angle data were bandpass filtered, using corner frequencies 3-6-12-14 Hz for the Refteks, 1-4-9-12 Hz for the OBH/S and 1-3-12-16 Hz for the land shots. Predictive deconvolution was also applied to compress the source pulse (Fig. 4.8 and Fig. 4.9). For the densely sampled offshore-onshore lines, stacking of adjacent traces in common shot gathers increased the signal to noise ratio. In Figure 4.8 two characteristic shot-receiver gathers are plotted in a W-E direction, belonging to

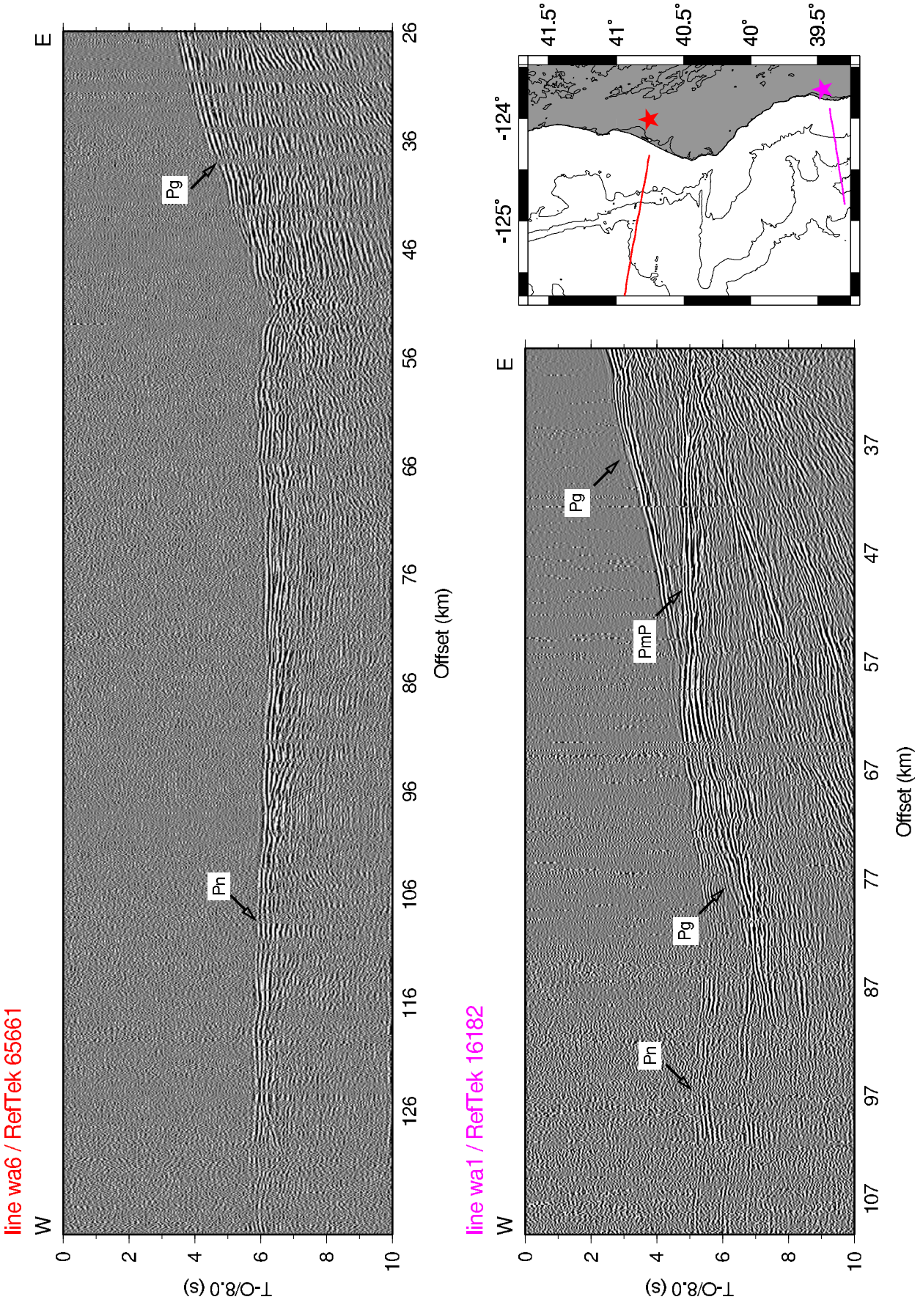

Figure 4.8: Minimum phase bandpass filtered data for two Reftek landstations in *wa6* and *wa1* offshore–onshore lines, respectively. Filter corner frequencies are 3-6-12-14 Hz. Predictive deconvolution has been applied, and data are displayed with a linear moveout correction of 8 km s^{-1}. P_g, P_mP and P_n phases are indicated. Inset map shows the positions of the shots and receivers in the corresponding colors for each plotted section (wa6:red, wa1:purple).

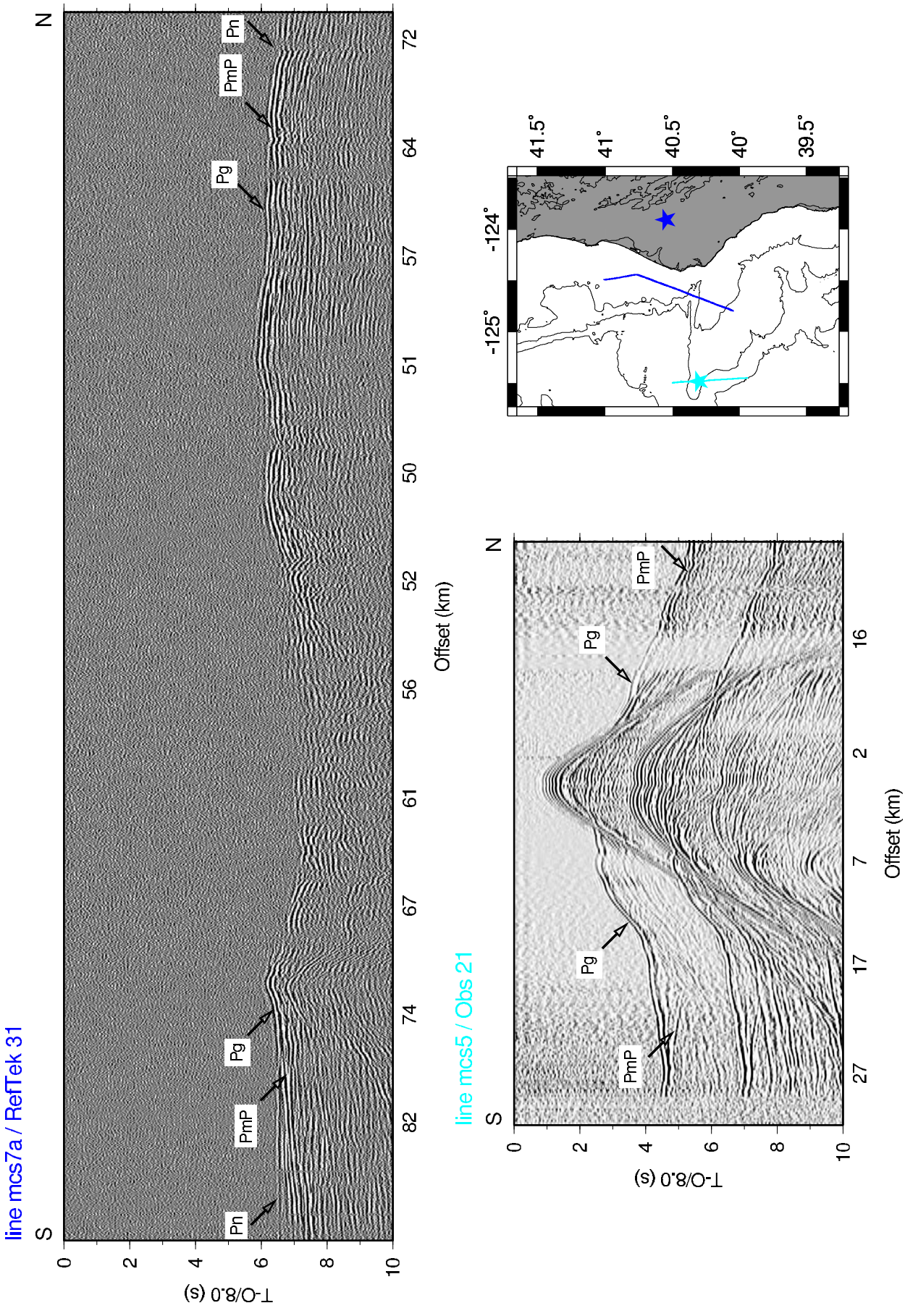

Figure 4.9: Minimum phase bandpass filtered data for an OBS and a Reftek landstation, respectively. Filter corner frequencies are 3-6-12-14 Hz for the RefTek and 1-4-9-12 Hz for the OBS. Predictive deconvolution is applied and data are displayed with a linear moveout correction of 8 km s^{-1}. P_g, P_mP and P_n phases are indicated. Inset map shows the positions of the shots and receivers in the corresponding colours for each plotted section. Note that shooting track includes turns (obs:light blue, 3dland:blue).

two receivers in the densely sampled lines north and south of the Mendocino fault (MTF), respectively. In Figure 4.9 two shot-receiver gathers with a S-N direction belong to an OBS and a land seismograph respectively, receiving offshore shots along two different lines.

In general, for W–E profiles, the P_mP arrivals in the sections north of MTF tend to increase in offset for receivers further inland, whereas for profiles south of the MTF the P_mP arrivals are observed in similar offsets (Fig. 4.10). For both W–E and N–S profiles, P_mP reflections are more clear in the south of MTF (Fig. 4.9). All these P_mP arrivals suggest a flat oceanic Moho in the south of MTF and a thin Gorda crust that is gently subducting beneath North America in the north. The steep bathymetric relief of the Gorda escarpment is imaged, close to the coast, in S–N offshore profiles as a sudden increase in the First arrivals (Fig. 4.9 RefTek 31). Data that sample the southeastern-most part of the Gorda crust close to MTJ have a high signal to noise ratio with non-continuous first and second traveltime arrivals (Fig. 4.9 RefTek 31). Furthermore, the steep bathymetric relief of the accretionary prism to the north of MTJ and its transition to the abyssal plain westwards produces diffractions and skews first and second arrivals on W–E profiles (Fig. 4.8 *wa6*).

Traveltime picks have been obtained for three phases: the refraction from the upper and lower crust (P_g), the reflection from the crust-mantle boundary (P_mP), and refractions from the upper mantle (P_n) (Fig 4.10). In total, 23808 P_g, 21503 P_mP and 14629 P_n picks were obtained. Visual inspection of all picks within similar receiver groups revealed instruments with time shifts of 1 sec. The observation was first confirmed through the experiment log books as time shifts due to possible GPS clock errors and subsequently either corrected or not incorporated in the modelling. Outliers were also removed on the basis that they were independent individual picks having great differences from picks of neighbouring instruments in the same group. Finally, traveltimes were also obtained for first arrivals using only the available first arrival P_g and P_n picks. In total, 34338 first arrival picks, received at 449 instruments, were selected (Fig. 4.11 and 4.12).

Picking of traveltimes was not performed for all traces in the common-receiver gathers since it will result in a very large number of data that requires longer computer run times for the inversion. Since for some shooting tracks the shot spacing is every 50 m and the receiver spacing around 1 km, the rays from two similar picks in adjacent traces will sample the same cells in the model, especially in coarser grids, without yielding additional information. The strategy used was simply to pick more densely in parts of the data with high signal to noise ratio.

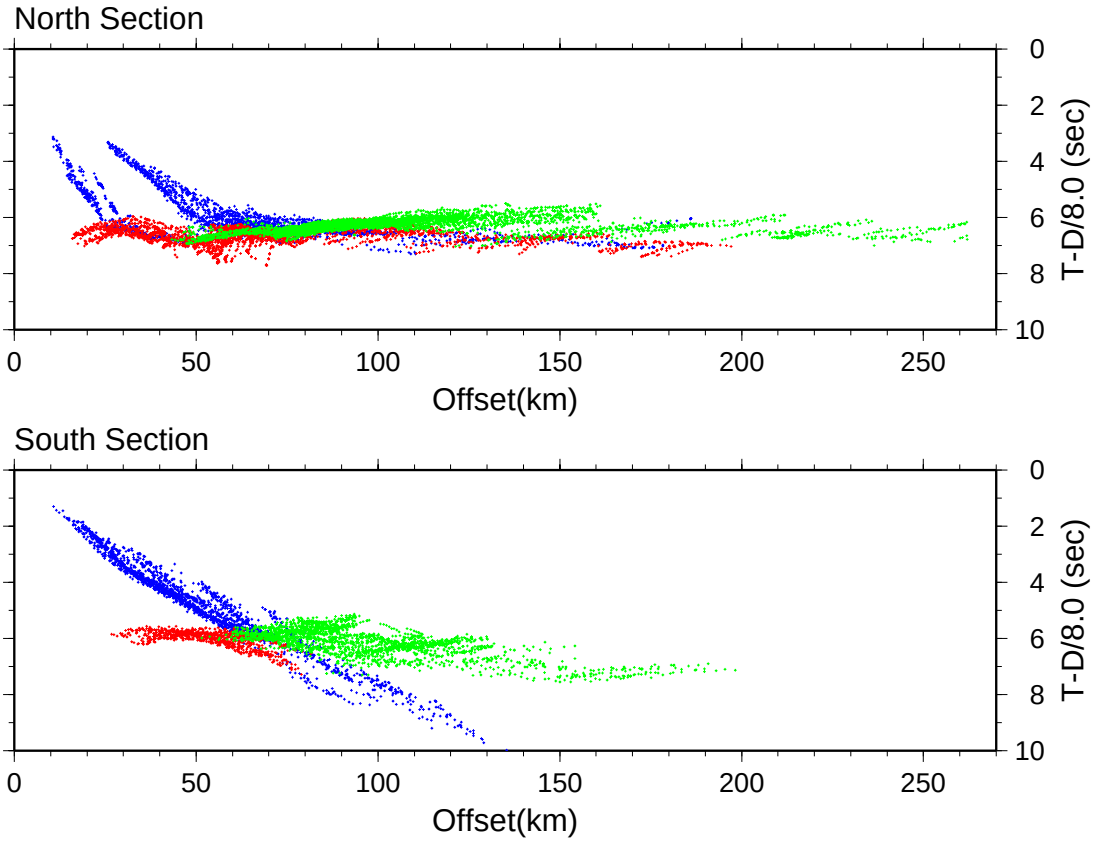

Figure 4.10: Travel time picks versus offset for shots and receivers, north and south of MTF respectively. The P_g arrivals are marked with blue, P_mP arrivals with red and P_n arrivals with green. Note that picks from OBH/S and 3D land array are not included.

These clear parts of the data were not only observed in short offsets, where P_g was visible as the first arrival, but also at far offsets, where the arrival of P_n is very clear (e.g. Fig. 4.8 and 4.9).

In Fig. 4.13, we plot the mean distance between two picks for different receiver groups, respectively. The densely sampled lines north of MTJ, *wa6* and *wa8* (Fig. 4.13 a), have an average mean picking spacing (MPS) of 4 km, whereas the densely sampled lines in the south of MTJ , *wa1* and *wa2* (Fig. 4.13 b) have an average MPS of 3.4 km. For the lines *wa3* the mean MPS is 8.4 km, although for most of the receivers the MPS is between 1 and 4 km. Receivers with higher MPS are mainly receiving arrivals from offline shots (shots south – receivers south, shots north – receivers north) where identification of arrivals was more difficult than inline shots. The mean MPS for the 3D land array is 5.8 km, whereas for the OBH/S the mean MPS is 6.4 km (Fig. 4.13 c). For most receivers offshore the mean MPS is 4.8 km except the OBH/S along *wa1* and *wa2* that have great picking distance (Fig. 4.13 c). The land profiles *calib*,*line1*, *line6*, *line9* have a

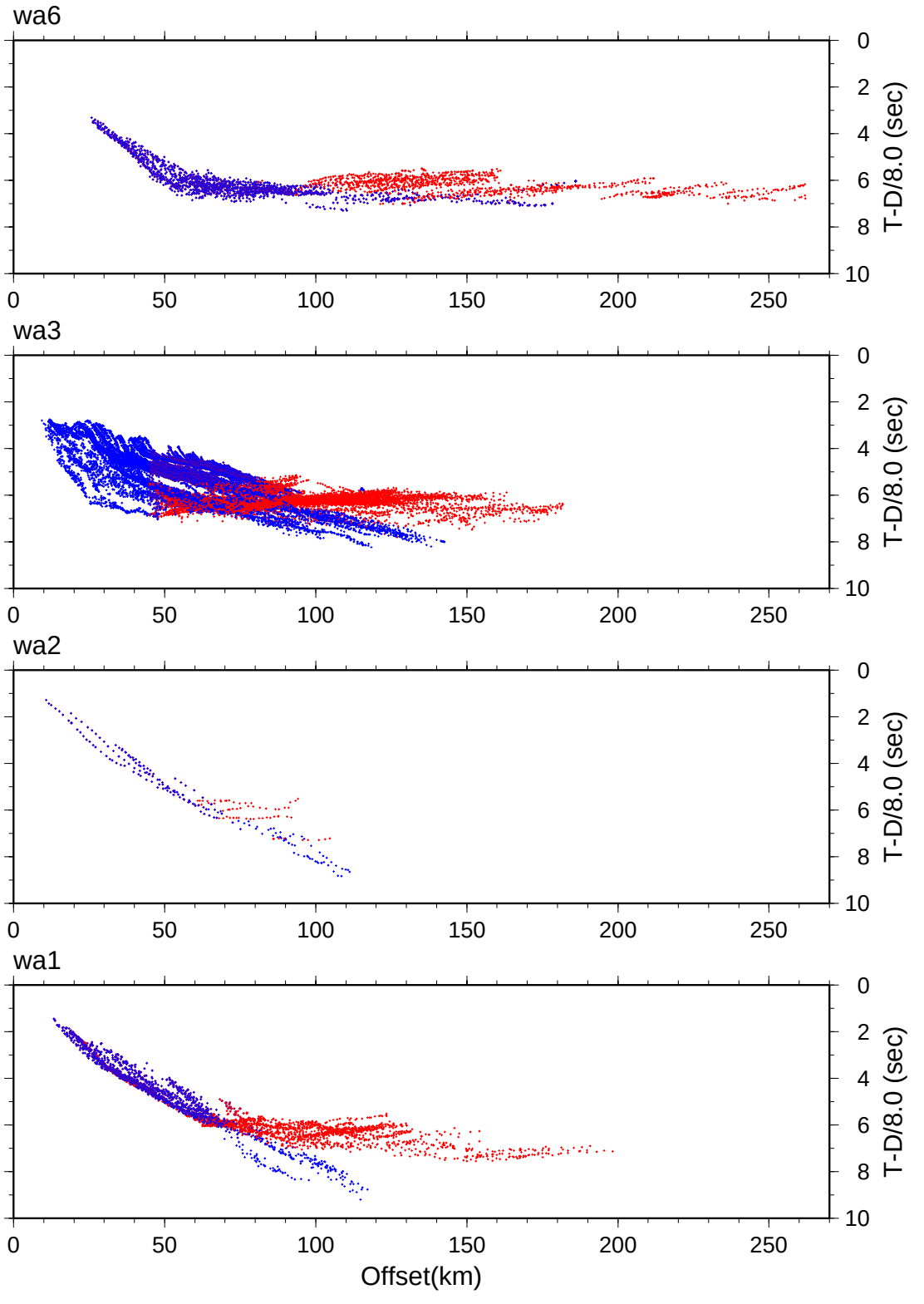

Figure 4.11: First arrival traveltime picks versus the offset for the offshore-onshore lines *wa1*, *wa2*, *wa3*, and *wa6*, from south to north respectively. Upper mantle first arrival picks are marked in red, and P_g picks, that recorded as first arrivals only in shorter offsets, are marked in blue. The P_g arrivals are superimposed.

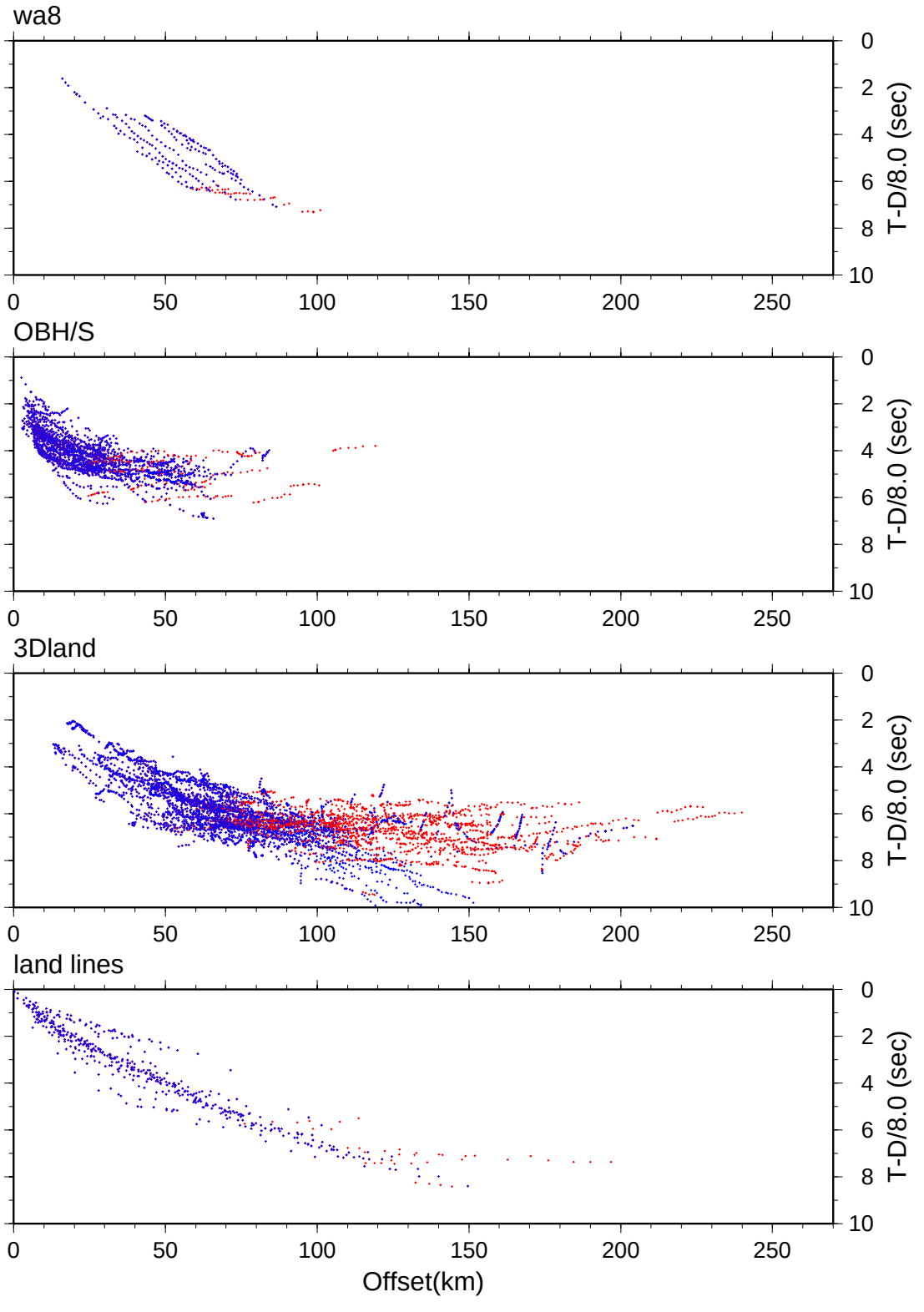

Figure 4.12: First arrivals plotted versus offset for the offshore-onshore line *wa8*, the OBH/S array, the 3D land array, and the four land lines, respectively. Upper mantle first arrival picks are marked in red, and P_g picks, that recorded as first arrivals only in shorter offsets, are marked in blue. The P_g arrivals are superimposed.

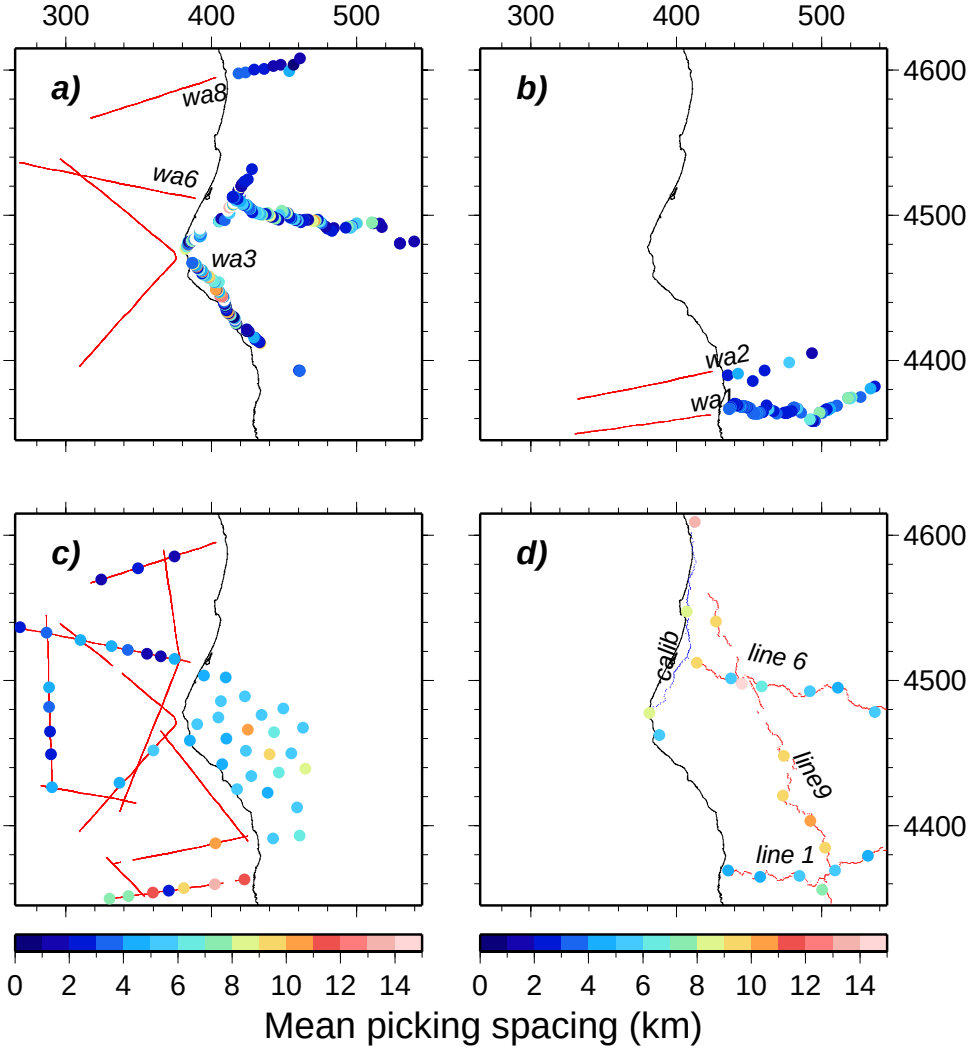

Figure 4.13: Mean spacing (MPS) between two picks in common-receivers gathers is plotted in colour scale at the location of the receiver. (a) MPS for picks in lines *wa3*, *wa6*, and *wa8*, (b) MPS for picks in lines *wa1* and *wa2*, (c) MPS for 3D land array and OBH/S picks, and (d) MPS for picks in land lines *calibration*, *line1*, *line6*, *line9*.

mean MPS of 8.7 km (Fig. 4.13 d).

Although the mean picking distance shows the followed picking pattern, it does not reveal any information about changes in picking density within a particular source-receiver gather. In Fig. 4.14, we plot the minimum distance between two picks for different receiver groups. The densely sampled lines around MTJ and northwards, *wa3*, *wa6*, and *wa8*, have for a large number of instruments a

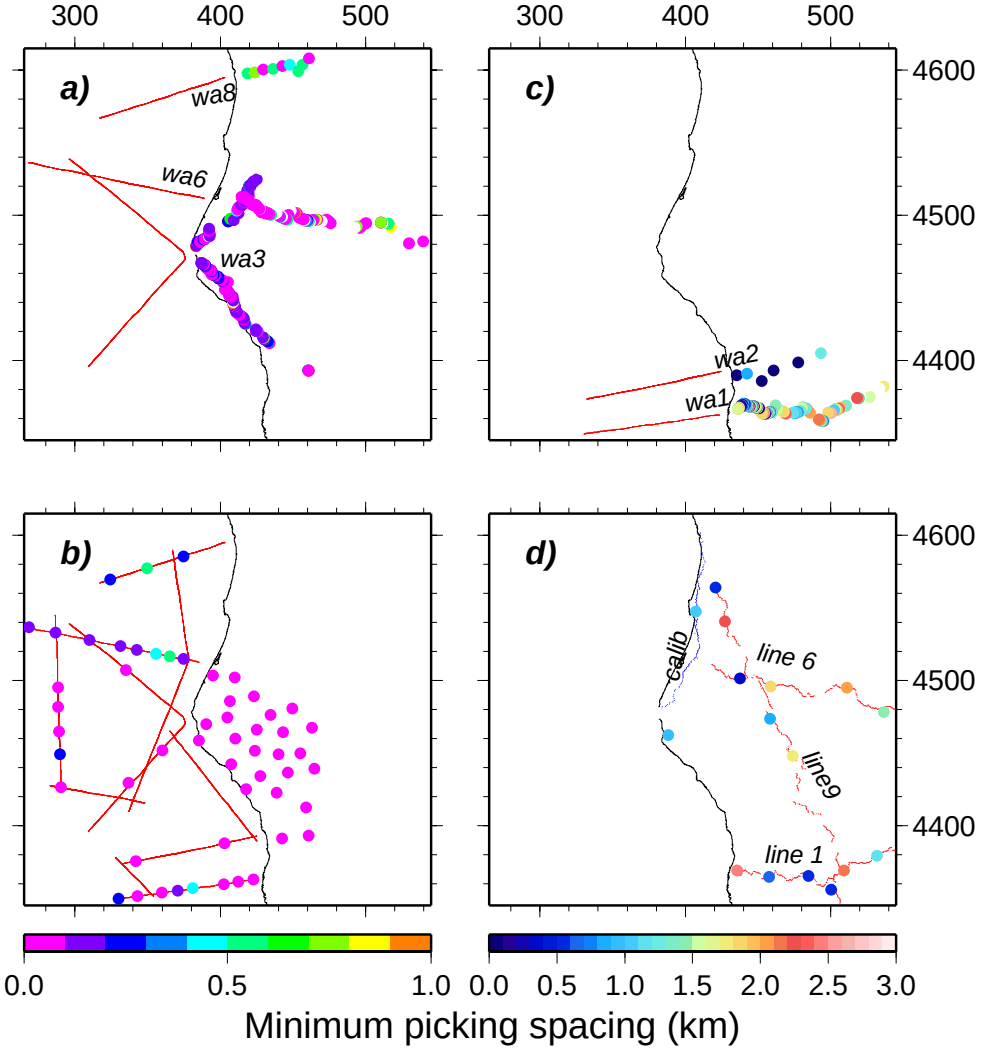

Figure 4.14: Mimimum spacing (mPS) between two picks in common-receivers gathers is plotted in colour scale at the location of the receiver. (a) MPS for picks in lines *wa3*, *wa6*, and *wa8*, (b) MPS for 3D land array and OBH/S picks, (c) MPS for picks in lines *wa1* and *wa2*, and (d) MPS for picks in land lines *calibration*, *line1*, *line6*, *line9*. Note that a) and b) are plotted in different colour scale than c) and d).

minimum picking spacing (mPS) of 50 m, which is the shot spacing, and almost all the receivers in these lines do not exceed the mPS of around 0.7 km (Fig. 4.14 a). The same patterns are observed for the 3D land array and most OBH/S picks (Fig. 4.14 b). For the lines *wa1* and *wa2* the mPS is increased to an average of 1.5 km (Fig. 4.14 c), whereas for the land profiles *calib*,*line1*, *line6*, *line9* most picks are obtained for mPS between 0.5 and 2.5 km (Fig. 4.14 d).

From all the above we conclude that the available picks should image velocity features larger than 2 km in lateral size along the densely sampled lines, whereas for the general 3D structure the lateral resolvability is at best ∼5 km. An inversion strategy that starts with a coarse grid size and progress gradually in denser grids will ensure that the coarser 3D structure will develop first and the smaller details, along the offshore-onshore lines, will build up on top of this 3D background structure (see section 4.4).

Generally, the quality of the data is very good with all major phases clearly visible, allowing confident picking. Land data and especially the calibration line tend to be more noisy. The uncertainty for the offshore-onshore lines was estimated as 60 ms for P_g, 100 ms for P_mP, and 80 ms for P_n. For the OBH/S and 3D land array the uncertainties assigned are 70 ms for P_g, 100 ms for P_mP, and 90 ms for P_n. The uncertainties for the noisy calibration line were assigned as 80 ms, 150 ms, and 100 ms whereas for the rest of the land lines were 60 ms, 150 ms, and 100 ms for P_g, P_mP and P_n, respectively. Uncertainties for first arrivals are the same as for P_g and P_n picks.

4.4 Modelling

4.4.1 Three-dimensional tomographic method

The three-dimensional tomography modelling of the study area was performed using the FAST algorithm by Zelt & Barton (1998). The choice of this approach was based on its computational efficiency and speed, especially, for the forward calculation of traveltimes in large model volumes as in our case. The major drawback of our choice is the inability of inverting simultaneously for velocity and interface depth parameters using reflected phases.

4.4.2 Initial Model construction

The starting model for the inversion of the Mendocino dataset was constructed inverting simple 1D velocity models using the Jive3D tomography algorithm (Hobro et al., 2003). The model consists of two layers: a water layer with constant velocity of 1.46 kms^{-1}, and a crustal and upper mantle layer with a smoothly varying velocity gradient. The bathymetric grid, constracted from the National Geophysical Data Center track observations, combined with the USGS land topography was used as the interface between the two layers, with a node spacing of 0.1 km. The crustal layer is defined as a three-dimensional grid with a horizontal velocity node spacing of 5 km, and a vertical node spacing of 0.5 km. Initial inversions for the crustal layer, constrained by the P_g picks only, were performed. In the first steps we used a large enough weighting regularisation factor in the misfit function (see eq. 2.79) to ensure that our evolving model will start as an estimated model that traces rays to most of the observed picks, evolves to a 1D velocity structure independently from our initial choice and then develops gradually to a smooth 3D structure. This smooth crustal model was used as an initial model for the subsequent tomography modelling using the code of Zelt & Barton (1998) (Fig. 4.15).

4.4.3 Forward model parameterisation

The velocity model occupies an area of 280 km by 270 km and extends for 52 km depth with the top of the model at 3 km above sea level. The coordinate system used in this study is in km and has been transformed from longitudes and latitudes using the Universal Transverse Mercator (UTM) projection with X being 500 km at the centre of UTM grid zone 10 at 123°W, and Y being the distance from the

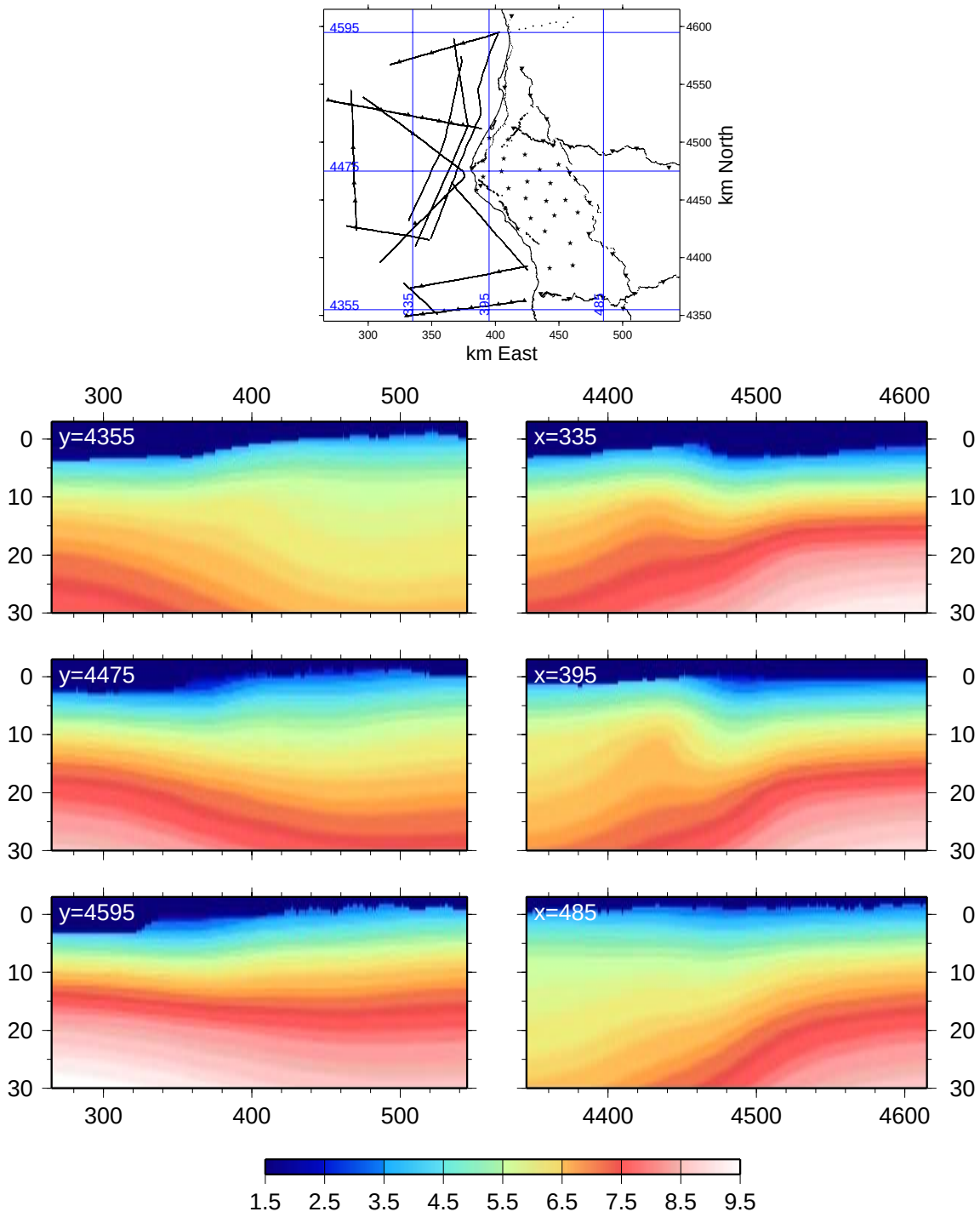

Figure 4.15: Vertical profiles through the 3D initial velocity model used for the tomography modelling. This smooth velocity model was developed from the inversion of simple 1D velocity models using P_g picks and applying large regularisation factor using the tomography code by Hobro et al. (2003). Inset map shows the shot and receiver positions and marks the surface traces of this profiles (blue lines).

equator. The grid size for the forward calculation of traveltimes depends on the errors introduced due to the bathymetry/topography parametrisation. When a ray propagates from the source to a receiver at sea level it will cross the bathymetry

interface. Assuming a bathymetry grid spacing of 0.5 km, seafloor at depth 1.76 km will be assigned as 2 km depth and therefore a ray that is supposed to travel with a soft sediment velocity (e.g. 1.6 kms^{-1}) or bedrock velocity (e.g. 3.5 kms^{-1}) will travel this additional distance of 0.24 km with 1.46 kms^{-1} water velocity, introducing an error between 14 ms and 100 ms. Discretisation of the bathymetry at 0.25 km will reduce this error to 7–50 ms. Since our pick uncertainties are greater than 60 ms, grid spacing of 0.25 km incorporates the introduced errors. However, since the forward calculation of traveltimes for this grid spacing is eight times slower and requires more than 200 Gb of disk space for the storage of the finite difference time files, we chose to perform the major part of the modelling with a 0.5 km grid, using the finer grid only at later stages. The forward grid with node spacing of 0.5 km results in $561 \times 541 \times 105 = 31867605$ nodes to be timed by the raytracing algorithm, whereas a node spacing of 0.25 km results in $1081 \times 1121 \times 209 = 253266409$ nodes to be timed.

4.4.4 Traveltime inversion and regularisation

In general, we expect a larger vertical than horizontal velocity gradient, which requires different regularisation strengths. The degree of vertical with respect to horizontal smoothing can be controlled by the parameter s_z (eq. 2.82) but it was set to 1 since we chose to control the vertical smoothing only by the inverse cell size. The behaviour of the inversion was tested by inspection of isovelocity contour plots of two-dimensional cross-sections. Finally, for each inversion step five different values of λ (eq. 2.82) were tested and the model with the best fit was chosen to continue to the next step.

Starting with the initial model described in the previous section and using the 0.5 km grid spacing for the forward calculation, the model has been inverted using 34338 first arrivals. The model is initialised using only arrivals from the 2D land lines and the 3D OBH/S array in a 15 km lateral and 2 km vertical inversion grid. We gradually reduce the inversion cell size to $10 \times 10 \times 1$ km, $5 \times 5 \times 0.5$ km, and $2.5 \times 2.5 \times 0.5$ km.

It might seem strange to initialise the model using traveltime picks from only part of the data, that actually have the greatest uncertainties and a sparse geometry, sampling only the land or the oceanic areas, individually. However, we expect significant velocity variations within the shallowest crust, that are predominantly controlled by this subset of the picks. This approach avoids having the model dominated by the more numerous, but inherently more ambiguous, onshore-offshore

picks. In addition, the general structure of the model is developed first, assisted by the coarse grid spacing. The velocity cells that are changed during the inversion are only those that are sampled by rays and their neighbours that are affected by smoothing. Thus, the use of coarse grids in the initial steps of the inversion ensures that most of the areas within the model are affected, whereas the direct use of a fine grid will affect the model only in small areas leaving the surrounding structure unchanged. The addition to the inversion of the rest of the picks, and the reduction of the inversion cell size will develop the model further, improving in detail in the areas of the densely sampled lines. Zelt & Barton (1998) suggested that the initial inversion model should be close to reality, to avoid local minima in the development of the model. The initialisation approach described here, assisted by the high degree of smoothing, ensures that the model will develop towards the actual structure even if the initial model in the inversion is not so close to reality. To decrease the calculated traveltime errors (see previous section) we resampled the velocity model to a 0.25 km cell size. After calculating the traveltimes to this finer grid, the inversion performed once again for the $2.5 \times 2.5 \times 0.5$ km inversion cell size. The final first arrival velocity model for the 0.25 km forward grid size has an χ^2 of 1.9 and an RMS traveltime misfit of 96 msec. Table 4.1 gives the final χ^2 and the RMS misfit for each grid size step.

		First			P_g		
Forward grid (km)	Inverse Grid (km)	Steps	χ^2	Misfit (msec)	Steps	χ^2	Misfit (msec)
0.5	Initial		106.4	682		90	643
	$15 \times 14 \times 2$	8	15	278	5	11.2	258
	$10 \times 10 \times 1$	8	6.8	178	5	8.4	195
	$5 \times 5 \times 0.5$	8	4	139	13	4.5	143
	$2.5 \times 2.5 \times 0.5$	7	2.4	109	7	2.8	117
0.25	$2.5 \times 2.5 \times 0.5$	1	1.9	96	1	1.9	90

Table 4.1: The total RMS misfit and χ^2 for each grid size for the first arrival model and the P_g model.

Apart from the widespread method of inverting first arrivals for a lithospheric layer which includes the crust and the upper mantle, we also inverted for a crustal layer using P_g picks only. In this way we aim to resolve the lower crust better, using P_g picks that are second arrivals after the P_n picks in the far offsets (Fig. 4.11, 4.12); in contrast, using only first arrivals is likely to mask the lower crustal structure. This crustal velocity layer, with the same lateral dimensions as the first arrival model but only 40 km deep, was inverted using 23808 P_g refracted

arrivals. Starting with the initial model described in the previous section and using the 0.5 km grid for the forward calculation, we initialised the model using only arrivals from the 2D land lines and the 3D OBH/S array in a 15 km lateral and 1 km vertical grid. We gradually reduced the inversion cell size to $10 \times 10 \times 1$ km and $5 \times 5 \times 0.5$ km. The final P_g velocity model has an χ^2 of 1.9 and an RMS traveltime misfit of 90 msec. Table 4.1 gives the χ^2 and the RMS misfit for each grid size step.

The final residuals between observed and calculated traveltimes for each receiver group are shown in Fig. 4.16 and 4.17 for the first arrival model and 4.18 and 4.19 for the P_g model. Although most of the traveltime picks are well fitted within the assigned uncertainty limits with the majority of the residuals less than 100 msec, short offset calculated arrivals to the OBH/S receivers are much faster in comparison with the observed ones. That means that the velocity structure close to these instruments is much faster that it should be. The vertical inversion cell size of 0.5 km could not recover the near-surface sediment structure, complementary to the introduced errors by the coarse parametrisation of the bathymetry, especially for receivers within the water column (OBH). Despite that, we consider that the recovered near-surface velocity structure represents the true average.

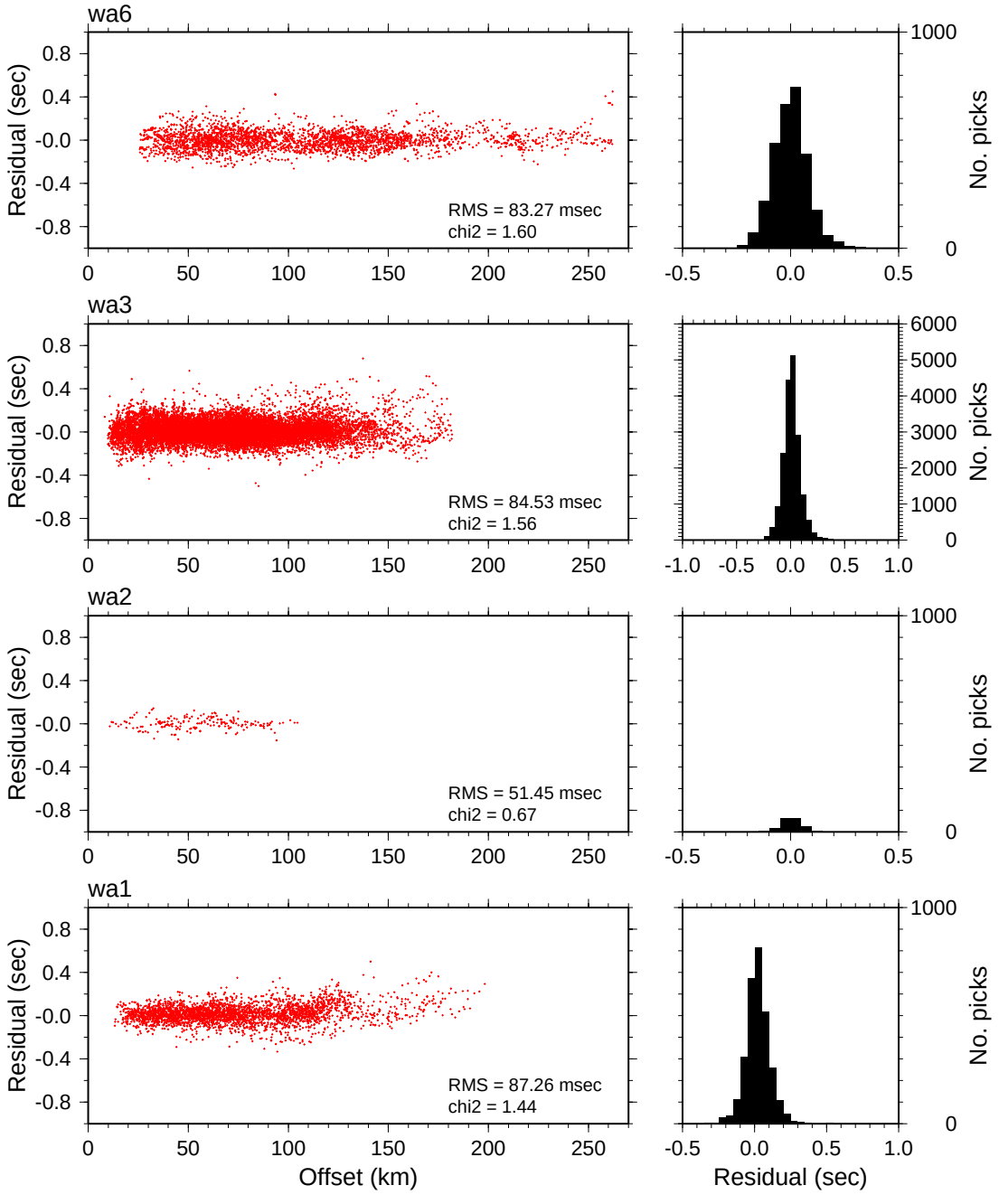

Figure 4.16: Residuals for the first arrival final model plotted versus the offset for the offshore-onshore lines *wa1*, *wa2*, *wa3*, and *wa6*, from south to north respectively. The RMS residual and the χ^2 for each group are also indicated. The histograms give the number of picks for residual values in 0.05 sec bins.

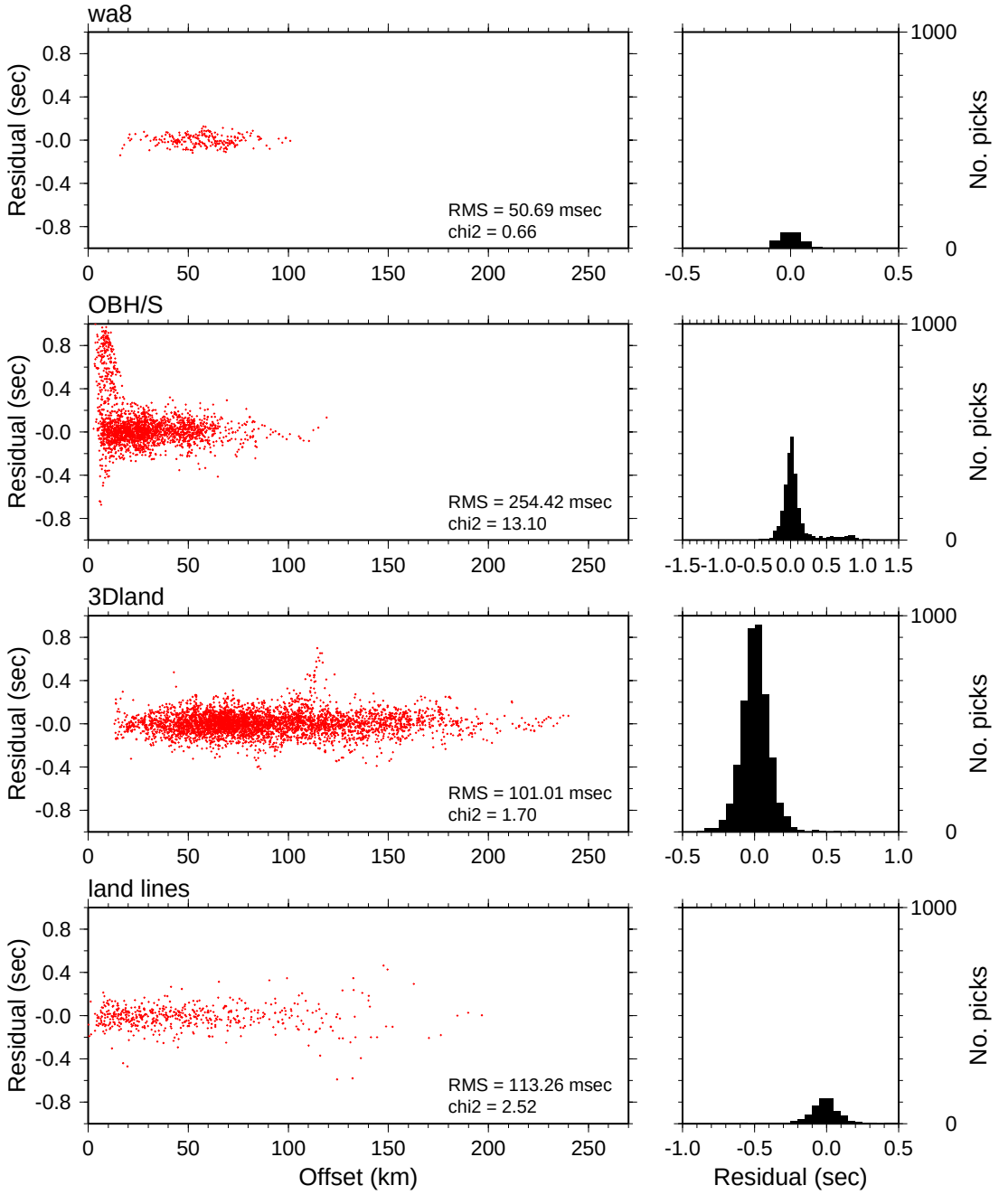

Figure 4.17: Residuals for the first arrival final model plotted versus offset for the offshore-onshore line *wa8*, the OBH/S array, the 3D land array, and the four land lines, respectively. The RMS residual and the χ^2 for each group are also indicated. The histograms give the number of picks for residual values in 0.05 sec bins.

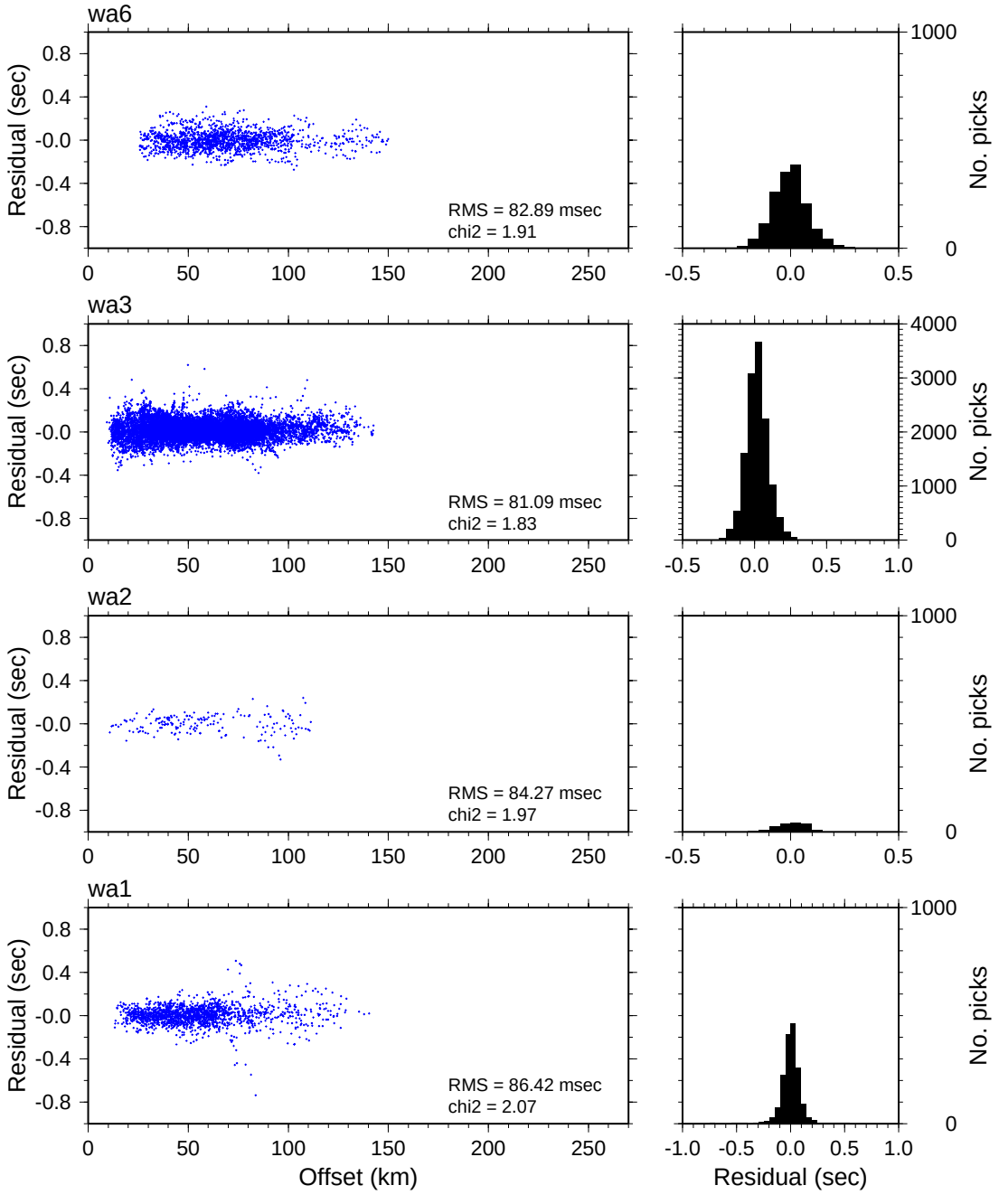

Figure 4.18: Residuals for the P_g arrival final model plotted versus the offset for the offshore-onshore lines *wa1*, *wa2*, *wa3*, and *wa6*, from south to north respectively. The RMS residual and the χ^2 for each group are also indicated. The histograms give the number of picks for residual values in 0.05 sec bins.

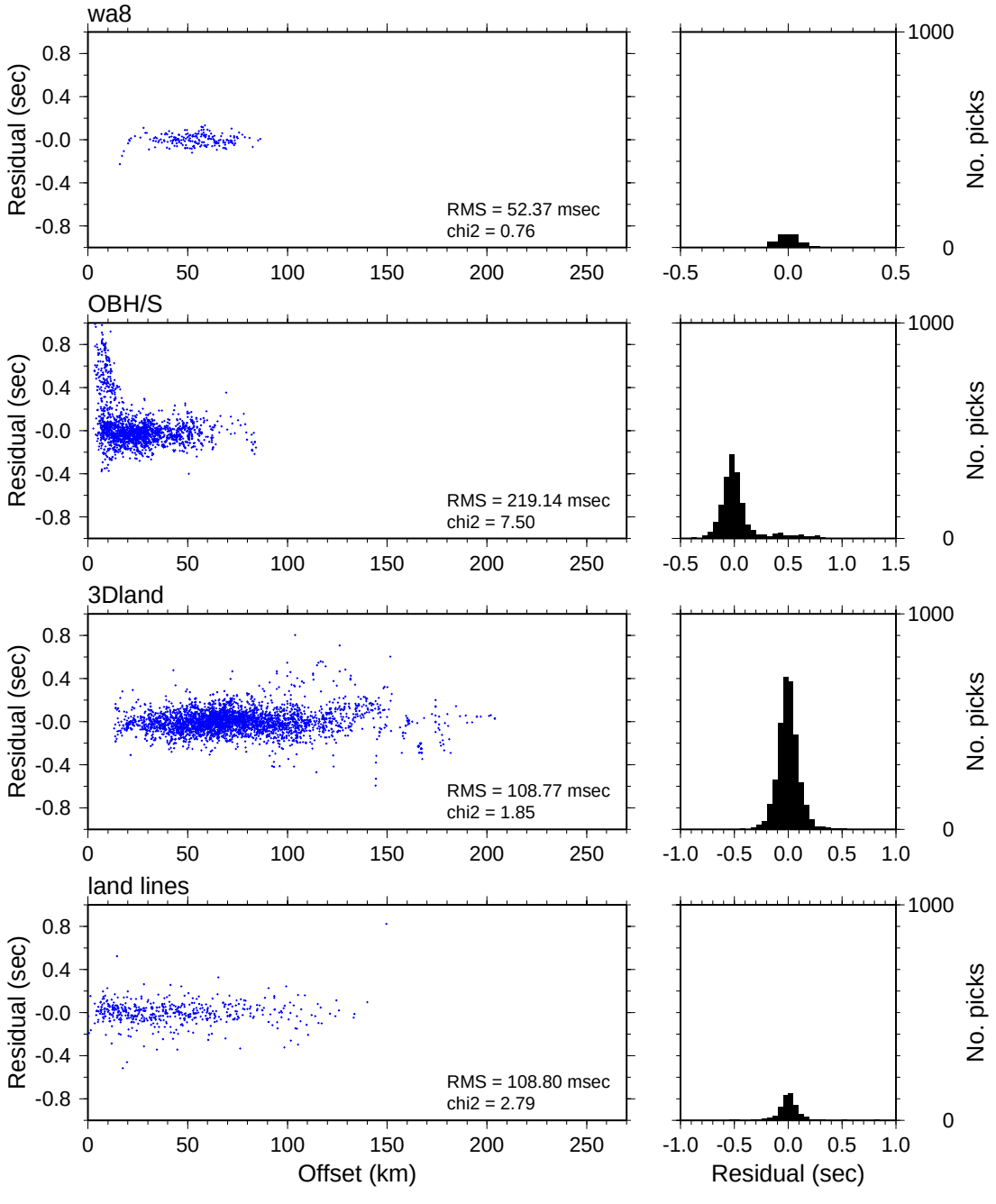

Figure 4.19: Residuals for the P_g arrival final model plotted versus offset for the offshore-onshore line *wa8*, the OBH/S array, the 3D land array, and the four land lines, respectively. The RMS residual and the χ^2 for each group are also indicated. The histograms give the number of picks for residual values in 0.05 sec bins.

4.5 Results

4.5.1 3D resolution analysis

The ray coverage through the final first arrival velocity model is shown in Fig. 4.20. In general, ray coverage is higher (> 10 rays per cell) for areas beneath the dense offshore-onshore lines *wa1, wa3, wa6* with places reaching as high as ∼1000 rays per cell. Particular offline areas that are well sampled by rays include the area between the two branches of line *wa3*, around Cape Mendocino, and the area close the onshore side of line *wa6*.

The resolvability of the velocity features in the first arrival model is tested with the checkerboard resolution test (Hearn & Ni, 1994). Three-dimensional sinusoidal velocity anomalies were added to the final velocity model and synthetic traveltimes were calculated for the same shot–receiver geometry. The sinusoidal anomalies are of the functional form $\sin(x)\sin(y)$, with a peak anomaly of ±5%. The resulting checkerboard model is on average equal to the final model, being within the linear limits of the inversion (Zelt, 1998). The ±5% variation from the final model is large enough to provide a traveltime perturbation greater than the noise level, without considerably changing the ray paths from those in the final model and keeping again within the linear limits of the inversion. Two different anomaly sizes were tested: a finer one of 20x20 km lateral size (Fig. 4.21) and a coarser of 30x30 km lateral size (Fig. 4.22). The calculated synthetic arrivals were inverted using the same approach as for the real data, starting from the original starting model.

In general, the model resolves at least $\pm 0.5\ \mathrm{km\ s^{-1}}$ velocity perturbations. The size of the resolved lateral features varies vertically and horizontally as it depends on the heterogeneous ray coverage of the experiment (Fig. 4.20). The best results for the 30 km checkerboard test are between 5 and 20 km depth (Fig. 4.22), and for the 20 km checkerboard test between 5 and 12 km depth (Fig. 4.21). In the Pacific area, the model is resolved for lateral features greater than 30 km in size up to 19 km depth, especially below lines *wa1*, *wa2* and *wa3*. Below the Vizcaino block and at ∼9–15 km depth both the 20 km and 30 km velocity checkerboards have been recovered (Fig. 4.21 and 4.22) quite well. Close to the Mendocino fault and the triple junction the model is resolved for features up to 20 km in lateral size for almost all depths (Fig. 4.21). The resolvability there and in the rest of the Gorda area becomes much better for the 30 km size checkerboard anomaly. In the North American crust most of the areas are resolved for features greater than

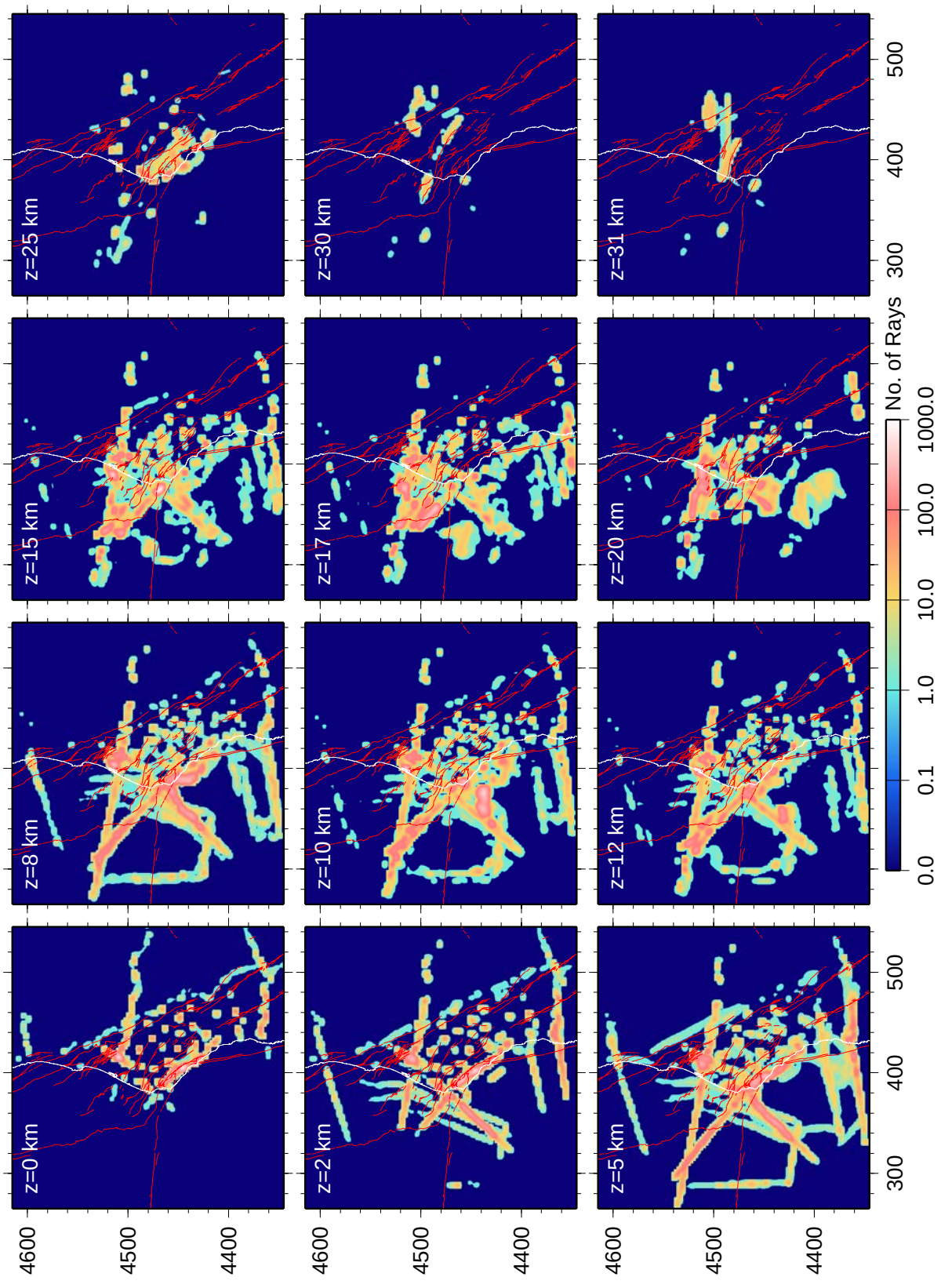

Figure 4.20: Ray coverage in the first arrival model at different depths. The colour-scale is logarithmic and represents number of rays passing through each cell. Coastline is marked in white and red lines the quaternary, USGS mapped, surface faults.

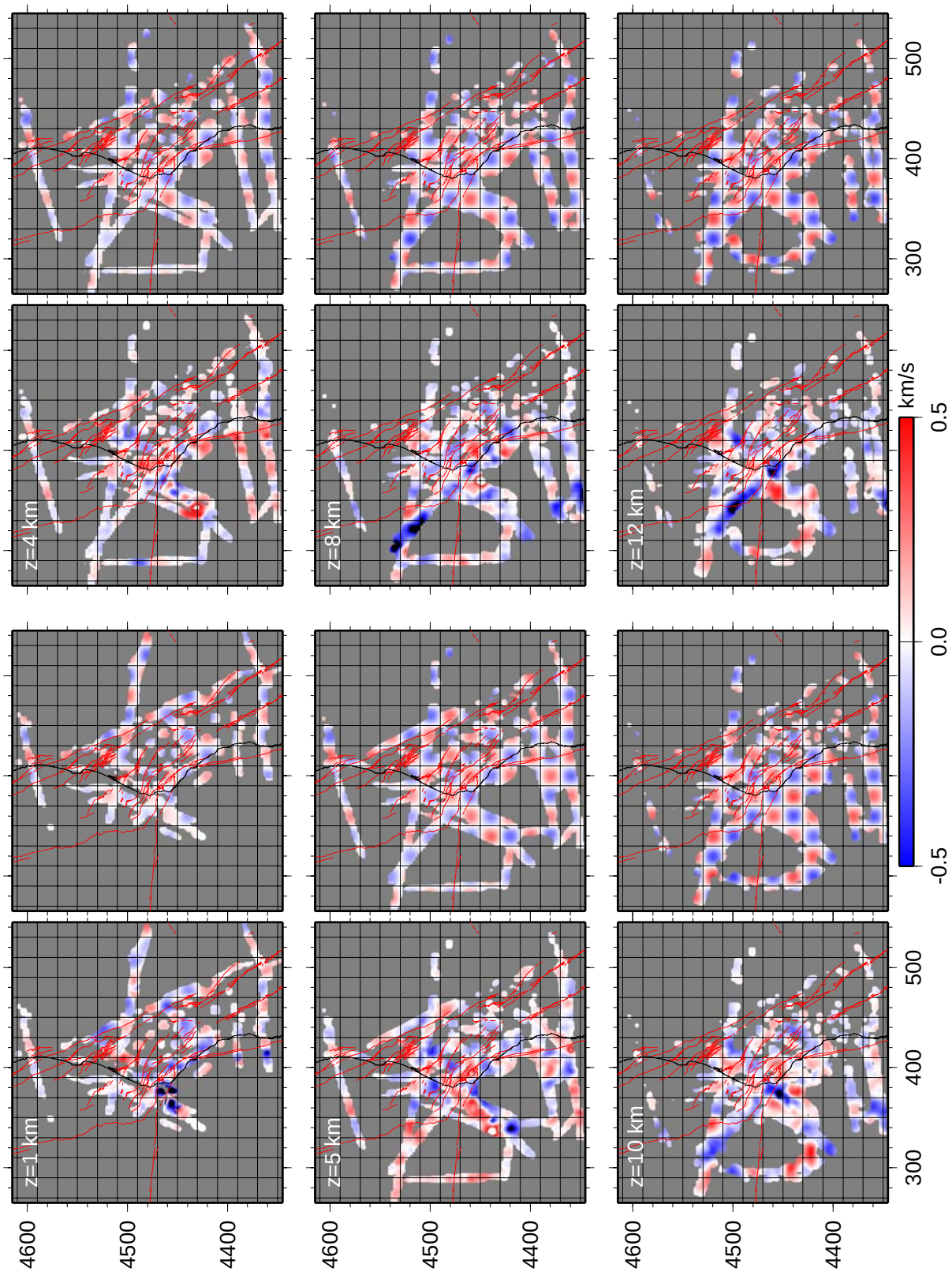

Figure 4.21: (continues in next page) Representative horizontal slices through the result of the checkerboard resolution test for anomalies 20 km in lateral size. For each depth right panels show the velocity perturbations added to the final model, and left panels are the recovered velocity perturbations at the same depths. For reference, the coastline is marked in black and the USGS mapped faults in red.

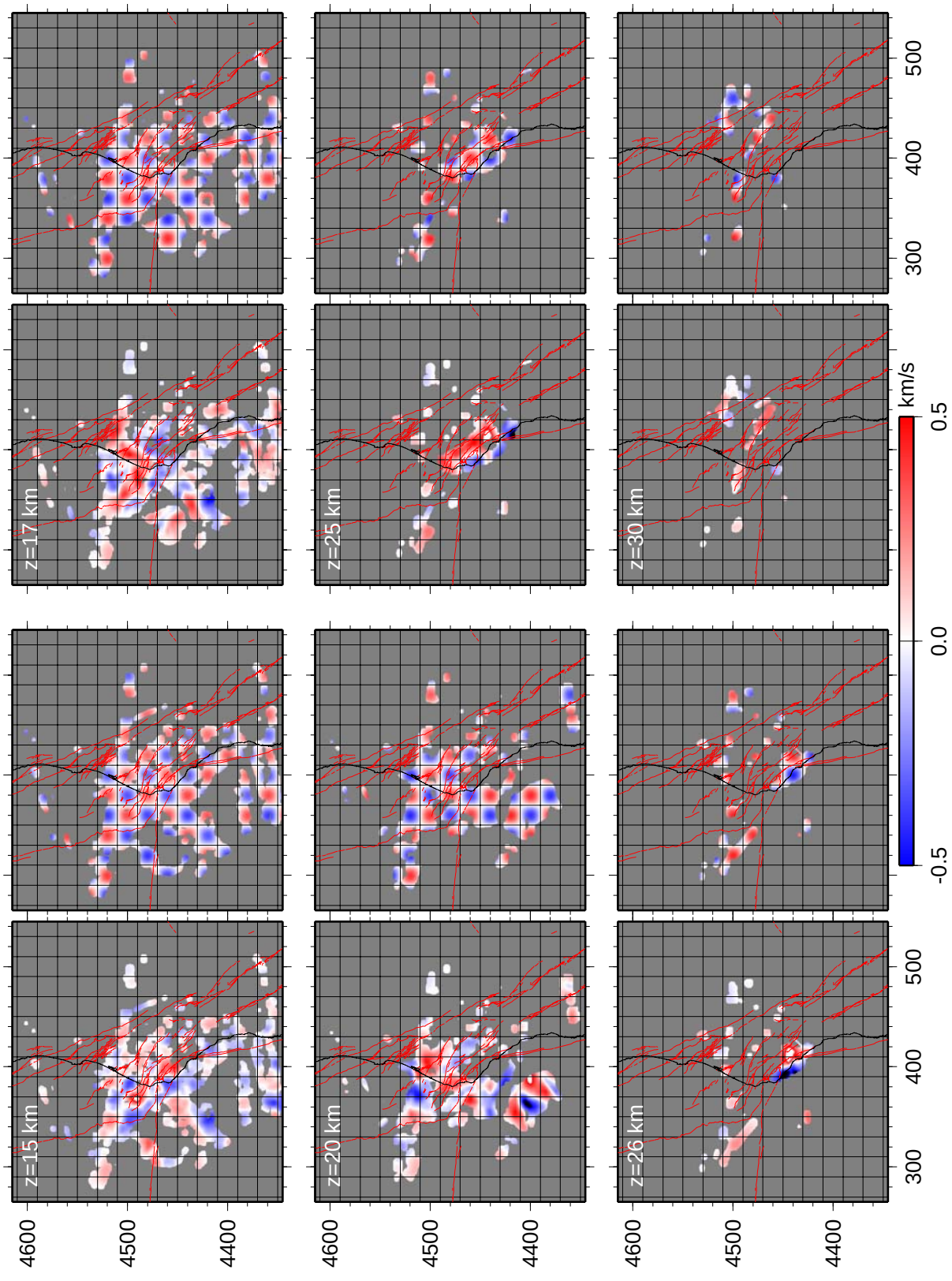
z=15 km
z=17 km
z=20 km
z=25 km
z=26 km
z=30 km
4600
4500
4400
300
400
500
km/s
0.5
0.0
-0.5

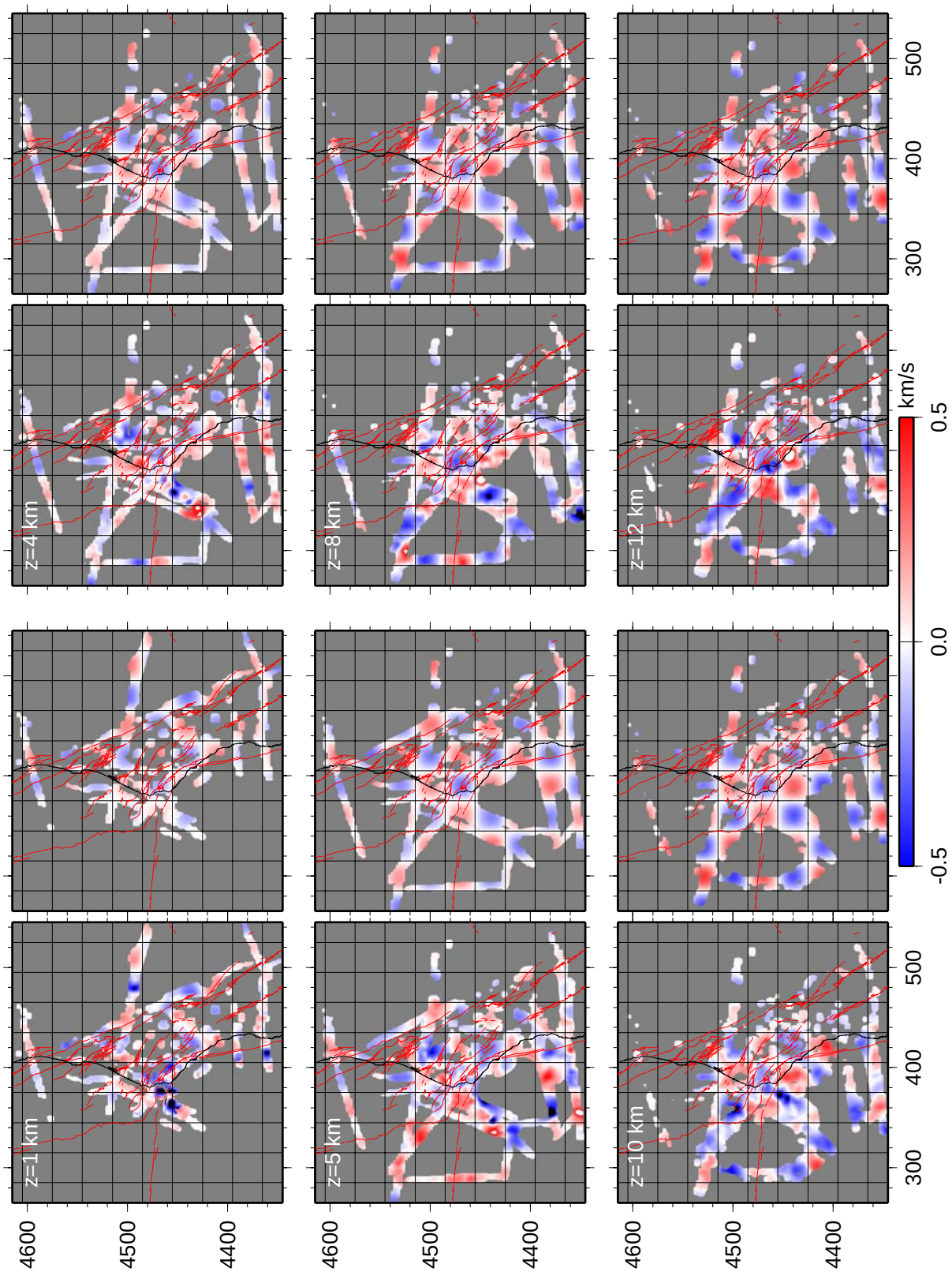

Figure 4.22: (continues in next page) Representative horizontal slices through the result of the checkerboard resolution test for anomalies 30 km in lateral size. For each depth right panels show the velocity perturbations added to the final model, and left panels are the recovered velocity perturbations at the same depths. For reference, the coastline is marked in black and the USGS mapped faults in red.

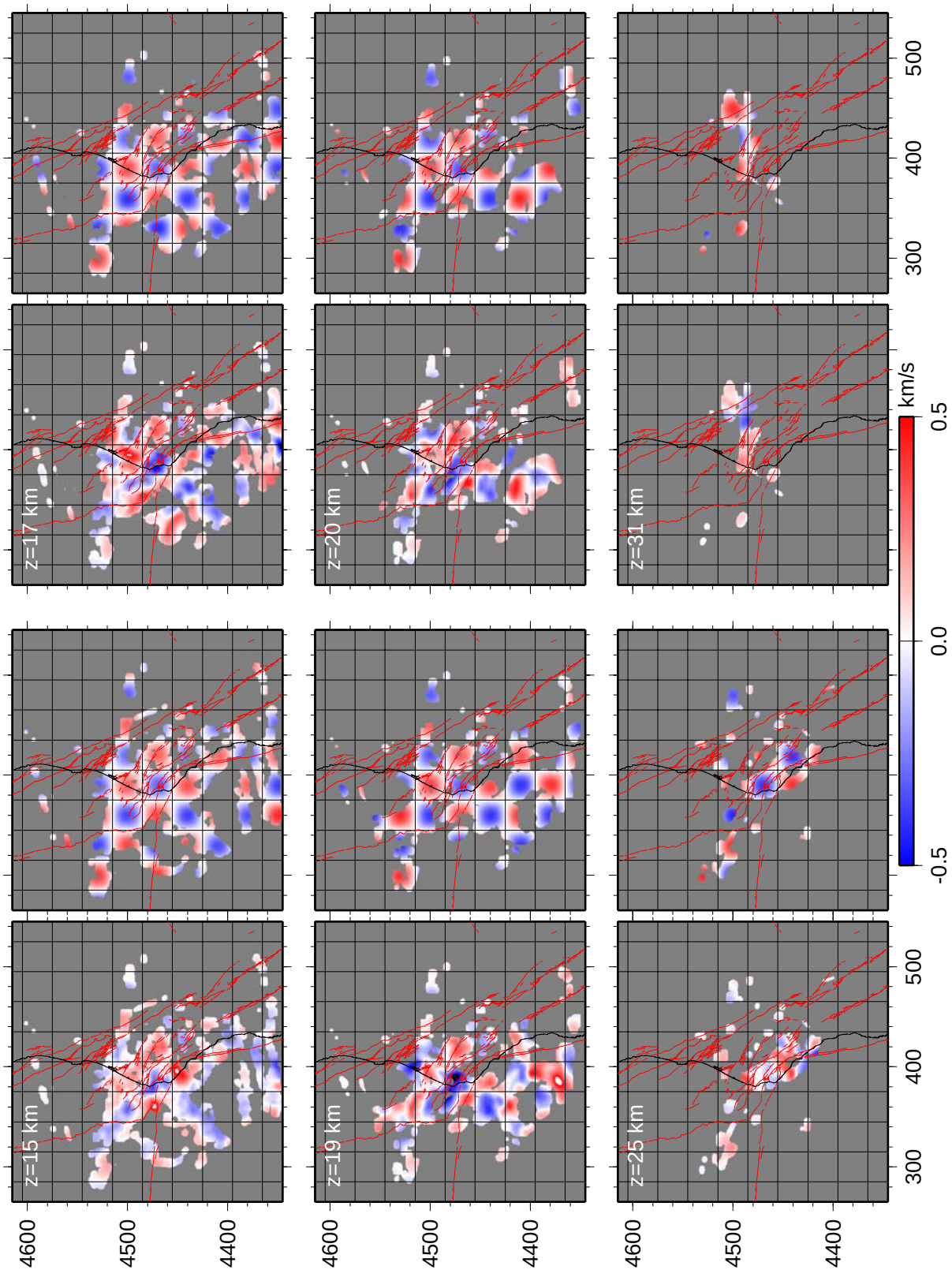
z=15 km
z=17 km
z=19 km
z=20 km
z=25 km
z=31 km
4600
4500
4400
300
400
500
km/s
0.5
0.0
-0.5

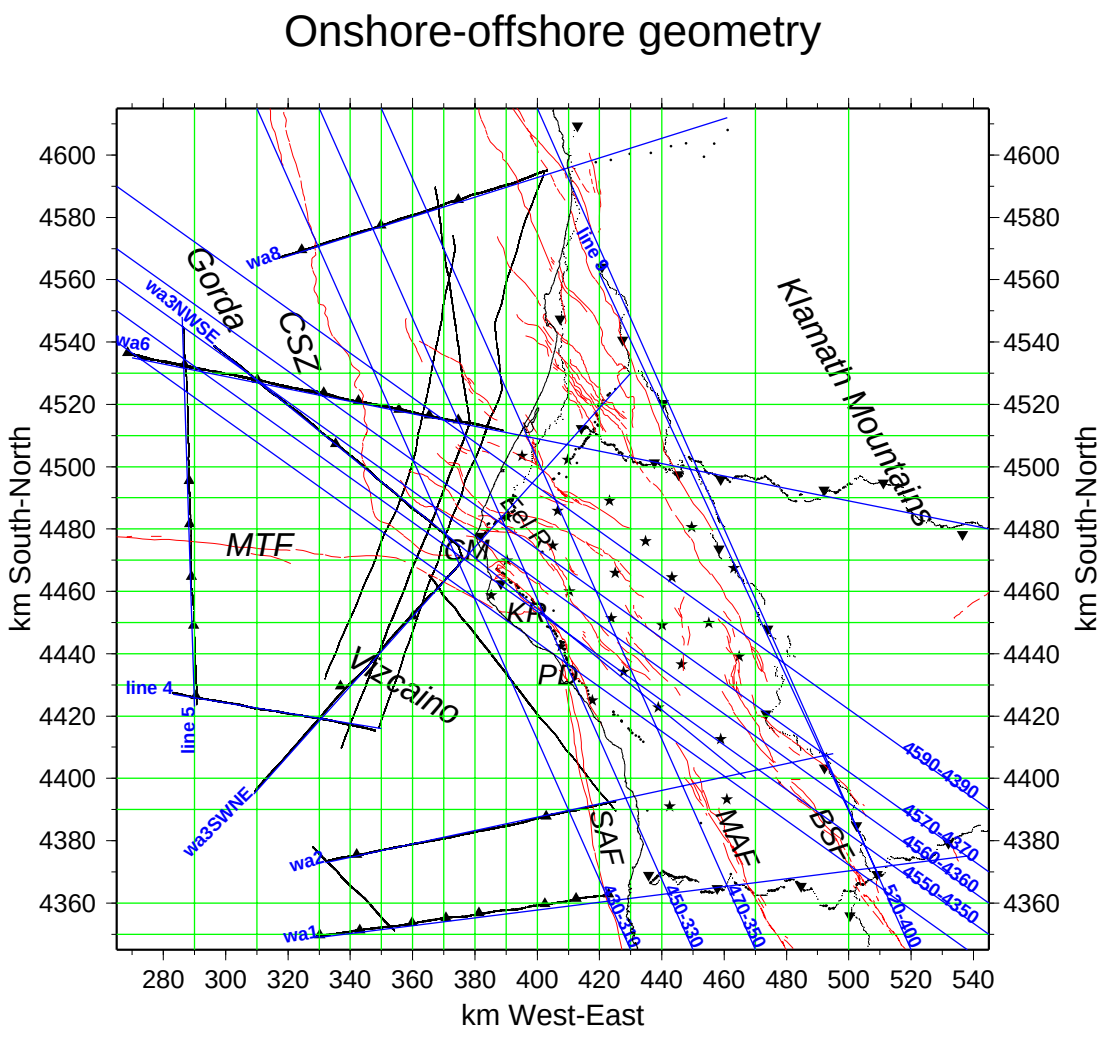

Figure 4.23: The tomography study area with shots lines offshore, shot positions onshore and all receiver positions. Green lines mark the position of E–W and S–N vertical profiles plotted in figures 4.25 and 4.27, respectively. Blue lines mark the position of diagonal vertical profiles plotted in figures 4.29, 4.28, 4.35, 4.36, 4.37, 4.38 and 4.39. The coastline is indicated and the red lines mark the quaternary, USGS mapped, surface faults. MTF: Mendocino Transform fault, CSZ: Cascadia subduction zone, SAF: San Andreas fault, MAF: Maacama fault, BSF: Barlett Springs fault, CP: Cape Mendocino, KR: King Range, PD: Point Delgada.

30 km in lateral size, but there are places, especially below lines *wa6* and *wa1*, that are resolved for 20 km size features.

4.5.2 Seismic structure

The areas specifically discussed in the text and the surface traces of the vertical profiles are indicated in Fig. 4.23. Horizontal slices through the final first arrival

model, at representative depths where the velocity structure is described in the text, are shown in Fig. 4.24. Similarly, vertical slices along a W–E direction are shown in Fig. 4.25, and along a S–N direction in Fig. 4.27. In general, lateral and vertical velocity perturbations are greater in magnitude but smaller in size at shallow depths, due to denser ray coverage. We describe the velocity model for the Pacific region and the Vizcaino block, the Gorda and Cascadia subduction area, and the North America region, assuming that the 8 kms^{-1} isovelocity contour roughly marks the Moho boundary. In reality, smoothing, inherent in the method of Zelt & Barton (1998), will not allow the Moho to be expressed in the models as a sharp velocity contrast but instead it will appear as a gradient zone. During the description of the final velocity model we refer to the horizontal plots by giving their depths (see Fig. 4.24), to the S–N and W–E vertical slices by giving the spatial coordinate where the slice was extracted parallel to the other lateral dimension (see Fig. 4.25, 4.27 and for locations Fig. 4.23), to diagonal vertical profiles by giving the spatial coordinates of their beginning and end (see Fig. 4.29, 4.28), and, finally, to vertical slices parallel with a particular shot line by their names (see Fig. 4.35, 4.36, 4.37, 4.38, 4.39). Slices have been selected to intersect the main point of interest.

Pacific region and Vizcaino structure

The rigid Pacific area is bounded by the Mendocino Fault in the north and the San Andreas fault in the east (see section 4.2.4). The shallowest 4 km is characterised by velocities lower than 4.5 kms^{-1} that cover the abyssal plain in the west, the continental slope to the east, and the Gorda escarpment to the north (e.g. Z=2–4 km, Y=4360 km, X=290–330 km in Fig. 4.24, 4.25, 4.27). In the south part of the Pacific area constrained by the data, the crustal structure reveals the old

Figure 4.24: (Next three pages) Horizontal slices through the final velocity model at various depths. In total, 18 horizontal slices have been plotted in order of increasing depth. Shadowed areas are not sampled by first arrivals in the forward step. The velocity scale is in km s^{-1} and each slice indicates its depth. Contours are plotted every 1 kms^{-1} starting from 1.5 kms^{-1}. The 6.5 kms^{-1} contour is bold and the 8 kms^{-1} is dashed. Hypocentres of relocated seismicity, described in Chapter 5, within 1 km of the profile and magnitude > 2 are shown as black crosses. Black solid line marks the coastline and red lines the quaternary, USGS mapped, surface faults. White lines mark the traces of the extracted vertical velocity profiles in figures 4.25, 4.27, 4.29, 4.28, 4.35, 4.36, 4.37, 4.38, 4.39. For clarity, E–W and S–E profiles traces are plotted in turn with diagonal profiles traces.

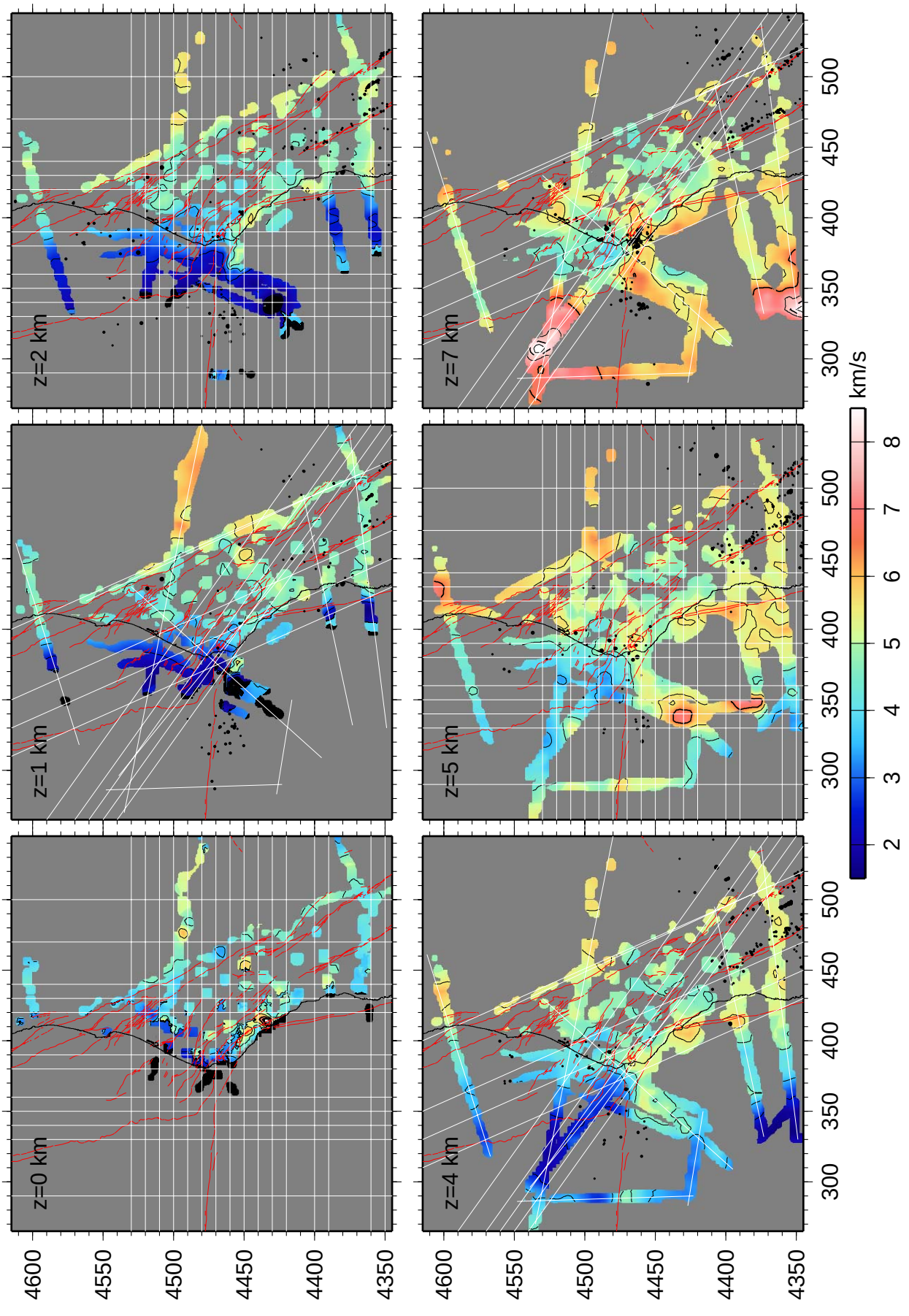
z=0 km
z=1 km
z=2 km
z=4 km
z=5 km
z=7 km
4600
4550
4500
4450
4400
4350
300
350
400
450
500
km/s
2
3
4
5
6
7
8

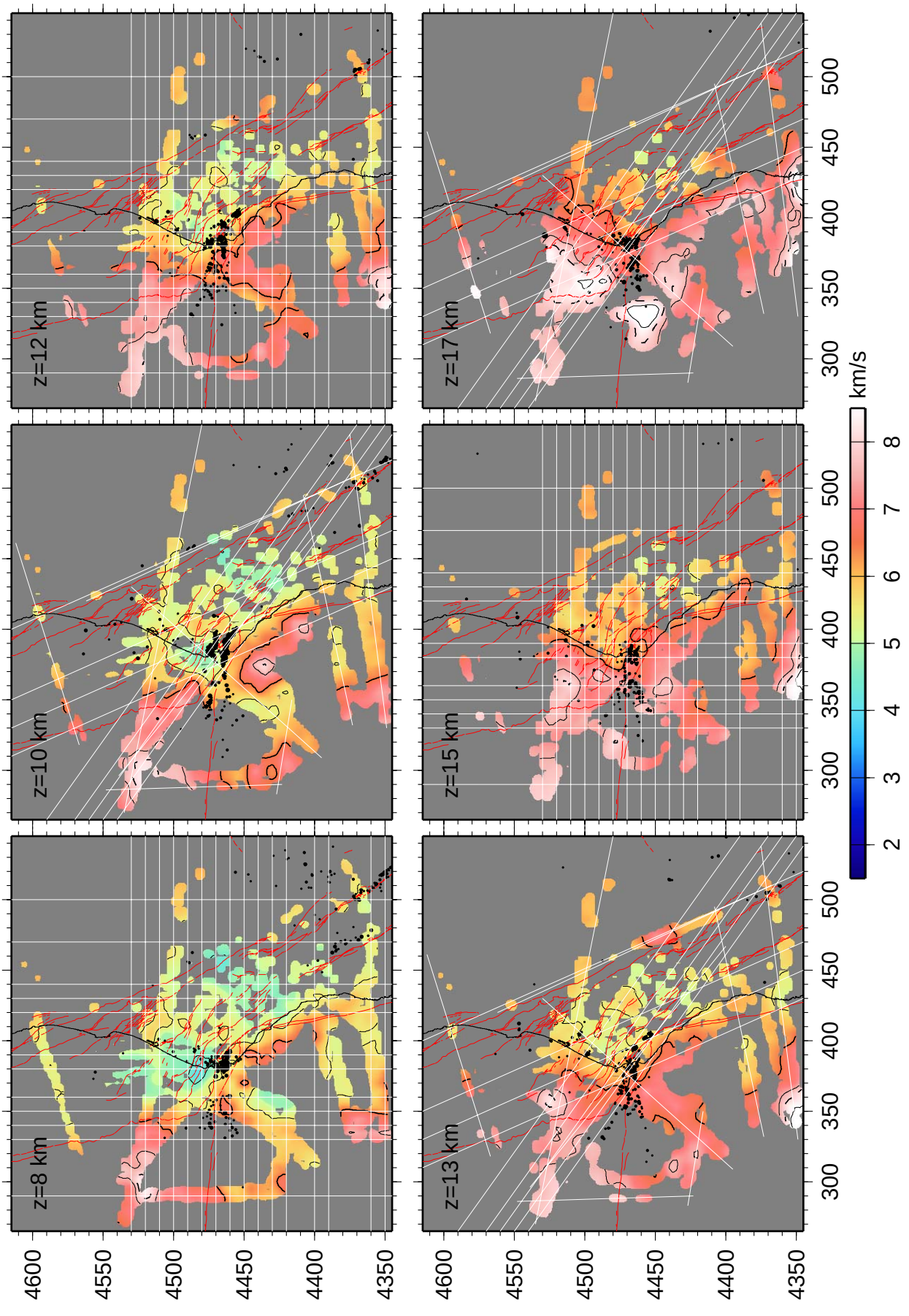
z=12 km
z=17 km
z=10 km
z=15 km
z=8 km
z=13 km
4600
4550
4500
4450
4400
4350
300
350
400
450
500
km/s
2
3
4
5
6
7
8

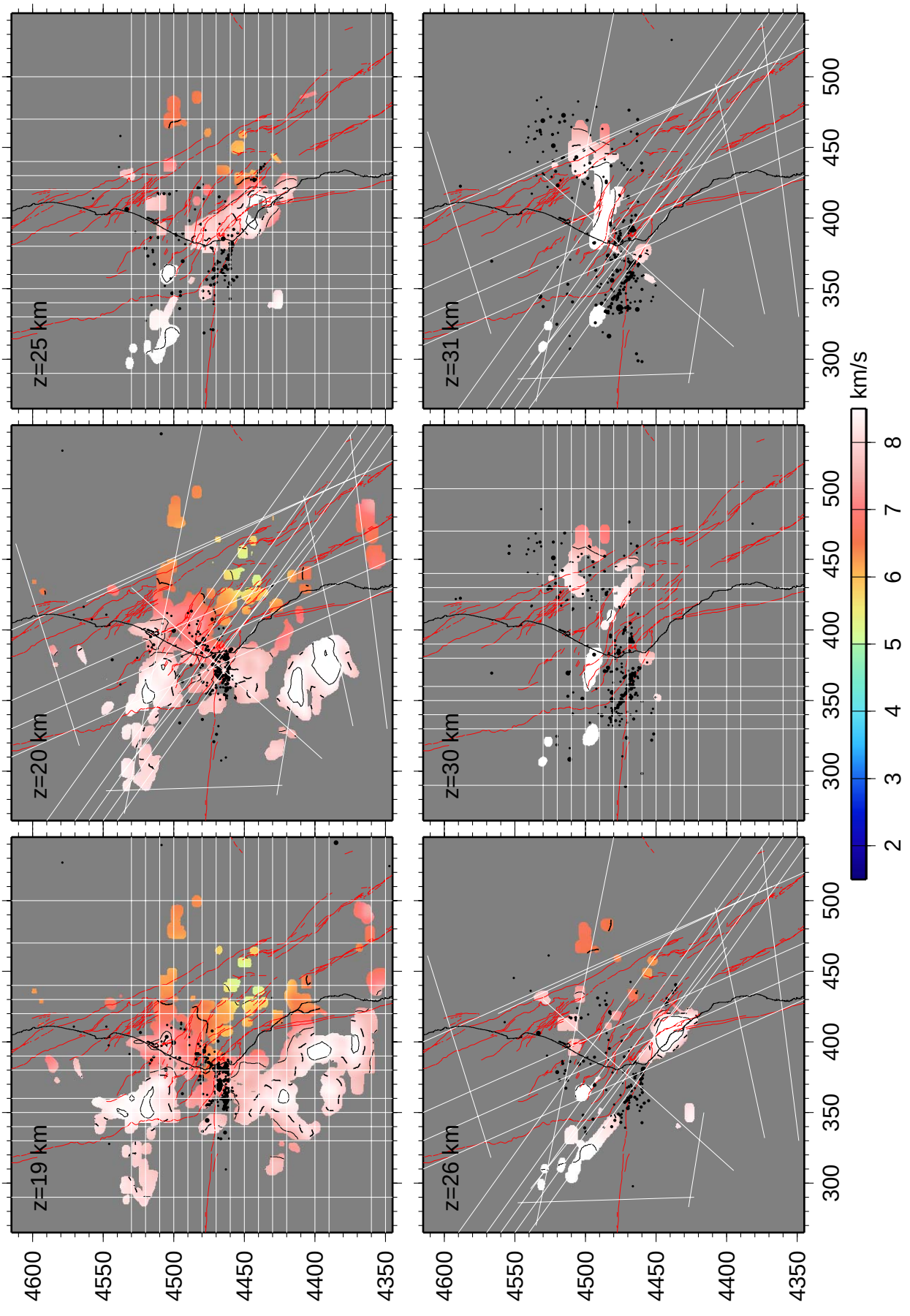
z=25 km
z=31 km
z=20 km
z=30 km
z=19 km
z=26 km
4600
4550
4500
4450
4400
4350
300
350
400
450
500
km/s
2
3
4
5
6
7
8

Farallon accretionary wedge that it was created before the SAF initialisation. Its thickness increases towards the east (Y=4360 km, X=340–420 km in Fig. 4.24, 4.25 and 4.35 a). Most of the wedge thickness has velocities between 4.5 and 6.0 kms^{-1}. This accretionary wedge is underlain by a high velocity layer with velocities higher than 6.5 kms^{-1}, and 5–10 km thick that dips at $\sim 5^{\circ}$ degrees towards the east. In the north part of the constrained Pacific area the crustal structure shows the Gorda escarpment with velocities lower than 6.5 kms^{-1} in the shallowest 12 km (X=290–360 km, Y=4460–4470 km, and Z=10–12 km in Fig. 4.24, 4.25, 4.27).

The northeast corner of the Pacific, in the Vizcaino block between the old Farallon accretionary wedge in the southeast and the Gorda escarpment along the MTF in the north, is characterised by velocities lower than 5.5 kms^{-1} in the shallowest 10 km (Y=4430-4450 km, X=360 km, and Z=5–6 km in Fig. 4.24, 4.25, 4.27). Below this area with low velocities a steep velocity gradient, at ∼10 km depth, increases values to more than 6.5 kms^{-1}, with an elongated high velocity region, roughly 65 km long and 30 km wide, trending NW–SE parallel to the coastline (Z=10 km in Fig. 4.24).

Velocities as high as 8.1 kms^{-1}, indicating mantle rocks, are found in the Pacific area as shallow as 12 km depth at the southwestern limits of our model (Fig. 4.35 a), gradually deepening to 18–19 km towards the SAF (Y=4350–4390 km and Z=19 km in Fig. 4.24, 4.25, 4.27 and 4.31). Generally in the resolved parts of the model, eastwards of 125°W, beneath the old Farallon accretionary wedge, the Pacific Moho is approximately flat at 18–19 km depth but dips smoothly to a maximum depth of 24 km beneath the Vizcaino block (Fig. 4.31).

The transition from the Pacific region to North America is marked by abrupt

Figure 4.25: (Next two pages) Vertical profiles through the final velocity model along a W–E direction (no vertical exaggeration). Shadowed areas are not sampled by first arrivals in the forward step. Each slice indicates the position where it was extracted and the surface trace of each profile is indicated on the inset maps on the right. Contours are plotted every 1 kms^{-1} starting from 1.5 kms^{-1}. The 6.5 kms^{-1} contour is bold and the 8 kms^{-1} is dashed. Hypocentres of relocated seismicity, described in Chapter 5, within 2.5 km of the profile and magnitude > 2 are shown as black crosses. The projected hypocenter of the Petrolia 1992 earthquake is marked as a white circle in the profile at 4460 km. Blue lines at the surface show the trace of the coastline, whereas red lines mark the position of various quaternary, USGS mapped, faults. SAF: San Andreas fault, MTF: Mendocino transform fault, CSZ: Cascadia subduction zone, MAF: Maacama fault, BSF: Barlett Springs fault, VIZ: Vizcaino block.

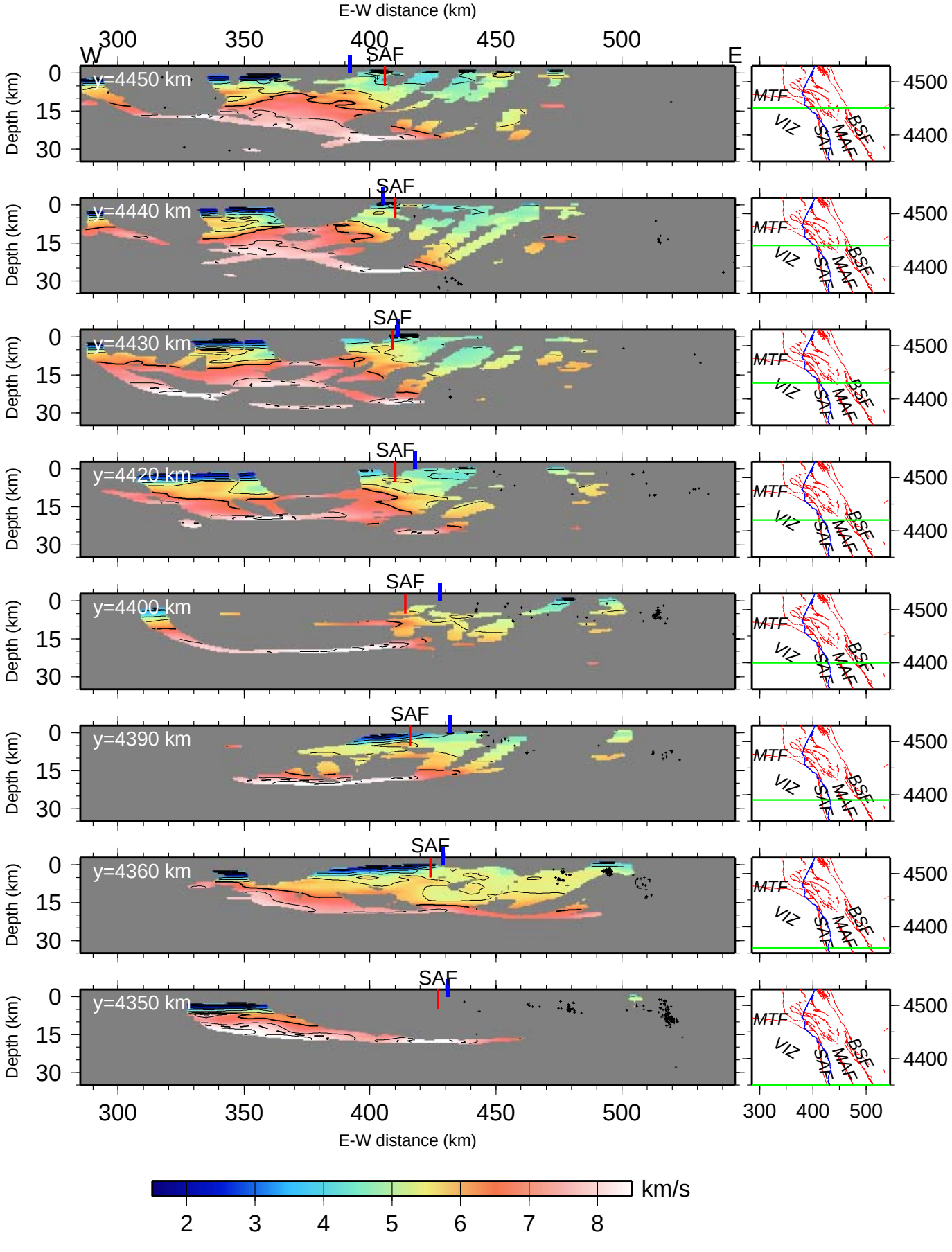
E-W distance (km)
300
350
400
450
500
W
E
SAF
y=4450 km
y=4440 km
y=4430 km
y=4420 km
y=4400 km
y=4390 km
y=4360 km
y=4350 km
Depth (km)
0
15
30
MTF
VIZ
SAF
MAF
BSF
4500
4400
km/s
2
3
4
5
6
7
8

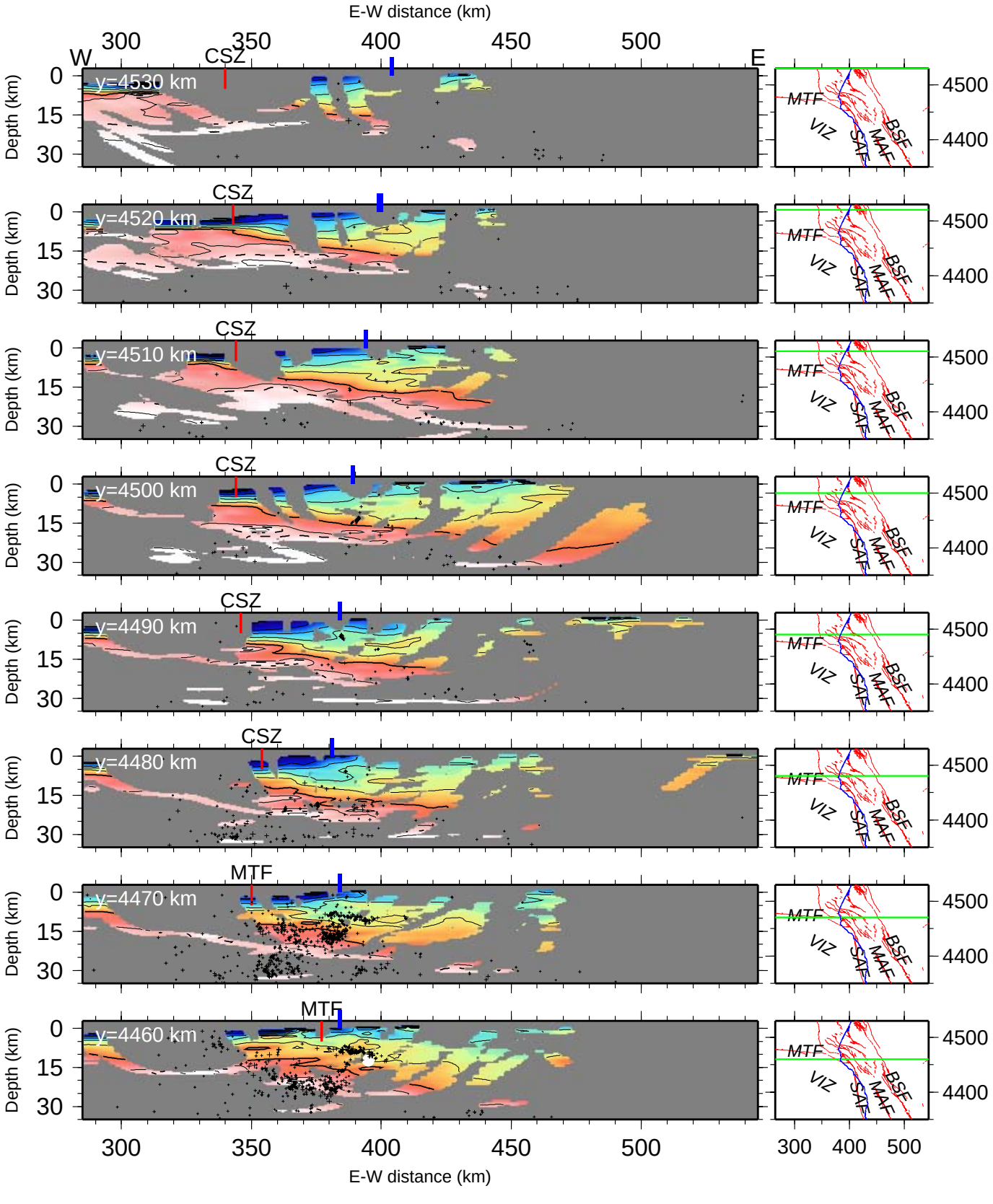
E-W distance (km)
300
350
400
450
500
W
E
CSZ
MTF
y=4530 km
y=4520 km
y=4510 km
y=4500 km
y=4490 km
y=4480 km
y=4470 km
y=4460 km
Depth (km)
0
15
30
4500
4400
VIZ
SAF
MAF
BSF
km/s
2
3
4
5
6
7
8

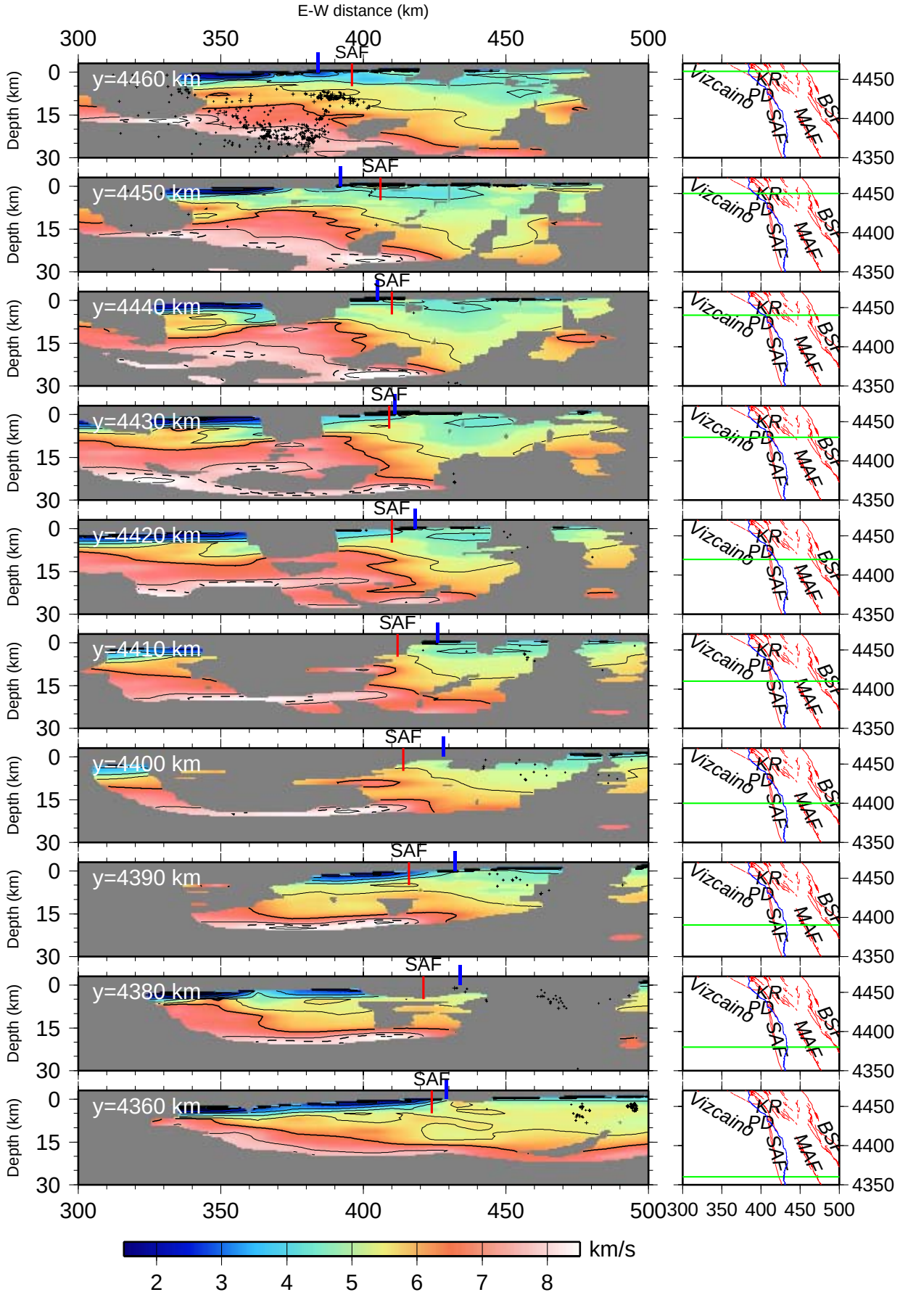
E-W distance (km)
300
350
400
450
500
Depth (km)
0
15
30
SAF
y=4460 km
y=4450 km
y=4440 km
y=4430 km
y=4420 km
y=4410 km
y=4400 km
y=4390 km
y=4380 km
y=4360 km
Vizcaino
KR
PD
SAF
MAF
BSY
4450
4400
4350
km/s
2
3
4
5
6
7
8

Figure 4.26: (Previous page) West-east vertical profiles through the final velocity model similar to Fig. 4.25 with the wider ray coverage of the $5 \times 5 \times 0.5$ km cell size. Each slice indicates the position where it was extracted and the surface trace of each profile is indicated on the inset maps on the right. Contours are plotted every 1 kms^{-1} starting from 1.5 kms^{-1}. The 6.5 kms^{-1} contour is bold and the 8 kms^{-1} is dashed. Hypocentres of relocated seismicity, described in Chapter 5, within 2.5 km of the profile and magnitude > 2 are shown as black crosses. The projected hypocentre of the Petrolia 1992 earthquake is marked as a white circle in the profile at 4460 km. Blue lines at the surface show the trace of the coastline, whereas red lines mark the position of various quaternary, USGS mapped, faults. SAF: San Andreas fault, MTF: Mendocino transform fault, CSZ: Cascadia subduction zone, MAF: Maacama fault, BSF: Barlett Springs fault, VIZ: Vizcaino block.

lateral changes of seismic velocities at the San Andreas fault. These lateral changes are marginally observed in W–E vertical cross-sections through the final models (Y=4350–4460 km, between X=390–430 in Fig. 4.25). A better picture of these is clearly imaged in velocity models with wider raycoverage, like the intermediate velocity model with $5 \times 5 \times 0.5$ km inversion cell size (Fig. 4.26). Moreover, map views of the 5.5 and 6.5 kms^{-1} isovelocity surfaces image a vertical jump of the isosurface at least 5 km deeper to the east (Fig. 4.30). The deeper velocity structure shows also an abrupt cessation of the resolved Moho velocities at 18–20 km east of the San Andreas fault (4380–4410 km in Fig. 4.26 at X=410–420 km). At Point Delgada and northwards, these vertical offsets are observed onshore, beneath the King Range, following the onshore branch of the San Andreas fault (Y=4440–4460 km, X=390–410 km and Z=15 km in Fig. 4.24, 4.25, 4.26, 4.30). The deeper velocity structure below King Range shows also an abrupt deepening of the Moho east of the San Andreas fault at 25 km depth (4420–4450 km in Fig. 4.26 and 4.31 at X=425 km).

Figure 4.27: (Next two pages) Vertical profiles through the final velocity model along a S–N direction (no vertical exaggeration). Shadowed areas are not sampled by first arrivals in the forward step. Each slice indicates the position where it was extracted and the surface trace of each profile is indicated on the inset maps on the right. Contours are plotted every 1 kms^{-1} starting from 1.5 kms^{-1}. The 6.5 kms^{-1} contour is bold and the 8 kms^{-1} is dashed. Hypocentres of relocated seismicity, described in Chapter 5, within 2.5 km of the profile and magnitude > 2 are shown as black crosses. Blue lines at the surface show the trace of the coastline, whereas red lines mark the position of various quaternary, USGS mapped, faults. SAF: San Andreas fault, MTF: Mendocino transform fault, CSZ: Cascadia subduction zone, MAF: Maacama fault, BSF: Barlett Springs fault, VIZ: Vizcaino block.

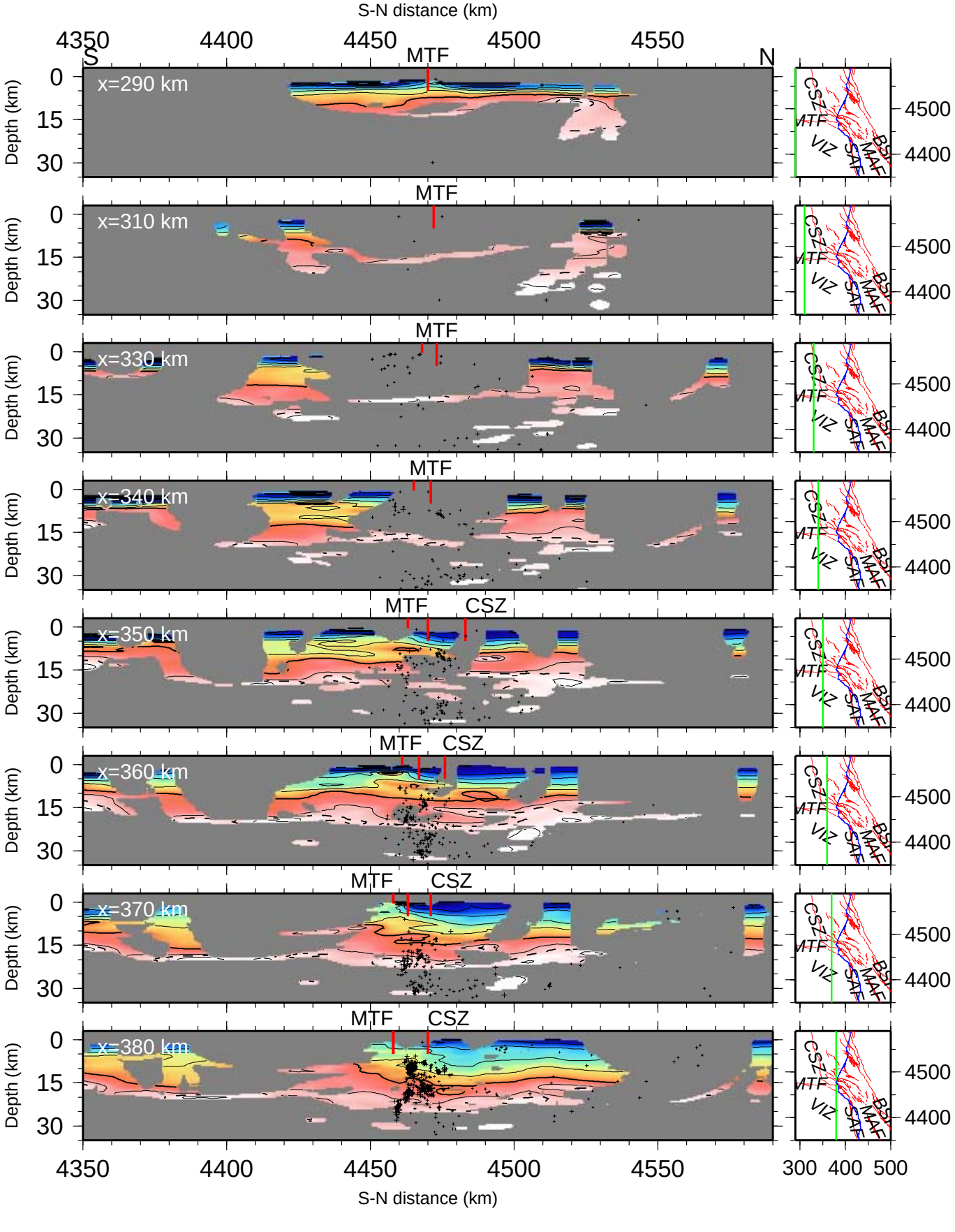
S-N distance (km)
4350
4400
4450
4500
4550
S
N
MTF
CSZ
x=290 km
x=310 km
x=330 km
x=340 km
x=350 km
x=360 km
x=370 km
x=380 km
Depth (km)
0
15
30
CSZ
MTF
VIZ
SAF
MAF
BSI
4500
4400
300
400
500
km/s
2
3
4
5
6
7
8

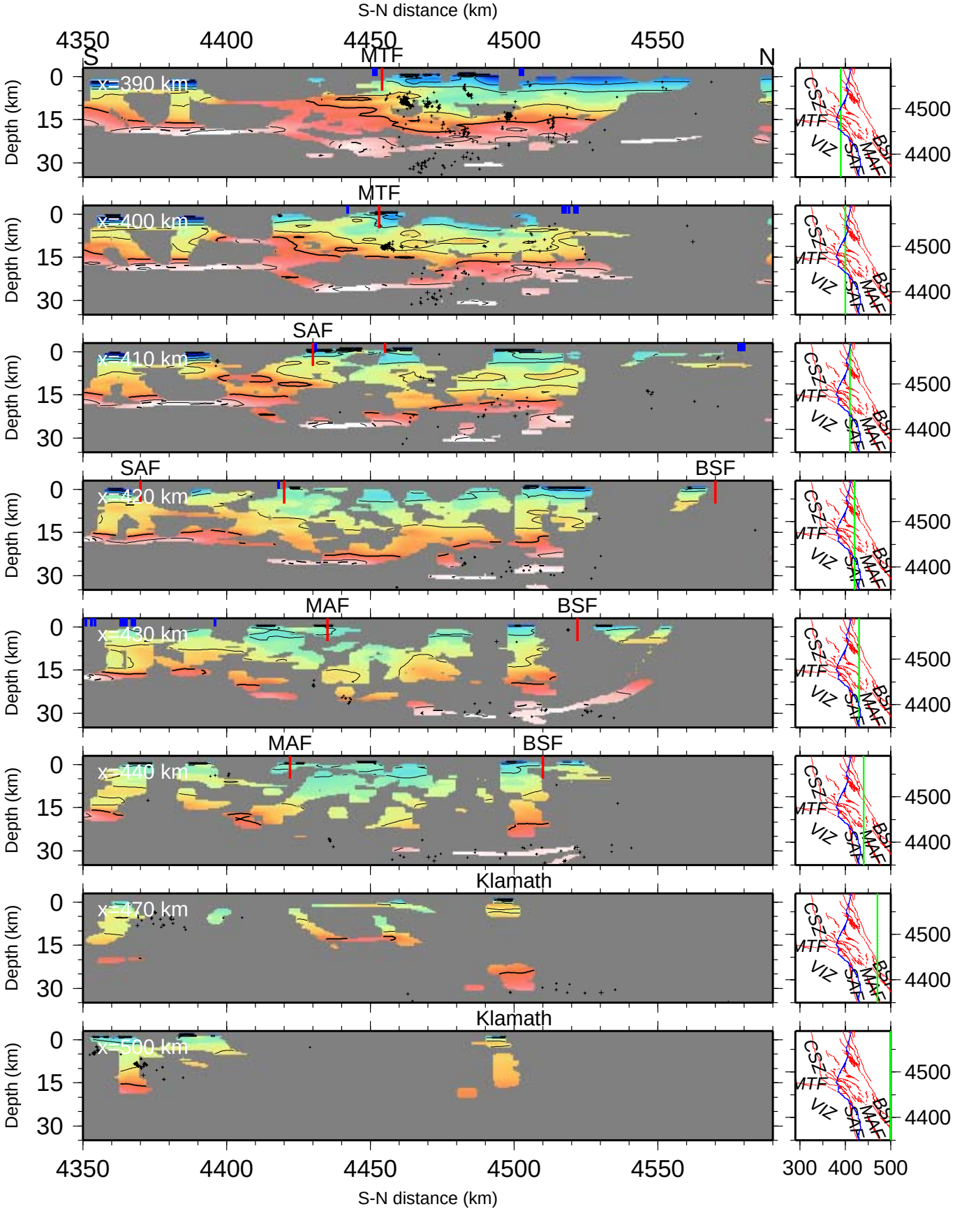
S-N distance (km)
4350
4400
4450
4500
4550
S
N
MTF
x=390 km
x=400 km
SAF
x=410 km
x=420 km
BSF
MAF
x=430 km
x=440 km
Klamath
x=470 km
x=500 km
Depth (km)
0
15
30
CSZ
MTF
VIZ
SAF
MAF
BSF
300
400
500
km/s
2
3
4
5
6
7
8

Gorda and Cascadia subduction zone structure

In general, north of the Mendocino fault, the upper oceanic crust (with velocities lower than 6.5 kms^{-1}) tends to be thinner (X=290–330 km and Y>4470 km) than in the Pacific region. The oceanic Gorda plate west of the accretionary wedge has a 1–2 km sedimentary cover with velocities lower than 4.5 kms^{-1}, underlain by a ∼2 km thick layer, with typical Layer 2 velocities between 4.5 and 6.5 kms^{-1} (X=290–330 km and Y=4500-4520 km in Fig. 4.25, 4.27). Layer 3 velocities between 6.5 and 7.2 kms^{-1} extend for 5–7 km deeper, resulting in a total igneous crustal thickness between 7–9 km. In the Cascadia subduction area the low velocity accretionary wedge, which is almost 10 km thick close to the coast, pinches out towards the west (Y=4500–4520–4530 km and X=340–430 km). Isovelocity contours higher than 5.5 kms^{-1}, dip at a low angle of ∼6° degrees from west to east, revealing the boundary between the overlying prism and the subducted Gorda crust (Fig. 4.30).

Finally, the transition from the Pacific plate to the Gorda region in the north, marked by an abrupt change of bathymetric relief across the Mendocino fault, reveals a decrease in seismic velocities at shallow depths across the Gorda escarpment (Fig 4.1). The escarpment itself shows basement velocities ∼5 km shallower than the oceanic basements north and south (X=290–360 km in Fig. 4.27).

NW to SE vertical cross-sections parallel to the Gorda-Pacific relative motion show gradual vertical shifts in velocities in the upper and lower Gorda crust, revealing a gradual deformation of the oceanic plate from the north to the south as it approaches the triple junction (Fig. 4.28). In the north, this deformation affects Gorda crustal areas with velocities higher than 6.5 kms^{-1} (4590/4390 km in Fig. 4.28), whereas southwards, close to the triple junction seems to affect shallower parts of the oceanic crust also. In particular, in the southernmost Gorda area, approaching the triple junction from NW to SE, velocities higher than 5.5 kms^{-1} are shifted deeper by 1–2 km in a series of vertical offsets (4550/4350 km in Fig. 4.28, Y=4490, X=350–370 km in Fig. 4.25, and Fig. 4.37 a). The Moho and the upper mantle in this area seem to follow a similar pattern. This observation is in agreement with those of Gulick et al. (1998) and Henstock & Levander (2003), who observed in the same area discontinuous reflections from the top of the subducting Gorda plate and the Moho, respectively. Moreover, Henstock & Levander (2003) observed a second arrival in the region adjacent to the Mendocino fault that was explained as a reflector parallel to but 7–8 km deeper than the Moho modelled by a shallower P_mP arrival. This second reflected arrival could be originated

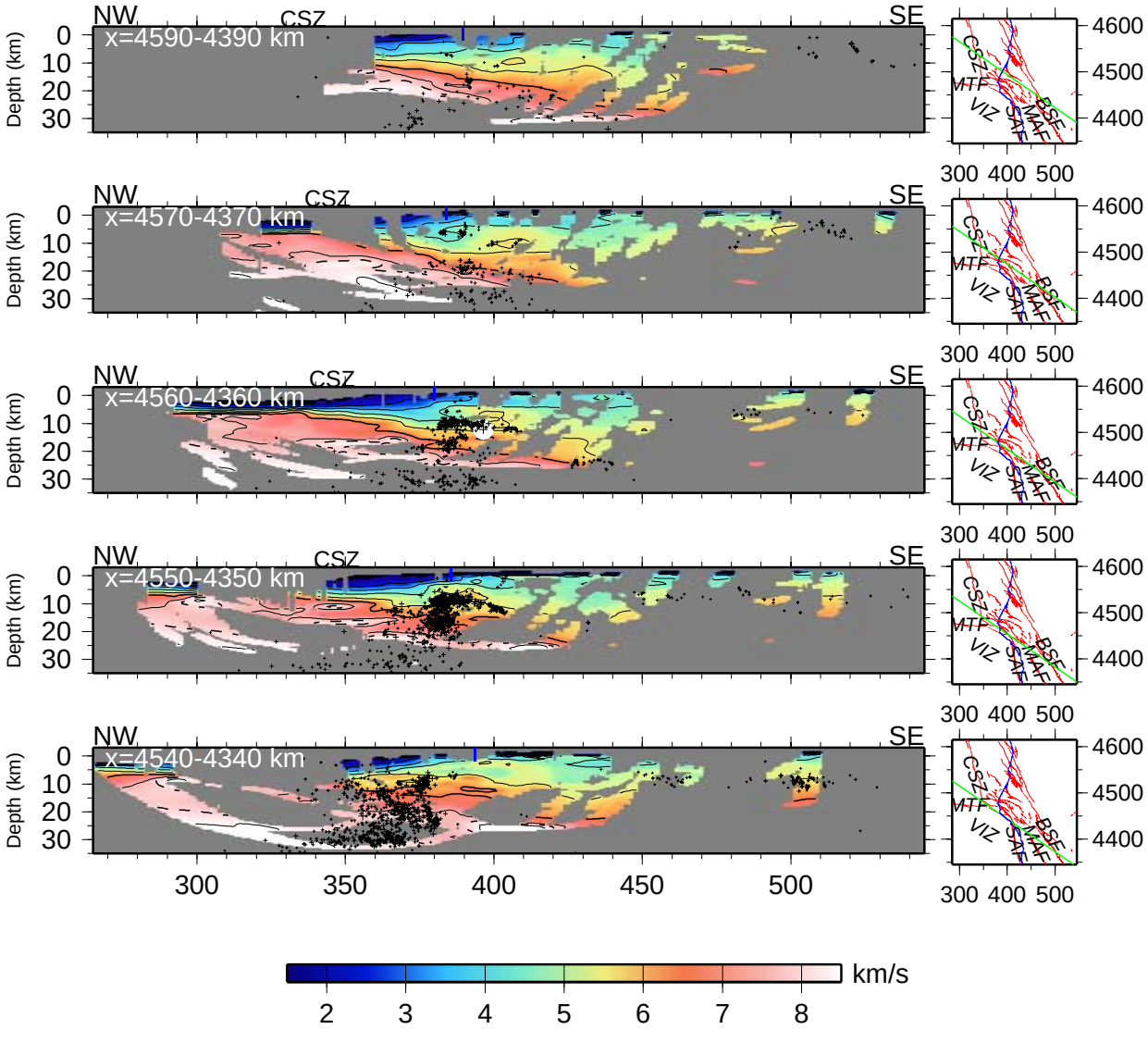

Figure 4.28: Vertical profiles through the final velocity model along a NW–SE direction parallel to the Gorda plate relative motion with respect to the Pacific plate (no vertical exaggeration). Shadowed areas are not sampled by first arrivals rays in the forward step. Each slice indicates the coordinates of its beginning and end and the surface trace of each profile is indicated on the inset maps on the right. Contours are plotted every 1 kms^{-1} starting from 1.5 kms^{-1}. The 6.5 kms^{-1} contour is bold and the 8 kms^{-1} is dashed. The projected hypocenter of the main Petrolia earthquake is marked as a white circle in profile 4560/4360. Blue lines at the surface show the trace of the coastline. SAF: San Andreas fault, MTF: Mendocino transform fault, CSZ: Cascadia subduction zone, MAF: Maacama fault, BSF: Barlett Springs fault, VIZ: Vizcaino block.

from one of these deeper fragmented parts of the Moho that are resolved in our study. Finally, the smoothed 8 kms^{-1} isovelocity surface deepens towards the triple junction indicating a downward bending of the subducted Moho close to the boundary with the Pacific plate.

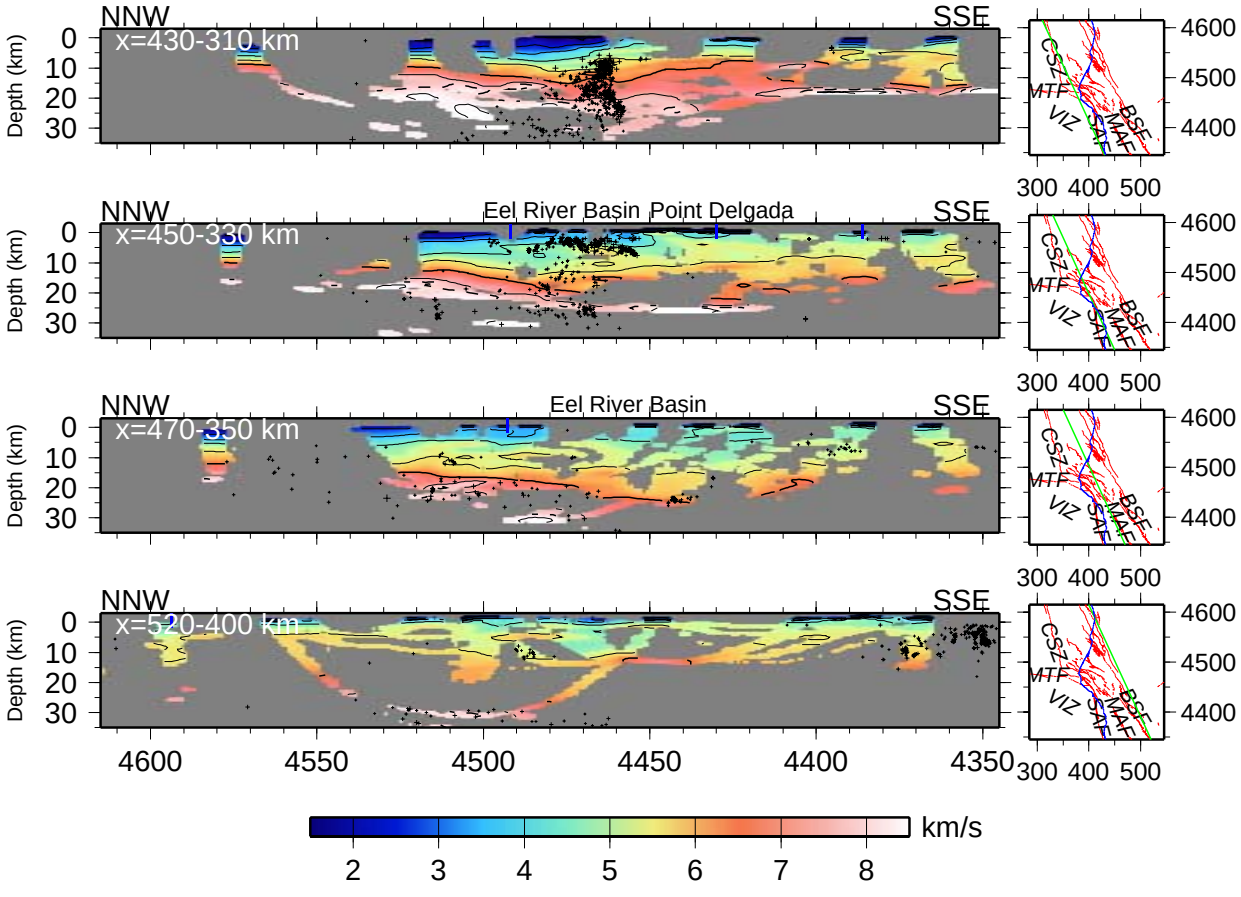

Figure 4.29: Vertical profiles through the final velocity model along a SSE-NNW direction (no vertical exaggeration). Shadowed areas are not sampled by first arrivals in the forward step. Each slice indicates the coordinates of its beginning and end and the surface trace of each profile is indicated on the inset maps on the right. Contours are plotted every 1 kms^{-1} starting from 1.5 kms^{-1}. The 6.5 kms^{-1} contour is bold and the 8 kms^{-1} is dashed. Hypocentres of relocated seismicity, described in Chapter 5, within 5 km of the profile and magnitude > 2 are shown as black crosses. Blue lines at the surface show the trace of the coastline.

North American structure

Within our survey area, most of the crustal thickness in North America consists of velocities lower than 5.5 kms^{-1} (Z=5–10–15–20 km) consistent with Franciscan accretionary complex rocks (Stewart & Peselnik, 1977). The maximum depth where these velocities are observed is at 20 km at around 40°N between the surface mapped traces of the Maacama and Barlett Springs fault zones (Z=20 km, Y=4450 km, and X=440 km in Fig. 4.24, 4.25, 4.27, 4.30, and 470/350 km in Fig. 4.29). This thickest upper crust is in the transition area between the strike-slip and the subduction regime. The sedimentary cover of the Eel River basin is observed on land up to 5 km depth as a NW-SE trending region with velocities lower than 4.5 kms^{-1}. (X=1–5 km, X=390–430 km, Y=4470–4510 km in Fig. 4.24, and

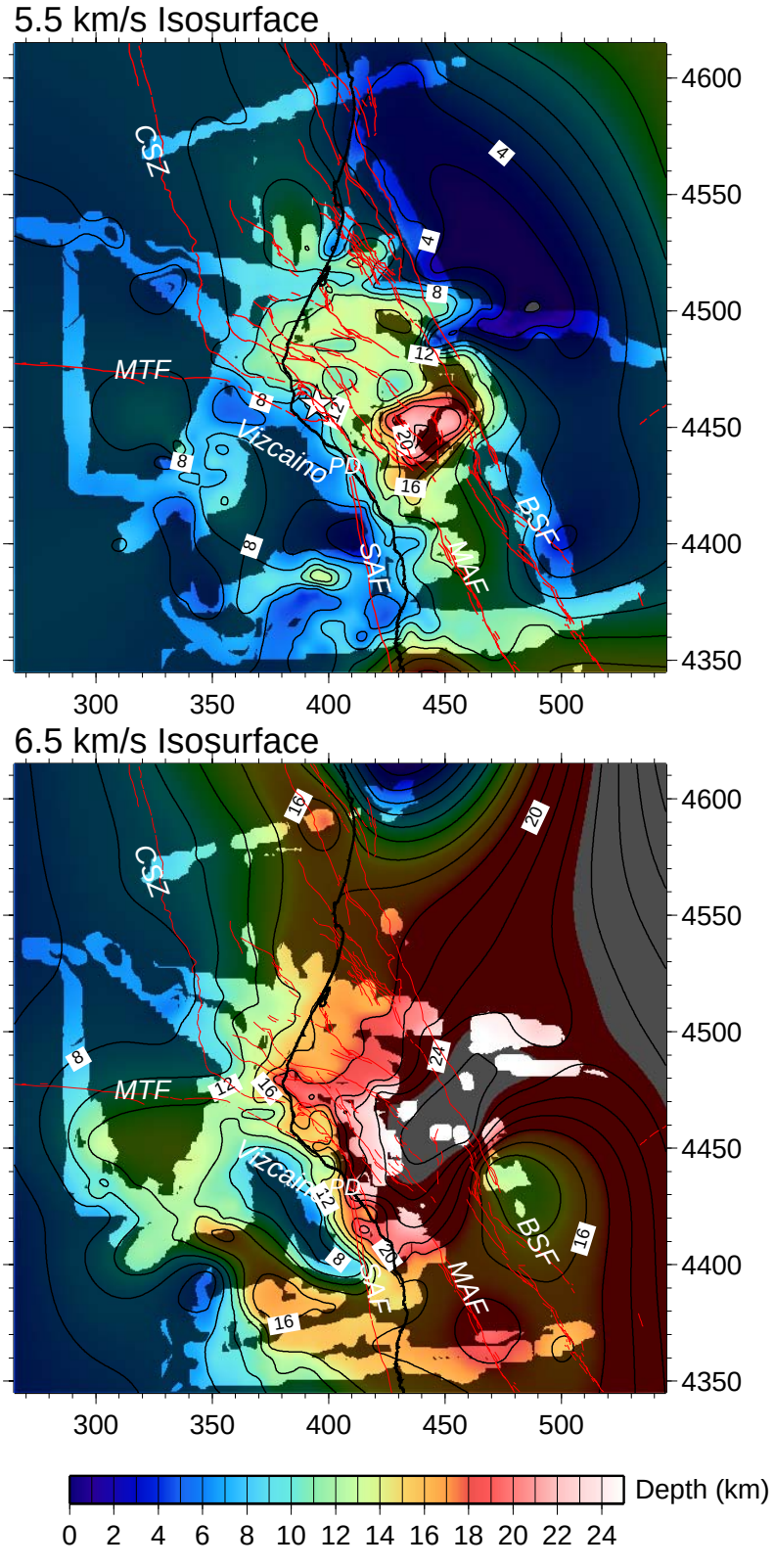

Figure 4.30: Map view of the smoothed 5.5 and 6.5 kms^{-1} isosurfaces through the final velocity model. Shadowed areas are not sampled by first arrivals in the forward step. The depth scale is in km. Contours are plotted every 2 km. Black solid line marks the coastline and red lines the quaternary, USGS mapped, surface faults. The projected hypocenter of the main, 7.1 Ms, 1992 Petrolia earthquake is marked as a white star on 5.5 kms^{-1} isosurface. SAF: San Andreas fault, MTF: Mendocino transform fault, CSZ: Cascadia subduction zone, MAF: Maacama fault, BSF: Barlett Springs fault, PD: Point Delgada.

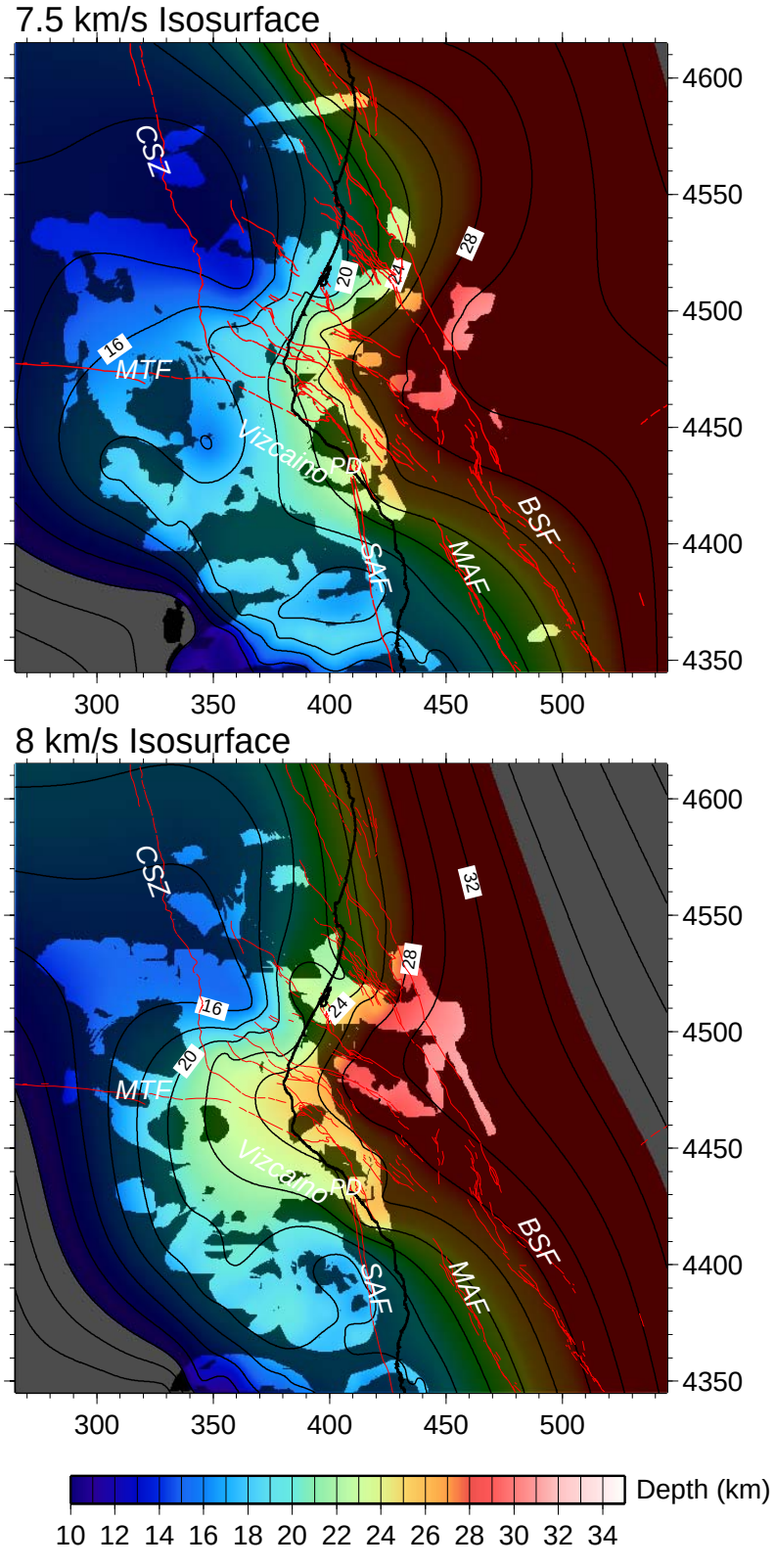

Figure 4.31: Map view of the smoothed 7.5 and 8 kms^{-1} isosurfaces through the final velocity model. Shadowed areas are not sampled by first arrivals in the forward step. The depth scale is in km. Contours are plotted every 2 km. Black solid line marks the coastline and red lines the quaternary, USGS mapped, surface faults. SAF: San Andreas fault, MTF: Mendocino transform fault, CSZ: Cascadia subduction zone, MAF: Maacama fault, BSF: Barlett Springs fault, PD: Point Delgada.

450/330 km in Fig. 4.29).

The easternmost part of the continental area, at a similar latitude to Cape Mendocino, shows layers with velocities higher than 5.5 kms^{-1} at depths as shallow as 1 km (Z=1–5 km). Vertical cross-sections across this feature (Y=4450–4490–4500 km and X=470–500 km in Fig. 4.25, 4.27) reveal a high velocity layer centred at 1 km depth. This layer overlies lower velocities before it passes again to higher velocities at 5 km depth. This feature is associated with the metamorphic and plutonic rocks of the southwestern edge of the Klamath terrane.

Smaller scale details within the North America crust are also revealed by the tomographic model. A high velocity anomaly (greater than 5.5 kms^{-1}) is visible at sea level at Point Delgada, south of Cape Mendocino (X= 0 km, Y=4430–4440 km in Fig. 4.24, 4.25, and 450/330 km in Fig. 4.29). The anomaly extends from Point Delgada northwestwards for almost 10 km but it does not extend deeper than 1 km. This high velocity region is well correlated with the mapped igneous rocks of Point Delgada consisting of basaltic pillow flows, sills and flow breccia (McLaughlin et al., 2000).

At a similar latitude to Point Delgada, but east of the Barlett Springs fault system, velocities at 13 km depth are greater than 6.5 kms^{-1} (Z=13 km, Y=4440 km, X=470 km in Fig. 4.24, 4.25, and Fig. 4.39 c). This feature has NW–SE trend and extent of 10 km. Velocities higher than 6.5 kms^{-1} within the shallower crust are also found in the northernmost part of our model at 5 km depth and close to the coast (Z=5 km in Fig. 4.24, and 4.38 a).

Velocities higher than 8.1 kms^{-1} are observed only beneath the central parts of the constrained North American region (Y=4470–4520 km, X=380–470 km). These velocities are visible at a maximum depth of 31 km and roughly north of the same latitude as Cape Mendocino and west of 123°20'W (Z=30–31 km and Y=4490 km in Fig. 4.24, 4.25, and 4.31). Upper mantle velocities are also observed at 25 km depth beneath King Range, but poorer ray coverage at these depths doesn't allow us to extend the boundary south along the coast (Y=4430–4450 km, X=390–420 km and Z=25 km in Fig. 4.24 and 4.31).

Comparison of first arrival and P_g models

After the description of the first arrival model it would be useful to compare it with the model calculated with the use of P_g arrivals only. The comparison is possible only for the area and depths constrained by the P_g model. In general, the differences, in most areas of the tomography models, are less than ± 0.5 kms^{-1}

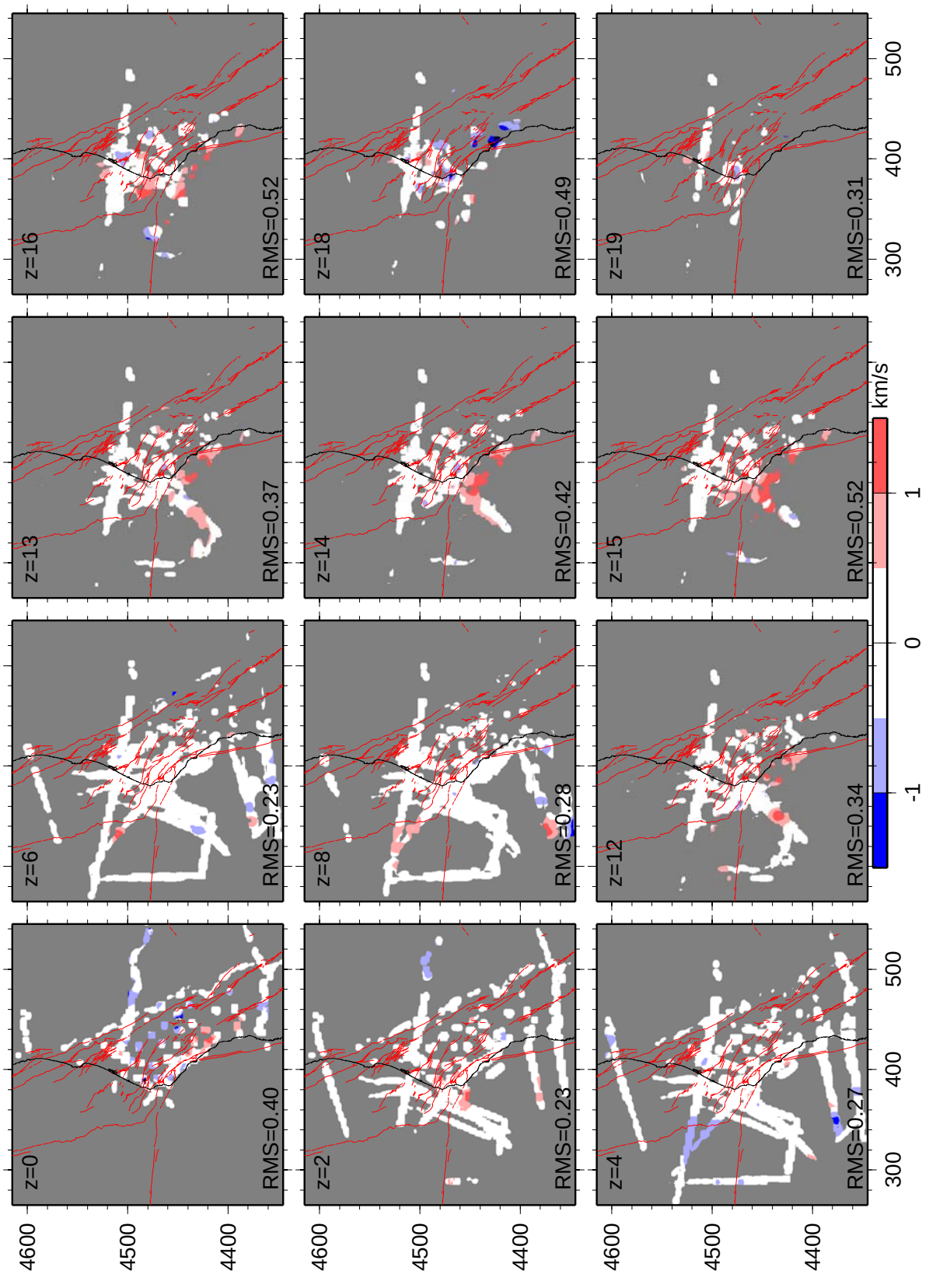

Figure 4.32: Difference between first arrival and P_g arrival model at different depths. The P_g model was subtracted from the first arrival model. The ray coverage is from the P_g model. The RMS difference for each slice is also indicated.

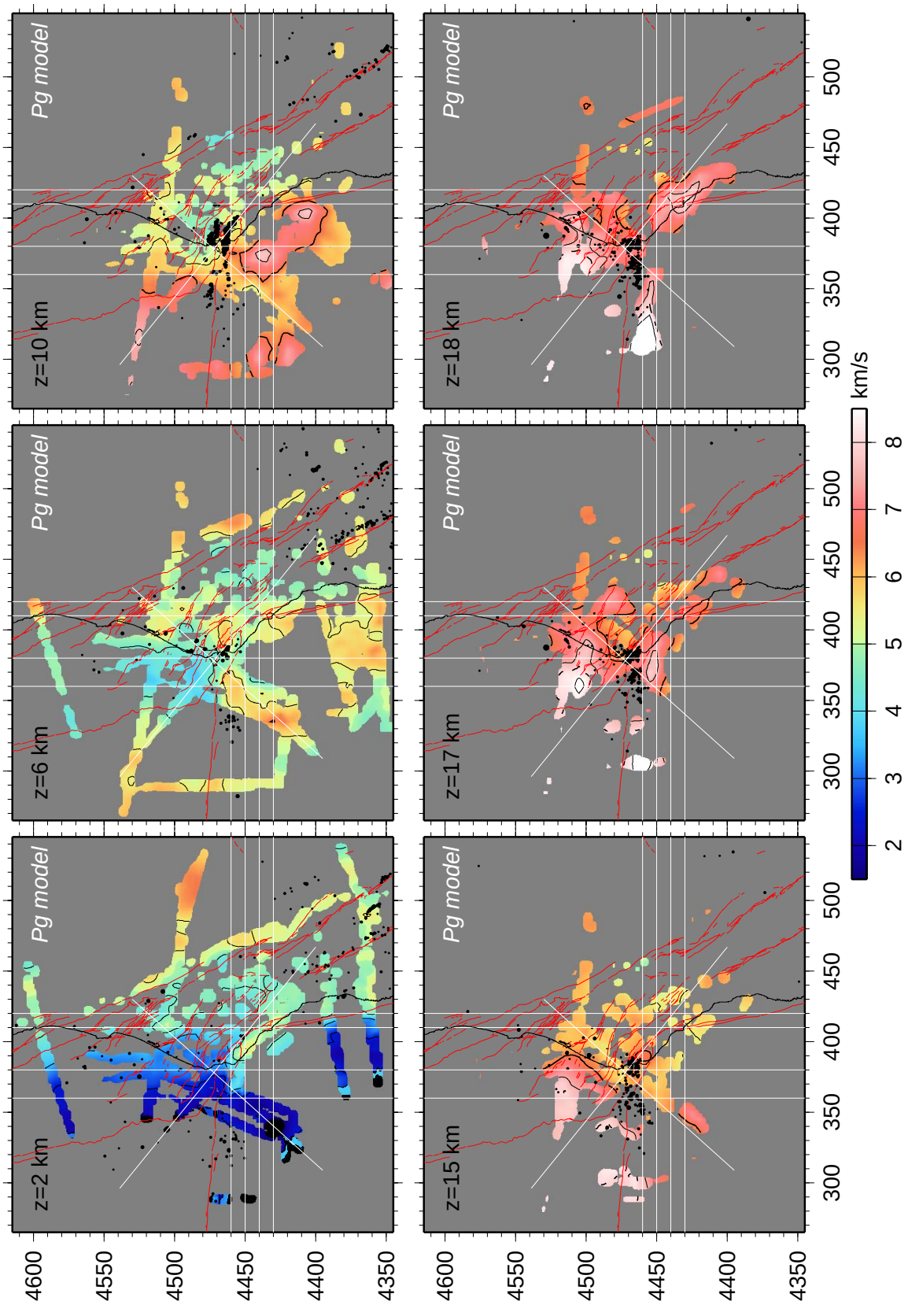

Figure 4.33: Horizontal slices through the final P_g velocity model at various depths. Shadowed areas are not sampled by P_g rays in the forward step. The 6.5 kms^{-1} contour is bold. Hypocentres of relocated seismicity, described in Chapter 5, within 1 km of the profile and magnitude > 2 are shown as black crosses. Black solid line marks the coastline and red lines the quaternary, USGS mapped, surface faults. White lines mark the traces of the extracted vertical velocity profiles in figures 4.34, 4.36 and 4.37.

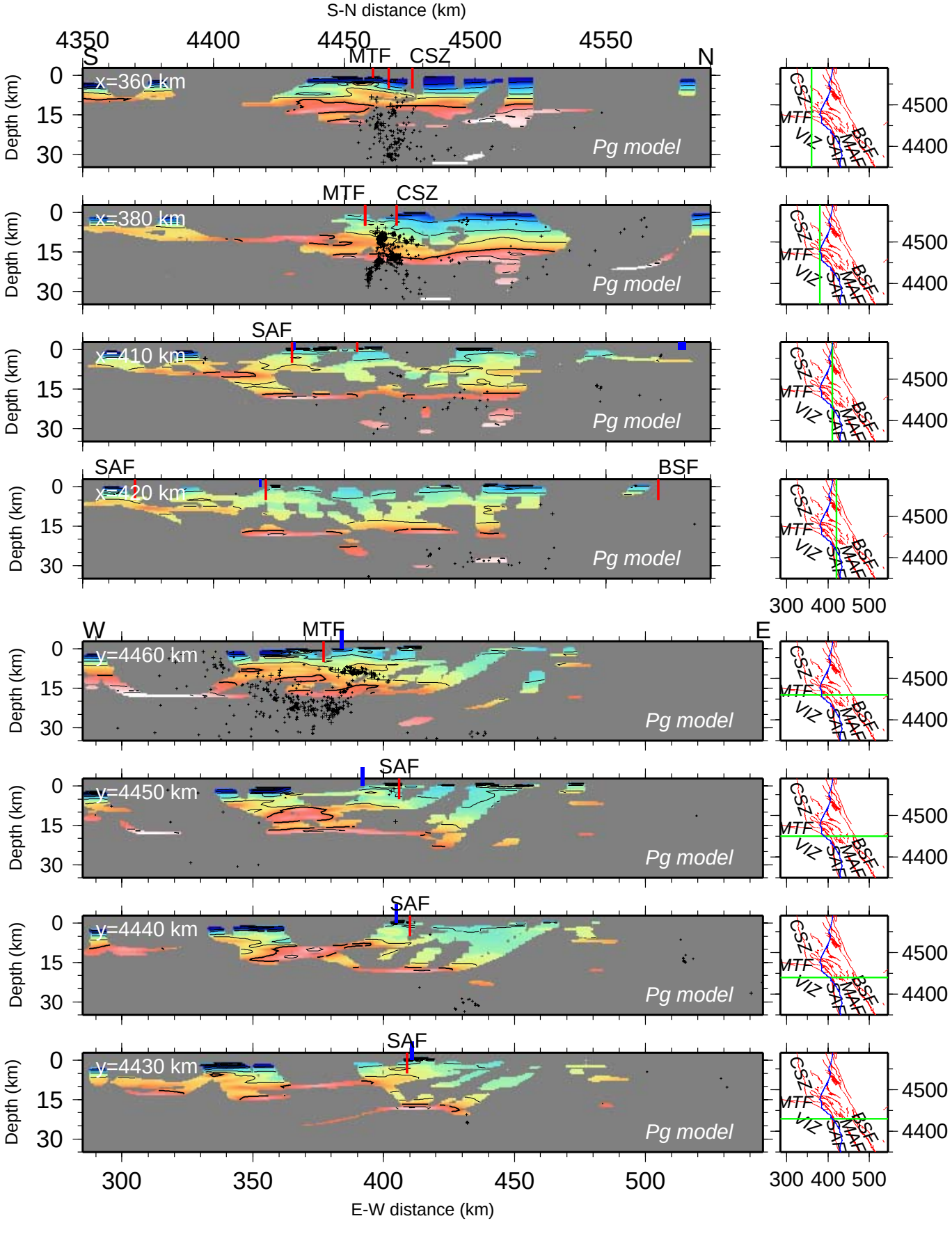
S-N distance (km)
4350
4400
4450
4500
4550
S
N
MTF
CSZ
x=360 km
x=380 km
SAF
x=410 km
BSF
x=420 km
Depth (km)
0
15
30
Pg model
W
E
y=4460 km
y=4450 km
y=4440 km
y=4430 km
300
350
400
450
500
E-W distance (km)
CSZ
MTF
VIZ
SAF
MAF
BSF
4500
4400
km/s
2
3
4
5
6
7
8

Figure 4.34: (Previous page) Vertical profiles through the final P_g velocity model along S–N and W–E direction (no vertical exaggeration). Each slice indicates the position where it was extracted and the surface trace of each profile is indicated on the inset maps on the right. The 6.5 kms^{-1} contour is bold. Hypocentres of relocated seismicity, described in Chapter 5, within 2.5 km of the profile and magnitude > 2 are shown as black crosses. Blue lines at the surface show the trace of the coastline, whereas red lines mark the position of various quaternary, USGS mapped, faults. SAF: San Andreas fault, MTF: Mendocino transform fault, CSZ: Cascadia subduction zone, MAF: Maacama fault, BSF: Barlett Springs fault, VIZ: Vizcaino block.

(Fig. 4.32). As most of the P_g picks are used already in the first arrival model, great discrepancies between the two models should not be expected in places where these P_g picks are observed as first arrivals. This is normally the case at shallow depths in the model (0–8 km in Fig. 4.32). Areas at shallow depths where the observed velocity difference between the two models is greater than ± 0.5 kms^{-1}, are mainly found at the end of some lines, like *wa1*, *wa3* and *wa6* (2–4 km in Fig. 4.32 and Fig. 4.23), where the large seperation between sources and receivers ensures that a P_n arrival is also observed, adding additional information to the velocity structure of these areas.

The lower crust is often constrained by P_g turning rays that are observed in the seismograms as second arrivals (see Fig. 4.8 and Fig. 4.9). The first arrival model uses only the P_n picks that have arrived earlier and therefore can only constrain these parts of the crust by energy travelling steeply through the crustal layer. Thus, we expect that the P_g arrival model will give a more detailed image of the lower crust in these areas. The comparison between the two models reveals that, between 10 km and the maximum depth resolved by P_g at $\sim$20 km, two areas show major discrepancies (Z=14-18 km in Fig. 4.32). The first area, that shows a greater than 1 kms^{-1} positive velocity anomaly, is centred at 15 km depth below the Vizcaino block (X=360–420 km, Y=4420–4460) and is well resolved by both models. The anomaly suggests that the first arrival model predicts higher velocities at these depths. The final P_g model shows the same high velocity anomaly at 10 km depth (Fig. 4.33), beneath the Vizcaino block, but separates it from the high velocity lower crust with a lower velocity layer. This layer between the shallower high velocity body and the expected top of the lowermost crust is resolved only in the P_g model (Z=10–15 km, Y=4450–4460 km and X=360–380 km in Fig. 4.33, 4.34). Thus, based on these observations, we suggest that the high velocity body at 10 km depth is not attached to the lowermost crust, but is incorporated in the upper crust of the Vizcaino block.

The second lower crustal discrepancy in the first arrival model is centred at 18 km depth and comprises an elongated negative anomaly south of Point Delgada (Z=18 km in Fig. 4.32). However, this observed difference in velocities is between a resolved area in the P_g model (Z=17–18 km, Y=4430–4440 km, X=410–420 km in Fig. 4.33, 4.34) and an area in the first arrival model where there are no first arrivals to pass through (Z=17 km, Y=4430–4440 km, and X=410–420 km in Fig. 4.24, 4.25, 4.27). Thus, the P_g model adds new information for the structure of an area unresolved in the first arrival model. Velocities higher than 6.5 kms^{-1} here show that the lower crustal layer observed offshore also extends onshore.

Comparison with other wide-angle models

Vertical velocity profiles have been extracted from the final tomography model along similar coordinates as previously published 2D wide-angle models. The ray coverage in these extracted profiles is generally worse than that shown in previous studies. Although the data are the same, the crooked line geometry that was assumed to be a straight line during the 2D modelling will result in models with apparently better ray coverage but it will not represent the real resolved 2D velocity structure. To make the comparison easier the 2D slices extracted from the final model are plotted with the ray coverage from a coarser inversion grid ($5 \times 5 \times 0.5$ km cell size). The 3D tomography model is also expected to have smoother velocity gradients than the 2D models developed with the irregular grid method by Zelt & Smith (1992). Unlike the tomography approach of Zelt & Barton (1998) used here, in the method of Zelt & Smith (1992) velocity layers are bounded by interfaces, constrained by reflected as well as refracted phases, that allow strong velocity contrasts.

Comparison with the 2D model of line *wa1* by Henstock et al. (1997) and Henstock & Levander (2000a) of line *wa1* (Fig. 4.7 c) yields similar upper crustal structure, although smaller scale heterogeneities are resolved in our new model (Fig. 4.35). Offshore, the depth to the basement that was constrained by the MCS data and kept fixed during the 2D inversion by Henstock & Levander (2000a) agrees well with the shallow velocity structure in the tomography profile that has only been constrained by P_g and P_n arrivals (X=0–40 km in Fig. 4.35). The old Farallon accretionary prism is defined as a layer thickening towards the east with velocities between 4.5 and 5.5 kms^{-1}. At the San Andreas fault this layer is offset by almost ∼5 km down to the east in both studies (X=∼90 km, Z=10–15 km in Fig. 4.35). Ray coverage in the 3D tomography model does not

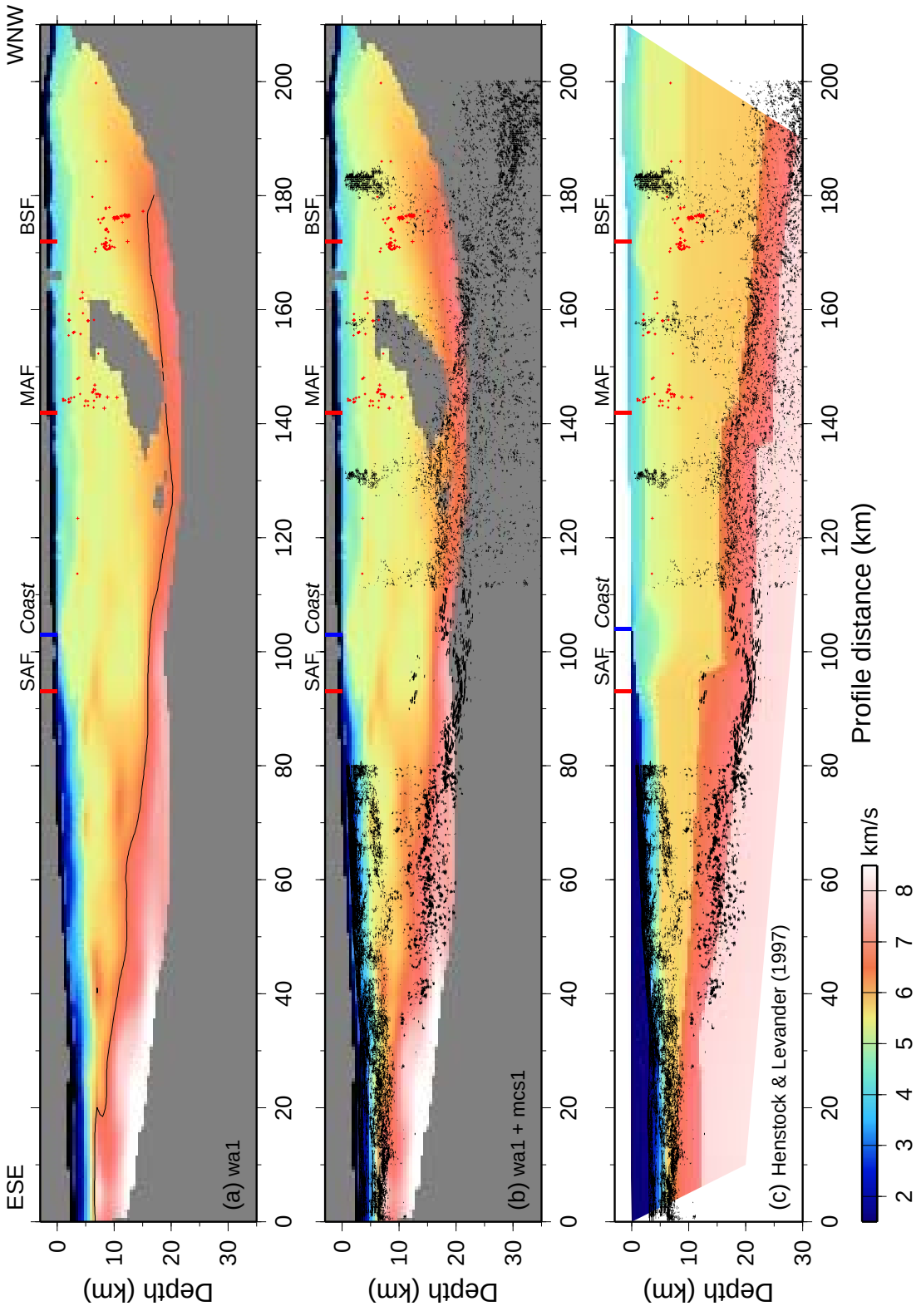

Figure 4.35: Comparison of a vertical slice along line *wa1* with the 2D model by Henstock & Levander (2000a). Hypocentres of relocated seismicity, described in Chapter 5, within 5 km of the profile and magnitude > 2 are shown as red crosses. (a) Velocity profile extracted from the final tomography model. The 6.5 kms^{-1} isovelocity contour is plotted. (b) The same with a continuous depth-migrated CMP section by Henstock & Levander (2000a) overlain. (c) 2D velocity model derived by Henstock & Levander (2000a). SAF: San Andreas fault, MAF: Maacama fault zone, BSF: Barlett Springs fault zone.

allow us to confirm that these vertical offsets continue in the lower crust and the Moho, as was suggested by Henstock et al. (1997) based on intra-crustal reflected phases. Although the 6.5 kms^{-1} isovelocity contour below SAF shows a gentle dip towards the east, east-west velocity profiles north of line *wa1*, image this abrupt transition below SAF that continues to the upper mantle (Y=4400-4420-4440-4460 km in Fig. 4.25 and 4.26). Similarly, the suggested vertical offsets in the lower crust below the Maacama and Barlett Springs faults, determined mainly by P_n, P_mP and near-vertical reflections (Henstock et al., 1997), are not imaged in the 3D tomography model (Fig. 4.35 a). The top of the lowermost crust at 6.5 kms^{-1} coincides offshore and onshore with a series of bright reflections on a depth-migrated reflection section of the same line by Henstock & Levander (2000a). These bright reflections are dipping from 7–8 km depth in the west to more than 20 km in the east end of the profile (Fig. 4.35 b). Henstock & Levander 's (2000) wide-angle model correlates only the onshore part of these reflections with the lowermost crust. Shallow depth-migrated reflections correlate well with the shallow velocity heterogeneities offshore (e.g. X=40, Z=8 km in Fig. 4.35 b). Finally, the deepest parts of the tomography model in the east (between X=140–200 in Fig. 4.35 a) suggest that the upper crust thins towards the east. This area is however constrained only by P_n picks from land stations in the east. Thus, in the absence of P_g and reflected arrivals to constrain the crustal velocities, the crustal structure is able to develop a higher vertical gradient and therefore create a velocity structure with an apparent 8 kms^{-1} velocity and an eastward decreasing thickness. Henstock & Levander (2000a) following the layer-interface parametrisation by Zelt & Smith (1992) and, using all available phases, are able to image this eastern deep structure in agreement with the observed depth–migrated reflections that have been interpreted as the Moho boundary (X=90 km and Z=20 km in Fig. 4.35 b).

The SW–NE segment of line *wa3* is compared with the same segment's velocity model and depth-migrated reflection data from Henstock & Levander (2003) (Fig. 4.36). In the offshore part of the profiles, shallow velocities reveal similarly the two basement ridges; the one which marks the southern end of the Vizcaino block and the Mendocino Ridge further northwards (X=15 km and 80–90 km, respectively). Between these ridges the wedge-shaped low velocity basement is resolved (Fig. 4.36). The tomography profile reveals a high velocity anomaly at 10–12 km depth (X=60–100 km in Fig. 4.36 a-b), which is at the edge of the high velocity body observed further eastwards, offline (10 km in Fig. 4.24). The P_g velocity model images this anomaly as a separate body from the lower crust (Fig. 4.36 b). The suggested bright reflection from the moho in the depth-migration section (X=40–

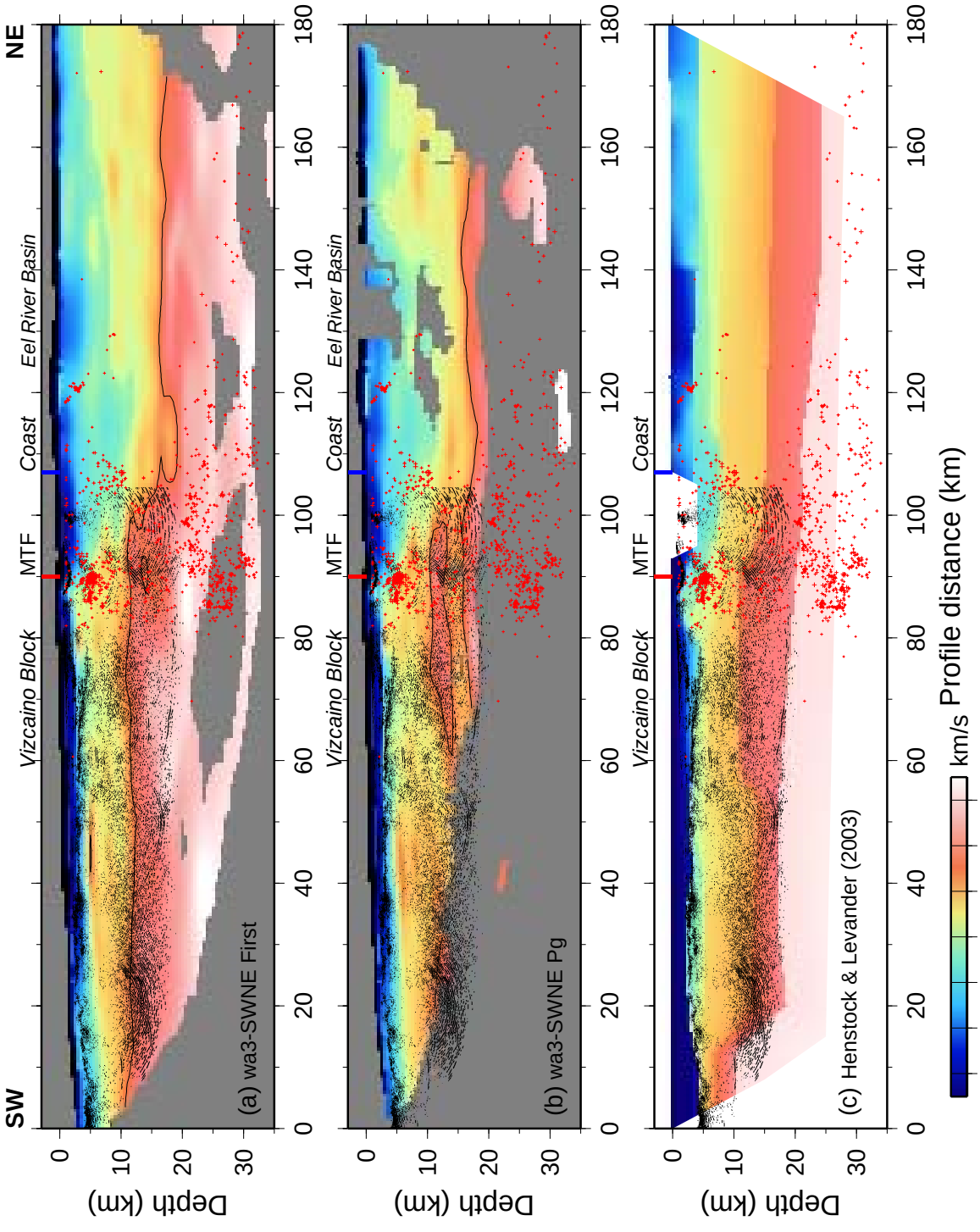

Figure 4.36: Comparison of a vertical slice along line *wa3SWNE* with the 2D model by Henstock & Levander (2003). Depth-migrated CMP section by Henstock & Levander (2003) is overlain. The 6.5 kms^{-1} isovelocity contour is plotted. Hypocentres of relocated seismicity, described in Chapter 5, within 5 km of the profile and magnitude > 2 are shown as red crosses. (a) Velocity profile extracted from the first arrival tomography model. (b) Velocity profile extracted from the P_g arrival tomography model. (c) 2D velocity model derived by Henstock & Levander (2003). MTF: Mendocino Transform fault.

90, Z=20 km in Fig. 4.36 b–c) is in good agreement with parts of our model that have velocities around 8.0 kms^{-1}. A zone of shallower chaotic reflectivity correlates with various velocity heterogeneities within the upper and lower crust in the tomography profile (X=50–100, Z=20 km in Fig. 4.36 a–b).

The onshore crustal structure of the SW–NE segment in line *wa3* shows the Eel River basin with very low velocities both in this study and that of Henstock & Levander (2003) (Fig. 4.36 a–c). The tomography model bounds with higher velocities the basin in the north, in agreement with Henstock & Levander (2003), but also in the south, revealing, at this particular cross-section, a basin at least 20 km wide and 5 km deep (Fig. 4.36 a). The velocity structure in the northern part of the line after the passage from the MTF shows similar features in both studies, with a thickened upper crust toward the north revealing the accretionary sequences (Fig. 4.36 a–c). Velocities around 8.1 kms^{-1}, at 30–31 km depth, that shallow to the north (Fig. 4.36 a) indicate the Gorda upper mantle.

For the NW–SE segment of line *wa3* (Fig. 4.37 a-c), the Gorda structure in the west part of the section, on both this study's profile and that of Henstock & Levander (2003), has a 1–2 km thick sedimentary layer overlying a normal oceanic crust, 7–10 km thick, with typical Layer 2 and Layer 3 velocities between 4.5–7.1 kms^{-1}. Similarly to line *wa1*, the depth to the basement that was constrained by the MCS data and kept fixed during the 2D inversion by Henstock & Levander (2003) agrees well with the shallow velocity structure in the tomography profile that was only constrained by P_g and P_n arrivals (X=0–80 km in Fig. 4.37). Very steep gradients and velocity irregularities at the northern edge of the tomography profile are the product of a few P_n rays that sample these deep parts of the section in almost vertical paths. A wedge shaped shallow area with low velocities is observable in both studies with a maximum depth close to the coast, representing the Eel River forearc basin offshore (X=50–100 km). The velocity structure of the lower crust immediately south of the trench shows abrupt velocity changes that offsets vertically areas with velocities between 6.5 and 8.1 kms^{-1} (X=80–110 km in Fig. 4.37 a). This non-smooth velocity structure in the tomography profile is in good agreement with discontinuous reflection surfaces observed in the depth-migrated cross-section (X=80–110 km in Fig. 4.37 a-b).

The addition of data from offline shots of the *wa3* NW–SE profile in the tomography study has enhanced the structure of the North America crust. The 2D data from this line do not constrain this area well. Thus, Henstock & Levander (2003) fitted the residuals in this area through a free inversion of a shallow 4 km thick layer, and by keeping the lower crust fixed in a structure that is close to that

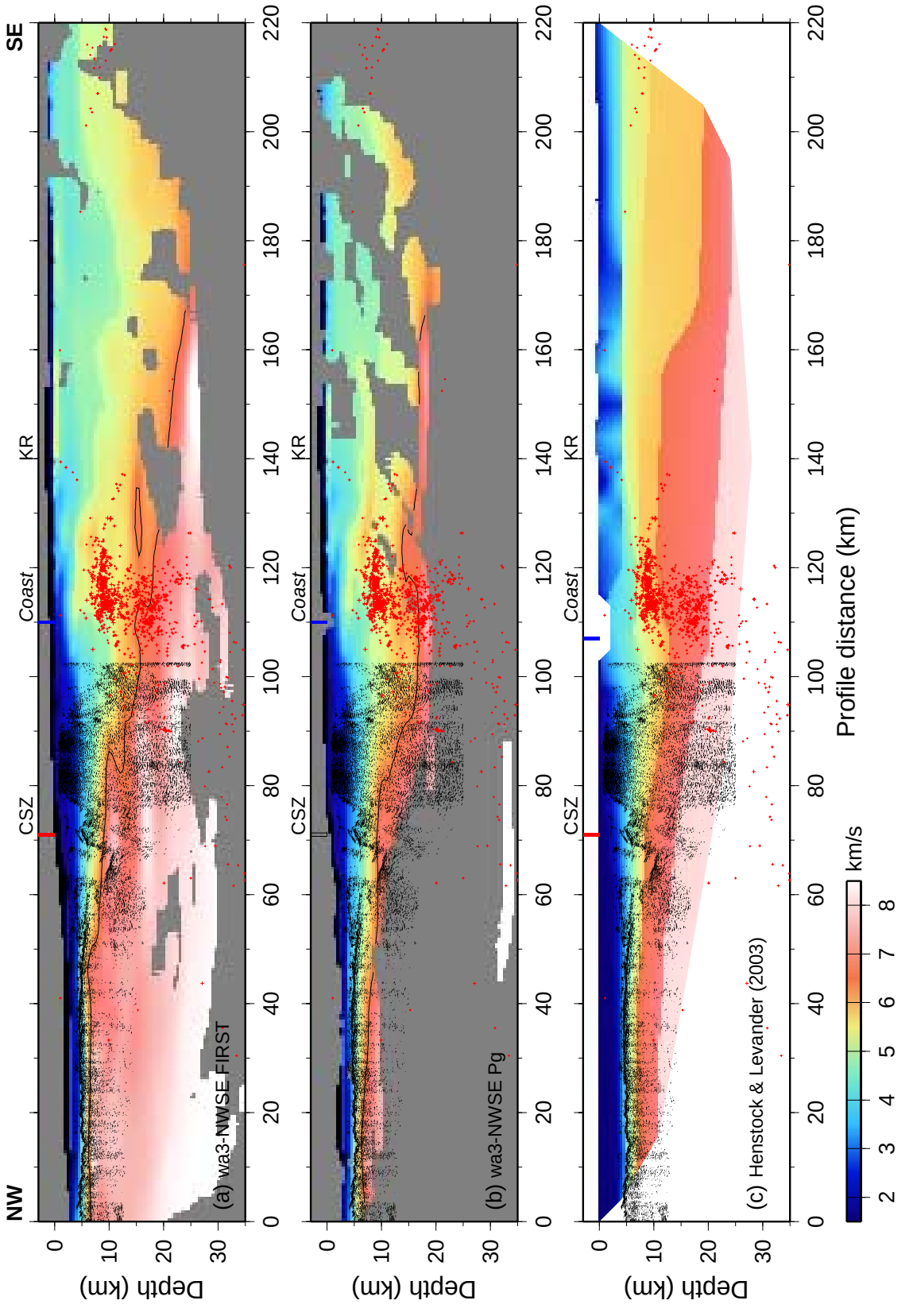

Figure 4.37: Comparison of a vertical slice along line *wa3NWSE* with the 2D model by Henstock & Levander (2003). Depth-migrated CMP section by Henstock & Levander (2003) is overlain. The 6.5 kms^{-1} isovelocity contour is plotted. Hypocentres of relocated seismicity, described in Chapter 5, within 5 km of the profile and magnitude > 2 are shown as red crosses. (a) Velocity profile extracted from the first arrival tomography model. (b) Velocity profile extracted from the P_g arrival tomography model.(c) 2D velocity model derived by Henstock & Levander (2003). CSZ: Cascadia Subduction Zone, KR: King Range

observed along the *wa1* in the same area. This approach will decrease considerably the velocities in the first 4 km to keep the same apparent velocity through the crust (X=140–220 km in Fig. 4.37 c). The use of additional information from offline shots constrains this area better in the tomography model, resulting in a crustal structure with lower velocities at greater depths and generally smoother velocity gradients in the continental crust. High velocities at shallow depths beneath King Range are now resolved and correlate well with the mapped igneous rocks of Point Delgada (Fig. 4.37 a-c). A thick upper crust with velocities lower than 5.5 kms^{-1} is also observed in the tomography model, consistent with Franciscan accretionary complex rocks (Stewart & Peselnik, 1977), and a maximum depth of $\sim$20 km. Finally, an increase of crustal velocities between the coast and the thick upper crust described earlier (X=110–160 km in Fig. 4.37 c) is shown in both studies although the correlation in depth is not always good. The extracted tomography profile onshore diverges to the NE of the receivers locations and tends to show North American structure at the edge of of King Range, whereas the crooked 2D line of Henstock & Levander (2003) samples directly the King Range terranes.

The onshore part of line *wa6* is in agreement with Beaudoin et al. (1996b), although the addition of the densely sampled onshore-offshore data resolves smaller scale velocity structures (Fig. 4.38 b). The Great valley area, modelled by Beaudoin et al. (1996b), is outside this tomography model to the east. In general, the high velocity Klamath terrane and the Franciscan accretionary complex rocks reveal the same features. Our model shows alternating high velocity Klamath layers and does not give an obvious Franciscan underthrust feature, although the missing shots from the Great Valley area will contribute more information in this area. The top of the subducting Gorda slab and the Moho boundary are in similar depths.

Comparison of a vertical profile extracted along the SE–NW *line 9* with the 2D velocity model along the same line by Beaudoin et al. (1996b) shows the same general velocity structure (Fig. 4.39 c). The upper crust comprises of small scale velocity structures, representing the intermixed Franciscan sediments and melange units, whereas a southern dipping zone of lower crustal velocities, in the north (X=160–240 km), images the subducting oceanic crust of the Gorda plate. Velocities greater than 8.1 kms^{-1} also dip to the south with a maximum resolved depth at 31 km (X=180–220 km in Fig. 4.39 c). The tomography model does not image the end of the Gorda slab to the south, as this is mainly constrained by P_mP arrivals in Beaudoin et al. (1996b) model. The thickening of the Franciscan

complex in the centre of the profile (X=130–180 km), suggested by Beaudoin et al. (1996b) to be tectonic, is also visible in this tomography study. Finally, smaller wavelength anomalies, that are not resolved in the very smooth model of Beaudoin et al. (1996b), are now imaged in the tomography profile; at ∼5 km depth high velocities (greater than 5.5 kms^{-1}) associated with the southern edge of the Klamath terrane, and at 13 km depth velocities greater than 6.5 kms^{-1}, revealing possibly some remnant Coast Range ophiolithic sequences (Fig. 4.39 c).

A vertical velocity profile extracted along *line 5* (Fig. 4.39 a), can be compared with the 2D model along the same line by Leitner et al. (1998). The sediment layer, constrained by MCS data by Leitner et al. (1998), is in agreement with the tomography model, with a sediment thickness increasing to the north toward the Mendocino ridge, pinching out against the ridge crest. North of the ridge the sediment layer is offset by faults where they offset the basement to the surface (X=90–100 km and Z=0–5 km in Fig. 4.39 a). Upper and lower crust seems in both models to be thicker on the south of the ridge. The crustal thickness decrease abruptly at X=40–50 km (Fig. 4.39 a), with the top of the lowermost crust and the Moho boundary within the Gorda plate being at ∼7 km and 10 km depth, respectively, for both models (X=90-100 km in Fig. 4.39 a).

In a similar comparison the *line 4* velocity profile (Fig. 4.39 b), shows good correlation with the model along the same line by Leitner et al. (1998). Shallow velocities that in the 2D model are constrained by MCS data are in good agreement with our model. Both models show the thickening of the upper crust towards the Vizcaino block eastwards. In addition, our tomography model reveals upper mantle velocities at ∼21 km depth (Fig. 4.39 b).

Finally, the coarse local earthquake tomography model by Verdonck & Zandt (1994) reveals similar features to this study. In particular, the Klamath terrane is imaged from the surface to a depth of 5 km in the same area as in this model (1–5 km of Fig. 4.24). Velocities higher than 5.5 kms^{-1} are also observed at shallow depths near Point Delgada. A general high velocity anomaly, at 5–10 km depth

Figure 4.38: (Next page) Vertical velocity profiles along the *wa8, wa6, wa2* lines. The map shows the position of the plotted profiles, marking *wa8* and *wa2* in yellow, from north to south respectively, and the W–E *wa6* line in blue. The 6.5 kms^{-1} isovelocity contour is plotted. Hypocentres of relocated seismicity, described in Chapter 5, within 5 km of the profile and magnitude > 2 are shown as red crosses. (a) Line *wa8*, (b) Line *wa6*, and (c) Line *wa2*. Traces of faults on the surface are marked in red and the coastline in blue. CSZ: Cascadia subduction zone, SAF: San Andreas Fault, MAF: Maacama Fault, BSF: Barlett Springs Fault.

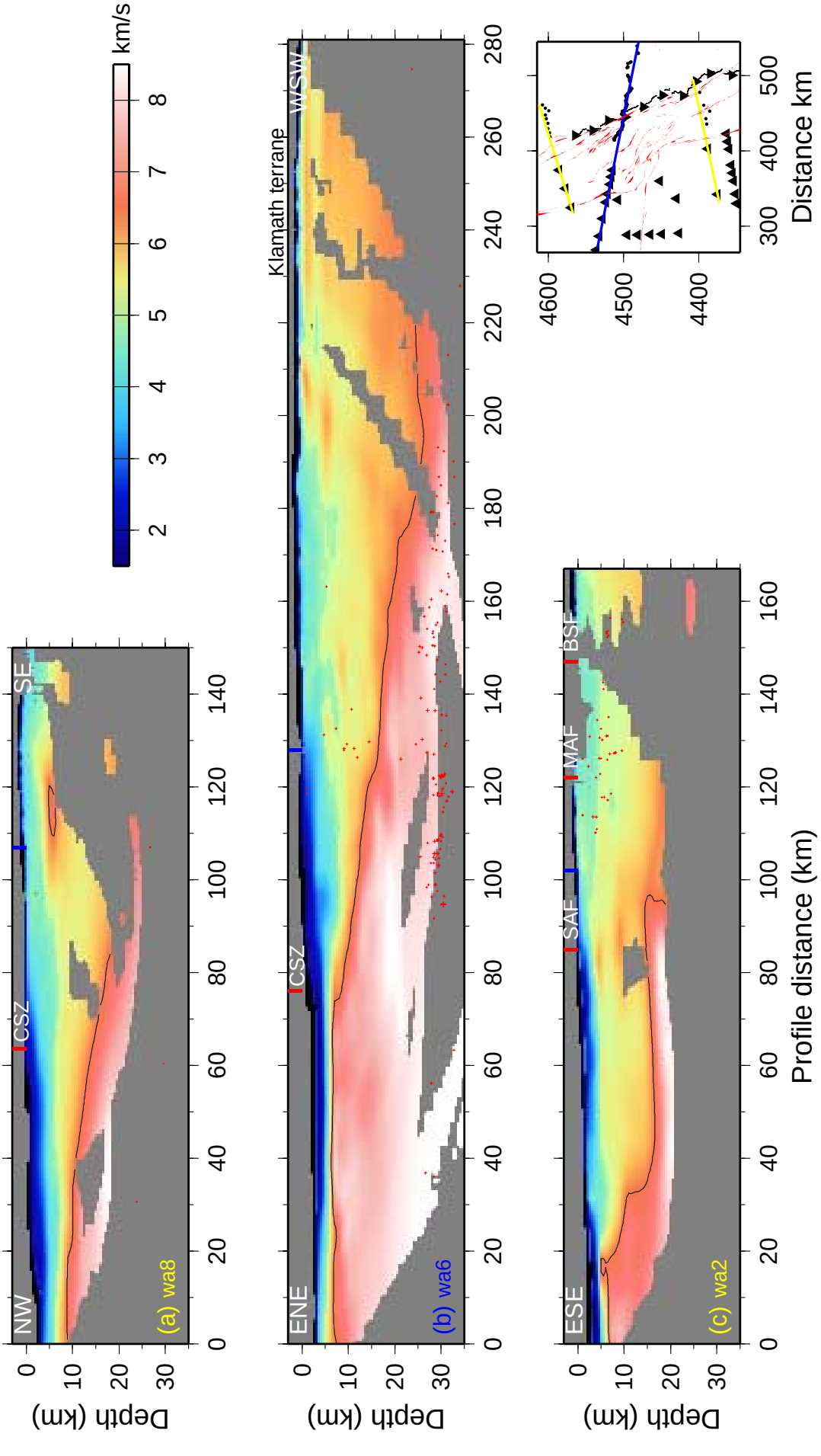
km/s
2
3
4
5
6
7
8
NW
SE
CSZ
(a) wa8
ENE
WSW
Klamath terrane
CSZ
(b) wa6
ESE
SAF
MAF
BSF
(c) wa2
Depth (km)
0
10
20
30
0
20
40
60
80
100
120
140
160
180
200
220
240
260
280
300
400
500
4400
4500
4600
Distance km
Profile distance (km)

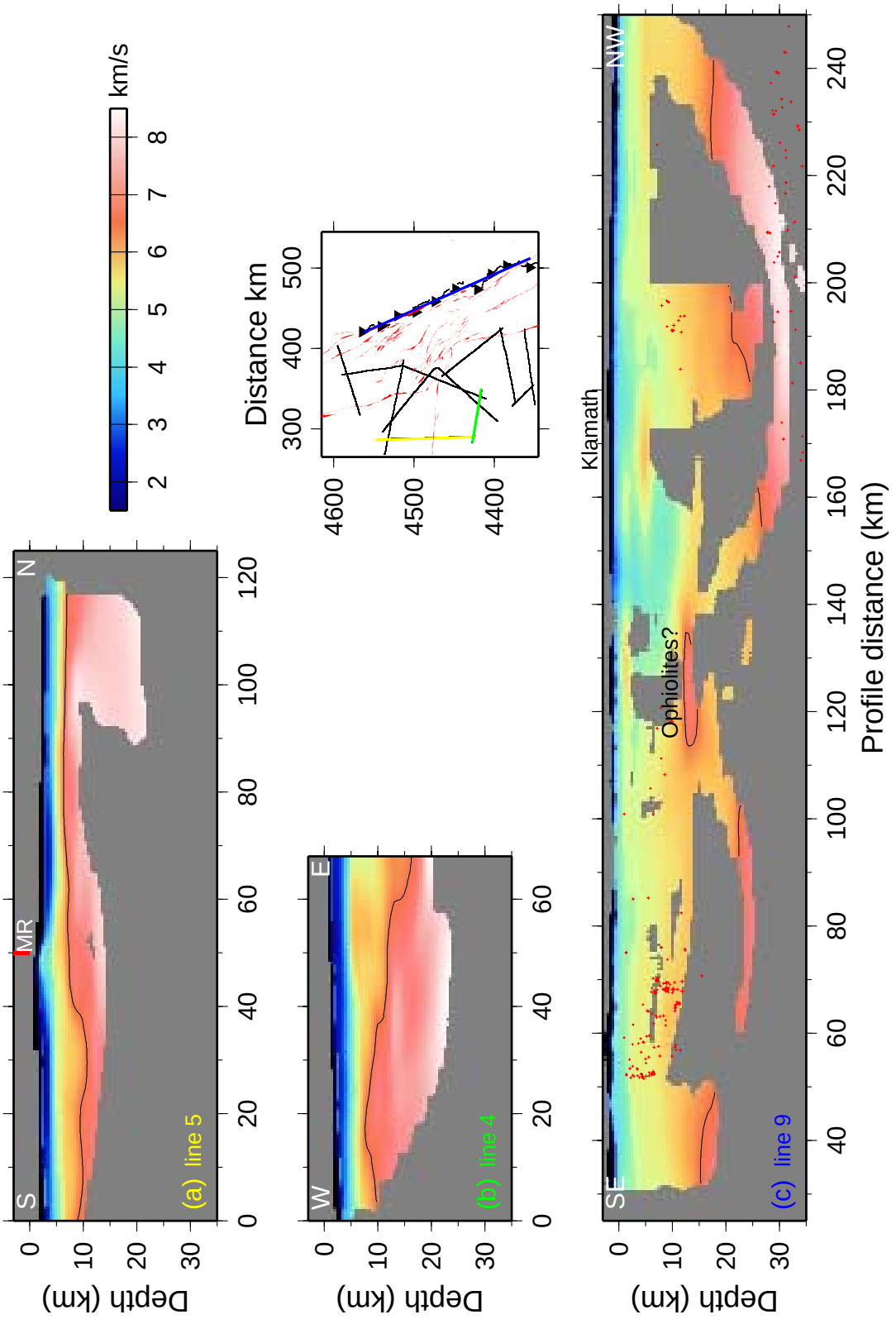

Figure 4.39: Vertical velocity profiles along the *line 5, line 4, line 9* lines. The map shows the position of the plotted profiles, marking the S–N *line 5* in yellow, the W–E *line 4* in green, and the SE–NW *line 9* in blue. The 6.5 kms^{-1} isovelocity contour is plotted. Hypocentres of relocated seismicity, described in Chapter 5, within 5 km of the profile and magnitude > 2 are shown as red crosses. (a) *line 5*, (b) *line 4*, and (d) *line 9* plotted in the same coordinates as the profile by Beaudoin et al. (1996b). MR: Mendocino Ridge.

below King Range and further offshore, is correlated with the Point Delgada mafic exposures (e.g. McLaughlin et al., 2000), although poor resolution at this area due to lack of seismicity will not rule out the possibility that the anomaly, observed by Verdonck & Zandt (1994), could be associated with the offshore velocity anomaly below the Vizcaino block observed in this study.

A combined discussion about the velocity structures described in this Chapter and the results of earthquake relocation, in the same area as the tomography experiment, is given at the end of Chapter 5 after the description of the earthquake relocation approach and its results.

Chapter 5

Earthquake relocation near Mendocino Triple Junction

5.1 Introduction

Although three-dimensional velocity models are very useful to infer the geological structure of a region, they represent just a snapshot in geological time. A complete picture requires an integration of the snapshot model with the dynamics and kinematics behind it, showing the possible evolution of the study area. Since the Mendocino Triple Junction region is characterised by a high level of seismicity, knowing the location of the earthquakes and their focal mechanisms allows us to describe aspects of the tectonics behind the present study. Earthquakes are routinely located by comparing observed arrival times with those predicted by a reference velocity model. Inaccuracies in the reference velocity model will introduce systematic errors in the locations and therefore in the dynamic model of the region.

In this study, we relocate 30664 events recorded from the Northern California Seismic Network (NCSN) between 1977 and 2002 near the Mendocino Triple Junction. Although absolute earthquake locations depend on the three–dimensional velocity structure between the event and the station, relative event locations within seismicity clusters can be improved through the use of source-specific station terms and waveform cross-correlation.

5.2 Relocation methods

5.2.1 Locating Earthquakes – Basics

Earthquake locations are routinely obtained by comparing observed P and sometimes S traveltime picks with calculated traveltimes in an assumed velocity model, and calculating the best fitting locations and origin times by minimising the misfit. Most location methods use 1D velocity models that introduce systematic errors into the solutions. These errors can be separated into absolute location errors produced by the neglected real 3D velocity distribution between the event source and the receiver, and relative location errors between closely spaced events. To eliminate the first requires exact knowledge of the 3D velocity structure, usually obtained by joint-hypocentre-velocity inversion algorithms (e.g. Zhang & Thurber, 2003; Eberhart Phillips & Michael, 1983; Thurber, 1983). Relative errors in event location can be, however, accounted for without solving for a new velocity structure. Station term methods (e.g. Frolich, 1979), master event methods (e.g. Evernden, 1969) and double difference methods (e.g. Waldhauser & Ellsworth, 2000) are possibly the most widespread techniques.

The total observed time in the j station's seismogram for the earthquake event i will be:

$$T_{ij}^{obs} = t_i + \tau_j(\mathbf{x}_i) + e_{ij} \tag{5.1}$$

where t_i and $\mathbf{x}_i$ are the origin time and location of the ith event, $\tau_j(\mathbf{x}_i)$ the travel time to the jth station from the source $\mathbf{x}_i$ and e_{ij} the picking error. Estimates of the source location can be obtained by minimising an appropriate norm of the residuals

$$r_{ij}(t_i, \mathbf{x}_i) \equiv T_{ij}^{obs} - t_i - \tau_j(\mathbf{x}_i), \tag{5.2}$$

making an initial estimate of the origin time t_i and position $\mathbf{x}_i$, and calculating the traveltime $\tau_j(\mathbf{x}_i)$ with the use of forward method through an assumed velocity model. For the traveltime calculation regional 1D velocity models are used assuming laterally homogeneous media giving a 2D function of time for distance and depth (Shearer, 1999).

Most of the available locations in earthquake catalogues are obtained using a traditional least squares method (Shearer, 1997). The traveltime T_{ij}^{obs} for event i and station j is from ray theory

$$T_{ij}^{obs} = t_i + \int_i^j u ds, \tag{5.3}$$

where u the slowness field and ds an element along the path. Since this equation is not linear, we use a first order Taylor expansion to linearise it as

$$T_{ij}^{obs} = t_i + \tau_j(\mathbf{x}_i) + \frac{\partial t_{ij}}{\partial \mathbf{m}_i}\delta\mathbf{m}_i, \tag{5.4}$$

where $\mathbf{m}$ are the four hypocentral parameters ($t_i, \mathbf{x}_i$ in equation 5.1 and 5.2). Similar to section (2.2.1) small perturbations $\delta\mathbf{m}$ of model parameters $\mathbf{m}$ will relate linearly to the traveltime misfit $\mathbf{r}$ as:

$$\frac{\partial t_{ij}}{\partial \mathbf{m}_i}\delta\mathbf{m}_i = \mathbf{r}_{ij}, \tag{5.5}$$

which can be compared to equation (2.50), where $\mathbf{r} = \mathbf{G}\delta\mathbf{m}$. The choice of traditional location methods for earthquake catalogues is due to the desire for consistency through time, making locations comparable to each other and not introducing systematic errors due to a possible change of the location algorithm. However, the use of the L2 norm as a measure of misfit, and consequently the least squares minimisation is not always the appropriate method (see section 2.2.2), since not all data have independent Gaussian errors. The L1 norm and the least absolute minimisation will be far more robust with respect to data outliers (see Shearer (1997) and Richards-Dinger & Shearer (2000) and references therein). The L1 misfit function to be minimised for n_i events and n_j stations becomes:

$$\Psi(t_i, \mathbf{x}_i) = \sum_{i,j} \frac{1}{\sigma_{i,j}} |T_{ij}^{obs} - t_i - \tau_j(\mathbf{x}_i)|, \tag{5.6}$$

where $\sigma_{i,j}$ the uncertainty of the traveltime picks. The system decouples into four sets of n_i independent equations, for each hypocentre parameter respectively, that can be solved independently.

5.2.2 Station Terms and Source Specific Station Terms

When a station records more than one nearby event, and the distribution of the residuals between the observed and calculated traveltimes has a nonzero mean, then the traveltime τ_j can be split into a common part s_j for all these events recorded in the particular station, and the individual traveltime τ_j' for each event-station pair. Putting this common time s_j, called the station term (ST), into equation 5.1, produces

$$T_{ij}^{obs} = t_i + \tau_j'(\mathbf{x}_i) + s_j + e_{ij}, \tag{5.7}$$

with the L1 misfit function to be minimised taking the form:

$$\Psi(t_i, \mathbf{x}_i, s_j) = \sum_{i,j} \frac{1}{\sigma_{i,j}} |T_{ij}^{obs} - t_i - \tau_j'(\mathbf{x}_i) - s_j|. \tag{5.8}$$

This equation will not decouple as equation 5.6, so the minimisation has to be performed in a two-step iterative procedure (Richards-Dinger & Shearer, 2000). First, the station terms are held fixed and the function is minimised for the hypocentral parameters. In the following step, the hypocentral parameters are held fixed and the function is minimised for s_j, where s_j is given as the weighted median (L1) or the weighted mean (L2). The observed traveltimes are effectively adjusted to include the station corrections, $T_{ij}^{'obs} = T_{ij}^{obs} - s_j$, and the relocation will iterate until a satisfactory fit is obtained.

Station terms represent overall corrections for all recorded events in one station. The use of a single time-shift correction for each station requires that errors in the assumed velocity model are due to heterogeneities at very shallow depths and that the event area is small compared to event-station separation and small compared to the scale length of velocity heterogeneities (Richards-Dinger & Shearer, 2000). When the recorded events in a station cover a big area all around the station, none of these requirements is true. Another approach is to separate the events into smaller groups of nearby events and to find a station correction for each group. In this way, each station will not have only one correction but various ones, each applied for specific source-station pairs. Therefore, as introduced by Richards-Dinger & Shearer (2000), the source specific station terms (SSST) represent the weighted median of residuals at a given station from N nearby events. When N equals the total number of events (n_{tot}) recorded in this station then the SSST is simply the ST case. On the other hand, when $N = 1$ a separate individual correction for each source-station pair will be applied, which is meaningless. To define the N nearby events, all the event locations are used to generate a 3D Delaunay tessellation and the N lowest-order natural neighbours around the requested event are selected (Richards-Dinger & Shearer, 2000). The minimisation uses the same two-step procedure as in the ST case.

5.2.3 Waveform methods

Waveform cross-correlation methods (WCC) methods are based on the assumption that comparison of waves generated by two similar sources, propagating along similar paths, will cancel out errors produced by the velocity heterogeneities along

the traveltime paths and will determine the relative event locations with respect to each other. In other words, the relative times between two or more closely spaced events are assumed to be independent of the far field velocity structure, but still depend on the velocity heterogeneities near the sources. The distance between these two events should be less than the wavelength of these heterogeneities to be independent of the near source velocity structure. Differential traveltimes between two closely spaced events, i and k, received in station j will be

$$\delta r_j^{ik}(\mathbf{m}_i, \mathbf{m}_k) = (T_j^i - T_j^k)^{obs} - (T_j^i - T_j^k)^{calc}, \tag{5.9}$$

which from equation (5.5) is equal (Waldhauser & Ellsworth, 2000) to

$$\delta r_j^{ik}(\mathbf{m}_i, \mathbf{m}_k) = \frac{\partial t_j^i}{\partial \mathbf{m}^i}\delta\mathbf{m}^i - \frac{\partial t_j^k}{\partial \mathbf{m}^k}\delta\mathbf{m}^k. \tag{5.10}$$

From equation (5.9) it is obvious that we can either obtain differential traveltimes from observed and calculated traveltimes or get them directly from cross-correlation of the waveforms. The latter requires no knowledge of the velocity structure and therefore is preferable as a mean of determining relative event locations independent from the assumed velocity model.

The WCC methods can be divided into two different approaches. In the first approach the differential traveltimes are used directly to calculate relative positions between events, like the double-difference approach by Waldhauser & Ellsworth (2000), where the equation $\mathbf{r} = \mathbf{G}\delta\mathbf{m}$ is inverted, with $\mathbf{G}$ consisting of the partial derivatives of 5.10. The second approach uses the differential traveltimes as additional information to the observed traveltime picks to solve for new set of adjusted picks by minimising the misfit to both the original picks and the differential times (Shearer, 1997). The linear relationship between the data $\mathbf{d}$ of observed times and differential times and the adjusted picks $\mathbf{T}$ will be $\mathbf{d} = \mathbf{GT}$. In both approaches, the correlation coefficient between waveforms can be used as means of differential weighting of data in the inversion.

5.3 Earthquake data and Velocity models

In this study, the P and S arrival time data of 37733 events occurring within the tomography study area between 1967-2002 and recorded in a network of ∼450 stations, are used (Fig 5.1). The picks are made by the Northern California Seismic

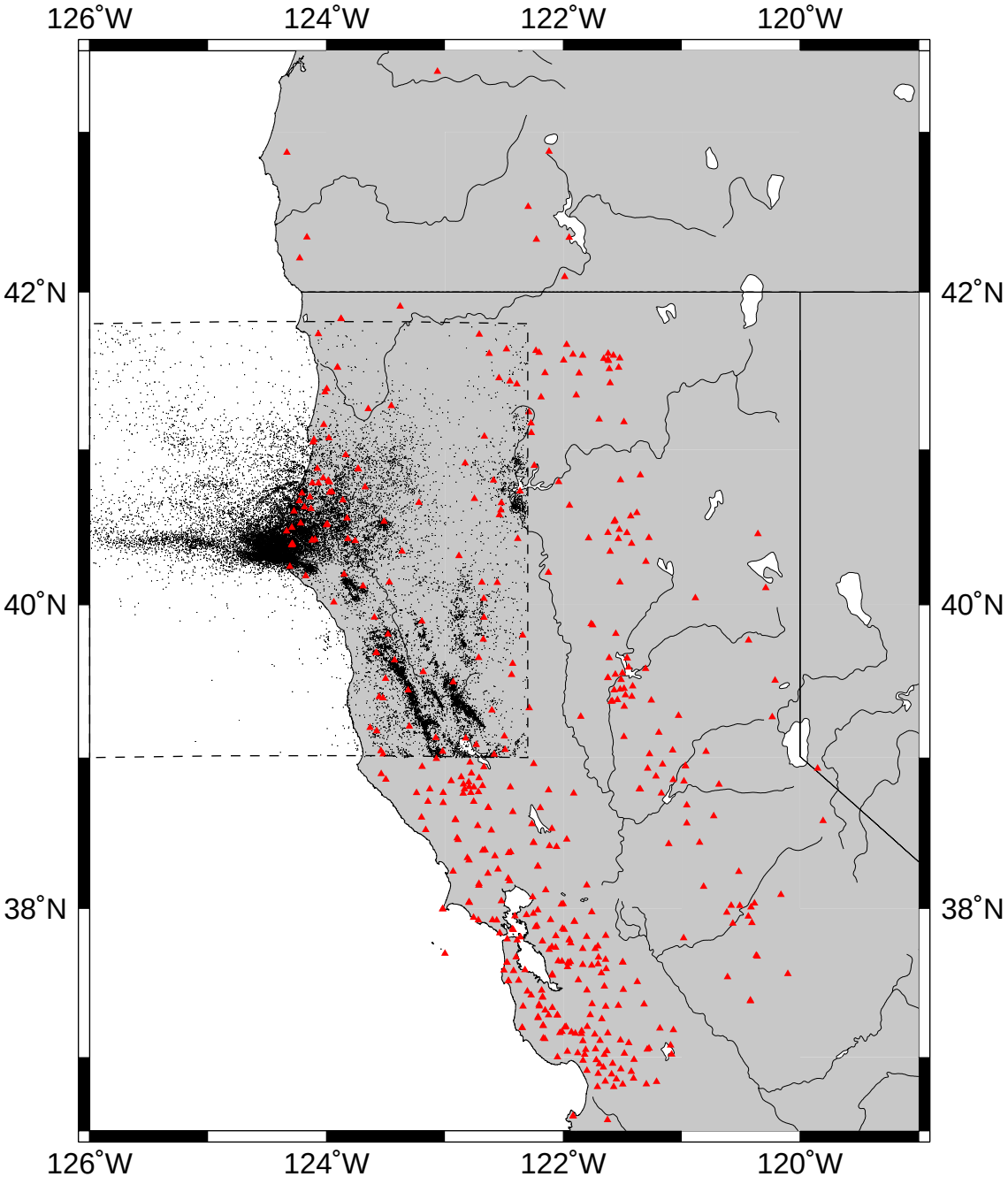

Figure 5.1: Earthquake locations used in this study, that lie within the area studied by tomography and recorded between 1964 and 2002. Red triangles mark all the seismic station (from NCSN) that received these events.

Network (NCSN) and used for a least squares inversion to obtain the event origin times and locations. The resulting hypocentre parameters, which comprise part of

the NCSN catalogue, publicly available from the Northern California Earthquake Data Center (NCEDC) (http://quake.geo.berkeley.edu/), were used in our study as initial positions in the relocation modelling. Waveform data were additionally obtained from the same source (NCEDC) for 16746 events occurred between 1984 and 2002.

The SSST relocation uses four different reference 1D velocity models, representing different regions within the study area. In this way, each event within the experiment area is relocated four times independently, but only the location which is calculated with the velocity model, that defines the box where the event belongs, is considered reliable. Moreover, events that do not belong in a specific box, although they are relocated, are not considered in our study. The tomography covered area is split into four distinctive areas in terms of earthquake sources and velocity structure: the Mendocino Fault area slightly offshore, the strike slip area southeast, the subduction and accretionary prism area offshore north, and the continental region east of the coast and north of Cape Mendocino (Fig. 5.2 a). All the 1D velocity models were obtained from a smooth 3D wide–angle model, sampled every 10 km laterally and 1 km vertically, that was produced by the tomographic inversion of the experiment described in Chapter 4. For each of the distinctive areas, we defined a box that is well covered by rays in the tomography model, sampled it every 5 km laterally, and took the mean of all the resulting profiles. A smooth sixth order polynomial fit to this mean model produced the models used in the relocation (Fig. 5.2 b). A comparison of these models with the NCSN models used for the same areas (Oppenheimer et al., 1992) reveals small differences in the continental areas and around Cape Mendocino. This is not the case, however, for the subduction and the accretionary prism area offshore, where it is clear that continental models are not appropriate (Fig. 5.2).

5.4 SSST and WCC application

Based on the four velocity models of Figure 5.2, we calculate P and S traveltime tables of range versus source depth at intervals of 1 km, with the raytracing equations for laterally homogeneous media described by Shearer (1999). The events are located with a Grid-Search algorithm. For each event-station pair, an initial 25 km cube is defined that surrounds the event location and the best grid point is estimated by comparing picks with the P and S predicted traveltimes interpolated from the traveltime tables. The median of these event positions for all stations is the new event location and a smaller cube is defined around it to improve the

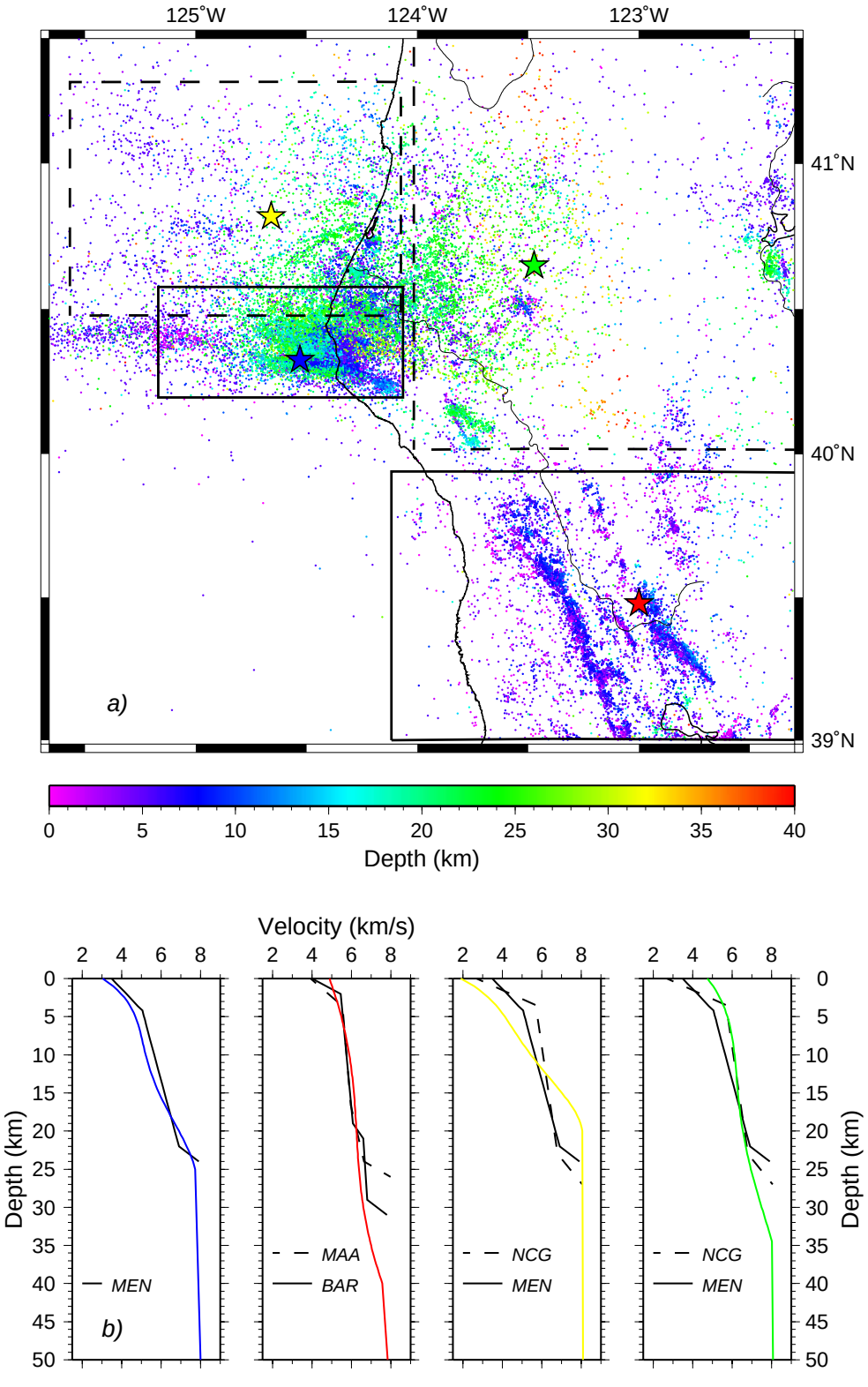

Figure 5.2: (a) NCSN Catalogue locations plotted versus depth. Bold and dashed boxes surround the four different areas studied. Coloured stars show roughly the centre of the sampled area where the velocity profiles were extracted for the SSST relocation. (b) The four velocity models used for each study area. Colours correspond to the coloured stars in a). Black solid and dashed profiles represent the NCSN velocity profiles for these areas. MEN: Cape Mendocino model, BAR: Barlett Springs Fault model, MAA: Maacama Fault model, NCG: Default Northern California model (Oppenheimer et al., 1992).

location. In this way starting from a 25 km cube we gradually reduce after 15 iterations to a 50 m cube, which is the relocation resolution. After each grid-search iteration the source specific station term is estimated for each source-station pair from a number of nearby events. The traveltimes are adjusted to include the SSST and relocation with the grid–search algorithm is performed once again for this particular iteration's cube size. The number N of nearby events and the maximum allowed distance between them is also defined and reduced in each iteration. In our case, it starts with 500 nearby events and a maximum cut-off distance of 50 km and gradually reduces after 15 iterations to 10 nearby events and maximum cut-off distance of 5 km. In this way the events are initially relocated by comparing them in clusters with a large number of nearby events and gradually they are sorted into smaller clusters. For a general receiver-event cut-off range of 100 km, 30664 events were relocated using SSST. These locations were used as input into the waveform cross-correlation technique described below.

The waveforms for 16746 events were low–pass filtered at 10 Hz, as it is generally found that the waveform cross-correlation is more stable at lower frequencies (e.g. Shearer, 1997). Cross-correlating the n waveforms for all possible source–event pairs would result to $n(n-1)/2$ applications per phase per station, which is over a million cross-correlation calculations. To avoid unnecessary computational cost we choose to cross-correlate events that are close to each other, as they are the possible candidates that will cross-correlate well. Similarly to the SSST relocation, we apply the Delaney tessellation and nearest neighbour technique (e.g. Astiz et al., 2000) limiting the cross-correlation to the 100 closest neighbours of each event. This will reduce the cross-correlation applications to $100n/2$ per phase per station. The cross-correlation functions were computed for windows of 3 s and 4 s around the picked arrival time, for P and S waves respectively, and the results were saved only for event pairs received in at least 10 individual stations with crosscorrellation coefficient higher than 0.5.

The grouping of closely spaced events into clusters with correlation coefficients higher than 0.55 follows. Two different clusters with n and m events, respectively, may correlate well to each other for only some events. To avoid merging these two clusters into one we define a threshold number of possible connections between the events of the two groups. For merging of two clusters into one, it is required that more than 5% of the nm possible connections between them have a correlation coefficient greater than 0.55. With this procedure we obtain 843 clusters in the study area and the events within each cluster are relocated relative to the average position of the cluster, producing 5199 relatively relocated events.

5.5 Location uncertainty estimation

Although true earthquake locations are unknown, it is obvious that some events will be better located than others. The absolute location accuracy is associated with assumptions made for the velocity structure of the area. Thus, we can estimate the variations in the event locations having used different reference 1D velocity models for the SSST relocation. Using the four applied velocity models in the SSST relocation (see section 5.2.3 and Fig. 5.1), which represent a wide

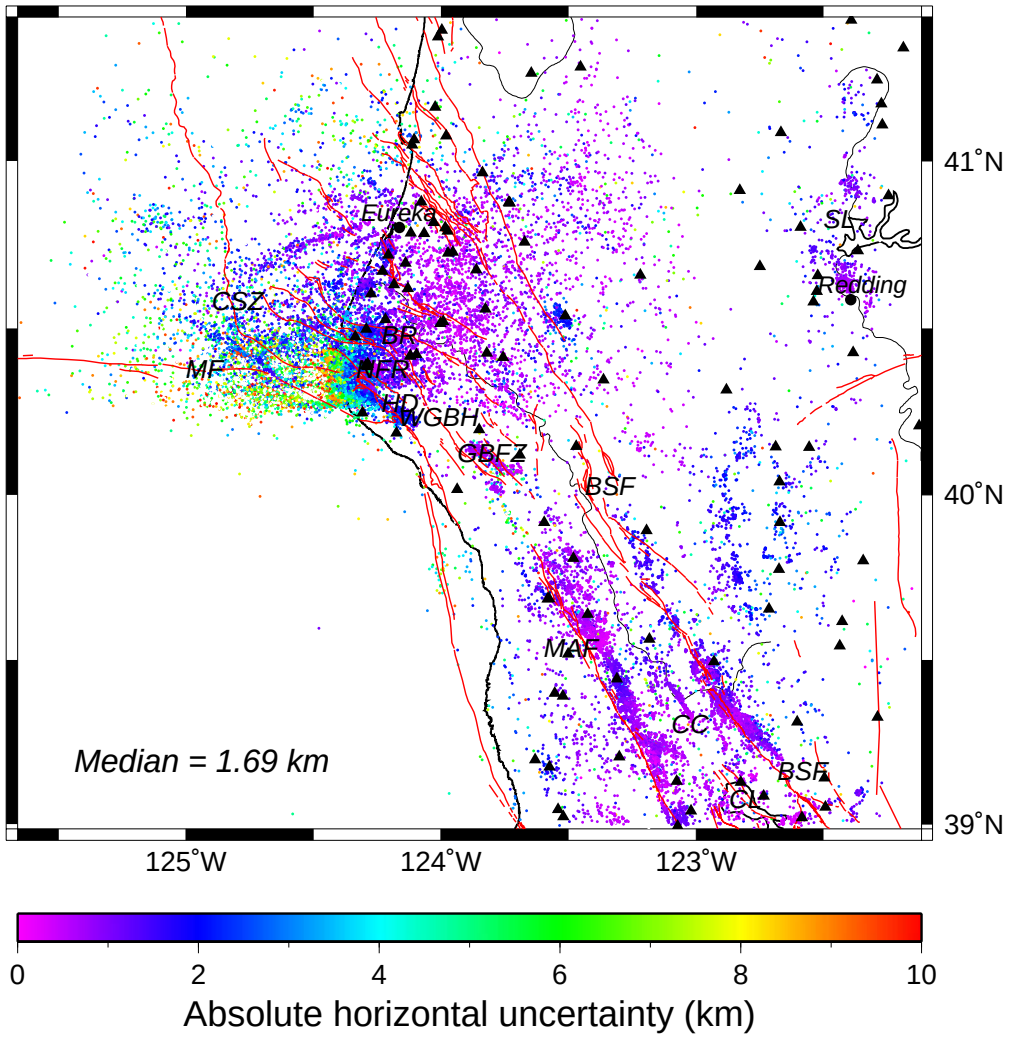

Figure 5.3: Absolute lateral uncertainties calculated from the scattering of locations when the four different velocity models of Fig. 5.1 are used. Black triangles mark stations, within study area, that recorded the events. Red lines mark the quaternary faults from USGS. CSZ: Cascadia Subduction Zone, MF: Mendocino Fault, WGBH: Whale Gulch–Bear Harbour fault zone, HD: Honeydew fault system, NFR: North Fork Road thrust system, BR: Bear River fault zone, CL: Clear Lake, MAF: Maacama fault zone, BSF: Barlett Springs fault zone, CC: Cloverdale cluster, SL: Shasta Lake, GBFZ: Gaberville–Briceland fault zone.

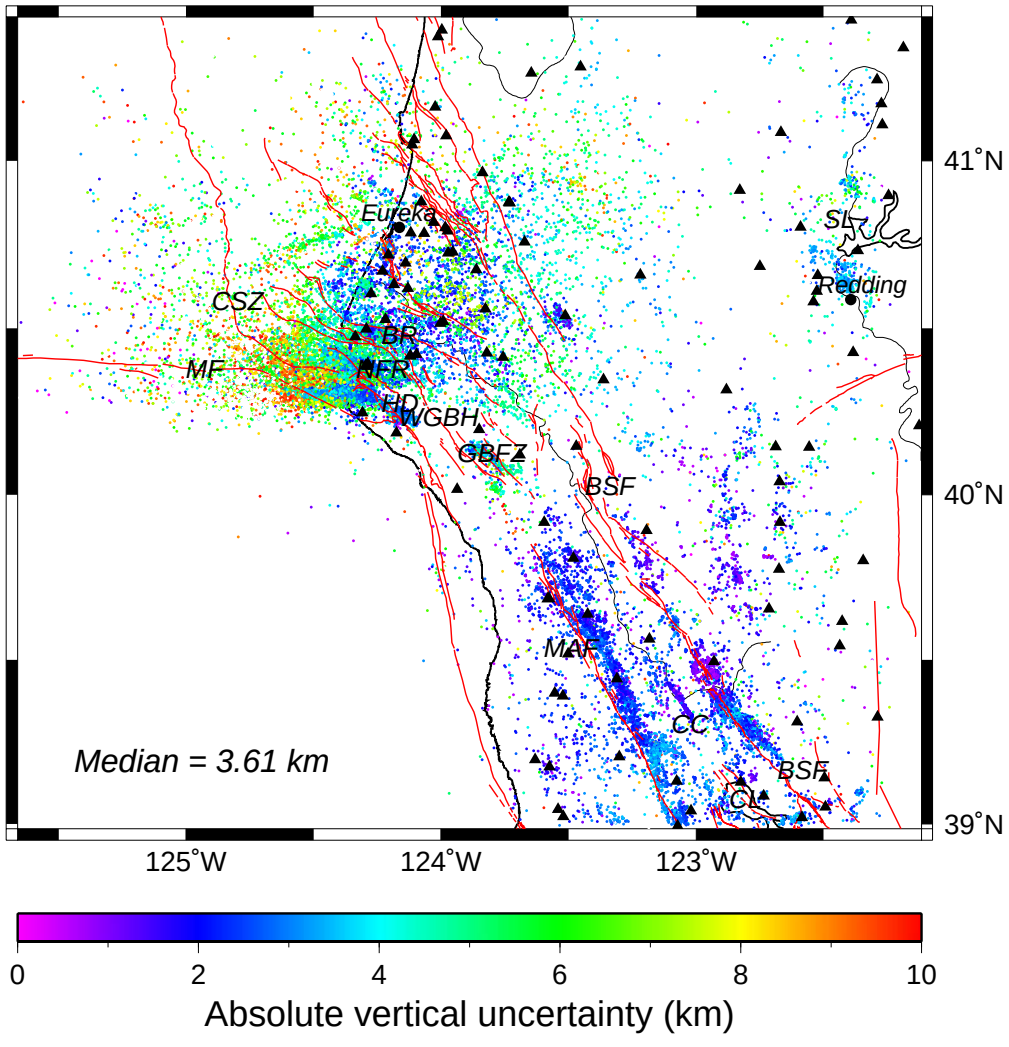

Figure 5.4: Absolute vertical uncertainties calculated from scattering of the locations when the four different velocity models of Fig. 5.1 are used. Black triangles mark stations, within study area, that recorded the events. Red lines mark the quaternary faults from USGS. CSZ: Cascadia Subduction Zone, MF: Mendocino Fault, WGBH: Whale Gulch–Bear Harbour fault zone, HD: Honeydew fault system, NFR: North Fork Road thrust system, BR: Bear River fault zone, CL: Clear Lake, MAF: Maacama fault zone, BSF: Barlett Springs fault zone, CC: Cloverdale cluster, SL: Shasta Lake, GBFZ: Gaberville–Briceland fault zone.

range of possible crustal models for the area, we estimate the mean position for each event and the standard horizontal and vertical deviation from this (Fig. 5.3 and 5.4).

These deviations represent how much each event position can change by using velocity profiles that do not represent the structure of the area. In reality, since the general velocity structure is well known from the tomography experiment, each of the used velocity profiles is not expected to perturb significantly. Therefore, the calculated horizontal and vertical deviation for each event represent

	No. events	±x, km	±z, km
Absolute estimation	30664	1.6	3.5
Relative estimation	5199	0.19	0.17

Table 5.1: Median absolute and relative standard errors in relocation

uncertainties that do not take into account a priori information for the velocity structure of the area and assume that it is unknown. Since these uncertainties represent the maximum expected errors, rather than discuss their absolute values, we describe mainly their differences between areas. In general, horizontal and vertical uncertainties are less in land areas that are well surrounded by stations, like the Maacama and Barlett Stream strike slip area, than areas offshore of Cape Mendocino and Eureka (Fig. 5.3 and 5.4). It is likely that the application of SSST relocation for events that are surrounded by stations will account for changes in the 3D velocity structure, whereas an SSST correction for events offshore may tend to introduce a systematic error/shift to all stations recording the events, without affecting the general residual fit. Although uncertainties are generally higher offshore they become larger west of Cape Mendocino where the interaction of the three lithospheric plates produces very strong lateral velocity variations. Another observable trend is the tendency of greater vertical errors for deeper events associated with the Gorda thrust (Fig. 5.4). The median absolute lateral uncertainty is 1.6 km and the vertical uncertainty is 3.5 km.

To estimate relative location uncertainties within each cluster during the Waveform Crosscorrelation relocation we applied a bootstrap approach in which we invert for the relative locations by applying random weighting to the differential traveltime data (see section 5.2.3). This method is based on the bootstrap approach of Billings et al. (1994) and Shearer (1997) in which random picking errors are added to the traveltime picks and the event are relocated multiple times to account for the location scattering due to uncertainties in the picks. We apply this random weighting in the inversion modelling and repeat the procedure 200 times to obtain a cloud of scattered locations for each event. The standard deviation from each mean event position will be then a relative error estimate. The WCC relocation is performed using as input event locations these obtained from SSST for all four velocity models. The median relative uncertainties are between 165 and 220 m laterally and between 135 and 200 m vertically. Table 5.1 summarises the location uncertainties.

5.6 Results–Discussion

5.6.1 Around Cape Mendocino

The catalogue locations reveal two big clusters of events at different depths. The first shallower cluster (Fig. 5.5 a), centered around 10–15 km depth, with subparallel directions to the mapped quaternary faults, whereas the deepest cluster (Fig. 5.6 a), centered further westwards at around 20–30 km depth, in a subparallel direction to the Mendocino fault and the southern edge of the subducted Gorda slab (Castillo & Ellsworth, 1993). Focal mechanisms of the seismicity offshore Cape Mendocino reveal left-lateral motion on steep northeast-oriented faults (Oppenheimer et al., 1993) associated with convergence between the Gorda and Pacific plates (Fig. 5.6 a).

Events in the area relocated with SSST and WCC show, in general, greater clustering and better alignment (Fig. 5.5 b,c and Fig. 5.6 b,c). Most of the shallow events southeast of Punta Gorda (PG) are concentrated in a double subparallel zone which possibly reveals the Whale Gulch – Bear Harbour fault zone (WGBH) and an unnamed fault zone slightly north (Fig. 5.5 b,c). The events are concentrated in two zones each ∼1 km in width and 5 km apart, centred at 10 km depth and dipping NE (Fig. 5.7.1). Moving to the northeast there is a very high concentration of events associated with the North Fork Road thrust system (NFR) or the Honeydew fault zone (HD) and/or unmapped faults extending offshore (Fig. 5.5 b,c). A cross-section through these clusters separates all these shallow North America events from deeper ones centred at 25 km depth (Fig. 5.7.2). In the north the Bear River fault zone (BR) seems to be active only in a small segment trending NW–SE (Fig. 5.5 b), since all other events in the area are located deeper (Fig. 5.6 b), related possibly to subduction processes.

Figure 5.5: (Next page) Locations of earthquakes around Cape Mendocino at less than 15 km depth. Colours show hypocentral depths. Red lines mark the quaternary faults as published from USGS. Solid black lines 1 and 2 show the position of the vertical cross-sections in Figure 5.7. Wiggled black solid lines mark the coastline and Eel River.(a) NCSN catalogue locations of the events that were relocated. Focal mechanisms of events occurred between 15 and 40 km depth and with $M > 4$ are shown. (b) Events relocated using SSST and WCC. (c) Events relocated using only WCC. CSZ: Cascadia Subduction Zone, MF: Mendocino Fault, WGBH: Whale Gulch–Bear Harbour fault zone, HD: Honeydew fault system, NFR: North Fork Road thrust system, BR: Bear River fault zone, CM: Cape Mendocino, PG: Punta Gorda.

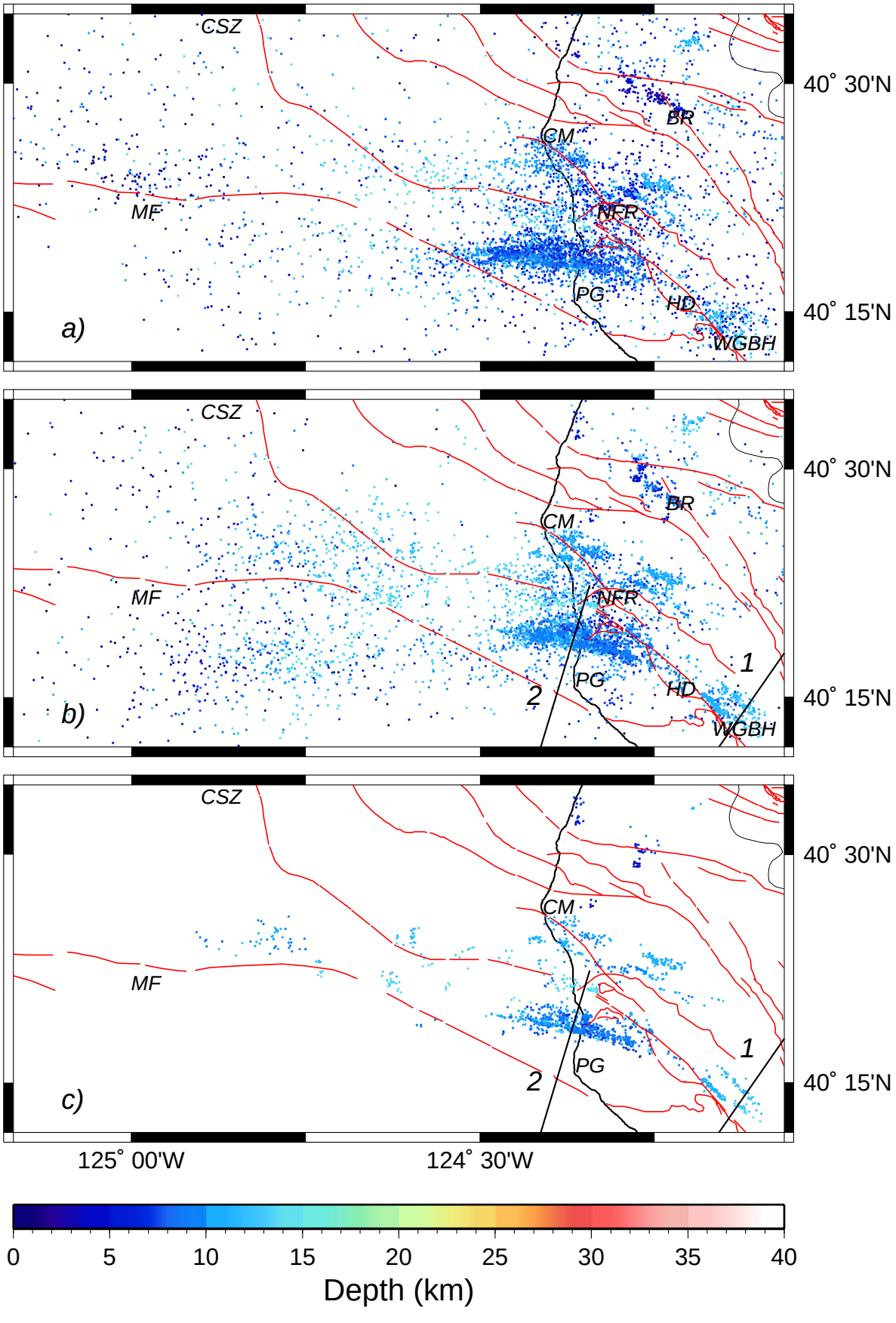
CSZ
MF
CM
BR
NFR
PG
HD
WGBH
1
2
a)
b)
c)
40˚ 30'N
40˚ 15'N
125˚ 00'W
124˚ 30'W
0
5
10
15
20
25
30
35
40
Depth (km)

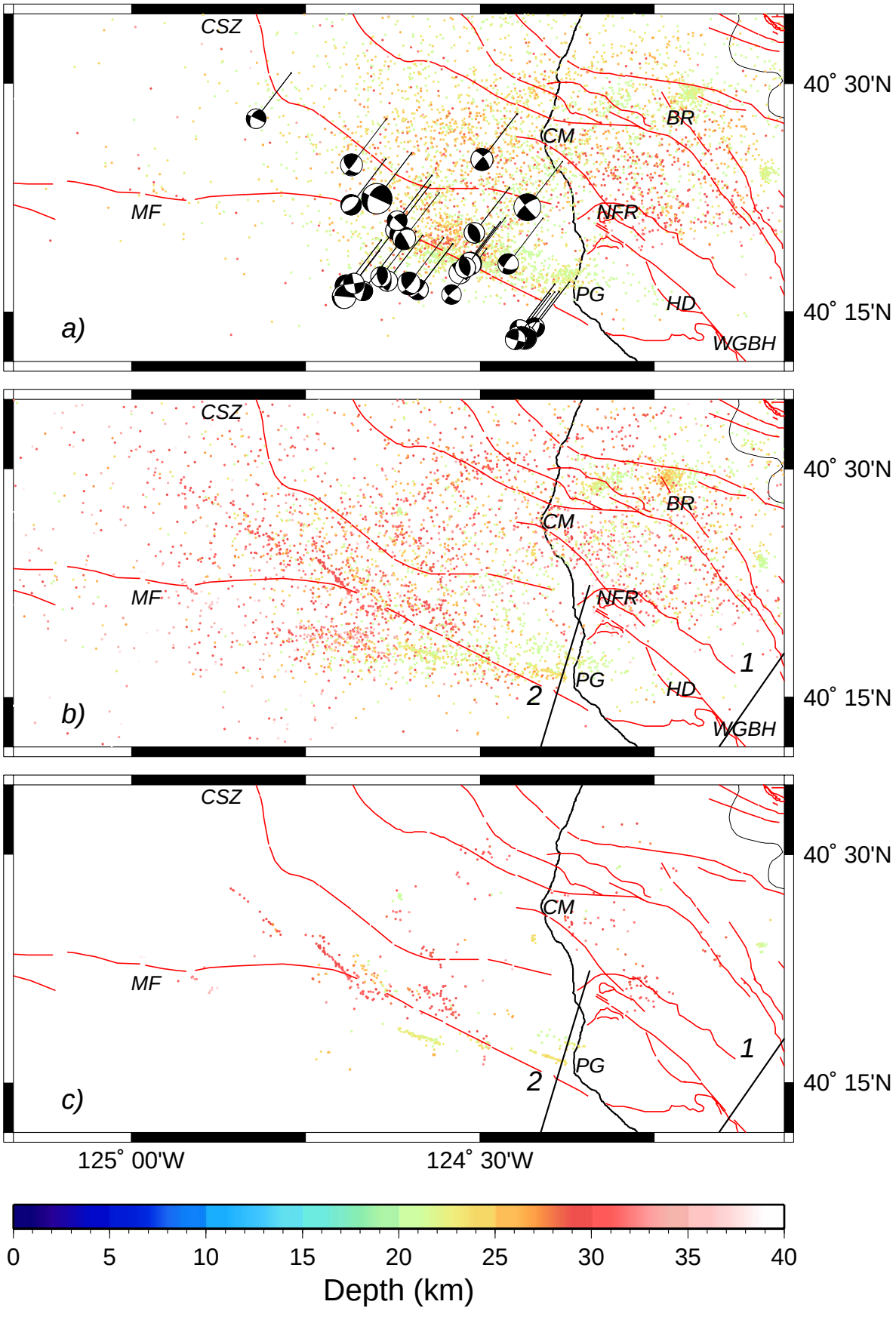
CSZ
MF
CM
BR
NFR
PG
HD
WGBH
a)
b)
c)
1
2
40˚ 30'N
40˚ 15'N
125˚ 00'W
124˚ 30'W
0
5
10
15
20
25
30
35
40
Depth (km)

Figure 5.6: (Previous page) Locations of earthquakes around Cape Mendocino at more than 15 km depth. Marked symbols and features are the same as in Fig. 5.5.

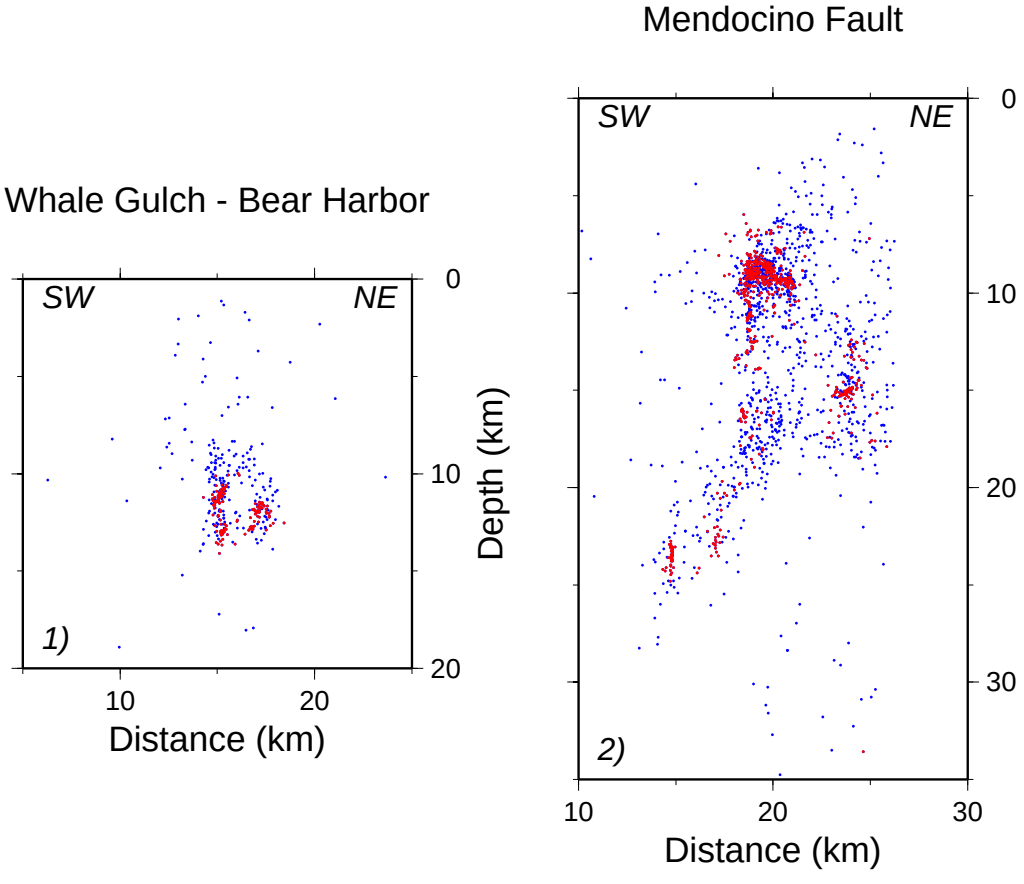

Figure 5.7: Vertical SW–NE cross-sections through the Mendocino Triple Junction area. Red dots mark events relocated with the additional use of WCC and blue dots mark all the relocated events. (1) Cross-section trough Whale Gulch – Bear Harbour fault zone. Cross-sections sample events from a 6 km thick lateral zone along the profiles. (2) Cross-section through the Mendocino fault zone and the North Fork Road thrust system. Cross-sections sample events from a 10 km thick lateral zone along the profiles.

West of Punta Gorda (PG) the WCC relocated events near the Mendocino Fault Zone show a WNW–ESE alignment (Fig. 5.6 c) between 15 and 25 km depth. Events along this alignment do not show a significant evolution through time and appear to be active simultaneously. A cross-section through this alignment reveal near vertical clusters at around 20–25 km depth, with a possible southwards dip (Fig. 5.7.2). We associate these clusters with the boundary between the subducting Gorda and the Pacific plate.

Further offshore and northwards, in the wedge between the Mendocino fault (MF) and the subduction trench (CSZ), a NW–SE alignment of deep events (20–35 km) is now clear (Fig. 5.6 b,c), with a tendency of deeper events to occur towards the south. These locations are associated with the interaction of the

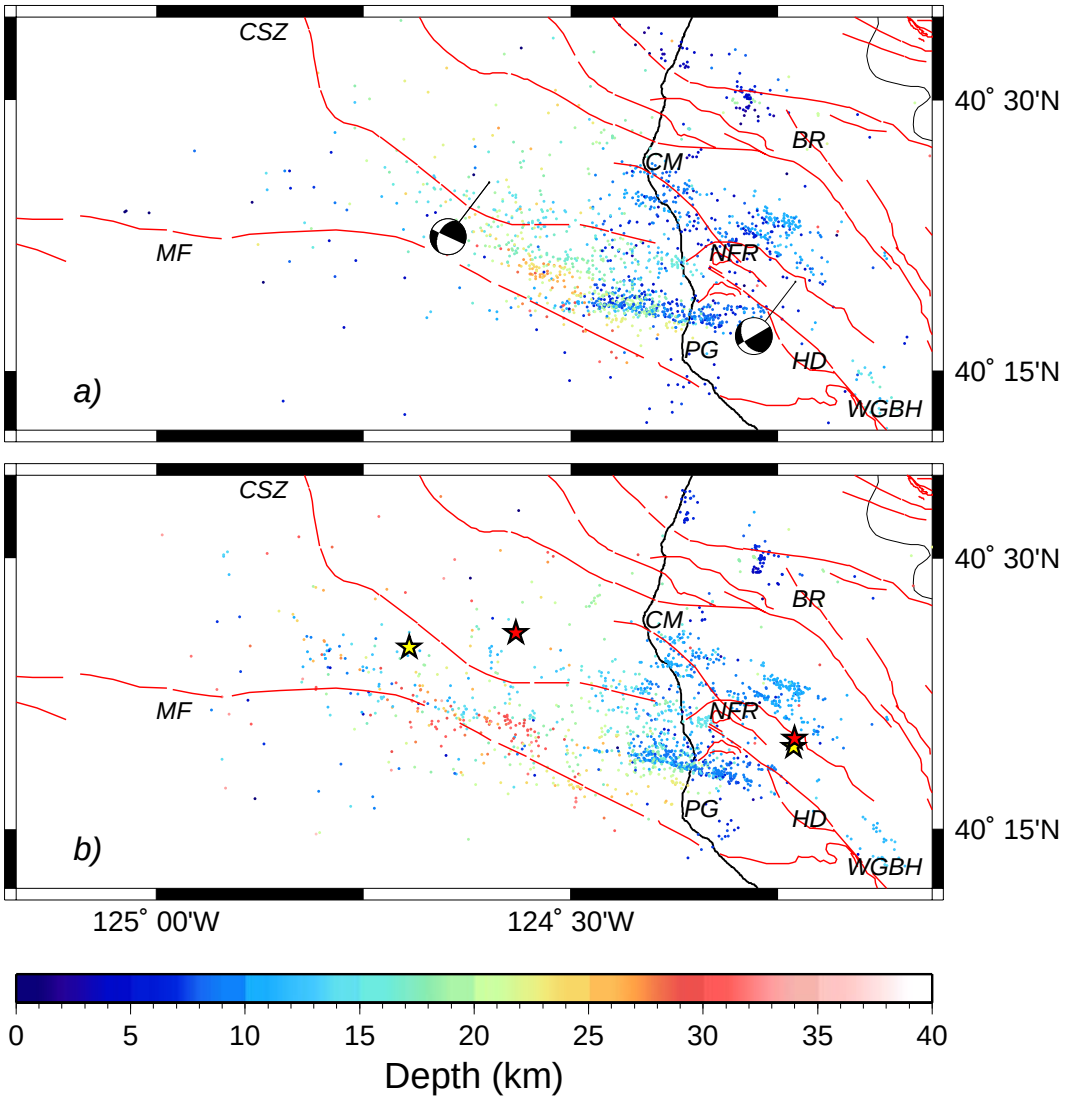

Figure 5.8: Locations of the Petrolia event and aftershocks for 25 April 1992 to 30 September 1992. Red lines mark the quaternary faults as published from USGS. Wiggled black solid lines mark the coastline and Eel River.(a) NCSN catalogue locations of the 1992 Petrolia aftershocks. Focal mechanism of the Petrolia event and its first main aftershock to the west is plotted. (b) Events relocated using SSST and WCC. Red stars mark the NCSN positions of the Petrolia event and its first main aftershock to the west, and yellow stars the relocated positions of the same events. CSZ: Cascadia Subduction Zone, MF: Mendocino Fault, WGBH: Whale Gulch–Bear Harbour fault zone, HD: Honeydew fault system, NFR: North Fork Road thrust system, BR: Bear River fault zone, CM: Cape Mendocino, PG: Punta Gorda.

subducting Gorda plate with the rigid Pacific plate and its possible fragmentation (e.g., Henstock & Levander, 2003).

Finally we relocate the main Petrolia event on 25/04/92 on roughly the same epicentre but 2 km deeper in the crust at 12.3 km. Its first aftershock is positioned further westwards at 21.6 km depth, and belongs possibly to the WNW-ESE cluster between MF and CSZ (Fig. 5.8 b and Fig. 5.6 b). The horizontal distance of 14.4 km between the NCSN and our location is higher than its calculated 10.7 km maximum horizontal uncertainty (see section 5.5). In general the shallow relocated aftershocks for 25 April 1992 to 30 September 1992 are concentrated in a rectangular area between Punta Gorda and Cape Mendocino and mainly westwards from the main event. Aftershocks tend also to concentrate along a WNW–ESE alignment offshore (Fig. 5.8 b) north of but parallel to the cluster associated with the southernmost Mendocino Fault Zone seismicity.

5.6.2 South-East Gorda Plate – Offshore Eureka

Earthquake catalogue locations offshore Eureka, northwest of Cape Mendocino are quite scattered with very shallow hypocentre locations to the west of the CSZ (Fig. 5.9 a). This is the result of poor station coverage, as offshore earthquakes are received only at stations on land. In addition, velocity models that represent mainly continental crust have been assumed for this area (Fig. 5.1). The strong lateral velocity changes from the oceanic crust in the west to the subduction regime and finally to the continental crust to the east, where all the stations are based, meant that the relocation with SSST was ineffective, and event locations were only slightly improved. Furthermore, due to the non-uniform station coverage and the relatively small number of events the waveform cross-correlation method relocates only a few events.

Despite all the relocation difficulties, a group of events west of Eureka is now visible along a northeast-southwest lineation at ∼20–30 km depth (Fig. 5.9 b). Focal mechanisms of events occurring between 20 and 40 km depth, show a NE–

Figure 5.9: (Next page) Locations of earthquakes offshore Eureka. Colours show hypocentral depths. Red lines mark the quaternary faults as published from USGS. Solid black line show the position of the vertical cross-sections in Figure 5.10. Wiggled black solid lines mark the coastline and Eel River. (a) NCSN catalogue locations of the events that were relocated. Focal mechanisms of events occurred between 15 and 30 km depth and with $M > 3$ are shown. (b) Events relocated using SSST and WCC. CSZ: Cascadia subduction zone.

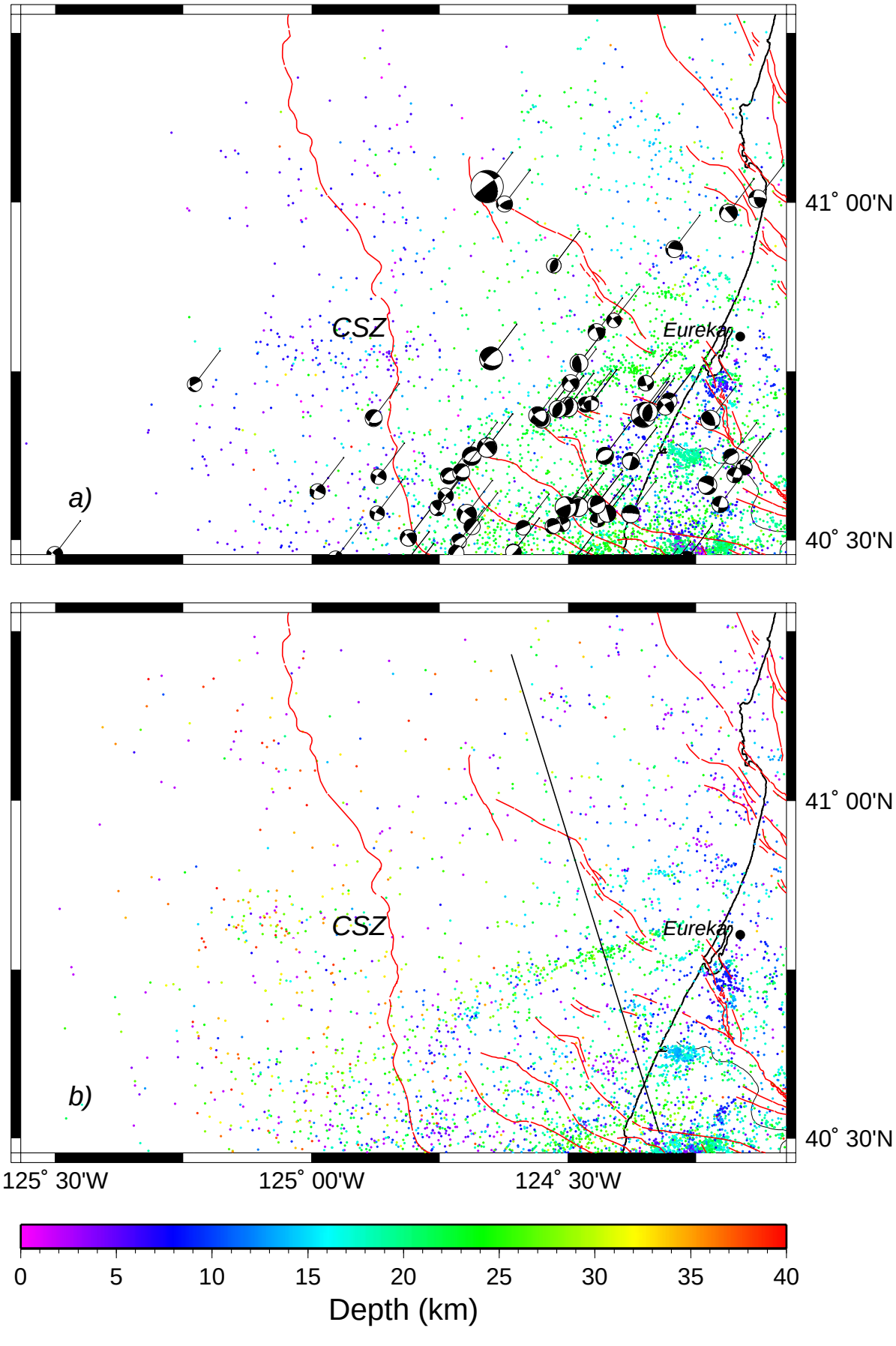
CSZ
Eureka
a)
41˚ 00'N
40˚ 30'N
CSZ
Eureka
b)
41˚ 00'N
40˚ 30'N
125˚ 30'W
125˚ 00'W
124˚ 30'W
0
5
10
15
20
25
30
35
40
Depth (km)

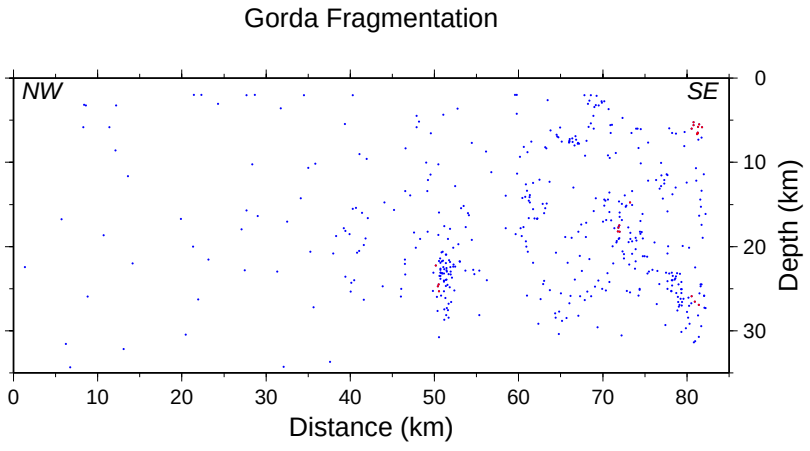

Figure 5.10: Vertical NW–SE cross-section through the subducting Gorda plate and the overlying accretionary prism. Red dots mark events relocated with the additional use of WCC and blue dots mark all the relocated events. The cross-section sample events from a 10 km thick lateral zone along the profile. The velocity profile at 450/330 km in Fig. 4.29 cuts through the same region in the tomography model, revealing that events deeper than 20 km are well within the subducting Gorda plate.

SW trend which is in contrast with the NW–SE oriented quaternary faults on the overlying accretionary prism (Fig. 5.9 a). We suggest that this group of events, located well within the subducting Gorda slab, represents the deformation of the southern part of the slab across left lateral strike slip faults; this supports Gulick et al. (2001), who suggested decoupling of the subducted slab from the North American accretionary prism. A NW–SE vertical cross-section shows this group of events below 20 km depth, at around 50 km offset, and suggests a high-angle fault plane (Fig. 5.10).

5.6.3 From Maacama to Barlett Springs fault zone

Catalogue locations north of Clear Lake are mainly distributed along the north section of the Maacama fault zone to the west and the Barlett Springs fault zone to the east (Fig. 5.11 a). Focal mechanisms of events occurred between 8 and 15 km depth, show near vertical fault planes with a NNW–SSE trend. Relocated events with SSST and WCC show greater clustering and better alignments along the same two major fault zones. Events in the Maacama fault zone are concentrated in a shallow zone of 6–7 km and with maximum depth ∼10 km. Barlett Springs relocated events are concentrated in a narrow lateral band but they extend almost

twice as deep (12–14 km) as the Maacama events. The eastward dipping fault plane is now clear from cross-sections (Fig. 5.12.3), as well as from concentration of NW-SE parallel alignments of similar depth events with increasing alignments depth towards the east (Fig. 5.11 c).

Another cluster of events, visible in both the catalogue locations and the relocations, is centred between the two major fault zones but not associated with any quaternary USGS mapped faults (Fig. 5.11). This cluster of events, called the Cloverdale cluster (USGS: http://quake.wr.usgs.gov/recent/reports/clover/), had a first swarm of events on April and May 2000 and remains active since. A vertical cross-section along the NW–SE strike (Fig. 5.12.4) reveals two major groups of events with the first occurring on April–May 2000 and the second ∼5 months later with hypocentres deeper to the south. More recent events move back shallower, northwards. A cross-section perpendicular to the cluster (Fig. 5.12.2) shows a near vertical fault plane. Although Castillo & Ellsworth (1993) suggested that near vertical fault planes in the strike slip system of Northern California represent mature faults, the Cloverdale swarms appear to have originated from a fault system with little recent activity.

5.6.4 East of Cape Mendocino to Lake Shasta

The continental region east of Cape Mendocino shows occurrence of events mainly in the west close to the coast (Fig. 5.13 and 5.14). Relocation with SSST shows better cluster alignments but only a few events could be relocated with WCC. Relocated events may be distinguished in two major groups. The first group at shallow depths relates with the quaternary faults to the west (Fig. 5.13). A vertical cross-section across the Garberville–Briceland fault zone shows a group of events occurring between 15–20 km depth in near vertical fault planes (Fig. 5.15). On the other hand, deeper earthquakes, at 20–40 km depth (Fig. 5.14), are mainly observed north of 40°15′S and east of 123°00′W and we spec-

Figure 5.11: (Next page) Locations of earthquakes north of Clear Lake. Colours show hypocentral depths and red lines mark the quaternary faults from USGS. Solid black line 1, 2, 3 and 4 show the position of the vertical cross-sections of Figure 5.12. Wiggled black solid lines mark the coastline, Eel River, and Clear Lake. (a) NCSN catalogue locations of the events that were relocated. Focal mechanisms of events occurred between 8 and 15 km depth and with $M > 3$ are shown. (b) Events relocated using SSST and WCC. (c) Events relocated using only WCC. CL: Clear Lake, MAF: Maacama fault zone, BSF: Barlett Springs fault zone, CC: Cloverdale cluster.

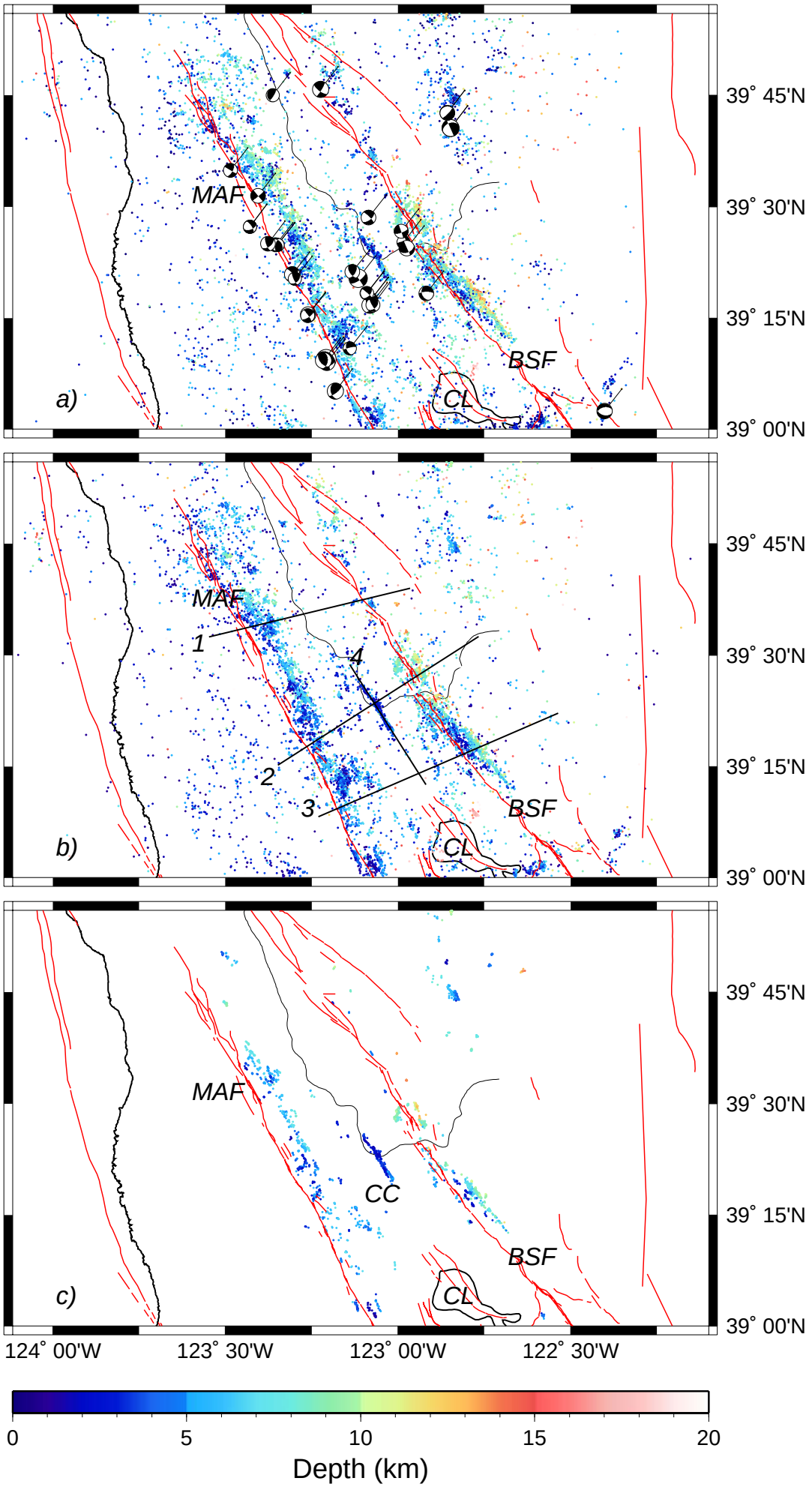
39˚ 45'N
39˚ 30'N
39˚ 15'N
39˚ 00'N
MAF
BSF
CL
a)
1
2
3
4
b)
CC
c)
124˚ 00'W
123˚ 30'W
123˚ 00'W
122˚ 30'W
0
5
10
15
20
Depth (km)

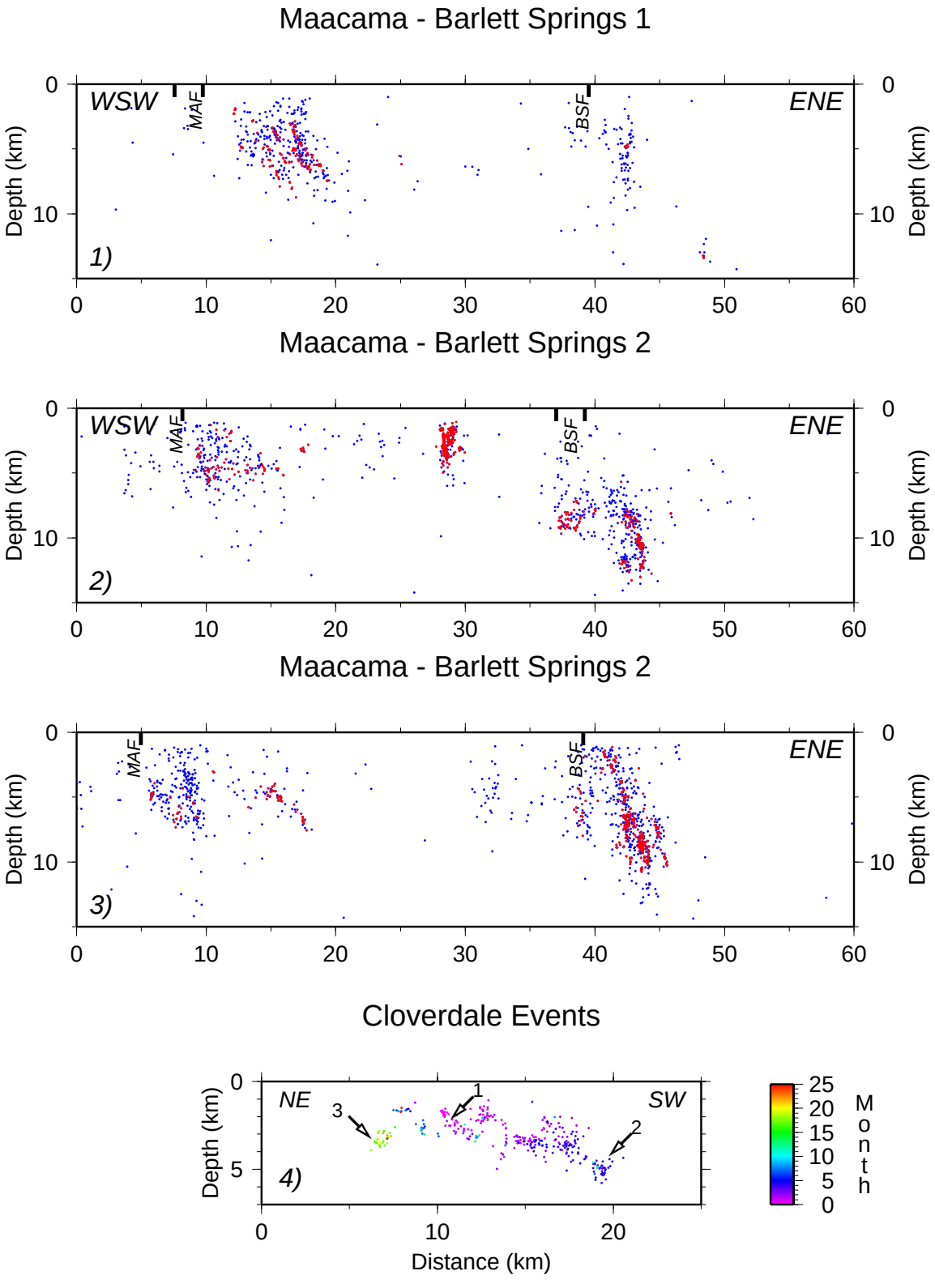
Maacama - Barlett Springs 1
WSW
ENE
MAF
BSF
1)
Depth (km)
0
10
0
10
20
30
40
50
60
Maacama - Barlett Springs 2
2)
Maacama - Barlett Springs 2
3)
Cloverdale Events
NE
SW
1
2
3
4)
5
Distance (km)
25
20
15
10
5
0
Month

Figure 5.12: (Previous page) (1–2–3) Vertical WSW–ENE cross-sections through the Maacama and Barlett Springs fault zones. Red dots mark events relocated with the additional use of WCC and blue dots mark all the relocated events. Cross-sections sample events from a 10 km thick lateral zone along the profiles. The traces of the mapped Maacama (MAF) and Barlett Springs (BSF) faults on surface are marked. (4) Cross-section along strike of the Cloverdale cluster. Different colours mark month of occurrence after the first recorded event on April 2000. Arrows mark three swarms occurring at different times in chronological order. The cross-section samples a 4 km thick lateral zone.

ulate that these are related to the subduction of the Gorda slab beneath North America. The second deeper cluster in the cross-section beneath Garberville–Briceland fault zone can be associated with the southernmost edge of the Gorda slab (Fig. 5.15) and is probably not related to the surface fault zone (McLaughlin et al., 2000). A third group of events is also observable near Lake Shasta and Redding with a cluster depth at around 25 km and within the North American plate above the depth where it is believed that the Gorda plate is subducting (see http://www.seismo.berkeley.edu/seismo/eqw/98.11.26.faq.html). Very shallow events in the area are possibly related to water releases from dams in the vicinity of Redding.

Figure 5.13: (Next page) Locations of earthquakes east of Cape Mendocino to Lake Shasta, with a maximum depth of 20 km. Colours show hypocentral depths. Red lines mark the quaternary faults. Solid black line shows the position of the vertical cross-section of Figure 5.15. Wiggled black lines mark the coastline, Eel and Sacramento rivers, and Shasta lake. (a) NCSN catalogue locations of the events that were relocated. (b) Events relocated using SSST and WCC. SL: Shasta Lake, GBFZ: Gaberville–Briceland fault zone, BSF: Barlett Springs fault zone.

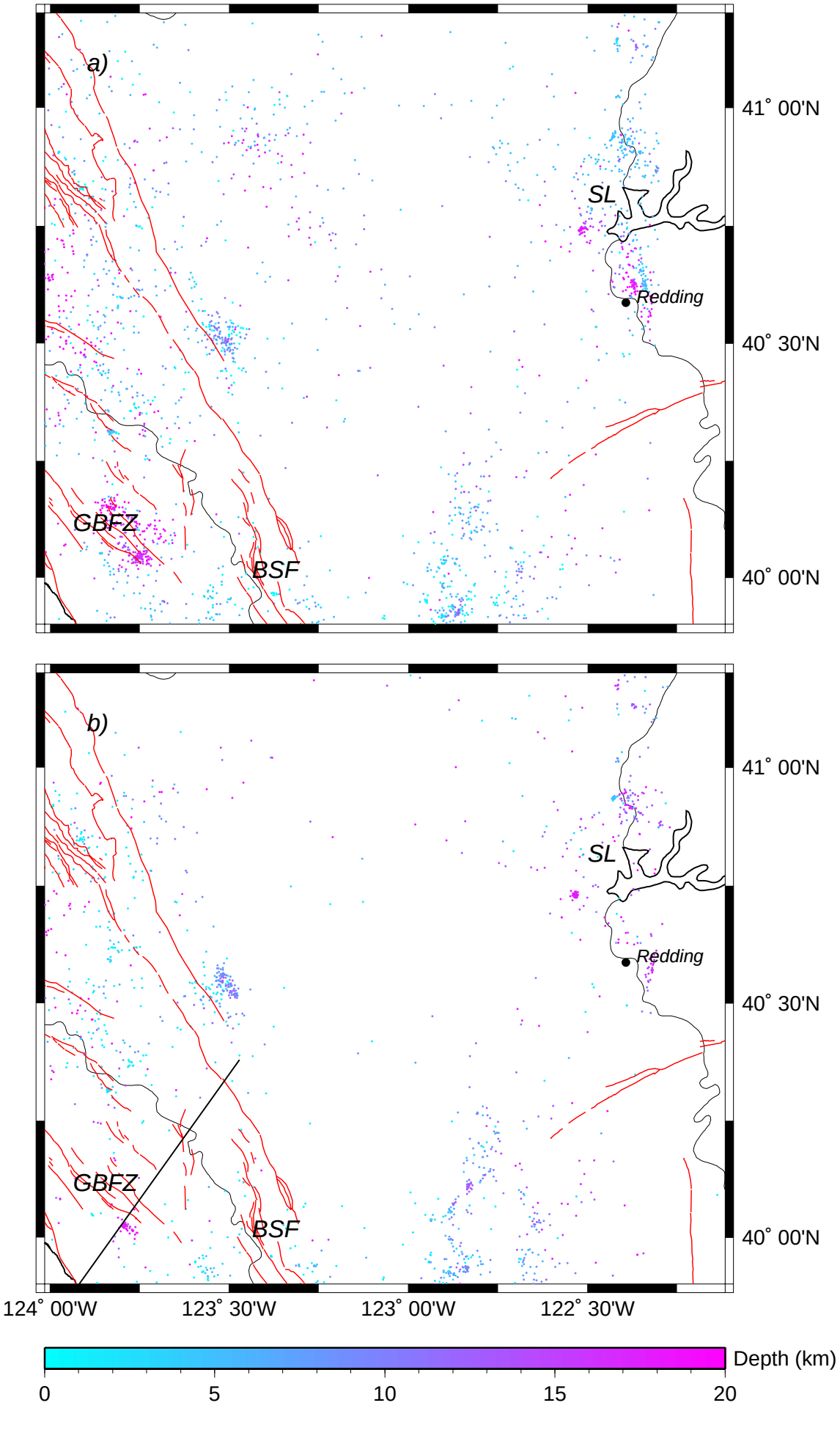
a)
b)
SL
Redding
GBFZ
BSF
41˚ 00'N
40˚ 30'N
40˚ 00'N
124˚ 00'W
123˚ 30'W
123˚ 00'W
122˚ 30'W
Depth (km)
0
5
10
15
20

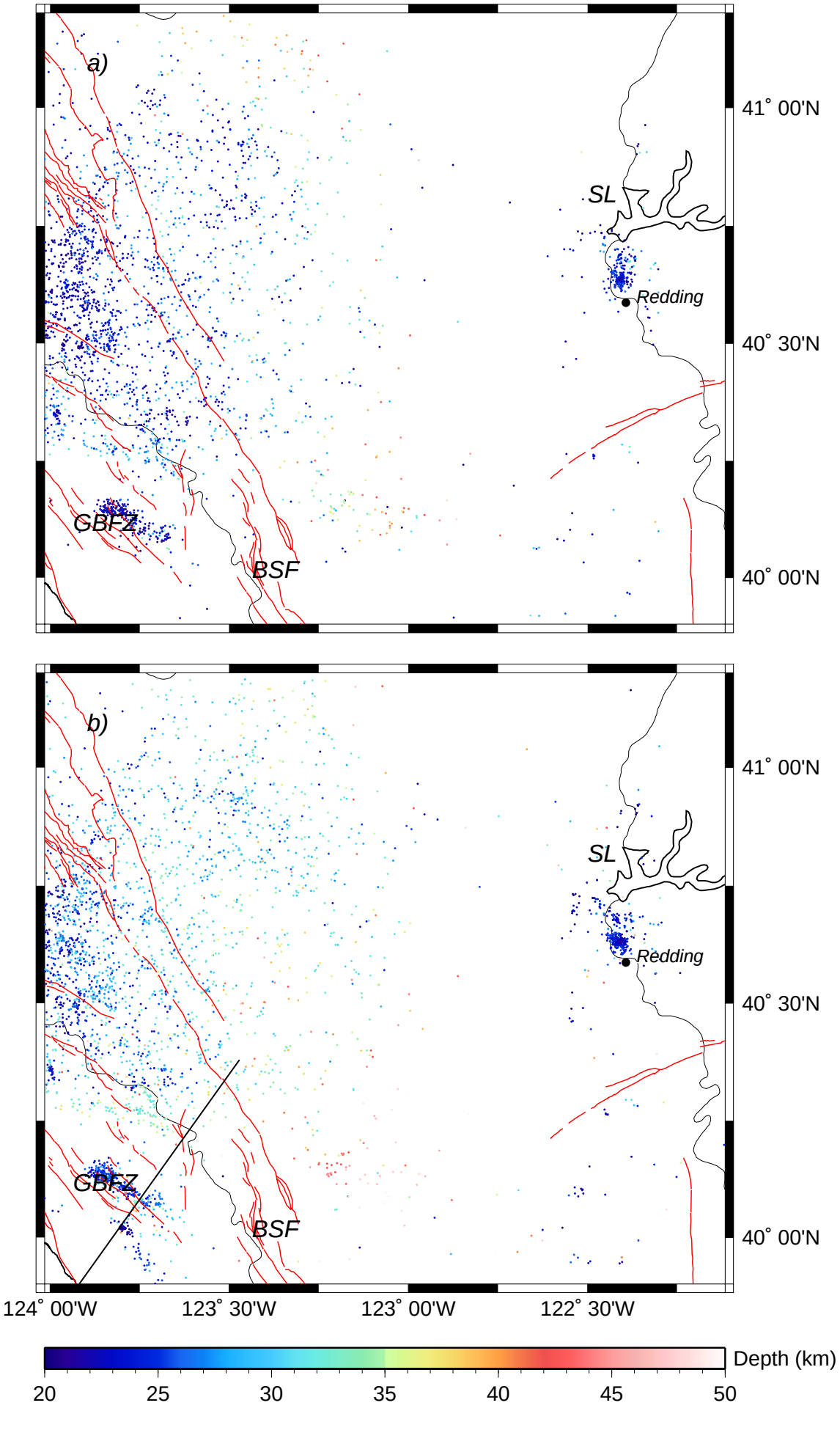
a)
b)
SL
Redding
GBFZ
BSF
41˚ 00'N
40˚ 30'N
40˚ 00'N
124˚ 00'W
123˚ 30'W
123˚ 00'W
122˚ 30'W
Depth (km)
20
25
30
35
40
45
50

Figure 5.14: (Previous page) Locations of earthquakes, between 20 and 50 km depth, east of Cape Mendocino to Lake Shasta. Colours show hypocentral depths. Red lines mark the quaternary faults. Solid black line shows the position of the vertical cross-section of Figure 5.15. Wiggled black lines mark the coastline, Eel and Sacramento rivers, and Shasta lake. (a) NCSN catalogue locations of the events that were relocated. (b) Events relocated using SSST and WCC. SL: Shasta Lake, GBFZ: Gaberville–Briceland fault zone, BSF: Barlett Springs fault zone.

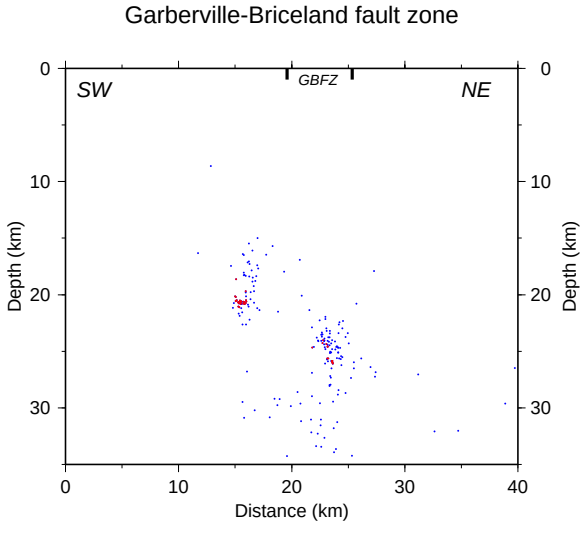

Figure 5.15: Vertical SW–NE cross-section across the Garberville–Briceland fault zone. Red dots mark events relocated with the additional use of WCC and blue dots mark all the relocated events. The cross-section samples events from a 10 km thick lateral zone. The trace of the mapped Gaberville–Briceland fault (GBFZ) on surface is marked.

5.7 Summary of relocation results

Relocation of earthquake around Mendocino Triple Junction region was performed using the Source Specific Station Term (Richards-Dinger & Shearer, 2000) and Waveform Cross-correlation (e.g. Shearer, 1997) methods. Calculated traveltimes were obtained using four average 1D velocity models from areas with different velocity structure. All these models are based on a smooth and coarse three dimensional model from active source seismic data described in Chapter 4. Absolute location uncertainties are approached by means of comparing the relocation results produced from the application of these four different velocity models. Uncertainties of events relative to each other are explored applying a bootstrap approach (e.g. Shearer, 1997) in the minimisation of the differential traveltimes during the WCC relocation.

Between Punta Gorda and Cape Mendocino events are concentrated in a shallow cluster associated with the strike slip system and a deeper one associated with the Mendocino transform fault itself. Shallow events are concentrated in steep NE dipping planes and correlate well with mapped Quaternary faults whereas deeper events show WNW–ESE active segments along the Mendocino fault with near vertical fault planes. Deep NW–SE alignments of earthquake epicentres between the Mendocino fault and the subduction zone are related with the two oceanic plates interaction and possible fragmentation of the Gorda southeast corner.

Offshore Eureka, in the northwestern part of our study area, despite the small numbers of WCC relocations, NE–SW event lineations at around 20–30 km depth are in contrast with the NW–SE mapped faults in the overlying accretionary prism giving further support to previous studies (e.g. Gulick et al., 2001) suggesting decoupling of the Gorda subducted slab from the accretionary prism.

Relocation in the area around the Maacama and Barlett Springs fault systems reveal alignments of events along these zones with eastward dipping high angle fault planes. A fault breaking evolution is also suggested from the relocated events of the Cloverdale earthquake swarm in between the two big fault systems.

Events relocated between Cape Mendocino and Lake Shasta at depths 20–40 km are associated with the subduction of the Gorda slab and map its southeast boundaries to an ESE projection of the Mendocino fault. Events are also concentrated in shallow clusters along the quaternary faults near the coast and shallow and deep events around Redding.

The combination of the relocated events with the active source 3D velocity model will provide extra information for the geodynamic evolution of the Mendo-

cino Triple Junction area.

5.8 Comparison of the 3D tomography model with relocated events

In this section a unified interpretation is made based on the tomography model results in Chapter 4 and the earthquake relocation in this Chapter. Although some of the relocated events are within unconstrained parts of the tomography model, a combined interpretation of these events and the constrained neighbouring velocity structures can give useful information for the tectonic evolution of the Mendocino Triple Junction area. On the other hand, there are aseismic areas that reveal interesting velocity features and will be discussed.

5.8.1 Strike slip system and Pacific–North America boundary

On the east side of the Pacific area, the offshore part of the San Andreas fault defines the boundary between the Pacific and the North American plate (Fig 5.16). The fault itself cuts the entire crust and offsets the top of the lower crustal layer about 5 km deeper to the east (Y=4380–4410 km, X=410–440 km, Z=15–20 km

Figure 5.16: (Next page) Simplified plate boundary model suggested from the tomography and the relocated results. Blue solid line marks the coastline and red lines the quaternary, USGS mapped, surface faults. (a) A 3D view of the Mendocino Triple junction and the plate boundaries in the area. The grey surfaces indicate the Pacific-Gorda, Pacific-North American, and Gorda-North America boundaries in a lateral direction. The 8 kms^{-1} Moho isosurface is plotted with colour and contours indicating its depth according to the colour scale on the right. The dark red ellipse represents the mafic velocities within the upper crust of the Vizcaino block. (b–c) Horizontal slices through the final velocity model at 25 and 30 km depths. Shadowed areas are not sampled by first arrivals in the forward step. The velocity scale is in km s^{-1} and each slice indicates its depth. The 6.5 kms^{-1} contour is bold and the 8 kms^{-1} is dashed. Hypocentres of relocated seismicity, described in Chapter 5, within 1 km of the profile and magnitude > 2 are shown as black dots. Green bold lines mark the plate boundaries suggested from the velocity models and the relocated events, and the green dashed line marks the extent of the Gorda plate at this depth suggested from relocated events. SAF: San Andreas fault, MTF: Mendocino Transform fault, CSZ: Cascadia subduction zone, MAF: Maacama fault zone, Barlett Springs fault zone, KR: King Range, PD: Point Delgada, CM: Cape Mendocino.

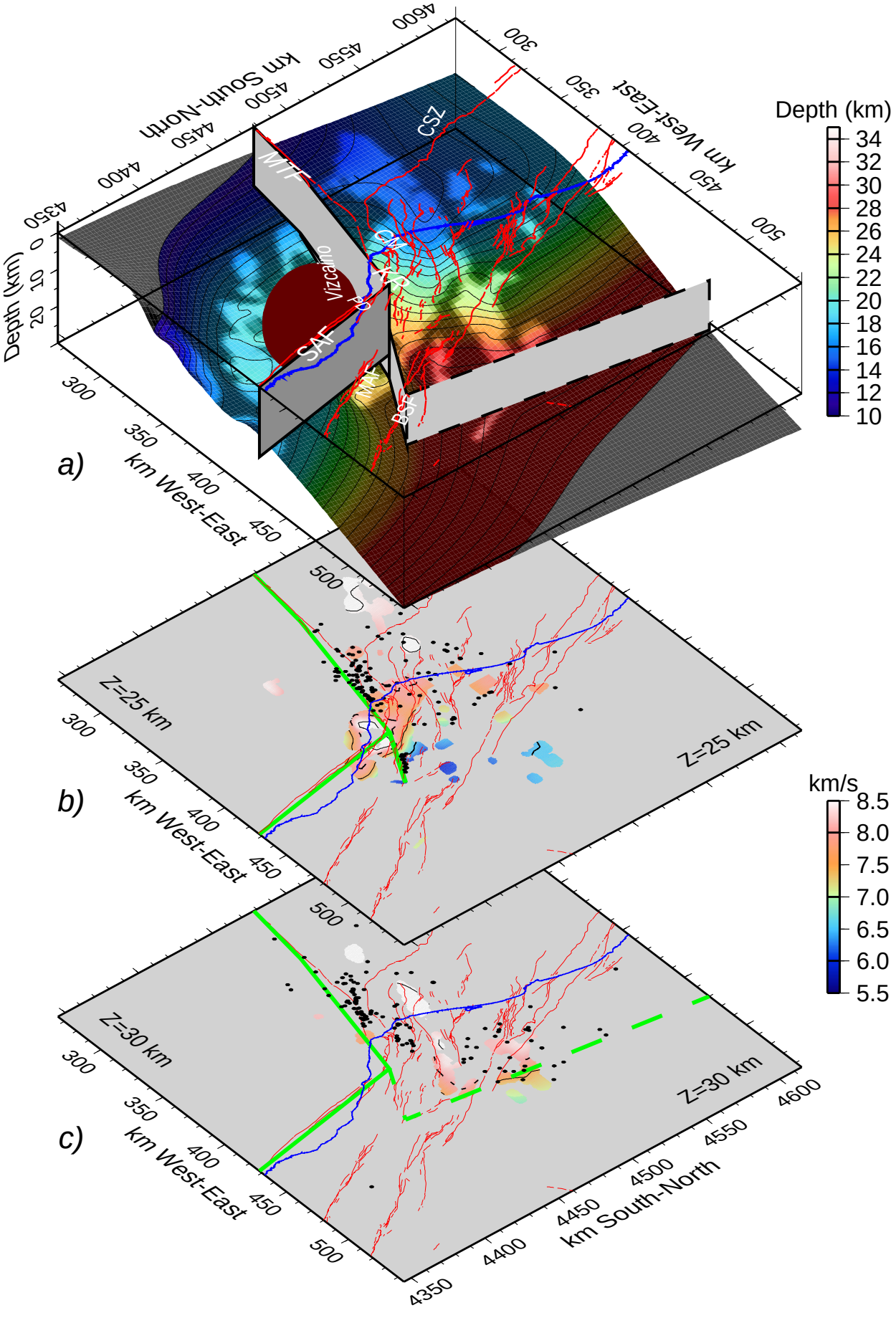
Depth (km)
34
32
30
28
26
24
22
20
18
16
14
12
10
km/s
8.5
8.0
7.5
7.0
6.5
6.0
5.5
a)
b)
c)
km West-East
km South-North
Depth (km)
Z=25 km
Z=30 km
MTF
CSZ
SAF
MAF
BSF
Vizcaino

in Fig. 4.26, 4.30). This structure was imaged by Henstock et al. (1997) in the southern part of our study area and interpreted to extend northwards (Hole et al., 1998), but is imaged in this tomography study extending from the south at 39°30'N northward up to the point where the San Andreas fault turns onshore at Point Delgada (Y=4400-4420-4440-4460 km, X=390–430 km, Z=15–19 km in Fig. 4.25, 4.27, 4.24). The San Andreas plate boundary continues then northwards beneath the King Range, onshore. Thus, we infer that the plate boundary north of Point Delgada lies onshore as was suggested by Henstock & Levander (2003), assigning the King Range as part of the Pacific plate, or as a sliver in the boundary zone. The tomography data do not show any lateral velocity change across the suggested offshore branch of SAF north of Point Delgada.

Velocities across the Maacama and Barlett Springs faults in places where most of the relocated seismicity is observed do not show any obvious strong lateral changes in the structure (X-470–500 km, Z=1-13 km in Fig. 4.27, 4.24, and 520/400 in Fig. 4.29). As the ray coverage in these areas is not very dense (see Fig. 4.20), there is also the possibility that our tomography model does not image lateral heterogeneities in these areas.

5.8.2 Gorda subduction near the triple junction

The deformation of the Gorda region, as the triple junction is approached from from the north, was imaged in both the tomography model and the earthquake relocations. Offshore and beneath the accretionary prism, NE-SW lineations of earthquake hypocentres at 20–30 km depth are correlated with lateral changes in Gorda slab velocities greater than 7.1 kms^{-1} (X=380, Y=4510, Z=22–27 in Fig. 4.27). Further south, lateral velocity changes, in a direction normal to the Gorda-Pacific relative motion, create vertical offsets as a series of velocity steps within the subducting Gorda plate, that near the triple junction affect the upper crust and cut also through the Moho. The relocated seismicity of the upper mantle is centred also in this deforming area (X=350–400 in Fig 4.28).

Close to the Mendocino Transform fault, seismicity is concentrated below 10 km depth, with some WNW-ENE alignments between 15–25 km depth and almost vertical fault planes (X=350-390, Y=4460 in Fig. 4.27 and 430/310 km in Fig. 4.29). This seismicity is almost entirely accommodated within the southernmost part of Gorda and there is no sign in the tomography model of Gorda subduction beneath the Pacific plate.

Although the surface seismicity correlates well with the north-facing escarp-

ment of the Mendocino fracture zone and the onshore North Fork Road thrust system, deeper earthquakes are located further south in an offshore extension of the King Range thrust zone on the northern border of the obducted King Range terrane (Z=10–25 km, X=350–390 km, Y=4560 km in Fig. 4.27 and 5.16). The deep offshore events align with the northern edges of the King Range high velocities (e.g. Z=25 km, X=390–420 km, Y=4420–4460 km in Fig. 4.24 and 5.16–b), and onshore events at the same depths beneath the Garberville-Briceland fault zone (e.g. Z=23–25 km, X=430 km, Y=4440 km in Fig. 4.24 and 5.16–b). Results from the P_g velocity model at 17—18 km depth show an arc-shaped velocity structure that is also bounded in the north by this seismicity (Fig. 4.33).

All these results, together with observations of discontinuous upper crust and Moho reflectors by Gulick et al. (1998) and Henstock & Levander (2003), and mapped basement faults by Gulick et al. (2001), suggest that the Gorda plate as it approaches the triple junction from the north is obstructed by the rigid Pacific plate, internally deformed and forced to subduct beneath North America by breaking into smaller segments. The boundary between the subducting Gorda and the Pacific plate is imaged as an offshore extension of the King Range thrust zone located southwards of the north-facing bathymetric escarpment (Fig. 5.16). The NW–SE alignment of relocated events beneath the Garberville-Briceland fault zone at the northern edges of King Range in combination with lateral velocity changes across this earthquake zone is possibly imaging, at this latitude, the southern edge of the subducting Gorda plate (Fig. 5.16–b). Therefore, the subducting Gorda slab fragments are passing behind the northeastern edge of the Pacific plate and flowing towards the southeast (Fig. 5.16–a). Mantle velocities beneath the Gorda slab are constrained to a maximum depth of 31 km beneath North America roughly at 123°30'W (Z=30–31 km, Y=4500–4520 km, X=380–440 km in Fig. 5.16–c). The relocated events at similar depths extend from the Mendocino fault towards the east-southeast and then following the resolved velocity pattern, turn to the north-northwest, revealing, at least for these latitudes, the vertical extent of the slab.

5.8.3 Petrolia April 1992 earthquake and aftershock sequence

Comparison of the Petrolia 1992 main event (7.1 Ms) and the aftershock sequence between April and September the same year reveals that the main shock's hypocentre is located in an area with velocities $\sim$5.5 kms^{-1}, at roughly what is

described earlier, in Chapter 4, as the down-warping boundary that defines the transition between the overlying North America crust and the subducting Gorda slab (Z=12.3 km, Y=4460 km in Fig. 4.25 and 4.30, and 4560/4360 km, Z=12.3 km in Fig. 4.28). This event triggered a swarm of events at shallower depths up-dip on the thrust boundary (Z=10 km, Y=4460 km in Fig. 4.25 and 4560/4360 km, Z=10 km,in Fig. 4.28) or within the overlying accreted terranes further south (4550/4350 km, Z=5–10 km in Fig. 4.28). A second group of events associated with the Petrolia earthquake is located deeper in the subducting crust, at ∼20 km depth, and along the subducting Moho , at ∼30 km depth (Y=4460 km in Fig. 4.25 and 4560/4360–4550/4350 km in Fig. 4.28). The location of the first main aftershock is well within the subducting slab further offshore and is possibly associated with a WNW–ESE alignment of relocated events (Fig. 5.16–b,c). Finally, southwards, most of the events between April and September 1992, tend to concentrate offshore along the west-east trending boundary between the Pacific and Gorda plate, beneath the Mendocino ridge (4540/4340 km in Fig. 4.28). The results of this study are in agreement with Oppenheimer et al. (1993), who suggested that the Petrolia event was a thrust on a east-dipping plane. Henstock & Levander (2003), based on a projection of the Petrolia hypocentre on line's *wa3NWSE* profile, which lies to the south of the event's hypocentre, inferred that the event is several kilometres shallower than the Cascadia plate boundary (see Fig. 4.37). The vertical cross-sections through our model, parallel with line *wa3NWSE*, that pass through the Petrolia sequence reveal that the main shock, and a swarm of events up-dip, correlate well with velocity boundaries that define the Cascadia thrust (4560/4360 km in Fig. 4.28). Moving slightly southwards in a similar profile to line's *wa3NWSE* the shallower events seem to occur within the North American crust (4550–4350 km Fig. 4.28 and Fig. 4.37). Thus, we conclude that the April 1992 Petrolia 7.1 Ms earthquake was an event on the Cascadia subduction boundary, or very close to this thrust within the overlying North American crust, and triggered smaller shallower events up-dip along the thrust and within the overlying highly faulted North American terranes, but also within the subducting slab and along the subducting oceanic Moho.

5.8.4 North American crust

The North American crust in our study area is characterised by smaller scale velocity structures, imaging the tectonically complex evolution of the accretionary sequences on the North America margin. In general, there is crustal thickening

close to the Mendocino triple junction area, which is in agreement with high uplift rates (Merritts, 1996), and high topography in the area. Features with velocities higher than 6.5 kms^{-1} and ∼10 km long with a NW–SE trend have been observed at 13 km depth at a similar latitude to Point Delgada, but east of the Barlett Springs fault, and at 5 km depth in the northernmost part of our model close to the coast. Fragmented parts of the Coastal Range ophiolite along a NW–SE trending zone could be responsible for these mafic velocity features. Outliers of the Coastal Range ophiolite, that have been displaced from the west side of the Great valley basement and have been incorporated into the Central belt of the Franciscan complex, have been mapped in this area trending NW–SE (McLaughlin et al., 1988). Most of these ophiolitic outliers have been displaced by faulting that predates the San Andreas fault system. Magnetic anomalies in the area also show these near-surface bodies with a similar trend (Jachens et al., 1995). The velocity model images also the high velocity Klamath terrane as a high velocity layer at 1 km depth overlying a lower velocity region. These lower velocities have been interpreted by Beaudoin et al. (1996b) as underthrust Franciscan rocks beneath the the Klamaths. Zucca et al. (1986), based on a north-south seismic refraction line close to the eastern edge of this model, imaged a similar structure of alternating positive and negative velocity gradients. A smaller feature with high velocities is also observed on the surface of the model without any deep root, and is associated with mapped igneous rocks of Point Delgada (e.g. McLaughlin et al., 2000).

5.8.5 Vizcaino block structure

The high velocity body that is observed beneath the Vizcaino block offshore coincides with a positive gravity anomaly observed by Jachens & Griscom (1983), Griscom & Jachens (1989) and Blakely et al. (1997). This anomaly is associated also with a magnetic anomaly (e.g. Griscom & Jachens, 1989) and it has been suggested that it might be caused by a belt of ophiolitic rocks offshore (Jachens & Griscom, 1983). The final P_g velocity model indicates that this feature is independent from the lowermost crust and is incorporated in the upper crust (Fig. 4.33 and 4.34). Henstock & Levander (2003) suggested that the lower Pacific crust in the Vizcaino area is deformed with a 30 km north-south shortening. The absence of seismicity and the undeformed sediment cover in the area suggested that this block represents a strong deformation of the northeast edge of the Pacific plate that occurred in the past (prior to 11 Ma). However, the dipping of the 8 km s^{-1} isovelocity surface beneath the Vizcaino block indicates a crustal thickening in the

area as the independent high velocity layer within the upper crust of the Vizcaino block is stacked on top of the Pacific plate (Fig. 5.16). Whether this high velocity anomaly is an obducted Mesozoic ophiolitic sequence, or a remnant of the Farallon plate that has been obducted on the neighbouring oceanic crust during the initialisation of the strike slip system, remains unknown.

5.8.6 Slab window and tectonic model

This study images a high velocity mafic layer (higher than 6.5 km s^{-1}) at the base of the crust that dips gently from the Pacific plate eastwards, beneath North America. These high velocities beneath North America are constrained in the first arrival model up to Y=4410 km north, extending from the coast ~50 km eastwards (Z=19–20 km in Fig. 4.24). In addition, the P_g arrival model constrains these velocities further northwards (Z=18 km in Fig. 4.33), extending from the coast 20–30 km eastwards. The San Andreas strike slip system cuts through and offsets the lower crustal layer about 5 km deeper to the east. Thus, the tomography model suggests that the high velocity layer is attached to the overlying North America, as previously suggested (e.g. Henstock & Levander, 2000a; Hole et al., 1998). The Gorda plate was imaged to break and subduct beneath North America with its southernmost edge extending along a southeast direction (Fig. 5.16). The Gorda fragments are flowing past the edge of the Pacific plate, at the end of King Range terrane, into an area where the slabless window is expected. Lower velocities in the upper mantle north of Y=4360 km (see Z=19–20 km in Fig. 4.24) could image the presence of weak or strong asthenospheric upwelling into the slab window. Unfortunately, this tomography model does not constrain the upper mantle beneath North America, southeast of MTJ. A combined tomography approach that inverts for both the active source data used in this study and local earthquake data could constrain these depths.

5.9 Conclusions

From the wide-angle seismic tomographic study and earthquake relocation at the Mendocino Triple Junction area we conclude the following:

(1). A high velocity mafic layer at the base of the crust dips gently from the Pacific plate eastwards, beneath North America. The San Andreas fault system cuts the entire crust and offsets this layer ~5 km deeper to the east

suggesting that the high velocity layer is attached onshore to the overlying North America plate.

(2). The San Andreas fault passes onshore north of Point Delgada, assigning the King Range terrane as part of the Pacific plate or as a sliver in the boundary zone.

(3). The Gorda plate close to the Mendocino fault breaks and subducts beneath North America in a southeast direction with the southern edge of the plate being at the northernmost boundary of the King Range terrane. The tomography model does not resolve the upper mantle southeast of the triple junction to image weak or strong asthenospheric upwelling.

(4). The Petrolia earthquake, in April 1992, is a Cascadia thrust event that triggers shallower events up-dip on the thrust and within the North America accreted terranes, but also within the subducting slab and along the subducting oceanic Moho.

(5). High velocity anomalies within the upper North American crust are related to outliers of the Coastal Range ophiolites.

(6). An oceanic high velocity layer in the Vizcaino block upper crust lies on top of the Pacific crust and correlates well with gravity and magnetic data. This oceanic layer was obducted in the past and does not represent a present day deformation on the northeastern part of the Pacific plate.

Chapter 6

Summary and Conclusions

The aim of this thesis was to develop three-dimensional velocity models from two active source wide-angle experiments carried out around the Ascension Island, in equatorial South Atlantic and the Mendocino Triple Junction region, in North America. By doing that, some limitations of the active source tomographic methods could also be explored. Finally, in an attempt to get a more complete picture of the evolution of the Mendocino Triple Junction area, relative relocation of earthquake events occuring within the wide-angle experiment area was performed.

An overall summary of the tomography limitations that have been met through modelling these two datasets is given in this chapter, followed by brief conclusions on the results of both experiments. Finally, some thoughts for further or additional future work are given that are directly linked with the subject studied here.

6.1 Limitations of Forward–Inverse methods

The use of the tomography algorithms, Jive3D by Hobro et al. (2003) in Chapter 3 and FAST by Zelt & Barton (1998) in Chapter 4, leads to some conclusions about the algorithms themselves and about strategies for tomographic inversion in general.

The forward step Jive3D uses the ray perturbation method by Virieux & Farra (1991) and FAST the finite difference eikonal solver by Vidale (1990) with modifications by Hole & Zelt (1995). In general, using the finite difference eikonal solver proved to be almost an order of magnitude faster than the ray perturbation method in the same velocity model. In experiments with relatively small numbers of receivers and sources, like the Ascension Island experiment, this is not a major problem, whereas in much larger experiments, like the Mendocino Triple Junction experiment, the use of the ray perturbation method is an almost impossible task

for currently available computer processors.

The major drawback in most finite difference eikonal solvers is that they do not deal with reflected arrivals, or refracted energy that is not recorded as first arrival. A solution here may be the use of a layer stripping approach that models the shallowest velocity layer with its corresponding refracted phase first, and then moves gradually deeper keeping fixed the already modelled shallower layers. However, this requires that boundaries between the layers are known from reflected arrivals. Another disadvantage of the finite difference eikonal solver employed by Zelt & Barton (1998) is that it is less precise in the calculation of traveltimes than the raytracing approach. Comparison of the two forward methods in the final velocity model of Ascension Island in Chapter 2 revealed that the finite difference eikonal solver gives ∼10 ms more RMS misfit between the observed and predicted arrival times than the ray perturbation method, even when the forward grid used by the finite difference solver is denser than that used by the ray tracing.

Despite these advantages of the ray perturbation method over the finite difference eikonal solver, the ability of the latter to find an arrival time for all observed source-receiver pairs means that all observed traveltime picks contribute to the final model. When a final model represents only a part and not all of the observed traveltime picks, an independent assessment of the unmodelled picks should be carried out. Finally, the mathematical simplicity of the finite difference eikonal solver makes it easier to be incorporated into different tomographic algorithms.

A comparison between inversion algorithms is more difficult mainly because of the different parametrisation approaches. The model parametrisation in these cases is coupled to the forward method and is generally much coarser when the ray perturbation method has been employed. Experiments with OBH and OBS receivers over steep bathymetric relief require a fine parametrisation of the bathymetry, to avoid introducing considerable traveltime errors. Requiring the velocity grid to be similar to the overlying bathymetry parameterisation (e.g. Zelt & Barton, 1998) will increase considerably the computing processing and memory requirements.

The use of first arrivals and the one layer approach in the tomography inversion (e.g. Zelt & Barton, 1998) does not always ensure that the model is directly constrained at all depths. At far offsets, where only P_n is observed as first arrival, the absence of P_g to constrain the crust in the model can result in higher vertical gradients and therefore create structure with apparent velocity of 8 kms^{-1} and thinner crustal thickness as seen on the line *wa1* cross-section (Fig. 4.35). The geometry of a 3D experiment could ensure that most areas in the model space are

constrained by P_g and P_n first arrivals at all depths; it is desirable to explicitly model P_g first arrivals at all offsets as well as P_n first arrivals.

When the inversion step is performed simultaneously for more than one model layer and/or interface, it is essential that the regularisation strength can be independently specified for each of them. Moreover, in both studied areas the wavelength of the velocity anomalies is larger in the lateral direction than the vertical one. To obtain a final model that is able to resolve the finer structure and stronger velocity gradients in the vertical direction requires either a variable vertical-horizontal parametrisation ratio, and/or variable vertical-horizontal regularisation weighting ratio.

The final tomography model should be as independent as possible from the initial one. When the initial input model has a 3D structure assumed from *a priori* information, a way to achieve a relative independent final model is to apply very high initial regularisation to force the 3D initial model to develop a smooth 1D velocity structure and then gradually tend toward a more detailed 3D structure. A similar way to achieve this is to start with a very coarse grid spacing for the inversion, both vertically and horizontally. In this way the 3D initial model develops in the first steps into a very smooth structure, with almost 1D structure, and then develops gradually into a detailed 3D structure. The final model will therefore depend, in both approaches, only on this general 1D velocity structure. The first approach was applied in the Ascension Island dataset, and the second in the the Mendocino Triple Junction tomography.

To estimate the resolution of large 3D tomography models the non-linear 3D checkerboard test is applied. In this study, the effect of perturbation of traveltimes is tested by adding 3-5% negative and positive anomalies to the final models. Synthetic traveltimes are then calculated through these perturbed models, and using the same initial velocity model and inversion parameters, the modelling procedure is repeated. The resultant final models are compared with the original final models to determine whether the added velocity anomalies are resolved. The approach used for the Ascension dataset differs from this followed by Zelt (1998) and others, as the applied checkerboard anomalies alternate not only horizontally but also vertically. In this way, we obtained information about vertical, as well as horizontal, resolution. In particular, the size/volume of the resolved 3D velocity features is estimated, as well as the amplitude of the resolved velocity perturbations. For the Mendocino dataset the checkerboard anomalies were alternated only laterally, as the finite difference forward method used (Zelt, 1998) traces rays that preferentially travel through the high velocity anomalies, and therefore changes

considerably the ray paths from those in the final model.

6.2 Ascension Island crustal structure

The main objectives of volcanic island seismic studies were described at the beginning of Chapter 3. An overview of the geology and geophysics of the Ascension Island and the area between the Ascension and the Bode Verde fracture zones west of the Mid-Atlantic Ridge follows. The experiment layout and resulting wide-angle data were then described, followed by the detailed description of the tomography approach that was employed. The final velocity model was tested with gravity modelling and results of the checkerboard resolvability test were given together with the description of the main velocity features of the crustal layer and the Moho topography.

Within the shallow extrusive part of the Ascension edifice two main high velocity regions coincide with the highest topography on land and the gravity maximum off the west coast of the island, respectively. These features are connected with a high velocity intrusive core that is created either within or on the top of oceanic Layer 3 and is interpreted as a possible relic magma chamber. The $\sim$4 km thickness of the surface low velocity region is similar to that observed at Hawaii, Jasper Seamount and Great Meteor Seamount, suggesting a similar process of edifice construction. The mean density of the volcanic edifice is significantly less than that of normal oceanic crust and than load densities typically assumed in studies of flexure due to seamount loading. There is no simple flexural model that explains the shape of the Moho beneath the island, perhaps because of the long lived volcanism and the proximity of the island to the Mid-Atlantic Ridge and the Ascension Fracture Zone. There is no evidence for magmatic underplating beneath Ascension Island. This seismic study has been accepted for publication in *Geophysical Journal International*.

6.3 Mendocino triple junction seismic experiment and earthquake relocation

The background geology and geophysics of the complicated Mendocino Triple Junction area were discussed at the beginning of Chapter 4. The Mendocino dataset, a result of a series of 2D and 3D wide angle experiments acquired between 1992–1994, was then described. After the description of the tomography approach

and the results of a checkerboard resolution test, the results of a first arrival final model with the complementary results of a P_g arrival model were given. The final model is also compared with existing velocity models in the area by other authors.

In Chapter 5, the earthquake relocation performed in the Mendocino triple junction region was described. Following an overview of the earthquake location and relocation methods, and a description of the earthquake data and velocity models used in this study, we described the source specific station term and waveform crosscorrelation application. The location uncertainties were estimated and a discussion of the results was given. Finally, a discussion integrated the tomography model and earthquake relocation results.

The results of this study are in agreement with most previously published seismic studies, giving a unifying picture of the Mendocino triple junction velocity structure. Greater resolution in this study reveals high velocity bodies within the North America crust, originating possibly from Coastal Range ophiolithic outliers. The shallow strike slip events show greater clustering and better alignment after relocation, improving the study of particular earthquake swarms, such as the Cloverdale 2000 swarm. The San Andreas fault is imaged to cut through the crust and, therefore, separates the Pacific plate from North America. This boundary passes onshore north of Point Delgada, with the King Range terrane being a part of the Pacific plate, or a sliver in the boundary zone. Offshore, within the Vizcaino block, an oceanic high velocity body is observed within the upper crust and is independent from the underlying lower crust. North of the Mendocino fault the subducting Gorda slab seems to be internally deformed, as it approaches the triple junction, in a series of dipping vertical velocity offsets from northwest to southeast with intra-slab seismicity in NE–SW lineations. The relocated Petrolia earthquake in April 1992 is observed in the tomography model as a Cascadia thrust event, that triggers events up-dip and shallower within the North America accreted terranes, as well as, events deep into the subducting slab and the subducting Moho.

Early earthquake relocation results have been already made available to USGS in Menlo Park, CA, and will be followed by the final results, the wide-angle traveltime picks and the tomography model, in a combined effort to model the strong ground motions produced by the 1906 San Francisco earthquake, in Northern California.

6.4 Suggested further work

Although the results of this thesis can stand alone and add significant information for two contrasting geological regions, using a diversity of tomography methods and applications, there are still ways that can further improve the tomography modelling or the earthquake relocation approach.

The shape of the Moho beneath Ascension Island and its response into the loading of the volcanic edifice close to the Mid-Atlantic Ridge could be investigated more efficiently with flexure modelling which takes into account 3D density variations. Possible future wide-angle lines between Ascension Island and the MAR, or the Ascension Fracture Zone, may explain the behaviour of the Moho boundary due to loading in a complicated area like this.

For the Mendocino Triple Junction area, the developed velocity model is the result of P_g and P_n traveltime picks. The 21503 P_mP picks constrained the Moho boundary very well, at least in areas directly beneath the 2D lines and the 3D land array. Unfortunately, the only publicly available tomographic code that can invert simultaneously for layers and interfaces is that by Hobro et al. (2003), which currently requires unrealistic computer memory and processing times for an experiment of this size. Alternatively, a forward calculation of reflected traveltimes through the final first arrival model and an inversion for depth parameters only, by keeping the velocity model fixed, could produce a Moho interface that floats within the first or P_g arrival model.

The use of source specific station terms and waveform crosscorrelation to relatively relocate earthquake events within the tomography study area could be improved by direct use of the 3D velocity model to calculate the traveltimes from the earthquake hypocentres to the station positions. This will require an expansion of the final velocity model, or a smoother version of it, with the possible application of local earthquake tomography for the deeper parts of the lithosphere.

Finally, three-dimensional velocity models produced from active source and passive experiments can be used to quantify and assess the seismic risk in an area. Seismic response could be simulated with the use of the spectral element method (e.g. Komatitsch et al., 2004) in local 3D velocity models. This approach could be applied to the Mendocino area for periods up to 2 sec in parts with good ray coverage.

Bibliography

Astiz, L., Shearer, P. M., & Agnew, D. C., 2000. Precise relocations and stress change calculations for the upland earthquake sequence in southern California, *J. geophys. Res.*, **105**, 2937–2953.

Atkins, F. B., Baker, P. E., Bell, J. D., & Smith, D. G. W., 1964. Oxford expedition to Ascension Island, 1964, *Nature*, **204**, 722–724.

Atwater, T., 1970. Implications of plate tectonics for the Cenozoic tectonic evolution of western North America, *Geol. Soc. Am. Bull.*, **81**, 3513–3536.

Atwater, T., 1989. Plate tectonic history of the northeast Pacific and western North America, in *The Geology of North America, The Eastern Pacific Ocean and Hawaii*, edited by E. L. Winterer, D. M. Hussong, & R. W. Decker, vol. N, pp. 21–72, Geol. Soc. Am.

Beaudoin, B., Hole, J., & Klemperer, S., 1996. Mendocino Array Experiment, Tech. Rep. 96-008, IRIS.

Beaudoin, B. C., Magee, M., & Benz, H., 1994. Crustal velocity structure north of the Mendocino triple junction, *Geophys. Res. Lett.*, **21**, 2319–2322.

Beaudoin, B. C., Godfrey, N. J., Klemperer, S. L., Lendl, C., Trehu, A. M., Henstock, T. J., Levander, A., Holl, J. E., Meltzer, A. S., Luetgert, J. H., & Mooney, W. D., 1996. Transition from slab to slabless: Results from the 1993 Mendocino triple junction seismic experiment, *Geology*, **24**, 195–199.

Beaudoin, B. C., Hole, J. A., Klemperer, S. L., & Trehu, A. M., 1998. Location of the southern edge of the Gorda slab and evidence for an adjacent asthenospheric window: Results from seismic profiling and gravity, *J. geophys. Res.*, **103**, 30101–30115.

Benz, H. M., Zandt, G., & Oppenheimer, D. H., 1992. Lithospheric structure of

Northern California from teleseismic images of the upper mantle, *J. geophys. Res.*, **97**, 4791–4807.

Billings, S. D., Sambridge, M. S., & Kennett, B. L. N., 1994. Errors in Hypocenter Location: Picking, Model, and Magnitude Dependence, *Bull. Seismol. Soc. Am.*, **84**, 1978–1990.

Blackman, D. K. & Forsyth, D. W., 1991. Isostatic compensation of tectonic features of the Mid-Atlantic Ridge $25 - 27°30'$S, *J. geophys. Res.*, **96**, 11741–11758.

Blake, M. C., Jayko, A. S., & McLaughlin, R. J., 1985. Tectonostratigraphic terranes of the northern Coast Ranges, California, in *Tectonostratigraphic Terranes of the Circum-Pacific Region*, edited by D. G. Howell, pp. 159–186, Circum-Pacific Council for Energyy and Mineral Resources, Houston, TX, USA.

Blakely, R. J., Christiansen, R. L., Guffanti, M., Wells, R. E., DonnellyNolan, J. M., Muffler, L. J. P., Clynne, M. A., & Smith, J. G., 1997. Gravity anomalies, quaternary vents, and quaternary faults in the southern Cascade Range, Oregon and California: Implications for arc and backarc evolution, *J. geophys. Res.*, **102**, 22513–22527.

Bohannon, R. G. & Parsons, T., 1996. Tectonic implications of post-30 Ma Pacific and North American relative plate motions (vol 107, pg 937, 1995), *Geol. Soc. Am. Bull.*, **108**, 912–912.

Bohm, G., Galuppo, P., & Vesnaver, A., 2000. 3D adaptive tomography using Delaunay triangles and Voronoi polygons, *Geophys. Prospect.*, **48**, 723–744.

Bourdon, E. & Hemond, C., 2001. Looking for the "missing endmember" in South Atlantic Ocean mantle around Ascension Island, *Mineralogy And Petrology*, **71**, 127–138.

Brocher, T. M., McCarthy, J., Hart, P. E., Holbrook, W. S., Furlong, K. P., McEvilly, T. V., Hole, J. A., & Klemperer, S. L., 1994. Seismic evidence for a lower-crustal detachment beneath San Francisco Bay, California, *Science*, **265**, 1436–1439.

Brozena, J. M., 1986. Temporal and spatial variability of sea-floor spreading processes in the northern South-Atlantic, *J. geophys. Res.*, **91**, 497–510.

Bruguier, N. J., Minshull, T. A., & Brozena, J. M., 2003. Morphology and Tectonics of the Mid-Atlantic Ridge, $7 - 12°$, *J. geophys. Res.*, **108**, 2093, doi:10.1029/2001JB001172.

Burridge, R., 1976. *Some mathematical topics in seismology*, Courant Institute of Mathematical Sciences, New York University.

Cande, S. C. & Kent, D. V., 1995. Revised calibration of the geomagnetic polarity timescale for the late Cretaceous and Cenozoic, *J. geophys. Res.*, **100**, 6093–6095.

Caress, D. W., McNutt, M. K., Detrick, R. S., & Mutter, J. C., 1995. Seismic imaging of hotspot-related crustal underplating beneath the Marquesas Islands, *Nature*, **373**, 600–603.

Carlson, R. L. & Herrick, C. N., 1990. Densities and porosities in the oceanic-crust and their variations with depth and age, *J. geophys. Res.*, **95**, 9153–9170.

Carlson, R. L. & Raskin, G. S., 1984. Density of the ocean crust, *Nature*, **311**, 555–558.

Castillo, D. A. & Ellsworth, W., 1993. Seismotectonics of the San Andreas fault system between Point Arena and Cape Mendocino in Northern California: Implications of the development and evolution of a young transform, *J. geophys. Res.*, **98**, 6543–6560.

Charvis, P., Laesanpura, A., Gallart, J., Hirn, A., Lepine, J. C., de Voogd, B., Minshull, T. A., Hello, Y., & Pontoise, B., 1999. Spatial distribution of hotspot material added to the lithosphere under La Reunion, from wide-angle seismic data, *J. geophys. Res.*, **104**, 2875–2893.

Clarke, S. H., 1992. Geology of the Eel river basin and adjacent region - implications for late Cenozoic tectonics of the southern Cascadia subduction zone and Mendocino triple junction, *AAPG Bull.*, **76**, 199–224.

Dash, B. P. & Milsom, J., 1973. Gravity field of Ascension Island, South Atlantic, *Earth Planet. Sci. Lett.*, **21**, 79–84.

Dickinson, W. R., 1981. Plate tectonics and the continental margin of California, in *The geotectonic development of California: Englewood Cliffs*, edited by W. G. Ernst, pp. 1–28, Prentice-Hall.

Dickinson, W. R. & Snyder, W. S., 1979. Geometry of subducted slabs related to San Andreas transform, *J. Geol.*, **87**, 609–627.

Eberhart Phillips, D. & Michael, A., 1983. Three-dimensional structure, seismicity, and fault structure in the Parkfield region, central California, *J. geophys. Res.*, **88**, 8226–8236.

Evernden, J., 1969. Precision of epicentres obtained by small numbers of world-wide stations, *Bull. Seismol. Soc. Am.*, **59**, 1365–1398.

Farra, V., 1990. Amplitude computation in heterogeneous media by ray perturbation theory: a finite element approach, *Geophys. J. Int.*, **103**, 341–354.

Foulger, G. R. & Toomey, D. R., 1989. Structure and evolution of the Hengill-Grensdalur volcanic complex, Iceland - geology, geophysics, and seismic tomography, *J. geophys. Res.*, **94**, 17511–17522.

Freymueller, J. T., Murray, M. H., Segall, P., & Castillo, D., 1999. Kinematics of the Pacific North America plate boundary zone, northern California, *J. Geophys. Res.-Solid Earth*, **104**, 7419–7441.

Frolich, C., 1979. An efficient method for the joint hypocenter determination for large groups of earthquakes, *Comput. Geosci.*, **5**, 387–389.

Furlong, K. P. & Govers, R., 1999. Ephemeral crustal thickening at a triple junction: The Mendocino crustal conveyor, *Geology*, **27**, 127–130.

Godfrey, N., Beaudoin, B., Lendl, C., Meltzer, A., & Luetgert, J., 1996. 1993 Mendocino Triple Junction Experiment, Tech. Rep. 96-018, IRIS.

Godfrey, N. J., Beaudoin, B. C., & Klemperer, S. L., 1997. Ophiolitic basement to the Great Valley forearc basin, California, from seismic and gravity data: Implications for crustal growth at the North American continental margin, *Geol. Soc. Am. Bull.*, **109**, 1536–1562.

Godfrey, N. J., Meltzer, A. S., Klemperer, S. L., Trehu, A. M., Leitner, B., Clarke, S. H., & Ondrus, A., 1998. Evolution of the Gorda Escarpment, San Andreas fault and Mendocino triple junction from multichannel seismic data collected across the northern Vizcaino block, offshore northern California, *J. Geophys. Res.-Solid Earth*, **103**, 23813–23825.

Grevemeyer, I., Weigel, W., Schussler, S., & Avedik, F., 2001. Crustal and upper mantle seismic structure and lithospheric flexure along the Society Island hotspot chain, *Geophys. J. Int.*, **147**, 123–140.

Griscom, A. & Jachens, R. C., 1989. Tectonic history of the north portion of the San-Andreas fault system, California, inferred from gravity and magnetic anomalies, *J. geophys. Res.*, **94**, 3089–3099.

Gulick, S. P. S. & Meltzer, 2002. Effect of the nortward-migrating Mendocino triple junction of the Eel River forearc basin, California: Structural evolution, *Geol. Soc. Am. Bull.*, **114**, 1505–1519.

Gulick, S. P. S., Meltzer, A. S., & Clarke, S. H., 1998. Seismic structure of the southern Cascadia subduction zone and accretionary prism north of the Mendocino triple junction, *J. geophys. Res.*, **103**, 27207–27222.

Gulick, S. P. S., Meltzer, A. S., Henstock, T. J., & Levander, A., 2001. Internal deformation of the southern Gorda plate: Fragmentation of a weak plate near the Mendocino triple junction, *Geology*, **29**, 691–694.

Hammer, P. T. C., Dorman, L. M., Hildebrand, J. A., & Cornuelle, B. D., 1994. Jasper seamount structure - sea-floor seismic-refraction tomography, *J. geophys. Res.*, **99**, 6731–6752.

Hanan, B. B., Kingsley, R. H., & Schilling, J. G., 1986. Pb isotope evidence in the South-Atlantic for migrating ridge hotspot interactions, *Nature*, **322**, 137–144.

Harben, P. E., Hollfelder, J. R., & Rodgers, A. J., 1999. Experimentally determined coordinates for three MILS hydrophones near Ascension Island, Tech. Rep. UCRL-ID-136507, Lawrence Livermore National Laboratory.

Harper, G. D., 1980. The Josephine Ophiolite: Remains of a Late Jurassic marginal basin in northwestern California, *Geology*, **8(7)**, 333–337.

Hearn, T. M. & Ni, J. F., 1994. Pn velocities beneath continental collision zones: the Turkish-Iranian Plateau, *Geophys. J. Int.*, **117**, 273–283.

Henstock, T. J. & Levander, A., 1996. Mendocino Triple Junction seismic experiment: 1994 Onshore-Offshore and High Density Land recording, Tech. Rep. 96-017, IRIS.

Henstock, T. J. & Levander, A., 2000. Lithospheric evolution in the wake of the Mendocino triple junction: structure of the San Andreas Fault system at 2 Ma, *Geophys. J. Int.*, **140**, 233–247.

Henstock, T. J. & Levander, A., 2000. Impact of a complex overburden on analysis of bright reflections: A case study from the Mendocino triple junction, *J. geophys. Res.*, **105**, 21711–21726.

Henstock, T. J. & Levander, A., 2003. Structure and seismotectonics of the Mendocino Triple Junction, California, *J. geophys. Res.*, **108**, art. no.–2260.

Henstock, T. J., Levander, A., & Hole, J. A., 1997. Deformation in the lower crust of the San Andreas fault system in northern California, *Science*, **278**, 650–653.

Henstock, T. J., Levander, A., Meltzer, A. S., & Gulick, S. P. S., 1999. Deformation and mass transfer at the Mendocino triple junction: What Gorda gives up, North America receives, in *Seismological Research Letters*, vol. 70, p. 246.

Hestenes, M. & Stiefel, E., 1952. Methods of conjugate gradients for solving linear systems, *Nat. B. Stand. J. Res.*, **49**, 409–436.

Hieronymus, C. F. & Bercovici, D., 2001a. A theoretical model of hotspot volcanism: Control on volcanic spacing and patterns via magma dynamics and lithospheric stresses, *J. geophys. Res.*, **106**, 683–702.

Hieronymus, C. F. & Bercovici, D., 2001b. Focusing of eruptions by fracture wall erosion, *Geophys. Res. Lett.*, **28**, 1823–1826.

Hobro, J. W. D., 1999. *Three-dimensional tomographic inversion of combined reflection and refraction seismic travel-time data*, Ph.D. thesis, University of Cambridge.

Hobro, J. W. D., Singh, S. C., & Minshull, T. A., 2003. Three-dimensional tomographic inversion of combined reflection seismic travel-time data, *Geophys. J. Int.*, **152**, 79–93.

Hole, J. A., 1992. Nonlinear high-resolution 3-dimensional seismic travel time tomography, *J. geophys. Res.*, **97**, 6553–6562.

Hole, J. A. & Zelt, B. C., 1995. 3-D finite-difference reflection travel-times, *Geophys. J. Int.*, **121**, 427–434.

Hole, J. A., Beaudoin, B. C., & Henstock, T. J., 1998. Wide-angle seismic constraints on the evolution of the deep San Andreas plate boundary by Mendocino triple junction migration, *Tectonics*, **17**, 802–818.

Hole, J. A., Beaudoin, B. C., & Klemperer, S. L., 2000. Vertical extent of the newborn San Andreas fault at the Mendocino triple junction, *Geology*, **28**, 1111–1114.

Hosford, A., Lin, J., & Detrick, R. S., 2001. Crustal evolution over the last 2 m.y. at the Mid-Atlantic Ridge OH-1 segment, 35 degrees N, *J. geophys. Res.*, **106**, 13269–13285.

Howie, J. M., Miller, K. C., & Savage, W. U., 1993. Integrated crustal structure across the south central California margin - Santa-Lucia escarpment to the San-Andreas fault, *J. geophys. Res.*, **98**, 8173–8196.

Husen, S. & Kissling, E., 2001. Local earthquake tomography between rays and waves: fat ray tomography, *Phys. Earth Planet. Inter.*, **123**, 129–149.

Jachens, R. C. & Griscom, A., 1983. 3-dimensional geometry of the Gorda plate beneath northern California, *J. geophys. Res.*, **88**, 9375–9392.

Jachens, R. C., Griscom, A., & Roberts, C. W., 1995. Regional extent of great-valley basement west of the Great Valley, California - implications for extensive tectonic wedging in the California Coast Ranges, *J. geophys. Res.*, **100**, 12769–12790.

Julian, B. R. & Gubbins, D., 1977. Three-dimensional seismic ray tracing, *Geophys. J. Int.*, **43**, 95–113.

Klemperer, S. & Beaudoin, B., 1994. Cape Mendocino Calibration Experiment, Tech. Rep. 94-004, IRIS.

Klingelhöfer, F., Minshull, T. A., Blackman, D. K., Harben, P., & Childers, V., 2001. Crustal structure of Ascension Island from wide-angle seismic data: implications for the formation of near-ridge volcanic islands, *Earth Planet. Sci. Lett.*, **190**, 41–56.

Komatitsch, D., Liu, Q. Y., Tromp, J., Suss, P., Stidham, C., & Shaw, J. H., 2004. Simulations of ground motion in the Los Angeles basin based upon the spectral-element method, *Bull. Seismol. Soc. Amer.*, **94**, 187–206.

Krastel, S. & Schmincke, H. U., 2002. Crustal structure of northern Gran Canaria, Canary Islands, deduced from active seismic tomography, *J. Volcanol. Geotherm. Res.*, **115**, 153–177.

Lachenbruch, A. H. & Sass, J. H., 1980. Heat flow and energetics of San Andreas fault zone, *J. geophys. Res.*, **85**, 6185–6222.

Lay, T. & Wallace, T. C., 1995. *Modern Global Seismology*, Academic Press, California.

Leitner, B., Trehu, A. M., & Godfrey, N. J., 1998. Crustal structure of the northwestern Vizcaino block and Gorda Escarpment, offshore northern California, and implications for postsubduction deformation of a paleoaccretionary margin, *J. geophys. Res.*, **103**, 23795–23812.

Levander, A., Henstock, T. J., Meltzer, A. S., Beaudoin, B. C., Trehu, A. M., & Klemperer, S. L., 1998. Fluids in the lower crust following Mendocino triple junction migration: Active basaltic intrusion?, *Geology*, **26**, 171–174.

Liu, M. & Furlong, K. P., 1992. Cenozoic volcanism in the California Coast ranges - numerical solutions, *J. geophys. Res.*, **97**, 4941–4951.

Ludwig, W. J., Nafe, J. E., & Drake, C. L., 1970. *The Sea, vol 4*, vol. 4, chap. Seismic Refraction, pp. 53–84, Wiley-Interscience.

MacFarlane, D. J., 1968. *The structure of some Atlantic islands as deduced from gravity and other geophysical data*, Ph.D. thesis, Imperial College, London.

McCaughey, M. & Singh, S. C., 1997. Simultaneous velocity and interface tomography of normal incidence and wide-aperture seismic traveltime data, *Geophys. J. Int.*, **131**, 87–99.

McLaughlin, R. J., Blake, M. C., Griscom, A., Blome, C. D., & Murchey, B., 1988. Tectonics of formation, translation, and dispersal of the Coast Range ophiolite of California, *Tectonics*, **7**, 1033–1056.

McLaughlin, R. J., Sliter, W. V., Frederikson, N. O., & Harbert, W. P., M., 1997. Plate motions recorded in tectonostratigraphic terranes of the Franciscan Complex and evolution of the Mendocino triple junction, northwestern California, *U.S. Geological Survey Bulletin*, p. 60p.

McLaughlin, R. J., Ellen, S. D., Balke, B. C., Jayko, A. S., Irwin, W., Aalto, K. R., Carver, G. A., & Clarke, S. H., 2000. Geology of the Cape Mendocino, Eureka, Garberville, and southwestern part of the Hayfork 30 x 60 minute quadrangles and adjacent offshore area, northern California, *Miscellaneous field studies MF-2336*, p. U.S. Geological Survey.

Menke, W., 1989. *Geophysical Data Analysis: Discrete Inverse Theory*, International Geophysics Series, Academic Press, Revised edn.

Merritts, D. J., 1996. The Mendocino triple junction: Active faults, episodic coastal emergence, and rapid uplift, *J. geophys. Res.*, **101**, 6051–6070.

Minshull, T. A. & Brozena, J. M., 1997. Gravity anomalies and flexure of the lithosphere at Ascension Island, *Geophys. J. Int.*, **131**, 347–360.

Minshull, T. A. & Charvis, P., 2001. Ocean island densities and models of lithospheric flexure, *Geophys. J. Int.*, **145**, 731–739.

Minshull, T. A., Bruguier, N. J., & Brozena, J. M., 1998. Ridge-plume interactions or mantle heterogeneity near Ascension Island?, *Geology*, **26**, 115–118.

Minshull, T. A., Bruguier, N. J., & Brozena, J. M., 2003a. Seismic structure of the Mid-Atlantic Ridge, $8 - 9°$S, *J. geophys. Res.*, **108**, 2513, doi:10.1029/2002JB002360.

Minshull, T. A., Ishizuka, O., Mitchell, N., & Evangelidis, C., 2003b. Vertical motions and lithosphere rheology at Ascension Island, *Eos Trans. AGU*, **84**, Fall Meet. Suppl., Abstract V11B–06.

Mitchell, N. C., 2003. Susceptibility of mid-ocean ridge volcanic islands and seamounts to large-scale landsliding, *J. geophys. Res.*, **108**, 2397, doi:10.1029/2002JB001997.

Mohorovicic, A., 1910. Das Beben vom 8.X.1909: Jahrbuch des Meteorologischen Observatoriums in Zagreb (Agram), fuer das Jahr 1909, pp. 1-63, v.9, part 4, section 1.

Moser, T. J., 1991. Shortest path calculations of seismic rays, *Geophysics*, **56**, 59–67.

Moser, T. J., Nolet, G., & Snieder, R., 1992. Ray bending revisited, *Bull. Seismol. Soc. Amer.*, **82**, 259–288.

Nielson, D. L. & Stiger, S. G., 1996. Drilling and evaluation of Ascension #1, a geothermal exploration well on Ascension Island, South Atlantic Ocean, *Geothermics*, **25**, 543–560.

Nolet, G., 1987. Seismic wave propagation and seismic tomography, in *Seismic Tomography: With Applications in Global Seismology and Exploration Geophysics*, edited by G. Nolet, pp. 71–99, D.Reidel Publishing Company.

Officer, C. B., 1974. *Introduction to Theoretical Geophysics*, Springer-Verlag, New York.

Okubo, P. G., Benz, H. M., & Chouet, B. A., 1997. Imaging the crustal magma sources beneath Mauna Loa and Kilauea volcanoes, Hawaii, *Geology*, **25**, 867–870.

Oppenheimer, D., Klein, F., Eaton, J., & Lester, F., 1992. The Northern California Seismic Network Bulletin, January–December 1992, Tech. Rep. 93-578, U.S.Geological Survey.

Oppenheimer, D., Beroza, G., Carver, G., Dengler, L., Eaton, J., Gee, L., Gonzalez, F., Jayko, A., Li, W. H., Lisowski, M., Magee, M., Marshall, G., Murray, M., McPherson, R., Romanowicz, B., Satake, K., Simpson, R., Somerville, P., Stein, R., & Valentine, D., 1993. The Cape Mendocino, California, earthquakes of April 1992 - subduction at the Triple Junction, *Science*, **261**, 433–438.

Paige, C. C. & Saunders, M. A., 1982. LSQR - an algorithm for sparse linear-equations and sparse least-squares, *ACM Trans. Math. Softw.*, **8**, 43–71.

Parker, R. L., 1972. The Rapid Calculation of Potential Anomalies, *Geophysic. J. R. Astron. Soc.*, **31**, 447–455.

Povdin, P. & Lecomte, I., 1991. Finite difference computation of traveltimes in very contrasted velocity models:a massively parallel approach and its associated tools, *Geophys. J. Int.*, **105**, 271–284.

Press, W., S., T., W., V., & B., F., 1992. *Numerical Recipes in Fortran 77: The Art of Scientific Computing*, Cambridge University Press, Second Edition edn.

Rawlinson, N., Houseman, G. A., & Collins, C. D. N., 2001. Inversion of seismic refraction and wide-angle reflection traveltimes for three-dimensional layered crustal structure, *Geophys. J. Int.*, **145**, 381–400.

Richards-Dinger, K. B. & Shearer, P. M., 2000. Earthquake locations in southern California obtained using source-specific station terms, *J. geophys. Res.*, **105**, 10939–10960.

Scales, J. A., 1987. Tomographic inversion via the conjugate gradient method, *Geophysics*, **52**, 179–185.

Schilling, J. G., Thompson, G., Kingsley, R., & Humphris, S., 1985. Hotspot - migrating ridge interaction in the South Atlantic, *Nature*, **313**, 187–191.

Shaw, P. R. & Orcutt, J. A., 1985. Waveform inversion of seismic refraction data and applications to young Pacific crust, *Geophys. J. R. astr. Soc.*, **82**, 375–414.

Shearer, P. M., 1997. Improving local earthquake locations using the L1 norm and waveform cross correlation: Application to the Whittier Narrows, California, aftershock sequence, *J. geophys. Res.*, **102**, 8269–8283.

Shearer, P. M., 1999. *Introduction to Seismology*, Cambridge University Press.

Sleep, N. H., 1984. Tapping of magmas from ubiquitous mantle heterogeneities - an alternative to mantle plumes, *J. geophys. Res.*, **89**, 29–41.

Smith, W. H. F. & Sandwell, D. T., 1997. Global sea floor topography from satellite altimetry and ship depth soundings, *Science*, **277**, 1956–1962.

Smith, W. H. F. & Wessel, P., 1990. Gridding with continuous curvature splines in tension, *Geophysics*, **55**, 293–305.

Snieder, R. & Sambridge, M., 1992. Ray perturbation theory for traveltimes and ray paths in 3-D heterogeneous media, *Geophys. J. Int.*, **109**, 294–322.

Staudigel, H. & Schmincke, H. U., 1984. The Pliocene Seamount Series of La Palma/Canary-Islands, *J. geophys. Res.*, **89**, 1195–1215.

Stewart, R. & Peselnik, L., 1977. Velocity of Franciscan rocks to 8 kbar and 300°C, *J. geophys. Res.*, **82**, 2027–2039.

Sun, Y., 1993. Ray tracing in 3-D media by parameterized shooting, *Geophys. J. Int.*, **114**, 145–155.

Tarantola, A., 1987. *Inverse Problem Theory: Methods for Data Fitting and Model Parameter Estimation*, Elsevier.

Thurber, C., 1983. Earthquake locations and three-dimensional crustal structure in the Coyote Lake area, central California, *J. geophys. Res.*, **88**, 8226–8236.

Thurber, C. & Kissling, E., 2000. Advances in travel-time calculations for three-dimensional structures, in *Advances in Seismic Event Location*, edited by C. Thurber & N. Rabinowitz, pp. 71–99, Kluwer Academic Publishers.

Tong, C. H., Barton, P. J., White, R. S., Sinha, M. C., Singh, S. C., Pye, J. W., Hobbs, R. W., Bazin, S., Harding, A. J., Kent, G. M., & Orcutt, J. A., 2003. Influence of enhanced melt supply on upper crustal structure at a mid-ocean ridge discontinuity: A three-dimensional seismic tomographic study of 9 degrees N, East Pacific Rise, *J. geophys. Res.*, **108**, art. no.–2464.

Toomey, D. R., Solomon, S. C., & Purdy, G. M., 1994. Tomographic imaging of the shallow crustal structure of the East Pacific Rise at 9-degrees-30'N, *J. geophys. Res.*, **99**, 24135–24157.

Trehu, A. & et. al., 1998. Lithospheric evolution in responce to triple junction migration: Seismic images of the Mendocino Triple Junction region, MENDO94, The onshore/offshore experiment, OBS/OBH, Tech. Rep. 98-005, IRIS.

Van Avendonk, H. J. A., Harding, A. J., & Orcutt, J. A., 1998. A Two-dimensional tomographic study of the Cliperton transform fault, *J. geophys. Res.*, **103**, 17885–17899.

Verdonck, D. & Zandt, G., 1994. 3-dimensional crustal structure of the Mendocino Triple Junction region from local earthquake travel-times, *J. geophys. Res.*, **99**, 23843–23858.

Vesnaver, A. L., 1996. Ray tracing based on Fermat's principle in irregular grids, *Geophys. Prospect.*, **44**, 741–760.

Vidale, J. E., 1988. Finite-difference calculation of travel times, *Bull.Seismol.Soc.Am*, **78**, 2062–2076.

Vidale, J. E., 1990. Finite-difference calculation of traveltimes in 3 dimensions, *Geophysics*, **55**, 521–526.

Virieux, J. & Farra, V., 1991. Ray tracing in 3-D complex isotropic media - an analysis of the problem, *Geophysics*, **56**, 2057–2069.

Virieux, J., Farra, V., & Madariaga, R., 1988. Ray tracing for earthquake location in laterally heterogenous media, *J. geophys. Res.*, **93**, 6585–6599.

Waldhauser, F. & Ellsworth, W. L., 2000. A Double-Difference earthquake location algorithm: method and application to the Northern Hayward Fault, California, *Bull. Seismol. Soc. Am.*, **90**, 1353–1368.

Watts, A. B., 1994. Crustal structure, gravity-anomalies and flexure of the lithosphere in the vicinity of the Canary Islands, *Geophys. J. Int.*, **119**, 648–666.

Watts, A. B. & ten Brink, U. S., 1989. Crustal structure, flexure, and subsidence history of the Hawaiian Islands, *J. geophys. Res.*, **94**, 10473–10500.

Watts, A. B., ten Brink, U. S., Buhl, P., & Brocher, T. M., 1985. A multichannel seismic study of lithospheric flexure across the Hawaiian - Emperor seamount chain, *Nature*, **315**, 105–111.

Watts, A. B., Peirce, C., Collier, J., Dalwood, R., Canales, J. P., & Henstock, T. J., 1997. A seismic study of lithospheric flexure in the vicinity of Tenerife, Canary Islands, *Earth Planet. Sci. Lett.*, **146**, 431–447.

Weaver, B., Kar, A., Davidson, J., & Colucci, M., 1996. Geochemical characteristics of volcanic rocks from Ascension Island, South Atlantic Ocean, *Geothermics*, **25**, 449–470.

Weigel, W. & Grevemeyer, I., 1999. The Great Meteor Seamount: seismic structure of a submerged intraplate volcano, *Journal Of Geodynamics*, **28**, 27–40.

White, R. S., McKenzie, D., & O'Nions, R. K., 1992. Oceanic crustal thickness from seismic measurements and rare earth element inversions, *J. geophys. Res.*, **97**, 19683–19715.

Williamson, P. R., 1990. Tomographic inversion in reflection seismology, *Geophys. J. Int.*, **100**, 255–274.

Zandt, G. & Furlong, K. P., 1982. Evolution and thickness of the lithosphere beneath coastal California, *Geology*, **10**, 376–381.

Zelt, B. C., Ellis, R. M., Clowes, R. M., & Hole, J. A., 1996. Inversion of three-dimensional wide-angle seismic data from the southwestern Canadian Cordillera, *J. geophys. Res.*, **101**, 8503–8529.

Zelt, C. A., 1989. *Seismic structure of the crust and upper mantle in the Peace River Arch region*, Ph.D. thesis, Univ. British Columbia, Vancouver, B.C.

Zelt, C. A., 1998. Lateral velocity resolution from three-dimensional seismic refraction data, *Geophys. J. Int.*, **135**, 1101–1112.

Zelt, C. A. & Barton, P. J., 1998. Three-dimensional seismic refraction tomography: A comparison of two methods applied to data from the Faeroe Basin, *J. geophys. Res.*, **103**, 7187–7210.

Zelt, C. A. & Smith, R. B., 1992. Seismic traveltime inversion for 2-D crustal velocity structure, *Geophys. J. Int.*, **108**, 16–34.

Zelt, C. A., Hojka, A. M., Flueh, E. R., & McIntosh, K. D., 1999. 3D simultaneous seismic refraction and reflection tomography of wide-angle data from the central Chilean margin, *Geophys. Res. Lett.*, **26**, 2577–2580.

Zhang, H. & Thurber, C. H., 2003. Double-Difference Tomography: the method and its application to the Hayward Fault, California, *Bull. Seismol. Soc. Am.*, **93**, 1875–1889.

Zindler, A., Staudigel, H., & Batiza, R., 1984. Isotope and trace-element geochemistry of young Pacific Seamounts - implications for the scale of upper mantle heterogeneity, *Earth Planet. Sci. Lett.*, **70**, 175–195.

Zucca, J. J., Fuis, G. S., Milkereit, B., Mooney, W. D., & Catchings, R. D., 1986. Crustal structure of northeastern California, *J. geophys. Res.*, **91**, 7359–7382.

Index